CRANFIELD INSTITUTE OF TECHNOLOGY

DEPARTMENT OF AIRCRAFT DESIGN

COLLEGE OF AERONAUTICS

Ph.D. Thesis

Academic Year 1986

N.B.PARACHA

THE COMPRESSIVE POST-BUCKLING BEHAVIOUR OF THIN PLATES WITH CUTOUTS

Supervisor: Dr. Joseph Loughlan

February 1987

THIS WORK IS DEDICATED

TO MY LATE PARENTS

ACKNOWLEDGEMENTS

I wish to express my thanks to Dr. J Loughlan whose help, guidance and encouragement contributed a great deal to the project and whose pleasant personality made the stay at the institute very enjoyable.

The support and valuable advice given by all of my friends and colleagues is gratefully acknowleged.

I wish to express my sincere gratitude to my wife Gul for her love, care and understanding, and to my children Asad, Bilal and Beenish for their love and affection.

I am thankful to Mina Guneshpuri for her help in the wordprocessing.

Finally, I am grateful to Almighty Allah for giving me health and wisdom to accomplish this task.

ABSTRACT

This thesis presents an investigation of the buckling and post-buckling behaviour of plates with cutouts under uniform compression. The theoretical analysis developed for this purpose is based on a combined finite element/-spline procedure which formulates a mathematical represe-ntation of the membrane stresses within the plate accor-ding to its flat and unbuckled state. These mathematical representations are then utilised in the subsequent energy analysis to determine the point of initial buckling and in a semi-energy post-buckling analysis to determine behaviour of plate after initial instability. A comprehensive study is made with regard to buckling loads, in-plane displacements, out-of-plane deflections and the internal stress variations of simply supported square plates with centrally located circular and square cutouts. The analysis caters for the nonlinearity due to changes in the buckled shape in the post-buckling region. The results have, however, been presented for both single term and multiterm solutions. An experimental investiga-tion has also been conducted to obtain information on displacements and stresses. Plates with circular and square cutouts have been tested on a rig designed and manufactured at the College of Aeronautics. The present theoretical results have been compared with the

theoretical and experimental results of other investigators. The theoretical results are shown to be in fairly good agreement with the experimental results of plates with circular and square cutouts of various sizes.

CONTENTS

LIST OF FIGURES

NOMENCLATURE

a_i	Arbitrary integers to define 'x' terms of the deflection funtion
A_i, A_j, A_m, A_n	Coefficients in the deflection function
b	Width of the plate
b_j	Arbitrary integers to define 'y' terms of the deflection funtion
c	Radius of the hole
C_i	Coefficients of cubic B-spline
C_{ij}	Coefficients of bicubic B-spline
D	Plate flexural rigidity $D = \frac{E\,t^3}{12\,(1-\upsilon^2)}$
E	Young's modulus of elasticity
G	Modulus of elasticity in shear
I	Second moment of area
K	Buckling coefficient of a perforated plate
K_u	Buckling coefficient of an unperforated plate
M_x	Moment per unit width of plate perpendicular to the 'x' direction
M_y	Moment per unit width of plate perpendicular to the 'y' direction

M_{xy}	Twisting moment per unit width of a plate perpendicular to the 'x' direction
N_x	Mid-plane force per unit width of a plate in the 'x' direction
N_y	Mid-plane force per unit width of a plate in the 'y' direction
N_{xy}	Mid-plane shearing force per unit width of a plate
P	In-plane load corresponding to applied displacement
P_{cu}	Critical load of an unperforated plate
t	Plate thickness
U	Applied edge displacement
U_B	Strain energy due to bending and twisting
U_{cu}	Critical displacement of an unperforated plate
u	Displacement of a point in the middle plane of the plate in 'x' direction
M	Strain energy due to membrane stresses
v	Displacement of a point in the middle plane of the plate in 'y' direction
w	Out-of-plane deflection
x, y, z	Cartesian co-ordinates

ϵ_x	Direct strain in the 'x' direction
ϵ_y	Direct strain in the 'y' direction
γ_{xy}	Shearing strain in the xy plane
δ_x, δ_y	Direct stresses
τ_{xy}	Shearing stresses
$\delta_{x1}, \delta_{y1}, \tau_{xy1}$	Stresses corresponding to system 1
$\delta_{x2}, \delta_{y2}, \tau_{xy2}$	Stresses corresponding to system 2
$\delta_{x3}, \delta_{y3}, \tau_{xy3}$	Stresses corresponding to system 3
λ's	Knot positions in 'x' direction
μ's	Knot positions in 'y' direction
υ	Poisson's ratio

ϵ_x	Direct strain in the 'x' direction
ϵ_y	Direct strain in the 'y' direction
γ_{xy}	Shearing strain in the xy plane
δ_x, δ_y	Direct stresses
τ_{xy}	Shearing stresses
$\delta_{x1}, \delta_{y1}, \tau_{xy1}$	Stresses corresponding to system 1
$\delta_{x2}, \delta_{y2}, \tau_{xy2}$	Stresses corresponding to system 2
$\delta_{x3}, \delta_{y3}, \tau_{xy3}$	Stresses corresponding to system 3
λ's	Knot positions in 'x' direction
μ's	Knot positions in 'y' direction
υ	Poisson's ratio

CHAPTER ONE

INTRODUCTION AND REVIEW OF LITERATURE

INTRODUCTION AND REVIEW OF LITERATURE

1.1 Introduction

A thin flat plate under the action of in-plane compressive loading in its middle plane is deformed but remains completely flat when the edge forces are sufficiently small. By increasing the load a state is reached when the flat form of the equilibrium of the plate becomes unstable and the plate bends or buckles slightly. The in-plane load which is just sufficient to keep the plate in the slightly bent form is referred to as the critical or buckling load. Beyond this stage the membrane stresses come into play; the load-deflection relationship exhibits a stable character and the plate is still capable of carrying increased load without failure, provided, the post-buckling stresses in the plate remain in the elastic range.

For the past few decades structural members, fabricated from thin plates, have been the centre of immense research activity. During the design of thin walled structures it is essential to establish whether increased load can be carried after initial buckling and in order to understand the behaviour of a buckled structure, the

post-buckling analyses of plates and plated structures have been a focus of attention of many researchers.

The stressed skin of structures like steel bridges, aircraft wings and fuselages may contain holes. The knowledge of the influence of such holes on stress and deformation patterns is also relevant in the design of thin-walled structures. The buckling behaviour of perforated plates has been examined by a number of investigators in the past [8-31]. The work of the earlier researchers is summarised by Bulson [3]. The subject has also been reviewed by Preobrazhenskii [17]. The ultimate load carrying capacity of plates with cutouts has also been examined by some of these researchers [10,11,26-30] . The behaviour of thin plates with holes, with regard to deformations and internal stress variations in the post-buckling region, received relatively little attention [10, 26 & 29] and, therefore, needs to be investigated in greater detail.

The complexity of the pre-buckling stress distributions within a perforated plate and the stress free conditions around the hole boundary, make the buckling and nonlinear post-buckling analyses of a plate with a cutout a fairly involved task. The work presented in this thesis investigates the buckling and post-buckling behaviour of plates

with holes prior to collapse. The theoretical analysis has been developed for simply supported rectangular plates containing any shape of centrally located cutout and subjected to in-plane compressive loading. The analysis is, however, able to deal with non centrally located cutouts as well as any other type or combination of boundary conditions. The analysis procedure proposed by the author is briefly described as follows. The pre-buckling stress distribution is analysed by the finite element method, which is considered to be more accurate than the earlier methods where the plate was assumed to have an infinite length during the stress analysis. The stress data from the finite element analysis is then used to obtain a mathematical representation of the stresses through the application of a bicubic spline analysis, the details of which are described in chapter three. There are two major advantages of using bicubic spline functions in the energy evaluation during the buckling and post-buckling analyses. Firstly, in the post-buckling analysis, a very large number of finite elements are replaced with a relatively small number of spline panels which reduces computational effort and consequently allows the nonlinear post-buckling analysis to be achieved with reduced difficulty. Secondly, because a continuity up to the second derivative is achieved during the evaluation of bicubic spline functions, the stress

compatibility at the spline panel junctions greatly improves the accuracy of the analysis. The deflection function given by equation 4.1, and the stress functions obtained from the spline analysis are used in the Rayleigh-Ritz energy approach to obtain the buckling solution. In the post-buckling analysis, the stresses are classified into three stress systems as explained in chapter four. The stresses in system 1 are those obtained from the applied in-plane displacement assuming no lateral deflections. Stresses in system 2 are the post-buckling stresses of an unperforated plate assuming zero end compression and are obtained by solving the Von Karman compatibility equation according to an assumed lateral deflection system. The stress free boundary condition at the hole edge is achieved by applying back the post-buckling stresses determined from the Von Karman analysis at the hole boundary to obtain the stresses within the perforated plate which comprise stress system 3. Stresses in systems 1 and 3 are evaluated by the Combined finite element/spline analysis. The resultant stresses of the three systems are then used in the subsequent energy minimisation of the semi-energy post-buckling analysis. The post-buckling analysis is carried out for the case where buckled shape of the plate is allowed to change from its initial buckling mode, i.e. more than one term of the deflection function is

considered in the solution process.

Two types of loading - uniform displacement and uniform stress - have been investigated. Each type results in different displacement and stress patterns in the plate and consequently in different buckling behaviour. Figure 1.1 shows a schematic diagram of pre-buckling in-plane distortions. When a plate is subjected to uniform stress loading, the in-plane displacement of the loaded edge is non uniform because of the presence of hole. In the same way the stress distribution at the loaded edge is non uniform if the loaded edge is held straight during the loading process. Figure 1.2 illustrates the variation of pre-buckling stress σ_x at different sections for the two types of loading conditions according to the same average applied stress. Different patterns of stress variation can be noticed from these curves particularly at the loaded edge and at the minimum section. The uniform stress loading is seen to result in a higher stress concentration than the uniform displacement loading. The buckling analysis has been carried out for both these types of loading conditions. The post-buckling analysis has been carried out for the more practical case of uniform displacement loading. The proposed analysis or its modification is capable of handling other types of loading conditions, which generate non-uniform pre-

buckling stresses, in perforated or unperforated plates. One example is the locally distributed or patch loading in a propped structure.

The theoretical analysis has been applied to simply supported square plates with centrally located circular or square cutout. Experimental buckling and post-buckling results have also been obtained for these cases. In view of the fact that openings larger than half the size of the plates are unlikely to be used in practice, the theoretical evaluations of the results were confined to cutouts having a maximum diameter/side(for square cutout) equal to half the width of the plate. The variation of buckling load with hole size/shape has been presented and the theoretical results have been compared with the estimated experimental buckling loads. In the post-buckling region, load ~ in-plane-displacement behaviour, load ~ out-of-plane deflection behaviour and internal stress variation have been examined theoretically and comparisons have been made with the experimental results.

1.2 Unperforated Plates

The study of post-buckling and ultimate behaviour of plates and thin-walled structures has drawn the attention

of many investigators in the past four decades [48-58]. Reviews on the subject are also found in these publications and in references 1,2 and 3. For simple problems of rectangular plates with regular boundary conditions, exact solutions of the basic equilibrium equations may be achieved with little difficulty. Where exact solution is not possible, approximate energy and other numerical methods may be found useful. These include the Rayleigh Ritz energy approach, the Galerkin method, the Lagrangian multiplier method and more recently the finite element and finite strip techniques.

At the point of buckling, where out-of-plane deflections are about to grow, the stretching of the middle plane of the plate has negligible effect on the internal stresses in the plate. Thus the differential equations of equilibrium and compatibility and the energy solutions become fairly simplified. As the deflections start to increase, the stresses in the plate are accompanied by the stretching of the middle plane of the plate. The effects of these changes have to be taken into consideration in the post-buckling analysis.

In the energy approach, the strain energy due to bending and twisting is written in terms of approximate displacement functions which are represented by polyno-

mial or trigonometric series and arbitrary displacement coefficients. Each of these displacement functions has to satisfy boundary conditions at the loaded and unloaded edges. The loss in potential of the in-plane forces is also expressed in terms of the deflection coefficients and the Rayleigh Ritz Energy Method minimises the total potential of the structural system in terms of each of these coefficients to obtain the buckling solution. The lateral deflections grow after the initial instability and the stresses in the structure are due to bending and twisting as well as membrane action. The total strain energy stored in the structure is, therefore, the sum of strain energy due to bending/twisting and the strain energy due to in-plane forces. The semi-energy approach used in the post-buckling analysis minimises total strain energy with respect to the arbitrary deflection coefficients. The energy methods have been reviewed and used by many researchers in the past, notably by Rhodes and Harvey [55] and Loughlan [48], and have been found useful for the analysis of plates as well as thin walled beams, struts, columns and other structural members.

Galerkin's method can be used as an alternative to Rayleigh-Ritz solution. This requires the deflection functions to satisfy all the boundary conditions; but instead of evaluating energies the expression for out-of-

plane deflection is substituted in the basic equilibrium equation. Since the deflection function is approximate there is an error which needs to be made as small as possible. This is achieved by Galerkin's method . The method is, however, reported to be difficult to apply in the case of plates with highly irregular boundaries or complex loading conditions.

The Lagrangian multiplier method is discussed in reference 3. The critical stresses evaluated by the energy methods are always found to be higher than the true critical stress. In the Lagrangian multiplier method the approximate solution can be obtained in two ways which permits the computation of a lower as well as an upper limit to the true critical stress. In the energy method the total potential energy is minimised with respect to the undetermined coefficients in each of the terms of the deflection function. In the Lagrangian multiplier method the condition that the series expansion of the deflection function, as a whole, satisfies the boundary conditions is satisfied mathematically during the minimisation process by the use of Lagrangian multipliers. For satisfying the boundary condition for the entire function, as a whole, some constraining relationship has to be introduced. Limiting this relationship in the Lagrangian multiplier method has the effect of giving

the plate a greater edge freedom, thus reducing the critical stress. The minimisation of the total potential energy is subject to that relationship.

The finite element method [5,6] has been developed in the past two decades as a versatile technique of analysing problems associated with the behaviour of structures. The popularity of this method of analysis is due to the influx of digital computers and their power of handling the numerical techniques, as well as its ability to deal with complex geometries and boundary conditions. The stability analysis of plates by the finite element method involves the formulation of the initial stress stiffness matrix (also known as the geometric stiffness matrix) and the linear elastic stiffness matrix. These matrices are formulated by satisfying displacement compatibility at the element boundary and establishing continuity and equilibrium at each node. The linear buckling problem is a standard eigenvalue solution; the lowest eigenvalue determines the critical load and the corresponding eigenvector defines the buckled shape. The nonlinear post-buckling analysis is done by developing and solving incremental equilibrium equations. The variation of applied load and nonlinearity in the post-buckling region is solved incrementally or iteratively or by combinations of iterations and increments [11].

1.3 Plates with Holes

Two of the earliest published studies on the instability of simply supported rectangular plates with circular holes were by Levy et al [8] and Kumai [9]. Their work has been reviewed by Bulson [3] and Ritchie [10]. Levy et al presented a method for computing the compressive buckling load of a simply supported plate with a reinforced circular hole. Plates with unreinforced holes were also studied. They observed a small decrease in the buckling stress compared to that of an unperforated plate, maximum 14 percent, for unreinforced holes but noticed marked increases in the buckling stress by introducing hole reinforcements of the doubler type. Kumai [9] also studied the variation of buckling stress with the hole size for simply supported plates with circular holes. He reported 25 percent reduction in buckling load with respect to an unperforated plate as against 14 percent evaluated by Levy et al for the same plate. The distribution of pre-buckling stresses were assumed by these investigators to be the same as those of an infinite plate with a circular hole under uniform compression. The difference between the two types of results is attributed to the different deflection functions chosen for each analysis. Kumai's experimental results were in closer agreement with his theoretical results as compared

with those reported by Levy et al.

Buckling of simply supported plates with a central circular hole under uniform edge displacement has been analysed by A.L. Schlack Jr. [24 & 25]. He assumed polynomial functions to represent in-plane and out-of-plane displacements. These functions were used in the Ritz approach to derive an expression for the potential energy of the system in terms of the arbitrary constants. By differentiating with respect to each constant in turn a set of simultaneous equations was obtained. By putting the determinant equal to zero an expression for the critical displacement was found. An average value of end load corresponding to the critical displacement was used to evaluate critical loads. His experimental buckling load, defined as the inflection point on the load deflection curve, was in good agreement with his theoretical predictions.

Kawai and Ohtsubo [12] utilised the finite element formulation to obtain the initial in-plane stress distribution before buckling. Using this information the critical stress was determined by the Rayleigh-Ritz procedure. For numerical convenience the double integration encountered in the energy procedure were transformed into line integrals with the help of Gauss´ theorem. To

show the validity of the procedure, Kawai and Ohtsubo evaluated the buckling strength of perforated square plates with various boundary conditions and subjected to uniaxial compression. The out-of-plane deflections were represented by polynomial functions. The stress distribution of a square plate under a prescribed edge displacement was first analysed by the finite element formulation using constant stress triangular elements. The energy integrals for each element were summed up throughout the plate to obtain the total energy. The results obtained for the critical stress of a simply supported perforated plate subjected to uniform edge displacement were in good agreement with the theoretical and experimental results of Schlack [25] and Fujita [14] for various hole diameters [Fig. 1.3]. From this figure it is observed that the in-plane restraint conditions of the side boundaries has a considerable influence on the buckling stress of a perforated plate. For plates under uniform displacement loading with no restraint on the sides the buckling coefficient decreases first from 4.0 for a solid plate to 3.7 at c/b=0.35 and then increases to over 6 at c/b=0.7. For plates with a comparatively larger hole sizes, e.g. c/b=0.5 or higher, subjected to uniform edge compression the stress distribution at the loaded edge is such that the stresses are concentrated towards the sides [Fig. 1.2]. As explained in reference 12, a plate with

larger hole hole size can be represented by a simplified model of two strips which resist most of the applied stresses. The buckling coefficient depends on the width of these strips. The buckling coefficient increases as the width becomes smaller.

The buckling results presented by Kawai and ohtsubo [12] have been confirmed by Ritchie and Rhodes [10,26] who combined the finite element and energy method to investigate the buckling and post-buckling behaviour of plates with centrally located circular holes. Experiments were conducted on square plates with different hole sizes and comparisons with the theoretical predictions were given. The pre-buckling stress analysis was accomplished by the finite element method. Constant strain triangular elements were used to define the finite element grid. Stresses in each of the element were evaluated and this information was used during the subsequent energy evaluation. The buckling analysis was carried out for two types of loading - the uniform stress and the uniform displacement cases. The buckled shape was assumed fixed along the loaded direction of the plate and was allowed to change across the loaded direction. A deflection function of the following form was chosen to represent the buckled shape.

$$w = \sin \frac{k\pi x}{a} \sum_{n=1}^{N} A_n \cos \frac{n\pi y}{2b} \qquad n = 1,2,3,\cdots$$

Using the Rayleigh-Ritz energy approach, the total strain energy in 1/4 of the plate was calculated from the energy contribution of each of the triangular elements. Since the stresses within the elements were constant, the energy evaluation was straight forward. During the integration process the limits of integration were set to take care of the presence of the hole. The minimisation of the total energy with respect to each of the deflection coefficients thus leads to the solution of the typical eigenvalue problem. Ritchie's theoretical buckling loads compared reasonably well with other investigators and with his own experimental results; proving the validity of his theoretical approach. Figure 1.4 shows the variation of buckling load with the size for the two types of loading considered and a comparison with the results of reference 12. The buckling load is seen to reduce with increase in hole size for the uniform stress loading case as was reported earlier.

Azizian and Roberts [11,27] presented finite element solutions for the buckling and geometrically nonlinear elasto-plastic collapse behaviour of plates with holes. Triangular elements having three corner nodes and five degrees of freedom per node were used to model the plates. Bending action was represented by a nine degree of freedom polynomial. Established finite element proce-

dures were followed to find the critical stress and buckled mode shape. In the finite element formulation, the buckling problem is ultimately reduced to the solution of the equation:-

$$\text{Det} \left[KL \right] + C \left[KG \right] = 0$$

where [KL] is the linear elastic bending and membrane stiffness matrix, and [KG] is the geometric stiffness matrix which depends on the membrane stresses prior to buckling. The lowest eigenvalue C defines the critical load factor and the corresponding eigenvector the buckled shape. The solutions presented in reference 11 cover square plates with centrally located square and circular cutouts subjected to uniaxial compression, biaxial compression and pure shear according to different support boundary conditions. Azizian and Roberts concluded that for the simply supported plates subjected to uniaxial and biaxial compression the buckling load is almost independent of the hole size up to half the plate width (c/b=0.5). Their results, however, show a reduction in buckling coefficient of 17 percent at c/b=0.4 [Fig. 1.5]. The results presented in ref. 11 give a lower prediction of the buckling loads than those of ref. 10 and 12 [Fig. 1.3 and 1.4]. The main reason for this difference is the way in which uniform displacement of the loaded edge is

enforced. In the finite element evaluation of the pre-buckling stresses, uniform compression of the loaded edges is ensured in references. 10 and 12 by applying uniform displacement at the nodes and restraining the in-plane distortion of these nodes. Azizian [11], on the other hand, constrained the loaded edges to remain straight in the plane of the plate by introducing very stiff, two degrees of freedom, shear elements connecting adjacent nodes. This method cannot possibly ensure that the loaded edge be kept absolutely straight and nodes towards the middle of the edge are more likely to distort as the load is increased. In the uniform stress loading situation, where the the distortion in the middle of the edge is higher than the sides, the buckling loads reduce as the hole size becomes large. Since the buckling loads of ref. 11 lie between the buckling loads presented in reference 10 for the two types of loading, uniform stress and uniform displacement, it is reasonable to conclude that the introduction of the shear elements could not rigidly enforce uniform compression of the loaded edge.

The theoretical and experimental results of the buckling coefficient for simply supported plates with centrally located circular and square cutouts obtained by Narayanan and Chow [28] is presented in figure 1.6. The theoretical buckling loads were computed by the finite

element method suggested by Sabir and Chow [18]. The experimental buckling loads were obtained by the inflection point method [24]. The inflection point is defined as the load corresponding to the point where the rate of change of slope of the load ~ deflection curve is minimum. The curves for the variation of the theoretical buckling results show a reduction in the buckling coefficient with increase in the hole size which indicate that the theoretical results were obtained for the plates subjected to uniform stress loading. The experimental buckling coefficients are seen to decrease for hole size up to d/a=0.4 (a´/a for square cutout) and then increase for d/a=0.5. The scatter in the experimental results for the plates with same size circular holes indicate the inaccuracy of the inflection point method for estimating experimental buckling loads. The variation of the buckling coefficient for simply supported square plates with square cutout presented in ref. 22 [Fig. 1.7 II(b)] show a similar trend to that presented in ref. 28 [Fig. 1.6].

The work presented by different investigators on the buckling behaviour of perforated plates show that various methods of analyses exhibit similar trend of results provided the loading and boundary conditions are kept the same. The experimental buckling loads are shown to agree

more closely for the loading condition where the loaded edges are held straight during the application of the loads.

Most of the work on perforated plates has generally been confined to the study of the initial instability [8-33], particularly for plates with a centrally located circular or square cutout. Few investigations have been reported on the post-buckling behaviour of thin plates with cutouts. The published studies on the post-buckling behaviour of perforated plates are by Yu and Davis [30] and Rithchie and Rhodes [10,26]. The former reported experimental investigations on the buckling and the post-buckling behaviour of thin-walled cold-formed structural elements with centrally located holes. But a more extensive theoretical and experimental investigations on square and rectangular thin plates with circular holes has been carried out by Ritchie [10].

In addition to the boundary conditions at the plate edges the post-buckling analysis of plates with holes requires satisfying the stress free boundary conditions at the hole edge. Ritchie [10] achieved this by applying stresses at the hole edge which were equal and opposite to the post-buckling stresses obtained after solving Von Karman's compatibility equation for the unperforated

plate. Prior to the complete post-buckling solution, i.e. minimisation of the total strain energy, these stresses are evaluated in terms of the deflection coefficients. For a solution containing more than one term of the deflection function, the stress resultants to be applied at the hole edge would have to be evaluated for each combination of the deflection coefficients in the multi-term solution. This makes the entire analysis very laboricus if the deflection function used for the post-buckling analysis contains more than a single term. To reduce labour, Ritchie [10] used a single term solution in the post-buckling analysis, i.e. an approximation was made that the buckled shape did not change from its initial buckling mode but that only its magnitude changed. The theoretical load ~ edge compression plot, shown in figure 1.9, illustrates the linearity of the post-buckling curves due to this assumption. The comparison [Fig. 1.8] of the theoretical load ~ deflection plots with the experimental results show reasonably good agreement. The most significant feature of his theoretical analysis, however, is the investigation of the internal stress distribution prior to and after buckling until collapse. The comparison of the theoretical and experimental stress variations showed a good agreement for plates with small holes at all load levels [Fig. 1.10] and for plates with large holes at loads prior to

or just after buckling. The stress variations at higher loads for plates with circular holes of size 0.5 and 0.6 times the plate width did not show a good agreement between his theoretical and experimental results [Fig. 1.11]. Ritchie attributed this difference to the fixed buckled shape used in the post-buckling region which also affects the stress free boundary condition at the hole edge. In the author's opinion the use of constant strain elements which are known to give a poor representation of the in-plane stresses and the numerical evaluation of the energies in each of the element could be far more significant factors.

A geometrically non-linear analysis was presented by Azizian [11] for the elasto-plastic post-buckling investigation of perforated plates to predict the ultimate load carrying capacity. The analysis was carried out for uniaxially compressed square plates with width/thickness ratios from 20 to 80 and assumed initial imperfections. Since the analysis was limited to relatively thick plates, i.e. lower width/thickness ratios, internal stress variation associated with the large deflections have not been investigated and the work was concentrated on predicting the ultimate load carrying capacity of perforated plates. The concept of incrementing displacements rather than loads was used to develop incremental

energy equations. Starting from the initial deflection the successive positions on the load ~ deflection curve were reached by incrementing nodal displacements. Each increment was based on the information of the previous step. The post-buckling analysis procedure did not take into account the changes in the buckled shape which obviously limits the accuracy of the analysis. Another source of inaccuracy in the analysis is that non-conforming elements were used. The refinement of the finite element mesh does not considerably improve the inaccuracy due to the use of non-conforming elements. Besides, solutions of the elasto-plastic collapse of perforated plates having low width to thickness ratios was reported [11] to show very slow convergence with the increasing number of elements. This is perhaps due to the poor representation of the membrane stress state by the linear displacement triangular elements. In general, all finite element non-linear solutions are regarded computationally time consuming and require significant computer storage and, therefore, the solution proposed in reference 11 may have limitations in practical use.

An approximate method of predicting the ultimate carrying capacity and post-buckling behaviour of plates with width to thickness ratio of less than 125 containing circular and square cutouts under uniaxial compression

has been presented by Narayanan and Chow [28]. Experiments were conducted to examine four parametric variations related to the size of the plate, its thickness, size and shape (circular or square) of the cutout and its eccentricity. Tests were conducted to measure the buckling and ultimate loads and were continued well into the post-peak range. The load ~ deflection behaviour was monitored in the elastic and plastic zones. The theoretical elastic analysis developed by Horne and Narayanan [59] was employed for tracing the elastic loading behaviour of the perforated plate. The concept of the redistribution of the stresses at the minimum section of a perforated plate vis a vis an unperforated plate suggested by Ritchie and Rhodes [26] was used to compute the stress distribution across the hole in the post-buckled range as illustrated in figure 1.12. It is interesting to note that this concept was used only to predict the theoretical elastic loading curve and the total applied load was obtained by integrating the approximate post-buckled stress distribution at the loaded edge of the perforated plate given by the following equation.

$$\sigma_{xh} = \sigma_{cr}^{h} \left(\frac{\delta - \delta_o}{\delta} \right) + E(\delta^2 - \delta_o^2) \frac{\pi^2}{16 a^2} \cdot \left[\left(3 + \frac{a^2}{b^2} \right) - 4 \sin^2 \frac{\pi y}{b} \right]$$

δ is the deflection corresponding to the applied load, δ_0 is the initial deflection, a and b are the sides of a plate and σ^h_{cr} is the elastic critical stress of the perforated plate. The ultimate load was estimated from the point of intersection of a theoretical elastic loading curve with the unloading line obtained from the rigid plastic theory [Fig. 1.12].

The theoretical results presented by Narayanan and Chow [28] have been compared with their experimental results, test results of Ritchie and Rhodes [26] and the theoretical results of Azizian [11]. Figure 1.13 (a) compares the effect of square and circular holes upon the ultimate strength of the perforated plates. It is observed from this figure that there is a drop in strength with the increasing hole sizes. This corresponds to the loss of stiffness of the plate due to the presence of holes. The ultimate strength of the plates with a square cutout is seen to have marginally lower strength than the plates with a circular hole. Figure 1.13 (b) shows a comparison between the theoretical predictions of Narayanan and Chow [28] and the test results of Ritchie and Rhodes [26]. It is pointed out that the theoretical analysis by Narayanan and chow, which was based on small deflections, was carried out for thick plates, i.e. width/thickness ratios of 80 or less, and the plates tested by Ritchie and

Rhodes were relatively thin, i.e. width/thickness ratio of 162, and were obviously subjected to large deflections during these tests. The theoretical predictions of reference 28 is, therefore, not strictly applicable to the above tests. The comparison of ultimate strength of plates with a circular hole between the theoretical results of Azizian [11] and Narayanan and Chow [28] are presented in figure 1.13 (c). Azizian computed the ultimate strength of perforated plates using an elasic--plastic nonlinear finite element formulation whereas Narayanan and Chow obtained the results by using the approximate method outlined in the above paragraph. It is observed from figure 1.13 (c) that there is close agreement between the results obtained by the two methods. The predictions of the ultimate capacity of the perforated plates by Narayanan and Chow [28] can be considered to be reliable on the basis of comparison between the theoretical predictions and the experimental results. Since the analysis presented by them is based on small deflection theory, the theoretical predictions are not valid for thin plates, i.e. for plates with width/thickness values in excess of 80 or so.

Thin shear webs containing cutouts are often found in aircraft wings and fuselage bulkheads, the diaphragms of box girders and the webs of prefabricated plate girders.

The behaviour of thick walled webs with cutouts has been investigated theoretically and experimentally in 60´s and 70´s. With the increasing requirement of thin walled structures and the need of design optimisation, the analysis of thin shear webs became the focus of attention of many investigators. Significant contributions to the experimental and theoretical investigations aimed at obtaining detailed information on the post-buckling strength of perforated thin web plates have been undertaken at University College Cardiff since 1977 [35]. These studies relate to the variation of the buckling coefficient with hole size for plates with circular and square cutout under shear loading according to a variety of boundary conditions. The ultimate shear capacity of plate girders with openings in webs have also been investigated [35-37].

The variation of the critical shear stress coefficient ´k´ with the diameter of a central circular cutout in a square plate is illustrated in figure 1.15 [38]. The buckling coefficients decrease with the increase in hole size for both clamped and simply supported edges. It can be seen from this figure that for the case of plates containing circular holes there is a near-linear relationship between the shear buckling coefficient ´k´ and the diameter/plate width ratio. A similar trend is observed

for plates with square and rectangular cutouts from the graphs shown in figure 1.16. The load corresponding to elastic critical stress can be considerably improved by introducing a ring type reinforcement around a circular hole. It was reported by Narayanan et al [36,37] that in all cases the critical load equivalent to an unperforated plate was achieved by employing a relatively small size of reinforcement ring to a circular hole. For a plate with a square cutout having a reinforcement strip on two opposite sides of the cutout, the critical stress of an equivalent unperforated plate can be achieved if the total length of each strip is at least 1.5-times the width of the cutout and the thickness is at least three times the thickness of the plate. This is reported to be true for all practical widths of reinforcement as the variation of 'k' with the width of the reinforcement is very small.

Concentric holes in structural members are most widely used and, therefore, the majority of researchers have focused their attention on the stability analysis of perforated plates with centrally located cutouts. There are, however, practical situations where it is necessary to have openings away from the centre of the plate, e.g. liquid containing vessels have flap valves positioned near the bottom of the partitions to transfer fluid from

one chamber to another. In a recent publication, Sabir and Chow [19] presented a study on the elastic buckling behaviour of plates containing eccentrically located circular holes. They investigated the effect of the degree of the eccentricity of a circular hole and its size on the buckling loads of simply supported and clamped square plates subjected to uniaxial, biaxial and shear loads. The location of the hole was kept along a diagonal of the square plate in all cases. The finite element method was used to obtain the elastic buckling loads. The pre-buckling stresses were evaluated using the triangular and rectangular membrane elements which were based on assumed strain, rather than displacement, fields. These elements were combined with bending elements to carry out the buckling analysis. The results presented by Sabir and Chow [Fig. 1.14] show a decrease in the buckling loads of plates with eccentric holes as the hole size becomes larger. The reduction in the buckling load can also be observed with increase in the eccentricity of the holes. For concentric holes it has been demonstrated theoretically and experimentally [10 and 29] that for plate subjected to uniform displacement loading the buckling load increases with increasing hole size. The buckling results shown in figure 1.14 correspond more closely to constant stress loading case, i.e. the buckling loads reducing with increasing hole size.

The results of Ref. 19 for eccentrically located holes may, therefore, be limited to smaller hole sizes only for any practical applications.

1.4 SPLINE ANALYSIS

The discussion on the use of bicubic B-splines for surface fitting and the subsequent use of these functions in the current analysis is given in chapters three and four. The process is concerned with the mathematical representation of smooth continuous relationships between variables which are defined initially by a set of data points. A cubic spline consists of a set of cubic polynomial arcs joined end to end with continuity in magnitude and in the first and second derivatives at each joint (or knot). A cubic B-spline is a special type of cubic spline used in curve fitting and interpolation problems and is defined to have non zero values at four adjacent intervals between knots and is zero everywhere else (see chapter 3 for definitions). Because of the localness of B-splines, the problems of illconditioning associated with the cubic spline functions have been solved with a reasonable accuracy. A bicubic B-spline to represent a surface is obtained by the tensor product of the cubic B-spline functions defined in the cartesian axis system.

Bicubic B-splines have been used by the author in the theoretical analysis to represent the internal membrane stresses in the plate. B-splines were first introduced by Schoenberg [43] in 1946 but received little further attention. Some twenty years later, after the work by Curry and Schoenberg [44], a number of authors advocated their use in problems of curve and surface fitting, smoothing and interpolation. Amongst these researchers are Cox [39,41], De Boor [42], Hayes and Halliday [40], who made substantial contributions in this field. These authors presented basic concepts for the mathematical representation of cubic and bicubic B-splines, procedures for their numerical evaluation and techniques for least square curve fitting. The reader interested in the use of spline functions may also refer to the publications of references 45,46 and 47.

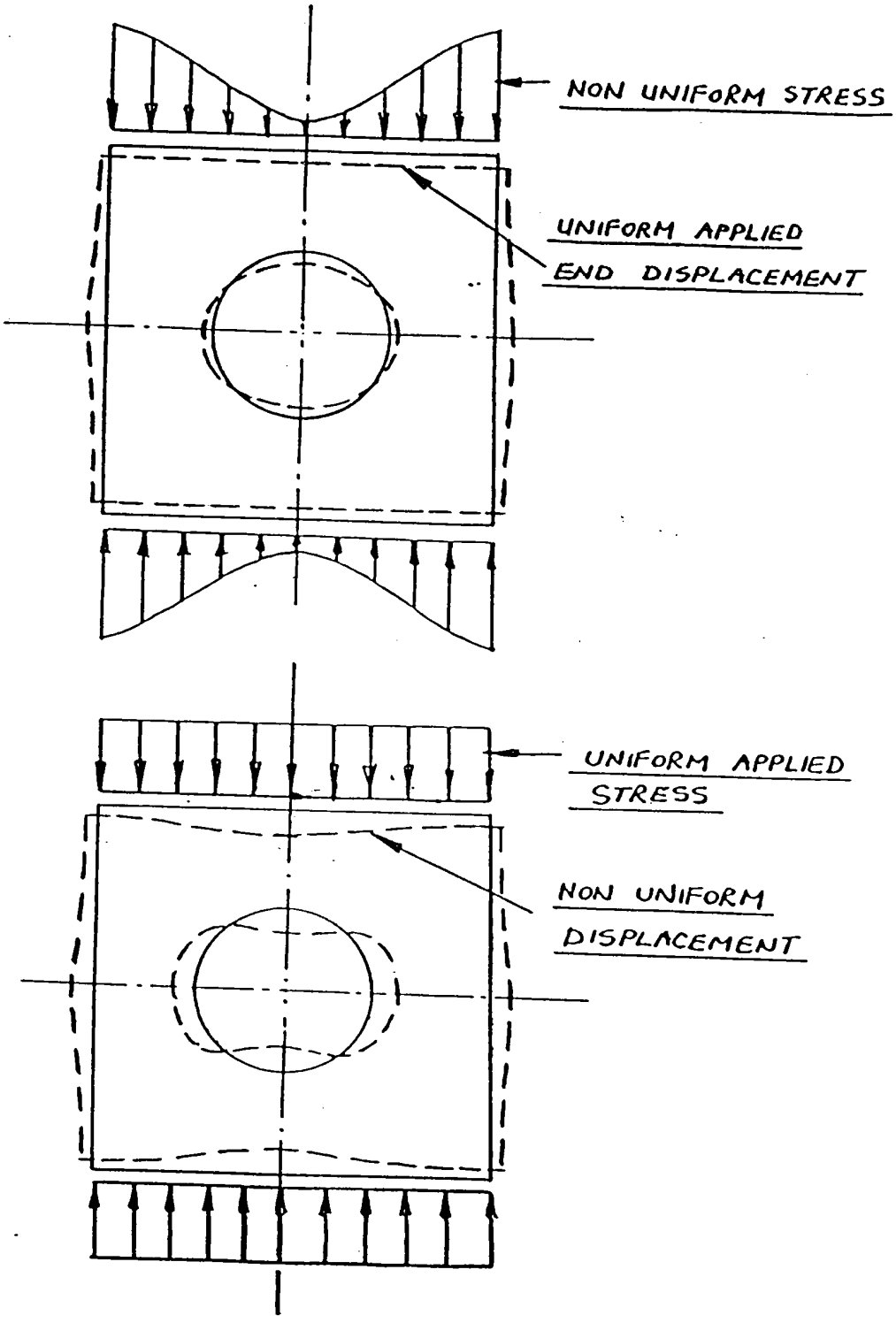

FIGURE 1.1 SCHEMATIC REPRESENTATION OF PRE-BUCKLING IN-PLANE DISTORTIONS

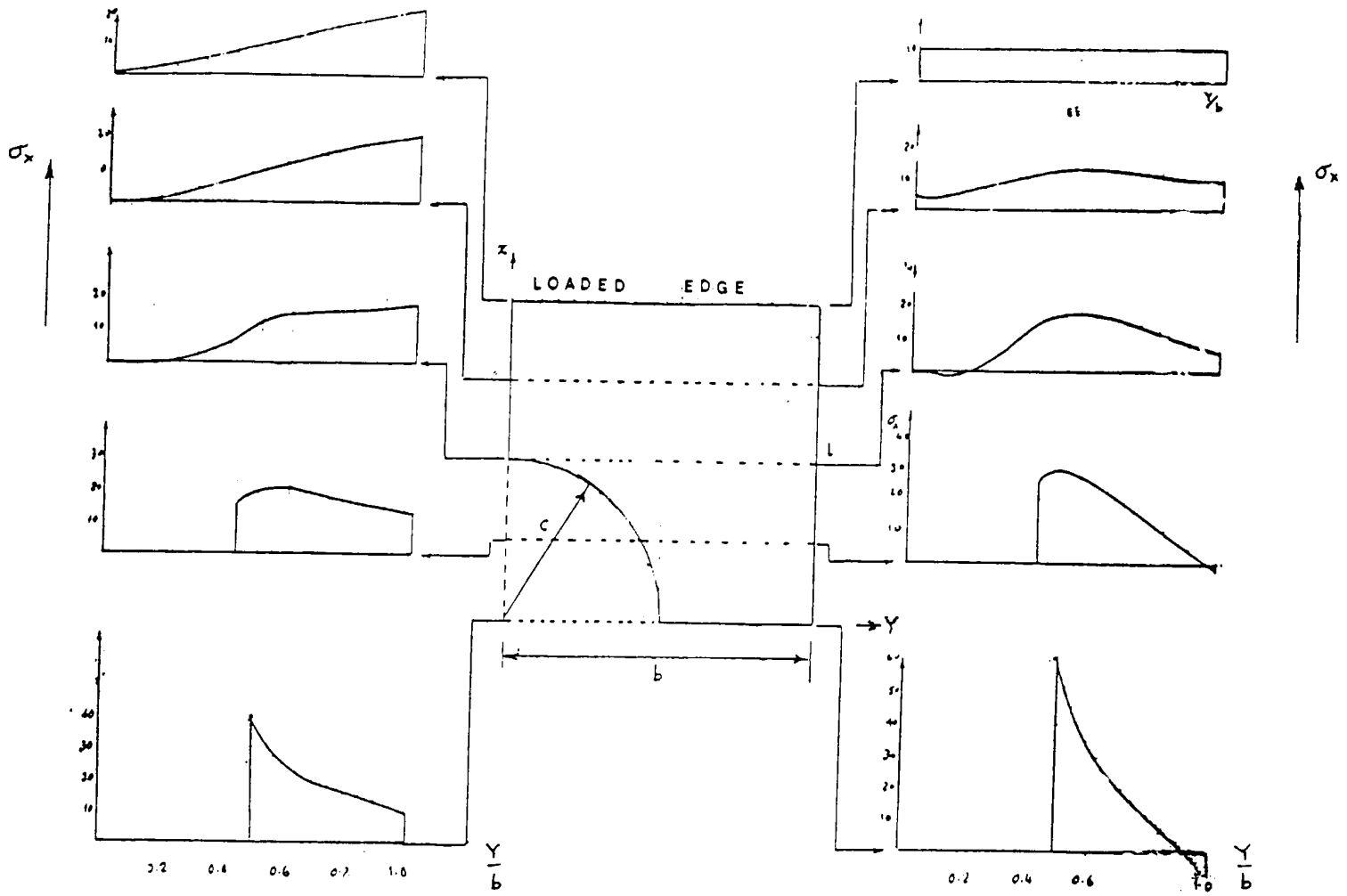

FIGURE 1.2 PRE-BUCKLING STRESS VARIATIONS AT DIFFERENT SECTIONS

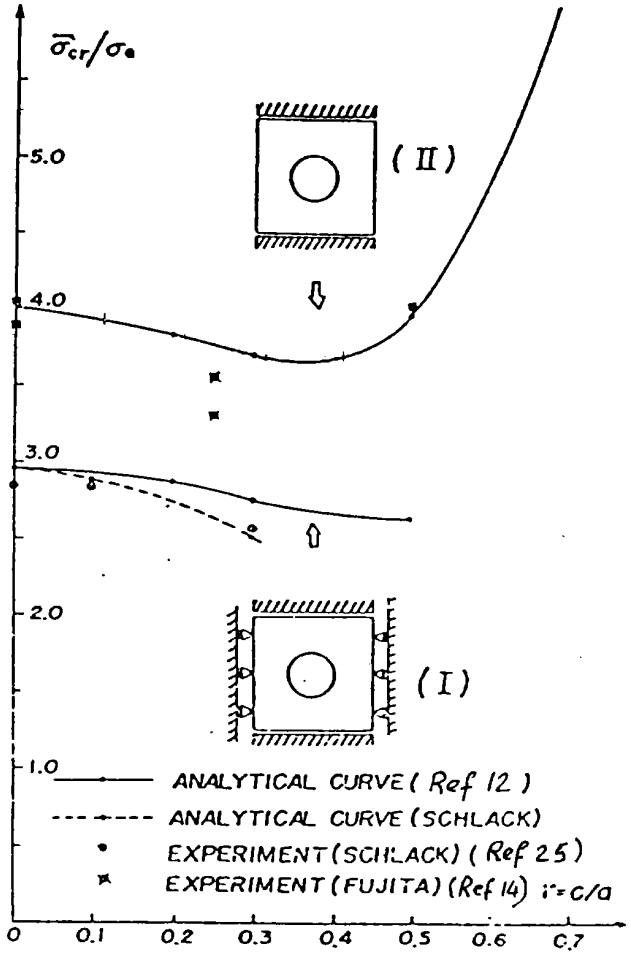

FIGURE 1.3 VARIATION OF CRITICAL STRESS WITH THE HOLE SIZE [REF. 12]

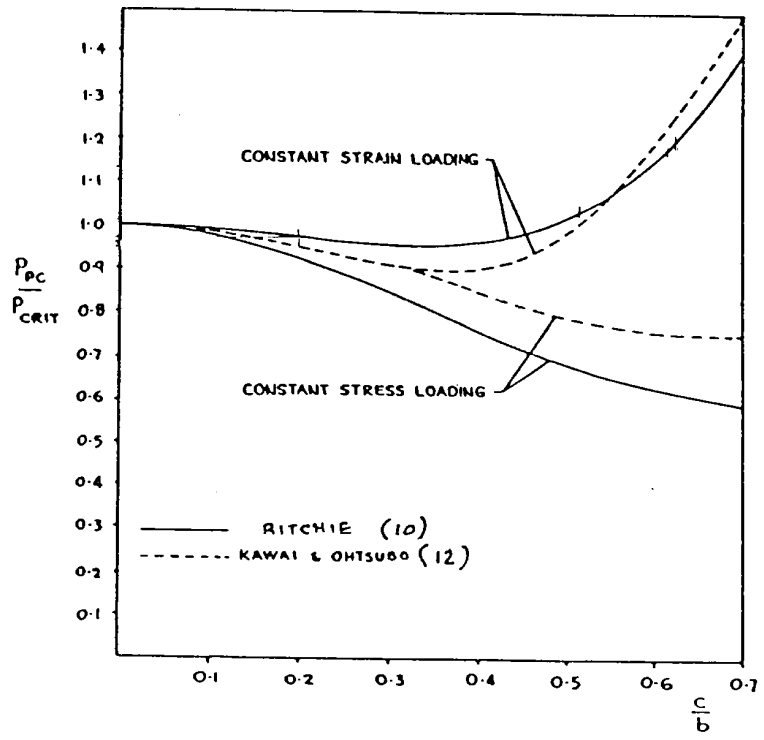

FIGURE 1.4 VARIATION OF THE CRITICAL LOAD WITH HOLE SIZE - PLATES WITH CIRCULAR HOLES [REF. 10]

c = RADIUS b = HALF PLATE WIDTH

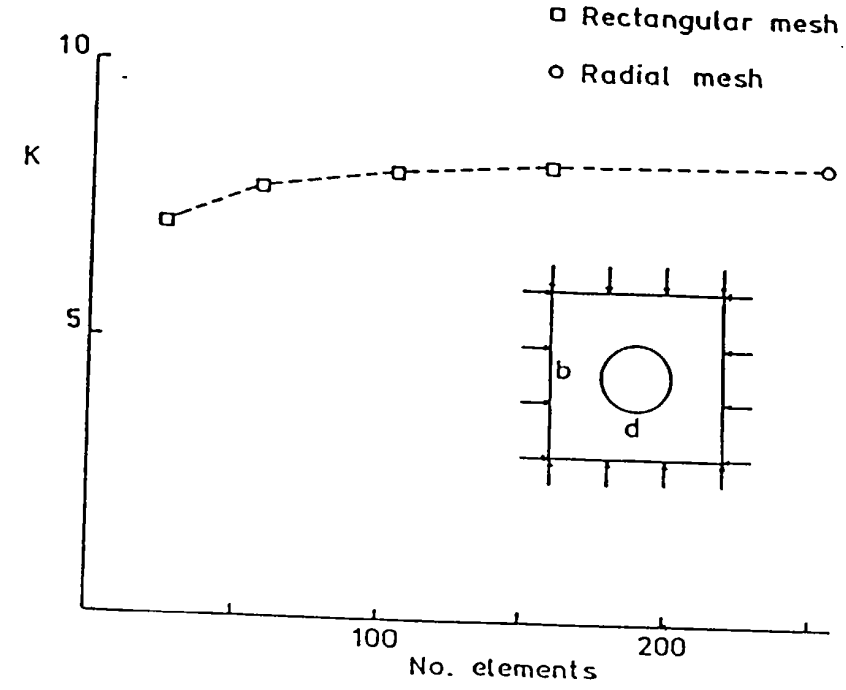

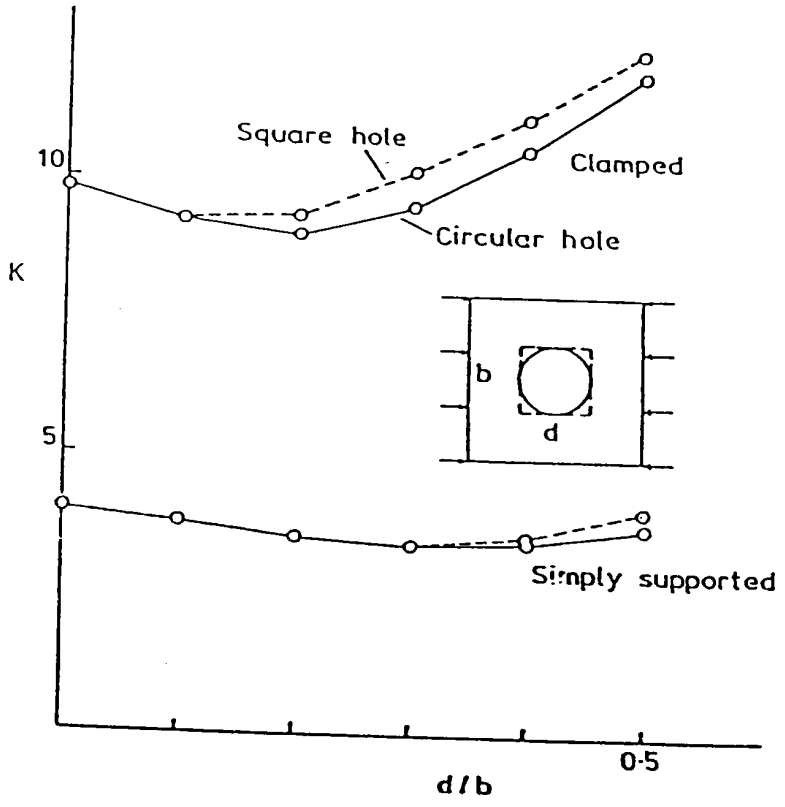

FIGURE 1.5 VARIATION OF THE BUCKLING COEFFICIENT WITH THE HOLE SIZE [REF. 11]

FIGURE ABOVE SHOWS UPPER BOUND CONVERGENCE OF 'K' FOR BIAXIAL LOADING

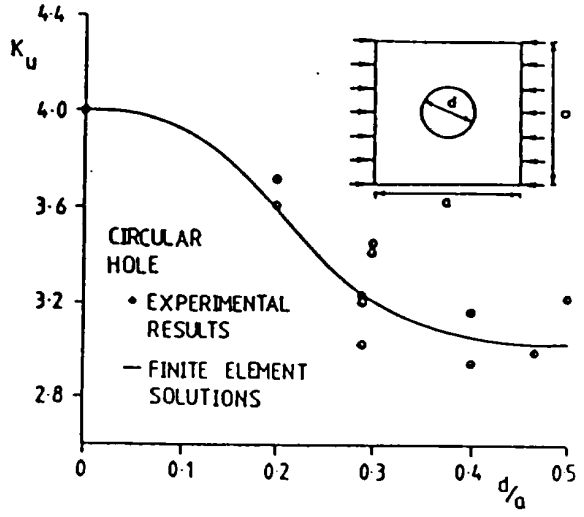

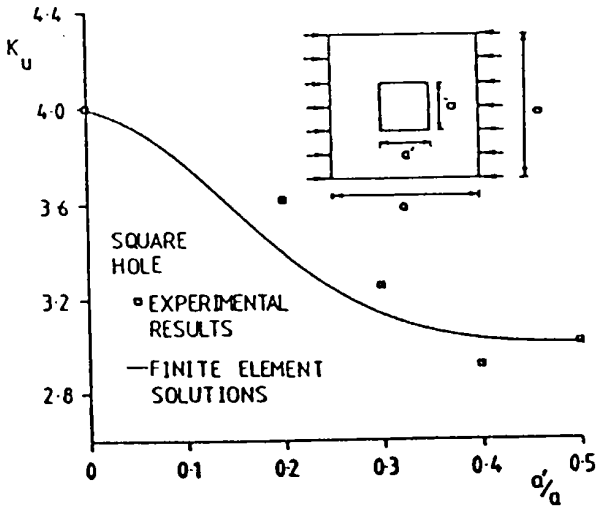

FIGURE 1.6 VARIATION OF THE BUCKLING COEFFICIENT WITH THE HOLE SIZE [REF. 28]

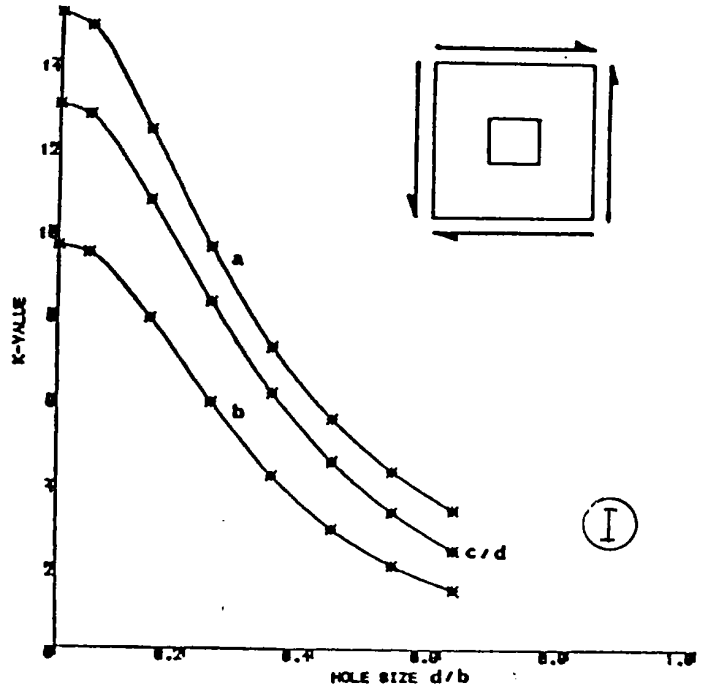

Buckling coefficient k versus hole/plate ratio for pure shear. (a) Clamped on all edges; (b) simply supported on all edges; (c), (d) clamped on two opposite edges, simply supported on other two.

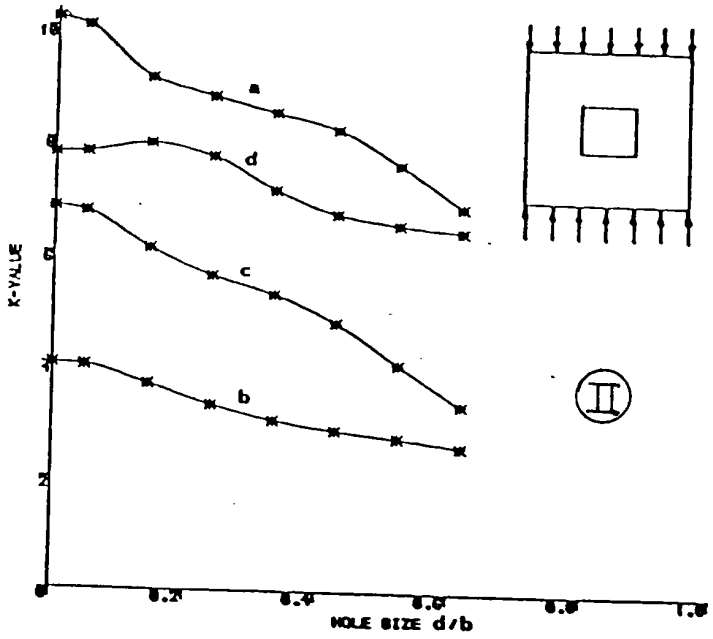

Buckling coefficient k versus hole/plate ratio for uniaxial compression. (a) Clamped on all edges; (b) simply supported on all edges; (c) clamped on loaded edges, simply supported on other two; (d) simply supported on loaded edges, clamped on other two.

FIGURE 1.7 BUCKLING COEFFICIENT K VERSUS HOLE/PLATE RATIO [REF. 22]

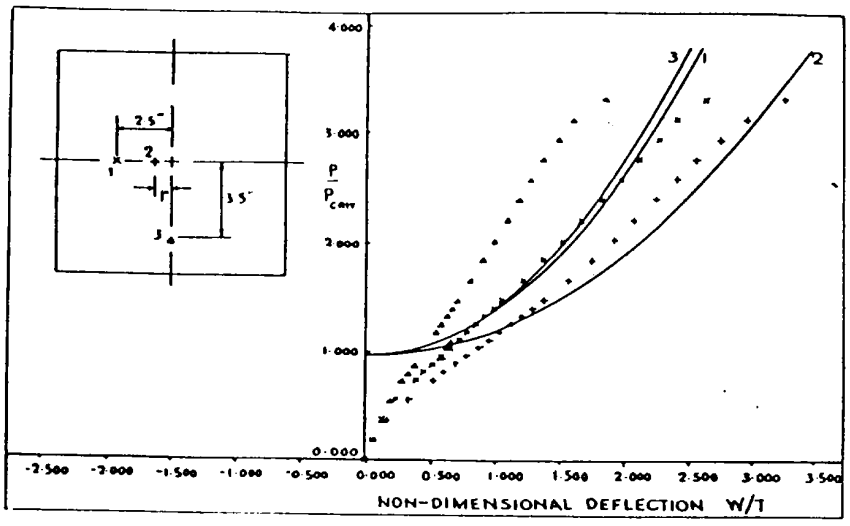

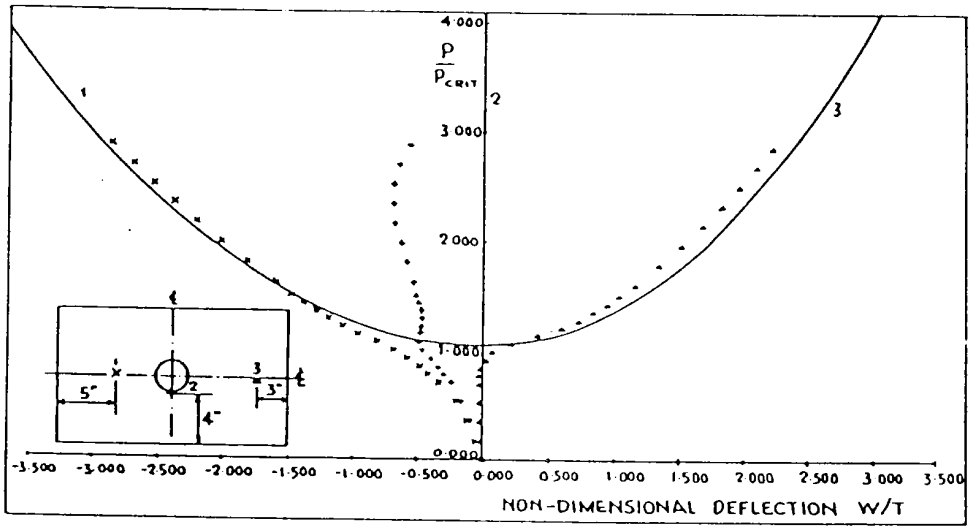

FIGURE 1.8 LOAD ~ OUT-OF-PLANE DEFLECTION [REF. 26]

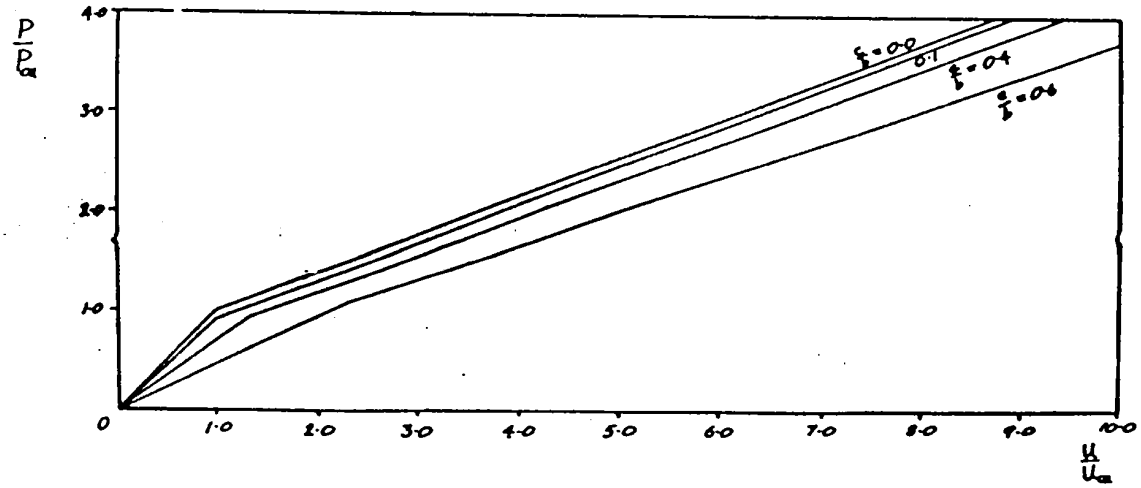

FIGURE 1.9 LOAD ~ EDGE COMPRESSION FOR VARIOUS HOLE SIZES PLATES WITH CIRCULAR HOLES [REF. 10]

c = RADIUS L HALF PLATE WIDTH

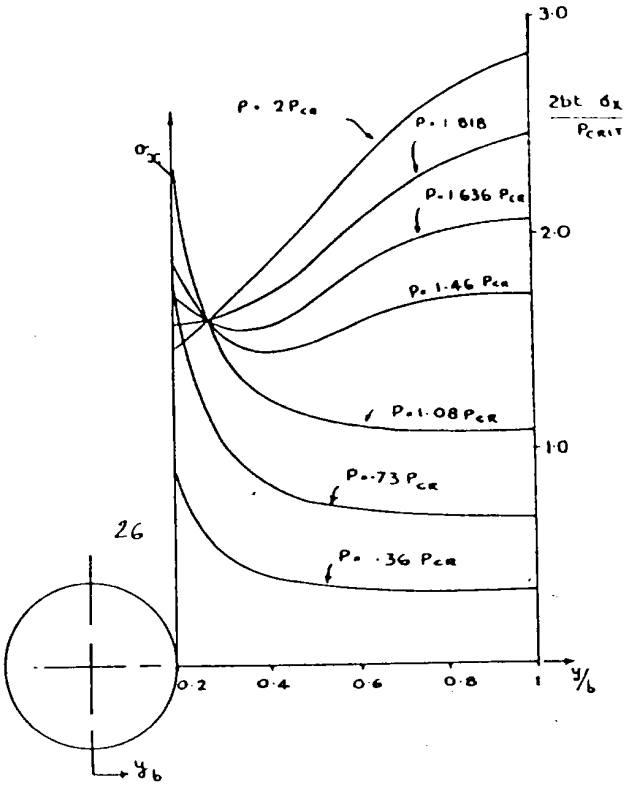

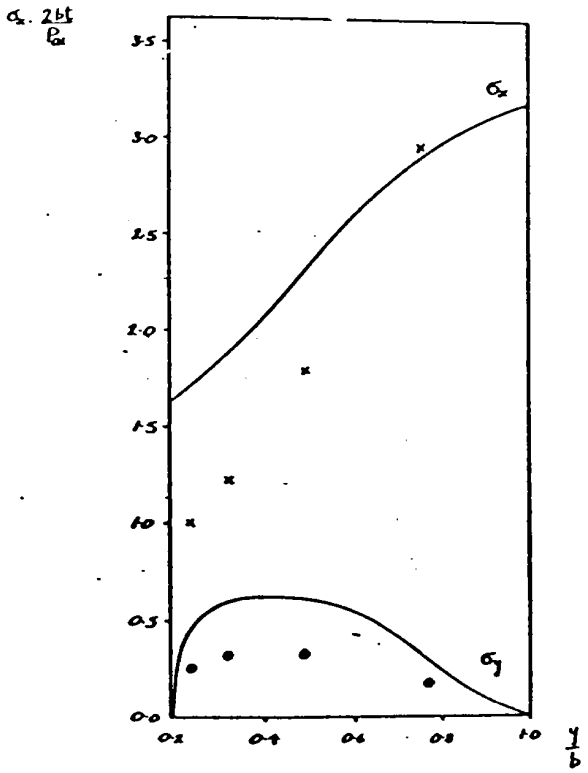

FIGURE 1.10 STRESS VARIATION AT THE MINIMUM SECTION
DIAMETER/PLATE WIDTH = 0.2 [REF. 10]

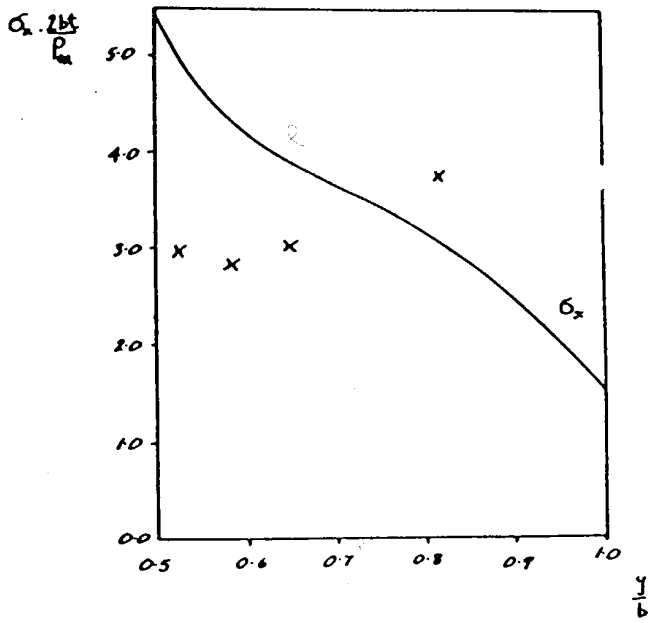

DIAMETER/PLATE WIDTH = 0.5

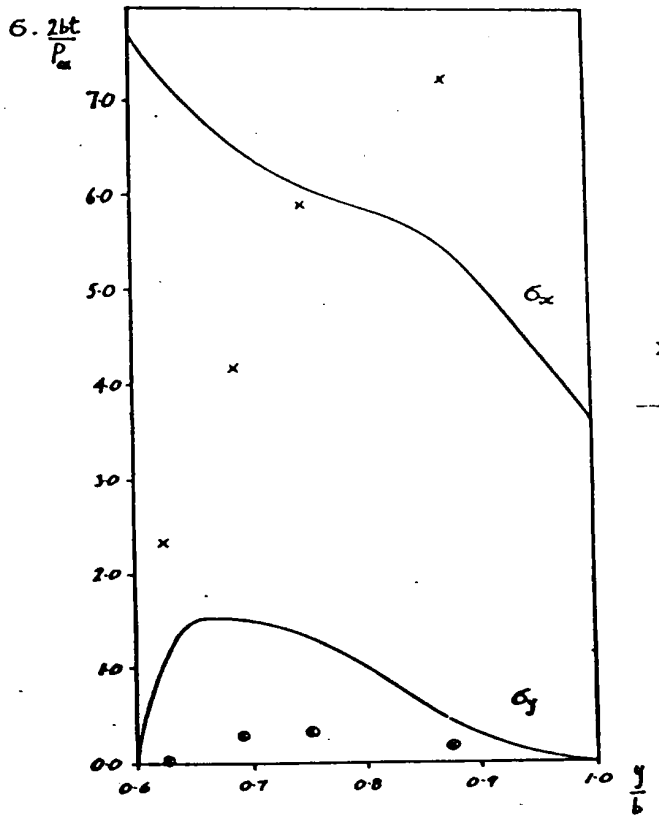

DIAMETER/PLATE WIDTH = 0.6

FIGURE 1.11 COMPARISON OF THE THEORETICAL AND EXPERIMENTAL STRESSES AT THE MINIMUM SECTION [REF. 10]

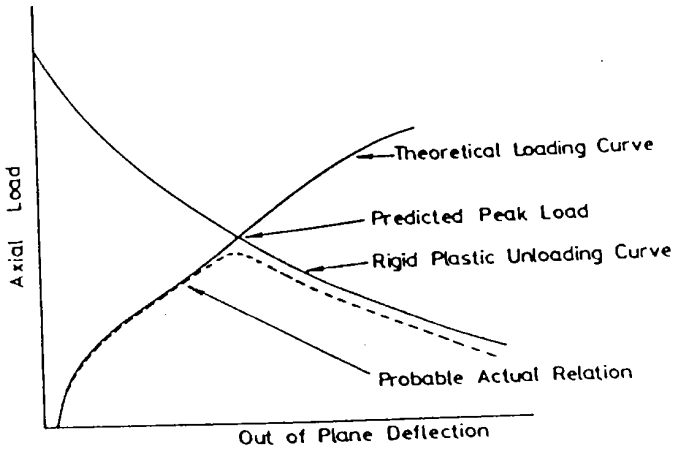

Load–deflection behaviour of an axially compressed plate.

$$\frac{a}{t}=70 \quad \frac{d}{a}=0.2 \quad \frac{\delta_e}{t}=0.145\,\frac{a}{t}\sqrt{\frac{\sigma_{ys}}{E}}$$

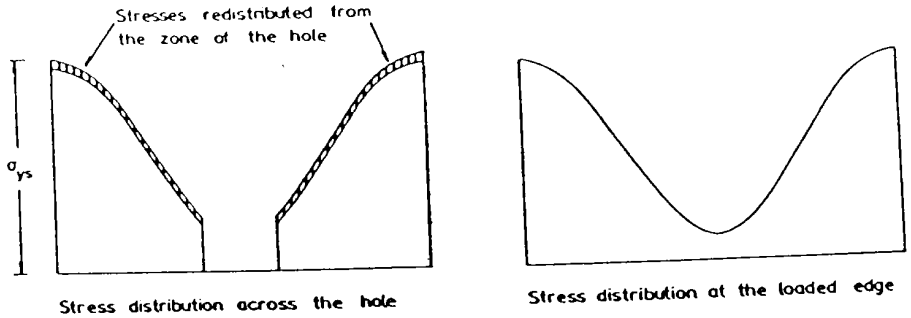

Typical stress distribution.

FIGURE 1.12 PREDICTION OF THE ULTIMATE CAPACITY OF PERFORATED PLATES [REF. 28]

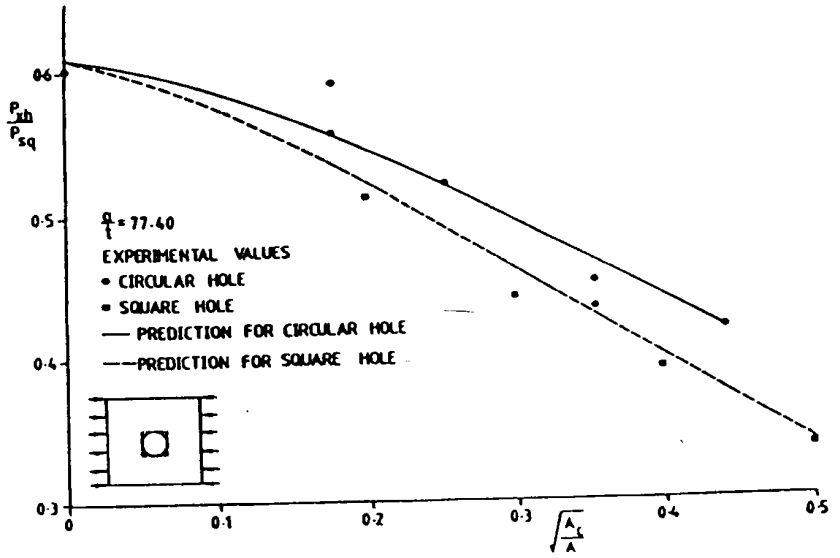

(a)

Ultimate strengths of perforated plates containing square and circular holes. (ref 28)

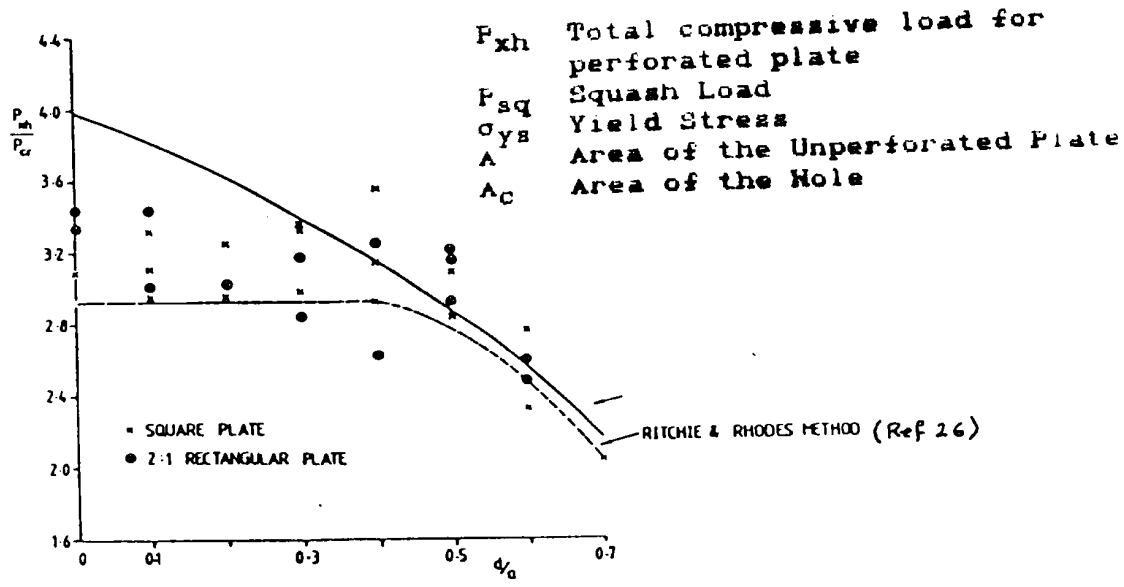

(b)

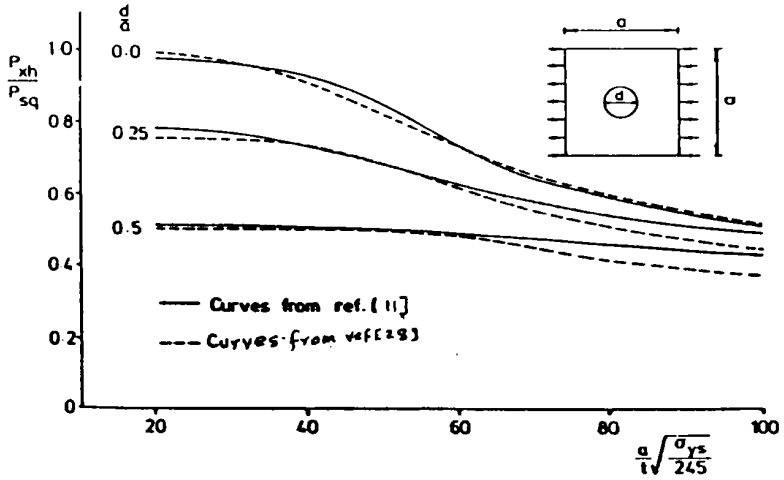

(c)

FIGURE 1.13 COMPARISON OF ULTIMATE STRENGTH OF PERFORATED PLATES PREDICTED BY DIFFERENT INVESTIGATORS [28]

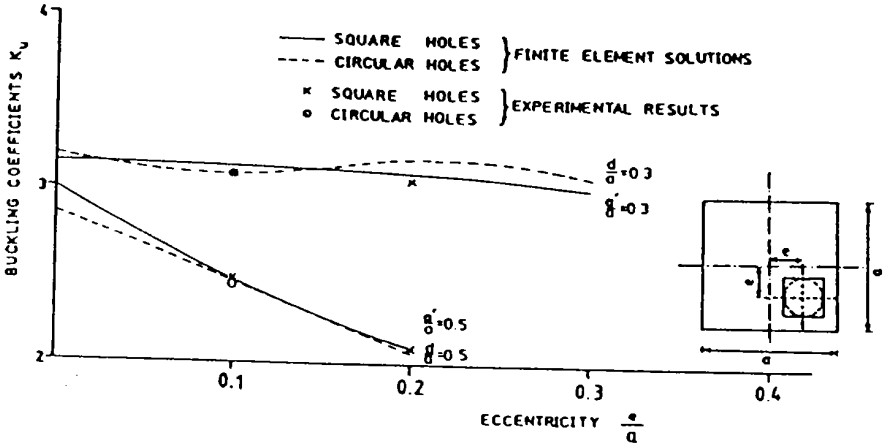

Comparison of buckling coefficients for uniaxially compressed square plates containing eccentrically located holes.

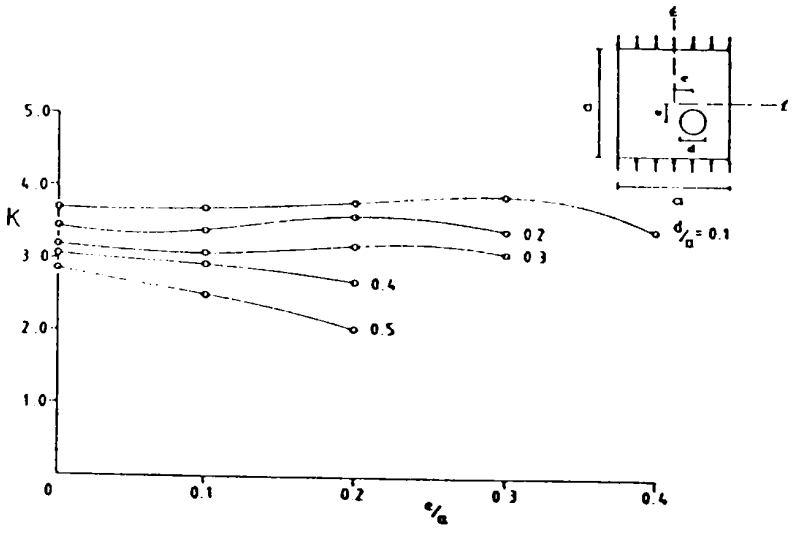

Variation of uniaxial buckling load for simply supported plates.

FIGURE 1.14 BUCKLING COEFFICIENTS OF PLATES CONTAINING ECCENTRICALLY LOCATED HOLES [REF. 19]

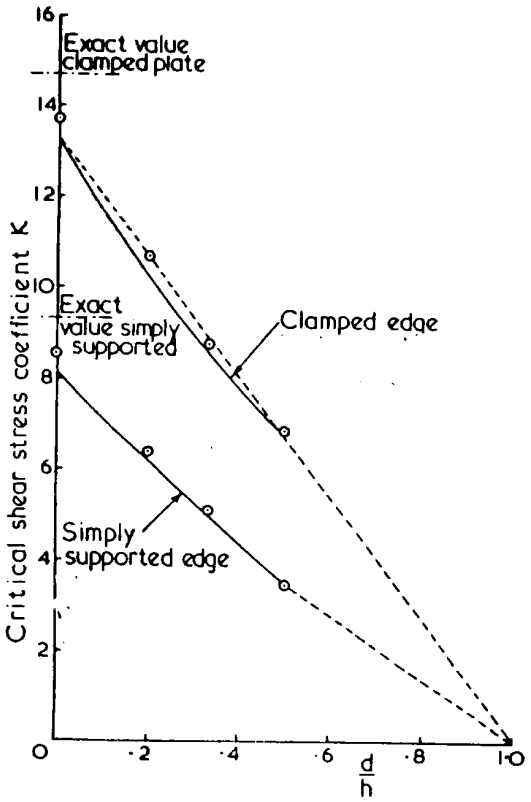

FIGURE 1.15 VARIATION OF THE SHEAR BUCKLING COEFFICIENT FOR PLATES WITH A CIRCULAR HOLE [REF. 38]

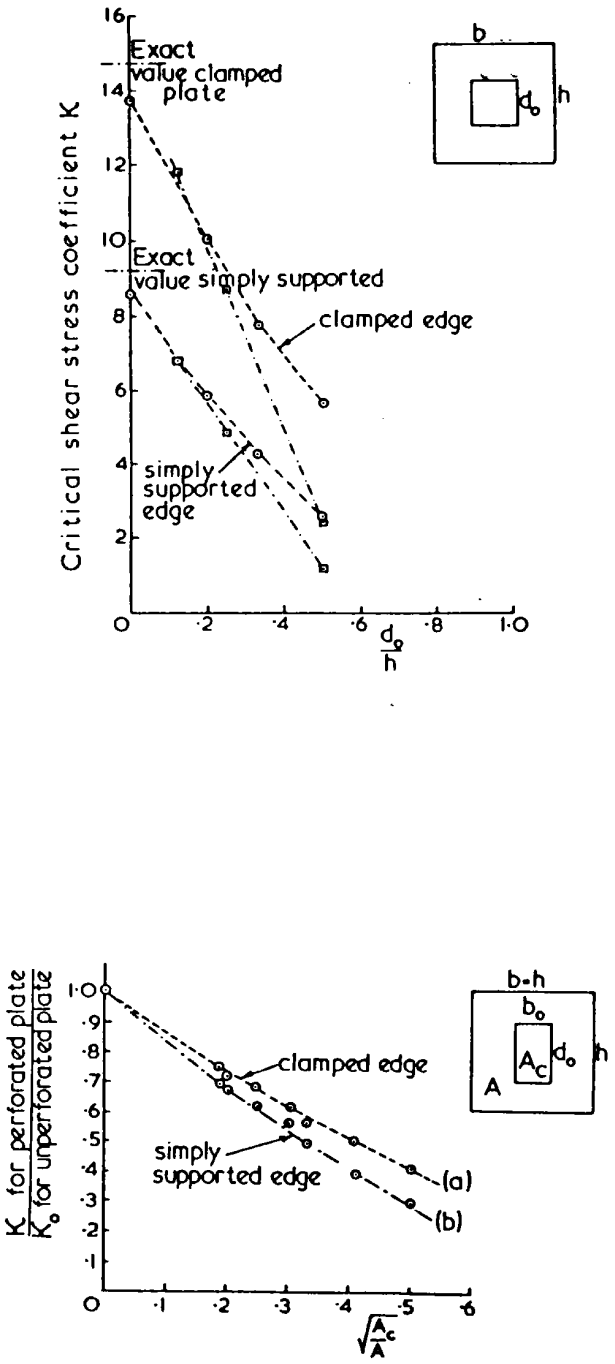

FIGURE 1.16 VARIATION OF THE SHEAR BUCKLING COEFFICIENT FOR PLATES WITH A SQUARE CUTOUT [REF. 38]

CHAPTER TWO

BASIC THEORY

BASIC THEORY

2.1 Introduction

A plate subjected to in-plane compressive loading has two types of deformations, i.e. in-plane displacements and out-of-plane deflections. Consequently the stress system in the plate consists of stress components which are due to in-plane loading, plate bending and the stretching of the middle surface of the plate. When the deflections are small, i.e. less than the thickness of the plate, then the analysis is based on the assumption that the middle plane of the plate does not stretch during bending. In this case the loads are entirely resisted by bending and twisting of the plate elements and the effects of shear are neglected. For a large elastic deflection analysis the effect of middle surface strains, which are present during bending, have to be taken into account.

2.2 Basic Equations

Consider a plate element acted upon by moments Mx, My and Mxy, vertical shear forces Qx and Qy, and a distributed load of intensity q over its upper surface as shown

in figure 2.1. Consideration of the equilibrium of this element leads to the following shear and moment equilibrium equations corresponding to the longitudinal, transverse and lateral directions, i.e. the x, y and z directions.

$$\frac{\partial Q_x}{\partial x} + \frac{\partial Q_y}{\partial y} + q = 0 \qquad 2.1(a)$$

$$\frac{\partial M_{xy}}{\partial x} - \frac{\partial M_y}{\partial y} + Q_y = 0 \qquad 2.1(b)$$

$$\frac{\partial M_{yx}}{\partial y} + \frac{\partial M_x}{\partial y} - Q_x = 0 \qquad 2.1(c)$$

Substituting expressions for Qx and Qy obtained from equations 2.1(b) and 2.1(c) into equation 2.1(a) we get the following relationship for lateral equilibrium in the z-direction.

$$\frac{\partial^2 M_x}{\partial x^2} + \frac{\partial^2 M_y}{\partial y^2} - \frac{2\partial^2 M_{xy}}{\partial x \partial y} = -q \qquad 2.2$$

If the lateral deflections are represented by w then the edge moments Mx and My can be expressed in terms of w by the following relationships.

$$Mx = -D\left(\frac{\partial^2 w}{\partial x^2} + \vartheta \frac{\partial^2 w}{\partial y^2}\right) \qquad 2.3(a)$$

$$My = -D\left(\frac{\partial^2 w}{\partial y^2} + \vartheta \frac{\partial^2 w}{\partial x^2}\right) \qquad 2.3(b)$$

where $D = Et^3/12(1-\upsilon^2)$, is known as the rigidity of the plate. The twisting moments on the plate element can be expressed in terms of w as follows.

$$Mxy = -Myx = D(1-\vartheta)\frac{\partial^2 x}{\partial x \partial y} \qquad 2.3(c)$$

Substitution of the expressions for Mx, My and Mxy into equation 2.2 then leads to the following equilibrium

equation.

$$\frac{\partial^4 w}{\partial x^4} + 2\frac{\partial^4 w}{\partial x^2 \partial y^2} + \frac{\partial^4 w}{\partial y^4} = \frac{q}{D} \qquad 2.4$$

If in addition to lateral load there are forces applied at the edge of the plate at the middle surface, the effect on plate bending can be considerable. If Nx and Ny are the edge compressive forces per unit length in the x and y directions respectively and Nxy and Nyx are the edge shearing forces per unit length as shown in figure 2.2, then the equilibrium of the element in the x and y directions gives rise to the following equations.

$$\frac{\partial Nx}{\partial x} + \frac{\partial Nxy}{\partial y} = 0 \qquad 2.5(a)$$

$$\frac{\partial Nxy}{\partial x} + \frac{\partial Ny}{\partial y} = 0 \qquad 2.5(b)$$

These equations are independent of the equilibrium equations considered earlier, i.e. equations 2.1 (a,b &c)

and due to this independence may be treated separately. To introduce the effect of these edge forces we consider the projection of Nx, Ny and Nxy on the z axis as shown in figure 2.2. The projections of the Nx and Ny forces are:

$$N_x \frac{\partial^2 w}{\partial x^2}\, dx\, dy + \frac{\partial N_x}{\partial x}\frac{\partial w}{\partial x}\, dx\, dy$$

$$N_y \frac{\partial^2 w}{\partial y^2}\, dx\, dy + \frac{\partial N_y}{\partial y}\frac{\partial w}{\partial y}\, dx\, dy$$

And those of the shearing forces Nxy and Nyx are:

$$2N_{xy}\frac{\partial^2 w}{\partial x \partial y}\, dx\, dy + \frac{\partial N_{xy}}{\partial x}\frac{\partial w}{\partial y} dx dy + \frac{\partial N_{xy}}{\partial y}\frac{\partial w}{\partial x} dx dy$$

Adding these projections and making use of equations 2.5(a) and 2.5(b) then gives the resultant force in the z direction as :

$$\left(N_x \frac{\partial^2 w}{\partial x^2} + 2N_{xy}\frac{\partial^2 w}{\partial x\, \partial y} + N_y \frac{\partial^2 w}{\partial y^2}\right) dx\, dy$$

The combined lateral and in-plane loads now give rise to the following equilibrium equation.

$$\frac{\partial^4 w}{\partial x^4} + \frac{2\partial^4 w}{\partial x^2 \partial y^2} + \frac{\partial^4 w}{\partial y^4} =$$

$$\frac{1}{D}\left(q + N_x \frac{\partial^2 w}{\partial x^2} + 2N_{xy} \frac{\partial^2 w}{\partial x \partial y} + N_y \frac{\partial^2 w}{\partial y^2}\right)$$

2.6

The stress resultants Nx, Ny and Nxy can also be defined in terms of a stress function F and these are expressed by the following relationship.

$$\delta_x = \frac{N_x}{t} = \frac{\partial^2 F}{\partial y^2} \qquad 2.7(a)$$

$$\delta_y = \frac{N_y}{t} = \frac{\partial^2 F}{\partial x^2} \qquad 2.7(b)$$

$$\tau_{xy} = \frac{N_{xy}}{t} = -\frac{\partial^2 F}{\partial x \partial y} \qquad 2.7(c)$$

If we now assume that the plate is subjected to in-plane forces only, then from equations 2.6 and 2.7 the following equilibrium equation is obtained.

$$\frac{\partial^4 w}{\partial x^4} + \frac{2\partial^4 w}{\partial x^2 \partial y^2} + \frac{\partial^4 w}{\partial y^4} =$$

$$\frac{t}{D}\left(\frac{\partial^2 F}{\partial y^2}\frac{\partial^2 w}{\partial x^2} + \frac{\partial^2 F}{\partial x^2}\frac{\partial^2 w}{\partial y^2} - \frac{2\partial^2 F}{\partial x \partial y}\frac{\partial^2 w}{\partial x \partial y}\right)$$

2.8

This equation is known as Von Karman equilibrium equation.

Now if the plate is subjected to large deflections, i.e. a few times greater than the plate thickness, then the effects of the middle surface strains present during bending have to be considered.

If u and v are the in-plane displacements in the x and y directions respectively and w is the out-of-plane deflection, then the strain components ϵ_x, ϵ_y and γ_{xy} are given by:

$$\varepsilon_x = \frac{\partial u}{\partial x} + \frac{1}{2}\left(\frac{\partial w}{\partial x}\right)^2 \qquad 2.9(a)$$

$$\varepsilon_y = \frac{\partial v}{\partial y} + \frac{1}{2}\left(\frac{\partial w}{\partial y}\right)^2 \qquad 2.9(b)$$

$$\gamma_{xy} = \frac{\partial u}{\partial y} + \frac{\partial v}{\partial x} + \frac{\partial w}{\partial x}\frac{\partial w}{\partial y} \qquad 2.9(c)$$

By taking second derivatives of ϵ_x, ϵ_y and γ_{xy} with respect to y, x and x & y respectively and adding the resulting expressions, we obtain the following single differential equation which links the middle surface strains to the out-of-plane deflection w.

$$\frac{\partial^2 \varepsilon_x}{\partial y^2} + \frac{\partial^2 \varepsilon_y}{\partial x^2} + \frac{\partial^2 \gamma_{xy}}{\partial x \partial y} = \left(\frac{\partial^2 w}{\partial x \partial y}\right)^2 - \left(\frac{\partial^2 w}{\partial x^2}\right)\left(\frac{\partial^2 w}{\partial y^2}\right) \qquad 2.10$$

The strains are now described in terms of the stresses through the use of the two dimensional stress-strain relationship for a linear elastic material.

$$\varepsilon_x = \frac{1}{E}(\delta_x - \vartheta \delta_y) \qquad 2.11(a)$$

$$\varepsilon_y = \frac{1}{E}(\delta_y - \vartheta \delta_x) \qquad 2.11(b)$$

$$\gamma_{xy} = \frac{1}{G}\tau_{xy} = \frac{2(1+\vartheta)}{E}\tau_{xy} \qquad 2.11(c)$$

Equations 2.7 and 2.11 can be substituted into 2.10 to obtain the following equation.

$$\frac{\partial^4 F}{\partial x^4} + \frac{2\partial^4 F}{\partial x^2 \partial y^2} + \frac{\partial^4 F}{\partial y^4} = E\left[\left(\frac{\partial^2 w}{\partial x \partial y}\right)^2 - \frac{\partial^2 w}{\partial x^2}\,\frac{\partial^2 w}{\partial y^2}\right] \qquad 2.12$$

Equations 2.8 and 2.12 were first derived by Von Karman in 1910 following the original work on large deflections by Kirchhoff in 1877 and the study of the use of stress functions by Foppl in 1907.

2.3 Elastic Strain Energy Stored in a Plate during Bending and Twisting

Consider a plate element under the action of moments Mx and My as shown in figure 2.3. The strain energy stored in a plate element is the sum of the work done by the bending moments Mx dy and My dx. The work done by the bending moment is 1/2 x moment x angle between the sides of the element after bending. This is illustrated in figure 2.4. The angle in the xz plane $\theta_x = -\partial^2\omega/\partial x^2$ and in the yz plane $\theta_y = -\partial^2\omega/\partial y^2$. The negative sign occurs because a downwards sagging curvature (positive) has a decreasing slope as x increases.

The strain energy stored in the plate element due to Mx and My is therefore given by:

$$dU_b = -\frac{1}{2}\left[M_x\frac{\partial^2 w}{\partial x^2} + M_y\frac{\partial^2 w}{\partial y^2}\right] dx\,dy \qquad 2.13$$

For the same element loaded by twisting moments Mxy and Myx as shown in figure 2.5 the strain energy stored is given by the following equation.

$$dU_t = M_{xy}\frac{\partial^2 w}{\partial x \partial y}\; dx\,dy \qquad 2.14$$

Substituting for the moments Mx, My and Mxy from equations 2.3 into equations 2.13 and 2.14 and combining, the strain energy stored in the plate element due to bending and twisting is thus given by the following equation.

$$dU_B = dU_b + dU_t$$

$$= \frac{D}{2}\left[\left(\frac{\partial^2 w}{\partial x^2} + \frac{\partial^2 w}{\partial y^2}\right)^2 - 2(1-\vartheta)\right.$$

$$\left.\left(\frac{\partial^2 w}{\partial x^2}\frac{\partial^2 w}{\partial y^2}\right) - \left(\frac{\partial^2 w}{\partial x \partial y}\right)^2\right] dx\,dy \qquad 2.15$$

For the complete plate the strain energy stored due to bending and twisting is found by integrating the above equation over the entire plate surface to obtain the following expression.

$$U_B = \frac{D}{2} \iint \left[\left(\frac{\partial^2 w}{\partial x^2} + \frac{\partial^2 w}{\partial y^2} \right)^2 - 2(1-\vartheta) \left\{ \frac{\partial^2 w}{\partial x^2} \frac{\partial^2 w}{\partial y^2} - \left(\frac{\partial^2 w}{\partial x \partial y} \right) \right\} \right] dx\, dy \qquad 2.16$$

Equation 2.16 is the equation for the elastic strain energy stored in a plate due to bending and twisting.

2.4 Elastic Strain Energy Stored in a Plate due to Membrane Stresses

Now consider a plate element which is subjected to in-plane stresses σ_x, σ_y and τ_{xy} as shown in figure 2.6. The strain energy stored in the element due to these mid-surface stresses is given by the following expression.

$$U_m = \frac{t}{2}\left[\delta_x \varepsilon_x + \delta_y \varepsilon_y + \tau_{xy}\gamma_{xy}\right] dx\, dy \qquad 2.17$$

Substitution of ϵ_x, ϵ_y and γ_{xy} from equations 2.11 in terms of σ_x, σ_y and τ_{xy} in the above equation we obtain the following relationship for the membrane energy stored in the element.

$$U_m = \frac{t}{2E}\left[\left(\delta_x + \delta_y\right)^2 - 2(1+\vartheta)\left(\delta_x \delta_y - \tau_{xy}^2\right)\right] dx\, dy \qquad 2.18$$

Substituting now for the stress σ_x, σ_y and τ_{xy} in terms of the Airy stress function F as defined by equation 2.7 and integrating over the entire plate gives the strain energy stored in the plate due to membrane action in terms of the stress function F as follows :

$$U_M = \frac{t}{2E}\iint\left\{\left[\frac{\partial^2 F}{\partial x^2} + \frac{\partial^2 F}{\partial y^2}\right]^2 - 2(1+\vartheta)\left[\frac{\partial^2 F}{\partial x^2}\frac{\partial^2 F}{\partial y^2} - \left(\frac{\partial^2 F}{\partial x \partial y}\right)^2\right]\right\} dx\, dy \qquad 2.19$$

2.5 Total Strain Energy

The total strain energy U stored in the plate is the sum of the strain energy due to bending and twisting U_B given by equation 2.16 and the strain energy due to the membrane strain energy U_M given by equation 2.19.

$$U = U_B + U_M$$

In the post-buckling analysis the stress function F is obtained in terms of out-of-plane deflection w by solving equation 2.12 (Von Karman compatibility equation) and satisfying the relevant stress conditions at the plate boundaries. Once F is known in terms of w then the total strain energy can be determined in terms of unknown deflection parameters in which out-of-plane deflections are originally defined. The minimisation of the total strain energy with respect to each of these parameters will determine these parameters. The out-of-plane deflections and internal stresses can then be determined at any stage in the post-buckling region.

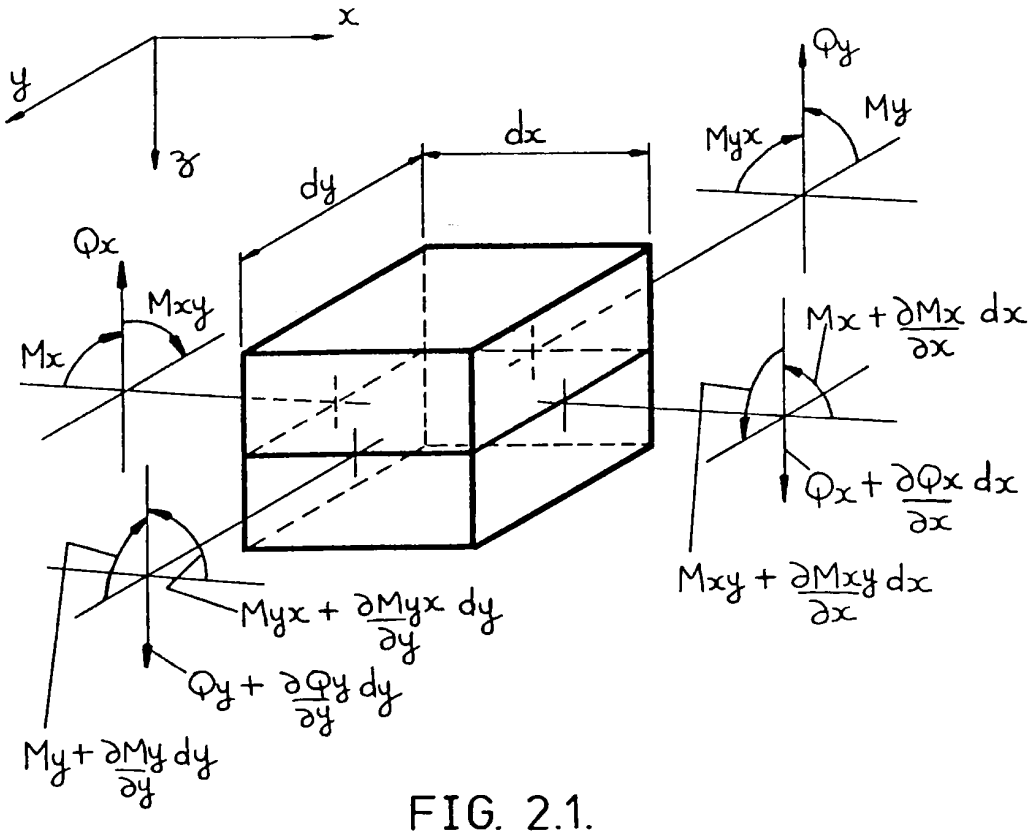
x
y
z
dx
dy
Qy
My
Myx
Qx
Mxy
Mx
Mx + ∂Mx/∂x dx
Qx + ∂Qx/∂x dx
Mxy + ∂Mxy/∂x dx
Myx + ∂Myx/∂y dy
Qy + ∂Qy/∂y dy
My + ∂My/∂y dy

FIG. 2.1.

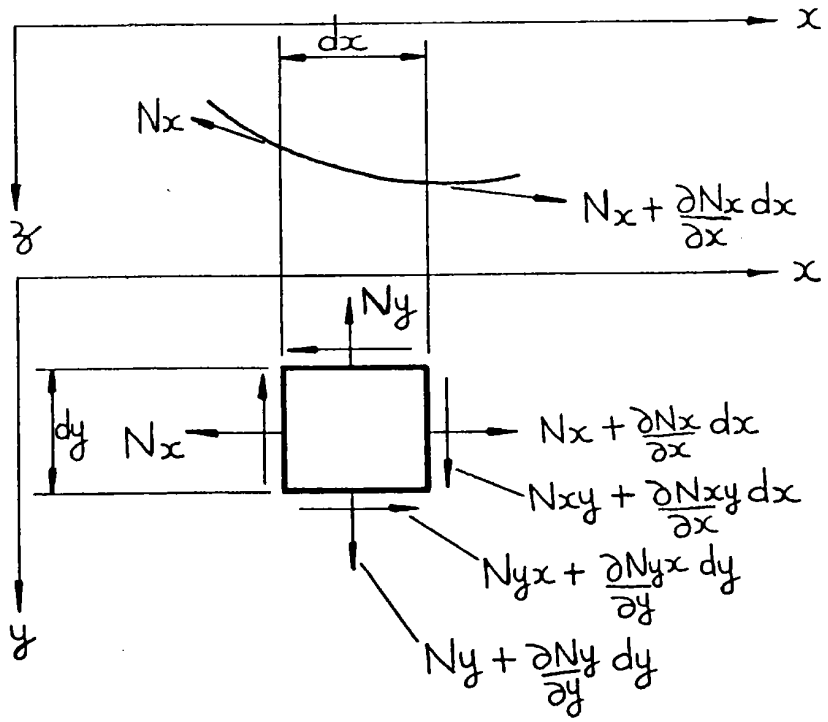
x
dx
Nx
Nx + ∂Nx/∂x dx
z
x
Ny
dy
Nx
Nx + ∂Nx/∂x dx
Nxy + ∂Nxy/∂x dx
Nyx + ∂Nyx/∂y dy
y
Ny + ∂Ny/∂y dy

FIG. 2.2

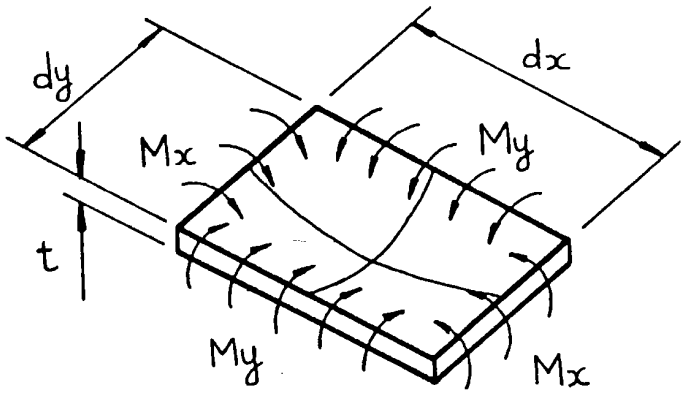

FIG. 2.3

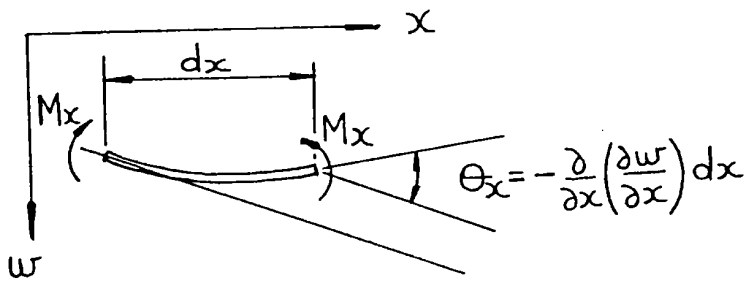

FIG. 2.4

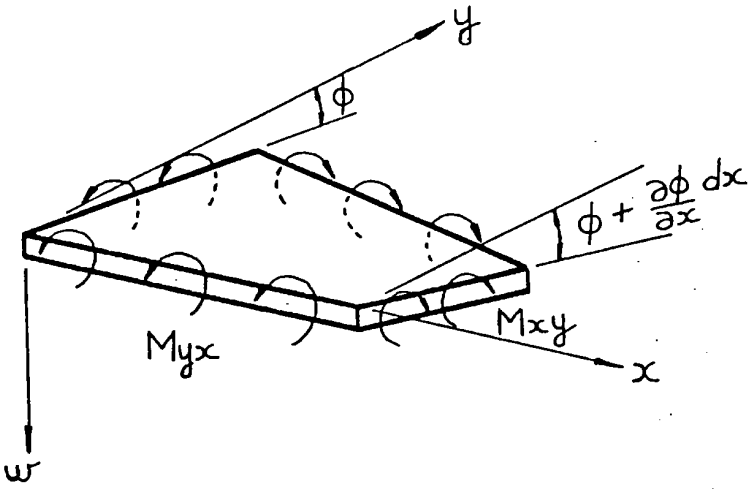

FIG. 2.5

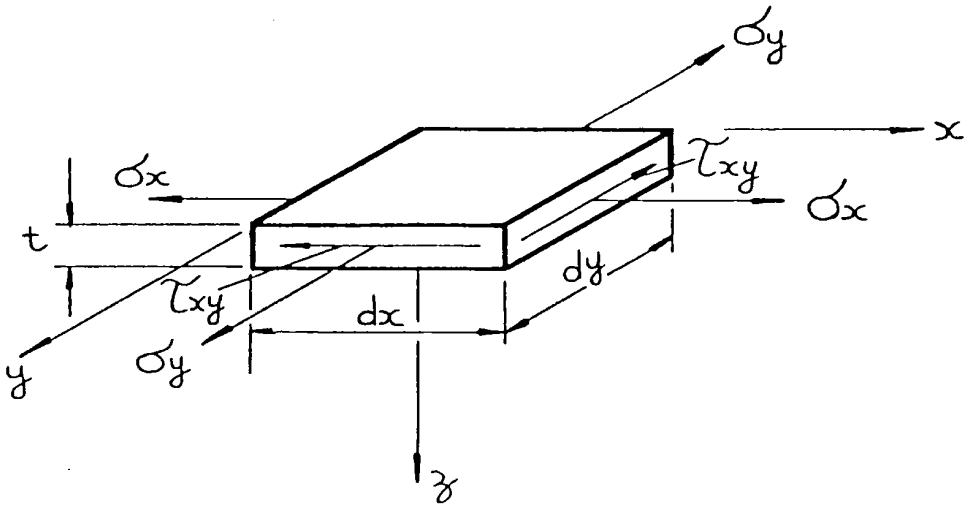

FIG. 2.6

CHAPTER THREE

SPLINE ANALYSIS

SPLINE ANALYSIS

3.1 Introduction

The current research is based on the concept of formulating a mathematical representation of the non-uniform internal stress distributions associated with perforated plates. The method developed for the current work obtains pre-buckling stress values at discrete points in the perforated plate by the finite element method and then uses this information to compute a best fitting spline surface for the mathematical representation of the stresses. These mathematical functions are then used in the energy approach for buckling and in the semi-energy post-buckling analysis.

As discussed in chapter one, the mathematical representation of the pre-buckling stresses, during the early period of research [8,9] on the buckling behaviour of the plates with cutouts, was determined by assuming the plate to have an infinite length. One example of such representation is given by Kumai [9] who described the pre-buckling stresses by the following relationships.

$$\delta_x = \frac{\delta_o}{2} e^{-2\alpha}\left[\cos 2\beta + \left(2 - 3e^{-2\alpha}\right)\cos 4\beta\right] \qquad 3.1(a)$$

$$\delta_y = \frac{\delta_o}{2}\left[2 + e^{-2\alpha}\left(3\cos 2\beta - \left(2 - 3e^{-2\alpha}\right)\cos 4\beta\right)\right] \qquad 3.1(b)$$

$$\tau_{xy} = \frac{\delta_o}{2} e^{-2\alpha}\left[-\sin 2\beta + \left(2 - 3e^{-2\alpha}\right)\sin 4\beta\right] \qquad 3.1(c)$$

Where α is the radius, β the angle measured from the x-axis, and σ_o is the end compressive stress.

While using an infinite plate length to estimate the pre-buckling stress variations did not give accurate results; the more recent finite element methods [10-12] have shown to require high computer time and to have data storage limitations, particularly in the non-linear post-buckling analysis. The present method of obtaining a mathematical representation of the internal stress distributions in a perforated plate requires the plate to be divided into spline panels which are fewer in number than the elements generally used in a finite element analysis. The strain energy evaluation thus involves a

comparatively small number of spline panels to the large number of finite elements required. The essential principles of a bicubic spline analysis are discussed and the basic spline equations are developed in this chapter. These equations will be used in the theoretical analysis described in chapter four.

3.2 The Choice of Functions to describe a Curve or a Surface

A curve can be defined, in a simple way, by polynomial functions which are computationally straight forward and fast and whose derivatives and integrals are easily arrived at. If the slopes change frequently or there are abrupt discontinuities like vertical tangents within a curve then polynomial equations may result in inaccuracies during computational work. One of the methods to overcome this problem is to link a number of pieces of low order (say cubic) polynomial curves. The continuity of these polynomial functions (also known as the spline functions) representing these curves and their derivatives are ensured during these functional representations. The concept can also be extended to describe a particularly contorted surface by choosing a number of small patches, each patch represented by suitable polynomial functions. For a simple surface a single patch

could be sufficient. The selection of the number and size of these patches or panels, the polynomial representation within a panel, the joining of the panels together to ensure the continuity of surface being described and thus of obtaining the overall functional representation of the entire surface are obviously the important parameters which have to be considered in the spline model representation of the given problem.

3.3 Cubic Spline Curves

A cubic spline curve consists of a set of cubic polynomial curve pieces joined smoothly end to end. The junction between two neighbouring pieces is known as a knot and each polynomial curve is joined to its neighbouring curve at those knots. Each piece of the curve in a cubic spline analysis has its own defining third degree polynomial. When joining the pieces in a cubic spline analysis, continuity of slope and curvature at the knots is maintained throughout. A spline function S(x) is illustrated schematically by the curve shown in figure 3.1 and the knot positions which join the individual pieces of the curve are indicated by the parameters

$\lambda_1, \lambda_2, \lambda_3, \ldots\ldots, \lambda_n$

where $\lambda_1 < \lambda_2 < \lambda_3 < \ldots\ldots < \lambda_n$

For the curve shown in figure 3.1, h=2.

S(x) is a function with the following properties

(a) In each of the intervals:

$$x \leqslant \lambda_1$$

$$\lambda_{j-1} \leqslant x \leqslant \lambda_j \qquad j=2,3,4,\cdots h$$

$$\lambda_h \leqslant x$$

S(x) is a polynomial of degree 3.

(b) S(x) and its derivatives up to the second order are continuous.

A cubic spline is considered by the writer to be a satisfactory function for fitting to data, as it is thought that continuity of the function and its first and second derivatives is more than adequate requirement for most practical problems. Thus a cubic spline consists of a set of (h+1) cubic arcs joined smoothly end-to-end. The spline curve is defined within a finite range $a \leqslant x \leqslant b$ where $a < \lambda_1$, and $b > \lambda_h$. In practice 'a' and 'b' are normally set as the smallest and largest data points respectively. Any cubic spline with knot positions $\lambda_1, \lambda_2, \lambda_3, \ldots, \lambda_h$ has a unique representation of the form:

$$S_x = \sum_{j=0}^{3} \alpha_j x^j + \sum_{i=0}^{h} \beta_i (x - \lambda_i)_+^3 \qquad 3.2$$

$$E_+ = \begin{cases} E & \text{when } E \geqslant 0 \\ 0 & \text{when } E < 0 \end{cases}$$

This representation contains h+4 basis functions, 4 power terms and h one sided cubics, the smallest number in terms of which the general cubic spline with h knots can be expressed. With this representation, the curve fitting problem becomes one of minimising

$$\sum_{r=1}^{m} [s(x_r) - f_r]^2 \qquad 3.3$$

with respect to the α_j and β_i. This can be achieved by finding a least square solution to the following system of linear equations.

$$\sum_{j=0}^{3} \alpha_j x_r^j + \sum_{i=1}^{h} \beta_i (x_r - \lambda_i)_+^3 = f_r \quad r = 1, 2, 3, \ldots m \qquad 3.4$$

The spline representation given by equation 3.2 is reported in the literature [46] to be computationally unsatisfactory. In particular, the equations 3.4 for

determining the α_j and β_j tend to be ill conditioned. Even if α_j and β_j have been determined, the subsequent evaluation of S(x) by means of equation 3.2 can suffer loss of accuracy through cancellation, as well as taking an unnecessary amount of computation.

3.4 Cubic B-Spline

A better and computationally more convenient representation of cubic spline has been provided [44] as the sum of the basis functions known as B-splines. Cubic B-splines are not simply joined end to end at knots as for the cubic splines described previously. A cubic B-spline is, in fact, a special form of cubic spline with the characteristic that it is finite over four adjacent intervals between knots and is zero elsewhere as illustrated in figure 3.2. Adjacent cubic B-splines overlap each other by three knot intervals, hence for any value of x there are four non zero cubic curves (see figure 3.4). Each cubic B-spline has the form of a cubic spline curve, i.e. it is a piecewise cubic polynomial curve, whose pieces, specifically four of them, join at knots and up to second order continuity exists throughout. It is, however, defined along the whole real line - its value outside the four knot intervals being zero.

With reference to figure 3.2 we specifically define a cubic B-spline $M_i(x)$ to be a cubic spline with knots $\lambda_1, \lambda_2, \lambda_3, \ldots\ldots, \lambda_h$ which is zero everywhere except in the range $\lambda_{i-4} < x < \lambda_i$. This defines $M_i(x)$ uniquely except for an arbitrary constant multiplier which can be chosen for numerical convenience. $M_i(x)$ has the same sign throughout its range and has a single maximum.

The general cubic spline can be expressed as the sum of the basis B-spline functions with internal knots $\lambda_1, \lambda_2, \lambda_3, \ldots\ldots, \lambda_h$, and has a unique representation in the range $a \leqslant x \leqslant b$ of the following form

$$S(x)=\sum_{i=0}^{h+4} C_i M_i(x) \qquad 3.5$$

Since each B-Spline needs four cubic splines to describe it, then the B-spline between 'a' and λ_1 will require three additional knots and so will the B-spline between λ_h and 'b'. (see figure 3.3). Therefore we need to introduce six additional knots

λ_{-3} λ_{-2} λ_{-1} and λ_{h+2} λ_{h+3} λ_{h+3}

with $\lambda_0 = a$ and $\lambda_{h+1} = b$

such that

$$\lambda_{-3} < \lambda_{-2} \leq \lambda_{-1} < a$$

and

$$b < \lambda_{h+2} \leq \lambda_{h+3} \leq \lambda_{h+4}$$

(For the spline curve shown in figure 3.3, h=2.)

These are arbitrary knots and can be chosen for numerical convenience. Except for possible differences in rounding error they do not effect the spline in the range of interest $a \leqslant x \leqslant b$. It has been reported in the literature and also verified by the author during the computational work that coincident end knots are best for numerical accuracy i.e.

$$\lambda_{-3} = \lambda_{-2} = \lambda_{-1} = a$$

$$\lambda_{h+2} = \lambda_{h+3} = \lambda_{h+4} = b$$

To illustrate the previous points discussed, we consider a cubic spline curve consisting of three pieces of cubic splines as shown in figure 3.3. This curve has two internal knots λ_1 and λ_2 and a range $a \leqslant x \leqslant b$ such that $a = \lambda_0$ and $b = \lambda_3$. Beneath this curve are the six cubic splines, four more than the number of internal knots, which are used to define it. It can be seen that all points along the cubic spline curve are associated with four cubic B-splines. As a general case if the cubic

spline curve is to be defined over (h+1) knot intervals, where h is the number of internal knots, than h+4 cubic B-spline are required to ensure that each knot interval has four non zero B-splines defined over it.

In equation 3.5 the c_i are known as the spline coefficients. In a curve fitting problem values for these coefficients are determined during a least square solution to the following observation equations.

$$\sum_{i=1}^{n} C_i M_i(X_r) = f_r \qquad r=1,2,\cdots m \qquad 3.6$$

where f_r are the data points to which spline curve is being fitted. The $M_i(x)$ in equation 3.3 are the functional representations of the cubic B-splines.

In computational dealings with splines the question of mathematical representation of the basis functions is of primary importance. In order to compute the values of the B-spline at data points a stable recurrence relation provided by Cox and De Boor is proved to achieve best computational results as compared to other form of explicit expressions (see refs. 40 - 42 for details). Most of the properties of B-spline can be derived from this relationship:-

$$M_{i,n}(x) = \frac{1}{\lambda_{i+n} - \lambda_i}\left[\frac{x - \lambda_i}{x_{i+n-1} - \lambda_i} M_{i,n-1}(x) + \frac{\lambda_{i+n} - x}{\lambda_{i+n} - \lambda_{i+1}} M_{i+1,n-1}(x)\right] \qquad 3.7$$

Where $M_{i,n}(x)$ is the B-spline of degree (n-1), so that $M_{i,4}(x)$ is the cubic B-spline. Because of the localness of the B-spline the starting value can be set to be,

$$M_{i,1}(x) = \begin{cases} (\lambda_{i+1} - \lambda_i)^{-1} & \lambda_i \leqslant x < \lambda_{+1} \\ 0 & \text{otherwise} \end{cases} \qquad 3.8$$

If we introduce a normalised B-spline $N_{i,n}(x)$ such that

$$N_{i,n}(x) = (\lambda_{i+n} - \lambda_i) M_{i,n}(x) \qquad 3.9$$

and the normalised recurrence is started with

$$N_{i,1}(x) = \begin{cases} 1 & \lambda_i \leqslant x < \lambda_{+1} \\ 0 & \text{otherwise} \end{cases} \qquad 3.10$$

Then equation 3.7 will take the following form:-

$$N_{i,n}(x) = \frac{x-\lambda_i}{x_{i+n-1}-\lambda_i} N_{i,n-1}(x) + \frac{\lambda_{i+n}-x}{\lambda_{i+n}-\lambda_{i+1}} N_{i+1,n-1}(x)$$

3.11

3.4.1 Derivation of the $N_{1,4}(x)$ for a Typical Spline Curve

A typical spline curve in the range $a \leqslant x \leqslant b$ is shown in figure 3.4. Using the recurrence relation for normalised B-spline given by equation 3.11, starting with normalised recurrence of equation 3.10, the following cubic equations for $N_{1,4}(x)$, $N_{2,4}(x)$, $N_{3,4}(x)$ and $N_{4,4}(x)$ can be derived:-

$$N_{1,4}(x) = \frac{(\lambda_{i+1}-x)^3}{(\lambda_{i+1}-\lambda_i)(\lambda_{i+1}-\lambda_{i-1})(\lambda_{i+1}-\lambda_{i-2})}$$

3.12(a)

$$N_{2,4}(x) = \frac{(x-\lambda_{i-2})(\lambda_{i+1}-x)^2}{(\lambda_{i+2}-\lambda_{i-1})(\lambda_{i+2}-\lambda_{i})(\lambda_{i+1}-\lambda_i)}$$

$$+\frac{(\lambda_{i+2}-x)(x-\lambda_{i-1})(\lambda_{i+1}-x)}{(\lambda_{i+2}-\lambda_{i-1})(\lambda_{i+1}-\lambda_{i-1})(\lambda_{i+1}-\lambda_i)}$$

$$+\frac{(\lambda_{i+2}-x)^2(x-\lambda_i)}{(\lambda_{i+2}-\lambda_{i-1})(\lambda_{i+2}-\lambda_i)(\lambda_{i+1}-\lambda_i)} \qquad 3.12(b)$$

$$N_{3,4}(x) = \frac{(x-\lambda_{i-1})^2(\lambda_{i+1}-x)}{(\lambda_{i+2}-\lambda_{i-1})(\lambda_{i+1}-\lambda_{i-1})(\lambda_{i+1}-\lambda_i)}$$

$$+\frac{(x-\lambda_{i-1})(\lambda_{i+2}-x)(x-\lambda_i)}{(\lambda_{i+2}-\lambda_{i-1})(\lambda_{i+2}-\lambda_i)(\lambda_{i+1}-\lambda_i)}$$

$$+\frac{(\lambda_{i+3}-x)(x-\lambda_i)}{(\lambda_{i+3}-\lambda_i)(\lambda_{i+2}-\lambda_i)(\lambda_{i+1}-\lambda_i)} \qquad 3.12(c)$$

$$N_4(x) = \frac{(x-\lambda_i)^3}{(\lambda_{i+3}-\lambda_i)(\lambda_{i+2}-\lambda_i)(\lambda_{i+1}-\lambda_i)} \qquad 3.12(d)$$

Each of these B-spline are multiplied with spline coefficients c_1 - c_4 obtained from least square curve fitting solution to obtain equation S(x).

Thus S(x) for the present case would be,

$$S(x)=C_1N_1(x)+C_2N_2(x)+C_3N_3(x)+C_4N_4(x) \qquad 3.13$$

where

$$N_1(x) = N_{1,4}(x) \qquad N_2(x) = N_{2,4}(x)$$

$$N_3(x) = N_{3,4}(x) \qquad N_4(x) = N_{4,4}(x)$$

This formulation is then extended to cover full range of spline curve for any number of internal knots between λ_1 - λ_n, which is given by the equation 3.3.

3.5 Choice of Knots

The number and position of knot will determine the accuracy to which a spline curve gives a closer fit. The two parameters can be chosen by a mixture of trial and error experience and general knowledge of the shape of required curve. As a general rule more and closer knots are needed where the behaviour of the curve changes

rapidly and less knots where it is changes slowly. However, with a little experience satisfactory positions of knots can be easily found after one or two trials; the exact position is often not too critical.

3.6 Spline Surface

In a surface fitting problem, we are given the data values f_r of a dependent variable f at points (x_r, y_r), r = 1,2,3,....,m, which are scattered arbitrarily in the (x, y) plane. To determine a suitable functional representation for the surface, we wish to fit to the f_r a bicubic spline function in the variables x and y. As in the case of one variable where a curve was defined in the range (a, b) which contained all the data points within that curve, a rectangle $a < x < b$, $c < y < d$ is defined in the (x,y) plane so as just to contain all the (x_r, y_r) in a surface. The two ranges (a, b) and (c, d) are then subdivided by sets of knots λ_i and μ_j respectively where λ_i correspond to the knot positions in the x-direction and μ_j correspond to the knot positions in the y-direction as shown in figure 3.5 such that :

$$a = \lambda_0 < \lambda_1 < \ldots < \lambda_{h+1} = b$$

$$c = \mu_0 < \mu_1 < \ldots < \mu_{h+1} = d \qquad 3.14$$

To represent the general bicubic spline we need a set of basis functions. These are derived as follows. The spline curves in the x-direction are represented by a set of basis functions based on the knot set λ_1 and those in the y direction are represented by a set of basis functions based on the knot set μ_j. The set of all cross-products of one function from each set provides a basis for the bicubic spline. In particular, the set B-splines $M_1(x)$ are based on the knots λ_1 and the corresponding set of B-splines $N_j(y)$ are based on the knots μ_j. Figure 3.6 shows an element of bicubic B-spline with functions to represent curves in x and y direction. Thus the B-spline for two directions are represented by:

$$M_i(x) \qquad i = 1,2,\cdots,h+4$$

$$N_j(y) \qquad j = 1,2,\cdots,k+4$$

3.15

thus we have a set of (h+4) (k+4) independent basis functions $M_1(x)\ N_j(y)$ and the bicubic spline can be represented by the following equation

$$S(x,y) = \sum_{i=1}^{h+4} \sum_{j=1}^{k+4} C_{ij} M_i(x) N_j(y) \qquad 3.16$$

where C_{ij} are spline coefficients corresponding each spline panel and are determined during the solution of a least square surface fitting problem.

$N_j(y)$ will be governed by similar equations as those for $M_i(x)$, i.e., equations 3.12, where knot positions λ_i are replaced by μ_j and the equations are now functions of y.

The notations $M_i(x)$ and $N_j(y)$ to define a spline surface differ slightly from those in section 3.4, where M was used to denote the B-splines as computed by the equation 3.7 and N was used to define the normalised B-splines as computed by the equation 3.11. Here we use M and N simply to distinguish between the B-splines in x and those in y; in practical applications both sets would be normalised B-splines.

It has been demonstrated in section 3.4 that we need four basis functions to define a B-spline curve in any interval with no interior knots. These basis functions are non-zero between these intervals and are zero everywhere else (basic definition of the B-spline). In a similar way, the basis functions $M_i(x)$ $N_j(y)$ are each non-zero only over a rectangle composed of 16 adjacent panel in a 4x4 arrangement, as shown in figure 3.5. Specifically, $M_i(x)N_j(y)$ is non-zero only when $\lambda_{i-4} < x < \lambda_i$ and $\mu_{j-4} < y < \mu_j$. Correspondingly at any point

(x,y), only 16 basis functions are non-zero. If this point lies in the panel R_{uv} (say), the non-zero are those with $u < i < u+3$, $v < j < v+3$. Therefore, all points in a single panel will have same functional representation involving 16 basis functions and the corresponding 16 spline coefficients which are pre-multiplied by each of these functions. The spline coefficients c_{ij} are determined during a solution of least square surface fitting problem. If we have a set of (h+4)(k+4) independent basis functions $M_i(x)\ N_j(y)$ and the bicubic spline are represented by the equation 3.16, we wish to find the values of C_{ij} which minimise

$$\sum_{r=1}^{m} \left[S(x_r, y_r) - f_r \right]^2$$

In other words to find the least square solution to the following equation

$$A Y = f$$

The matrix A has m rows and (h+4)(k+4) columns. The rth row consists of the values at the point (x_r, y_r) of all the basis functions $M_i(x)\ N_j(y)$. The vector C consists of

unknown coefficients c_{ij} , ordered correspondingly to the columns of A, and f contains m data values .

The knot positions λ_s and μ_s can be chosen arbitrarily under the same guidelines as described for the choice of knots for the spline curves in section 3.5.

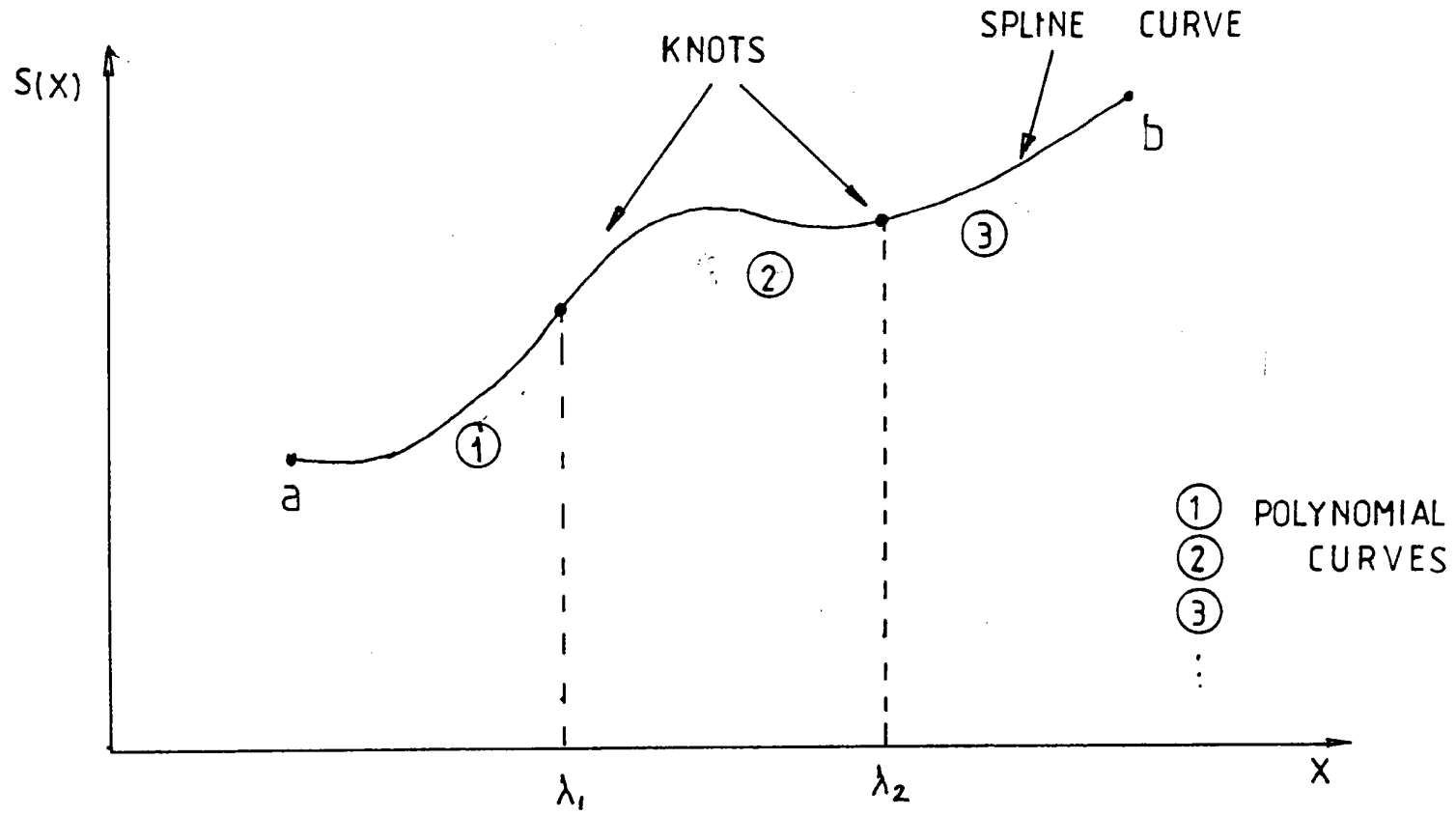

FIGURE 3.1 A TYPICAL SPLINE CURVE

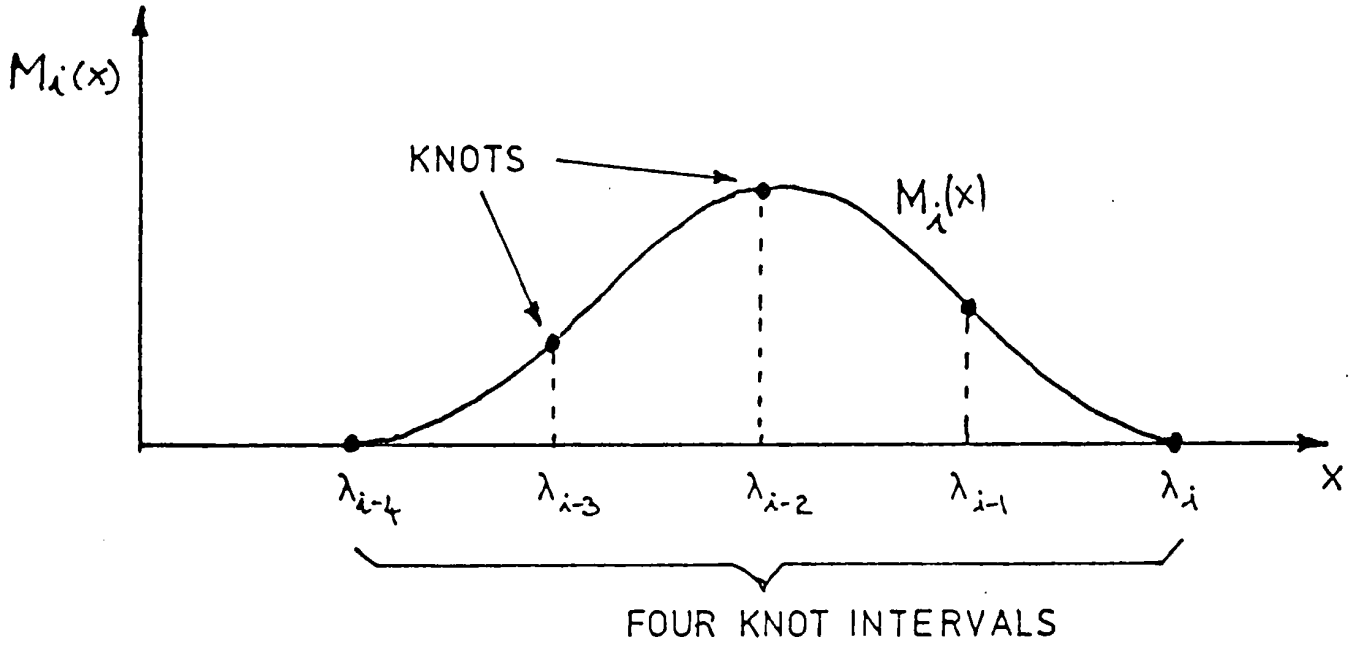

FIGURE 3.2 A TYPICAL CUBIC B - SPLINE

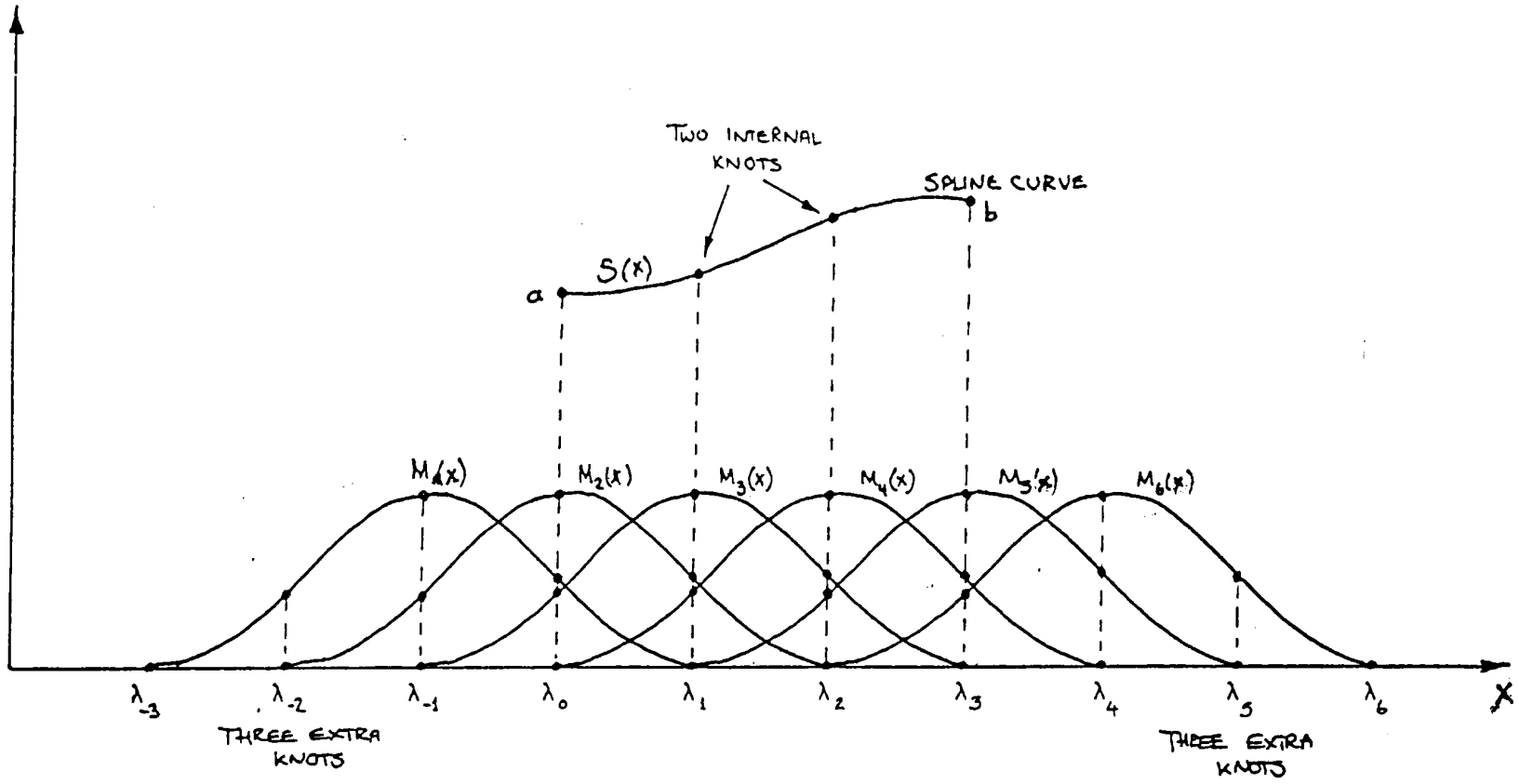

FIGURE 3.3 A SPLINE CURVE AND ITS BASIS OF B - SPLINES

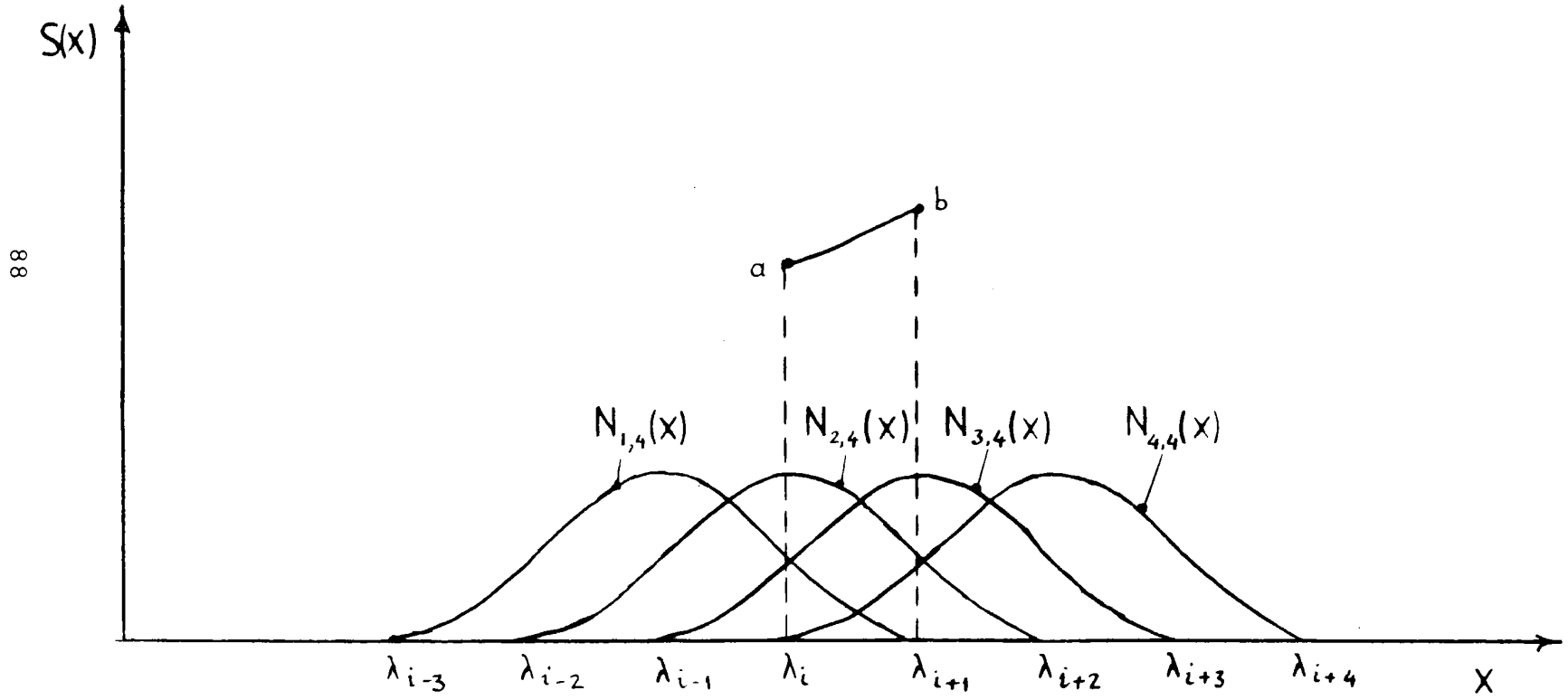

FIGURE 3.4 A TYPICAL B-SPLINE

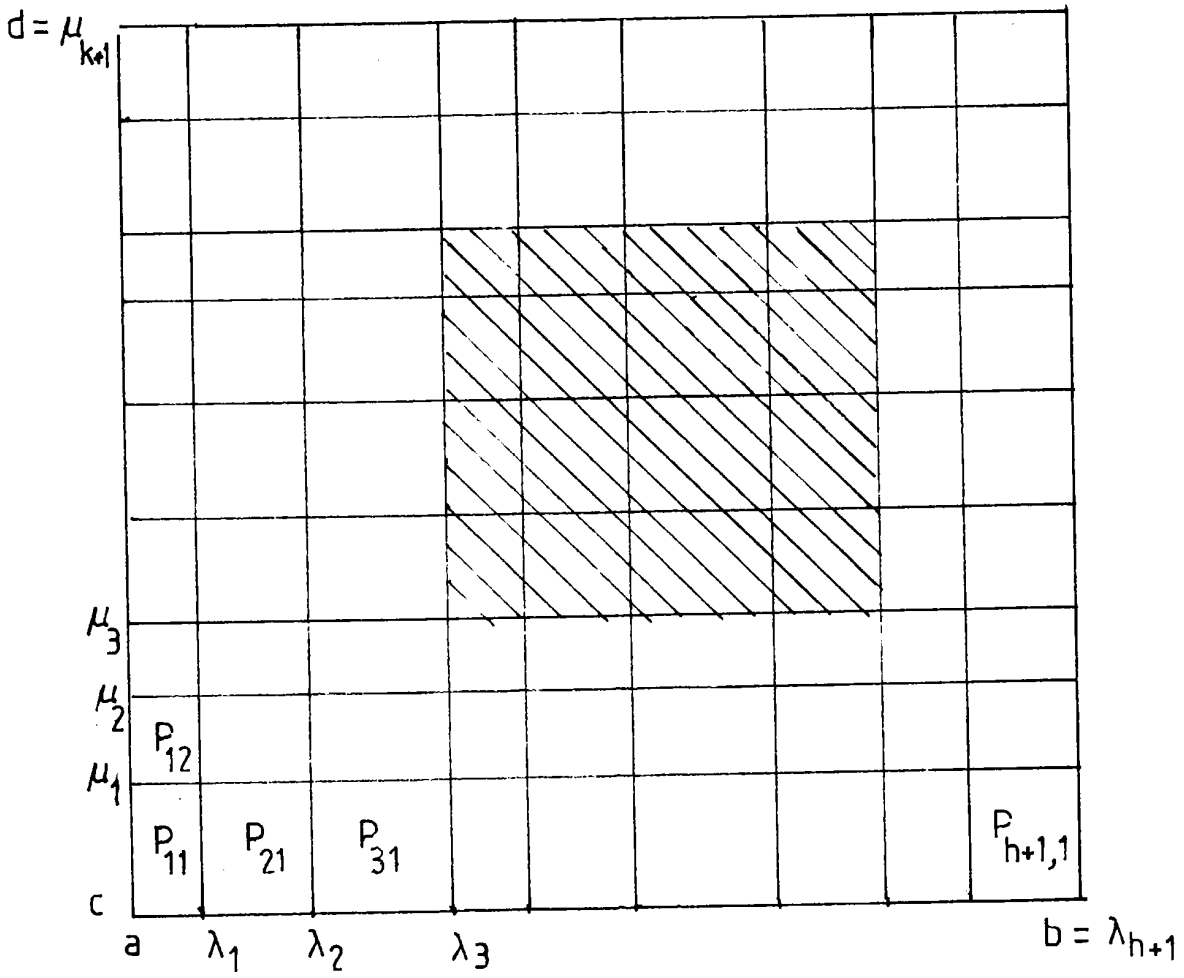

FIGURE 3.5 THE RECTANGLE P, DIVIDED BY KNOTS λ_i, μ_j INTO PANELS P_{ij}. THE SHADED AREA TYPIFIES THE 4x4 REGION OVER WHICH A BICUBIC B-SPLINE IS NON ZERO.

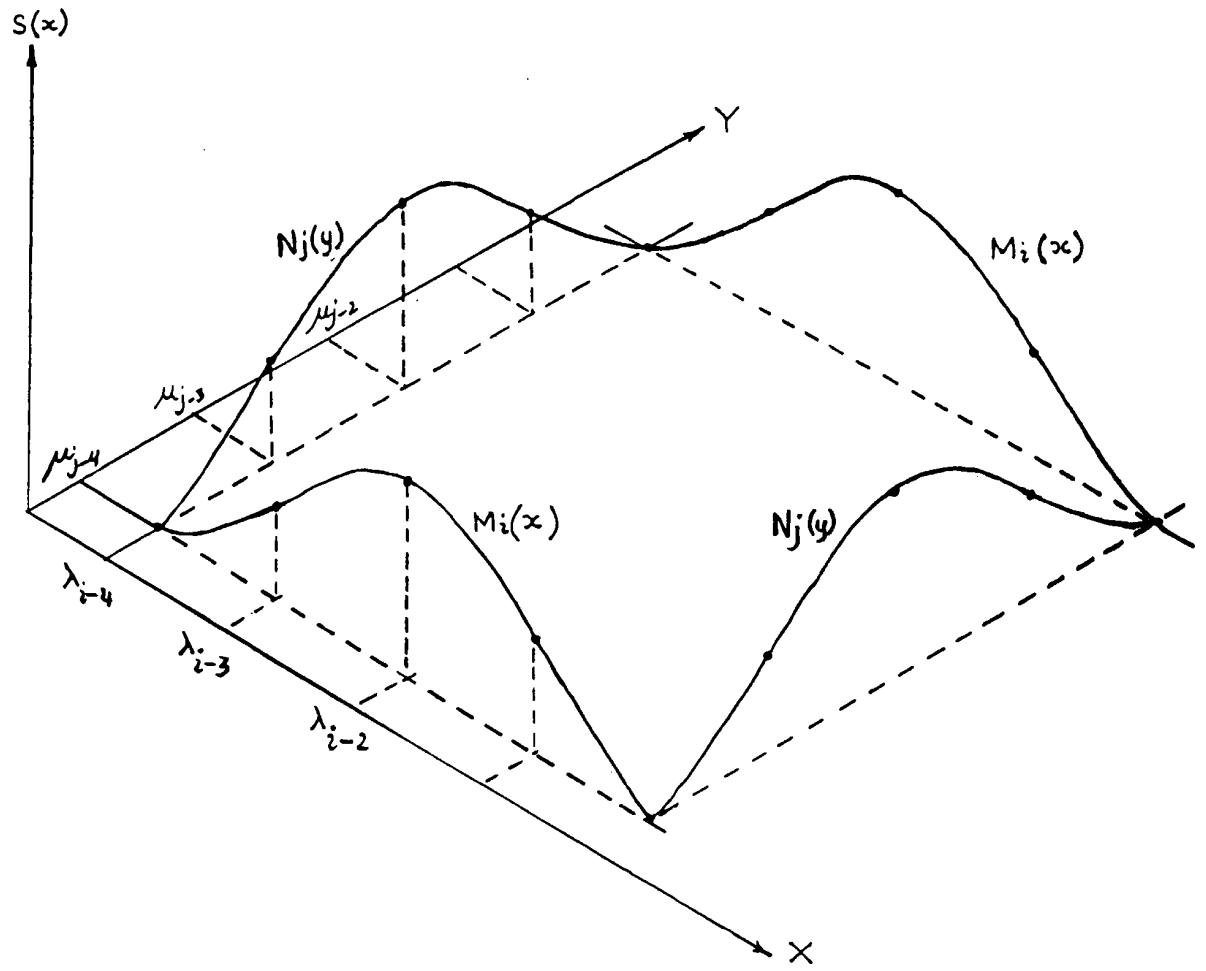

FIGURE 3.6 ELEMENT OF BICUBIC B - SPLINE

CHAPTER FOUR

THEORETICAL ANALYSIS

THEORETICAL ANALYSIS

4.1 Introduction

The theoretical analysis of the behaviour of a flat plate with a centrally located circular or square cutout under edge compression is described in this chapter. The study of the buckling and post-buckling behaviour of perforated plates involves an accurate prediction of displacements and of the membrane stresses within a plate prior to and after buckling. The analytical procedure to investigate the deformations and stresses in a perforated plate has been developed for the following loading and boundary conditions.

(a) Prior to Buckling

The plate is loaded in the direction of the x-axis to ensure that the stresses along the loaded edges are uniform. The sides $x = \pm 1$ are not uniformly displaced in this case. This case is referred to as the uniform stress loading.

The plate is loaded in the direction of x-axis in a manner such that the sides $x = \pm 1$ are uniformly displaced. This case will be referred to as the

uniform displacement loading.

The edges of the plate are simply supported, i.e. no out-of-plane deflections and no rotational restraint at the plate edges.

(b) After Buckling

The post-buckling analysis is carried out for the case of the uniform displacement loading only. The loaded edges are constrained to be held straight during the loading process.

All edges are simply supported. The unloaded edges are free to wave in-plane, i.e. the edges $y = \pm b$ are free from restraint in the plane of the plate. This means that the normal direct and shear stresses are zero at the unloaded edges.

In-plane normal and shear stresses are zero at the hole edge.

The analysis proposed by the author can be extended to cover other loading and boundary conditions as well as to any other shape or location of a cutout.

To demonstrate the detailed analysis procedure we consider a rectangular plate with a circular hole whose dimensions and axis system are shown in figure 4.1. The analysis has also been applied to a rectangular plate with a square cutout shown in figure 4.2. The plate dimensions for the two types of plates are as follows.

Plate Length ..... = 2l

Plate Width ..... = 2b

Plate Thickness ..... = t

Hole Radius ..... = c

Cutout Dimensions ....= 2 c (for a square cutout)

The out-of-plane deflection w of the plate is described by the following equation.

$$\omega = \sum_{i=1}^{m} \sum_{j=1}^{n} A_{ij} \cos \frac{a_i \pi x}{l} \cos \frac{b_j \pi y}{b} \qquad 4.1$$

$$a_i = 1,3,5... \qquad b_j = 1,3,5...$$

The A_{ij} are the unknown deflection coefficients to be determined to define the deflected shape. The deflection function in equation 4.1 automatically satisfies the simple support boundary conditions around the plate edges.

4.2 Outline of the Analysis Procedure

The following theoretical procedure has been developed for the analysis.

4.2.1 Procedure for the Buckling Analysis

(a) The stress variations within a plate containing a cutout are evaluated prior to buckling, by the finite element method.

(b) Using the information from process (a) above, a best spline surface fit is formulated to obtain mathematical expressions for the pre-buckling stresses.

(c) Using these mathematical representations of the stresses in conjunction with equation 4.1 for the deflections the critical load factor and the buckled shape are thus computed by applying the principle of minimum potential energy.

4.2.2 Procedure for the Post-buckling Analysis

(a) For the purpose of analysis, the post buckling stresses have been divided into the following three systems:-

Stress System 1 These are the membrane stresses in a perforated plate with no out-of-plane deflections and produced by the applied load/displacement. The stress distribution in this case is dependent only on the magnitude of the applied load/displacement. The stresses are evaluated by the finite element method and the nodal stresses are then used as data values in the bicubic spline analysis in order to formulate a mathematical representation of the stress system.

Stress System 2 This includes post-buckling stress components in an unperforated plate assuming zero displacements of the loaded edges. The stresses in this system, which are dependent on the magnitude of the out-of-plane deflection, are produced by the stretching of the middle surface of the plate. The stresses

in this system are represented by the Airy stress function F_2 and are evaluated by solving the Von Karman compatibility equation. The boundary conditions at the loaded and the unloaded edges are satisfied during the solution.

Stress System 3 While determining the post-buckling stresses in the stress system 2 we can satisfy the stress and displacement boundary conditions at the plate edges. For a post-buckling analysis of a perforated plate, however, stress free boundary conditions have to be satisfied at the hole edge. This can be achieved by first calculating post-buckling stresses at the cutout geometry from stress system 2 and applying these stresses in the opposite direction at the periphery of the cutout. The stresses thus generated within the perforated plate will constitute stress system 3. These stresses are computed under the same boundary conditions as those for the stress system 2.

Stresses in system 1 and system 3 are evaluated in the same manner as the pre-buckling stresses

outlined in section 4.3 and the stresses in system 2 are evaluated from the Airy stress function by solving the Von Karman Compatibility equation the details of which are given in appendix A.

(b) Expressions are then developed for the strain energy due to bending and twisting and due to the membrane stresses. The three stress systems outlined are thus superimposed to obtain the final stress pattern which is to be used during the energy calculations.

(c) The total strain energy is then minimised to obtain the final results for displacements and stresses.

4.3 Pre-buckling Stress Distribution

An accurate representation of the pre-buckling stresses is essential for the stability analysis. These stresses have been evaluated by the finite element method. Eight noded isoparametric elements have been used for the finite element formulation. Because of the symmetry of the plate geometry and loading only a 1/4 of the plate is

analysed. Typical mesh arrangements for square plates with circular and square cutouts are shown in figures 4.3 and 4.4 respectively. The analysis has been carried out for the case of simply supported edges and zero in-plane displacements were enforced on the symmetrical axes.

The nodal stresses obtained from the finite element analysis were used as data values to fit a bicubic spline surface for each of the stress components σ_{x1}, σ_{y1} and τ_{xy1} using the procedure described in chapter three. During the spline fit it was experienced that due to the abrupt discontinuity of the stresses at the hole edge at the centre of the plate the fitted values of the data overshot in the negative direction and the stress values became zero after few oscillations. It was, therefore, decided to ignore the the stress discontinuity at the edge of the hole and let the stresses follow the upward positive trend. During subsequent energy evaluations, the energy of the hole portion is obviously excluded and this is achieved by setting the appropriate integration limits. Equations 4.2 give the spline representation of σ_{x1}, σ_{y1} and τ_{xy1}, the direct and shear stresses in a perforated plate produced by uniform in-plane displacement loading and with no out-of-plane deflections present.

$$\delta_{x_1} = \sum_{i=1}^{h+4}\sum_{j=1}^{k+4} C_{x_{ij}} \quad M_i(x)\ N_j(y)$$

$$\delta_{y_1} = \sum_{i=1}^{h+4}\sum_{j=1}^{k+4} C_{y_{ij}} \quad M_i(x)\ N_j(y) \qquad 4.2$$

$$\tau_{xy_1} = \sum_{i=1}^{h+4}\sum_{j=1}^{k+4} C_{\tau_{ij}} \quad M_i(x)\ N_j(y)$$

$C_{x_{ij}}, C_{y_{ij}}$ and $C_{\tau_{ij}}$ are the spline coefficients and are obtained as a result of the least square surface fitting of the finite element nodal output values for the stresses $\sigma x_1, \sigma y_1$ and τxy_1 respectively. $M_i(x)\ N_j(y)$ are the basis functions described in chapter three and are dependent on the knot positions of the spline mesh arrangements for each of these stress components. 'h' and 'k' correspond to the number of interior knots in the x and y directions respectively.

4.4 Buckling Analysis

The Rayleigh Ritz energy method described in chapter two involves the choosing of a suitable deflected shape with arbitrary coefficients. The deflection function of equation 4.1 is used for the present buckling analysis. The strain energy stored in a plate due to bending and twisting given by equation 2.16 can be represented in the

following form :

$$U_B = \frac{D}{2}\iint \left\{\frac{\partial^2 w}{\partial x^2} \quad \frac{\partial^2 w}{\partial y^2} \quad \frac{\partial^2 w}{\partial x \partial y}\right\}^T \begin{bmatrix} 1 & \vartheta & 0 \\ \vartheta & 1 & 0 \\ 0 & 0 & 1-\vartheta \end{bmatrix} \left\{\frac{\partial^2 w}{\partial x^2} \quad \frac{\partial^2 w}{\partial y^2} \quad \frac{\partial^2 w}{\partial x \partial y}\right\} dx\,dy \qquad 4.3$$

Differentiation of w and substitution of the appropriate derivatives in equation 4.3 then gives the following equation for the strain energy due to bending and twisting.

$$U_B = \frac{D}{2}\iint \left[A\right]^T \left[M\right] \left[A\right] dx\,dy \qquad 4.4$$

The loss in potential energy due to the applied compressional displacement is given in the following form :

$$V_p = -\frac{t}{2}\iint w\,dx\,dy$$

$$W = \begin{bmatrix} \frac{\partial w}{\partial x} \\ \frac{\partial w}{\partial y} \end{bmatrix}^T \begin{bmatrix} \delta x & \tau xy \\ \tau xy & \delta y \end{bmatrix} \begin{bmatrix} \frac{\partial w}{\partial x} \\ \frac{\partial w}{\partial y} \end{bmatrix} \qquad 4.5$$

The stresses σ_x, σ_y and τ_{xy} correspond to an arbitrary applied displacement and have been formulated in the form of bicubic spline functions. For a specified applied displacement, a loading parameter ϕ is introduced which pre-multiplies equation 4.5 to determine the loss in potential energy corresponding to the specified applied displacement. After differentiating w with respect to x and y, V_p can be written in the following matrix form.

$$V_p = \phi \iint [A]^T [W] [A] \, dx \qquad 4.6$$

The matrices $[A]^T$ and $[A]$ relate to deflection parameters and are same as in equation 4.4. The function within the integral sign has to be integrated over the surface area of the plate taking due account of the cutout. Figure 4.6 shows 1/4 of the plate with area A being the portion of the plate containing the hole and area B being the rest of the 1/4 plate. The integration limits for the plate will therefore be as follows :

$$\iint dx\,dy = \int_0^c \int_{\sqrt{c^2-y^2}}^{\ell} dx\,dy + \int_c^b \int_0^{\ell} dx\,dy \qquad 4.7$$

Since the stresses are expressed in the form of spline functions, the energy evaluation is performed by integrating the functions over the surface area of each spline panel. The energy contribution of each panel is then added to obtain the energy stored in the plate. Figure 4.5 shows a typical spline mesh of 4x4 panels with panel P11 covering the hole portion. The limits of integration for the panel P11 are set so as to take account of the hole portion. The integral for the panel P11 will thus be given by :

$$\iint dx\,dy = \int_{\mu_4}^{\mu_5} \int_{\lambda_4+\sqrt{c^2-y^2}}^{\lambda_5} \qquad 4.8$$

Where $\lambda_4\mu_4$ and $\lambda_5\mu_5$ are the knot positions for the panel P11. For the remaining rectangular panels the limits of integration are governed by the appropriate λ and μ knot positions.

if

$$\frac{D}{2}\iint [M]\,dx\,dy = [K_B]$$
$$\iint [W]\,dx\,dy = [K_T] \qquad 4.9$$

then the total potential energy will be given by

$$V = U_B + V_P$$

$$V = [A]^T[A]\left\{[K_B] + \Phi\,[K_T]\right\} \qquad 4.10$$

Minimising the total potential with respect to the A_{ij} will then lead to the characteristic eigenvalue problem. The eigenvalues and the corresponding eigenvectors give the buckling loads and associated modes according to the number of degrees of freedom considered with the smallest eigenvalue corresponding to the point of initial instability and the associated eigenvector giving the buckled mode shape.

4.5 Post-buckling Analysis

In the post-buckling analysis the strain energy due to bending and twisting given by equation 2.16 is used. The energy due to in plane forces is described by equation 2.19 containing σ_x, σ_y and τ_{xy} which are the direct and shear stresses of the three stress systems described in section 4.1.

Thus

$$\begin{aligned} \delta x &= \delta x_1 + \delta x_2 + \delta x_3 \\ \delta y &= \delta y_1 + \delta y_2 + \delta y_3 \\ \tau xy &= \tau xy_1 + \tau xy_2 + \tau xy_3 \end{aligned} \qquad 4.11$$

The evaluation procedure for the stresses in each of the three stress systems will now be discussed. The mathematical formulations will then be used in equation 2.19 to evaluate the strain energy due the membrane forces.

4.5.1 Evaluation of Internal Stresses

4.5.1.1 Stresses in System 1

These are direct and shear stress components produced by a prescribed end displacement assuming that there is no out-of-plane deflection. These stresses grow linearly with increased displacement and the spline functions to represent the pre-buckling stresses given by equation 4.2 are multiplied by the critical load factor Φ_{cr} at the bifurcation point to obtain the internal stresses at the point of initial instability. These stress functions are simply augmented by the appropriate load factor to obtain the stresses in system 1 at any point in the post-buckling region. Thus :

$$\delta x_1 = \phi_p \sum \sum C x_{1ij} M_i(x) N_j(y)$$

$$\delta y_1 = \phi_p \sum \sum C y_{1ij} M_i(x) N_j(y) \qquad 4.12$$

$$\tau xy_1 = \phi_p \sum \sum C \tau_{1ij} M_i(x) N_j(x)$$

Where ϕ_p is the load factor corresponding to a specified end displacement divided by the critical load factor.

4.5.1.2 Stresses in System 2

These are the post-buckling stresses of an unperforated plate. The stresses in system 2 can also expressed in terms of stress functions.

$$\delta x_2 = \frac{\partial^2 F2}{\partial^2 y_2}$$
$$\delta y_2 = \frac{\partial^2 F2}{\partial^2 y_2} \qquad 4.13$$
$$\tau xy_2 = -\frac{\partial^2 F_2}{\partial x \partial y}$$

The stress function F_2 is obtained by solving the Von Karman compatibility equation [2.19]. This equation is rewritten here for convenience.

$$\frac{\partial^4 F_2}{\partial x^4} + \frac{2\partial^4 F_2}{\partial x^2 \partial y^2} + \frac{\partial^4 F_2}{\partial y^4} = E\left[\left(\frac{\partial^2 w}{\partial x \partial y}\right)^2 - \frac{\partial^2 w}{\partial x^2}\,\frac{\partial^2 w}{\partial y^2}\right] \qquad 4.14$$

The boundary conditions for F_2 are stated as follows :

(a) The displacements and the shear stresses are zero at the loaded edge. For the plate shown in figure 4.1

$$U\Big|_{x = \pm l} = 0$$

$$\frac{\partial^2 F_2}{\partial x \partial y}\Bigg|_{x = \pm l} = 0$$

(b) The unloaded edges are stress free, i.e. the normal and shear stresses are zero.

$$\frac{\partial^2 F_2}{\partial x^2}\Bigg|_{y = \pm b} = 0$$

$$\frac{\partial^2 F_2}{\partial x\, \partial y}\Bigg|_{y = \pm b} = 0$$

The post buckling solution offered by the present research is not limited to a fixed buckled shape after initial instability. Since the stress function F_2 is found in terms of the deflection coefficients $A_{ij}\ A_{mn}$, the loads which are applied back on the hole edge to ensure the stress free condition would have to be for each combination of $A_{ij}\ A_{mn}$ for some unit value of the deflection parameters. The evaluations of the stresses for the stress system 3 in a multiterm post-buckling solution will have to be for each of these combinations. The interdependence of the two stress systems, each one depending on the combinations of $A_{ij}\ A_{mn}$ makes the multiterm post-buckling solution fairly laborious. In order to reduce labour, the solution is restricted to only two terms along and multiterms across the loaded direction. During the application of the theory on square plates with a centrally located circular or square cutout it was observed that the results of a reasonable accuracy were achieved by taking only two x and two y terms of the deflection function given by equation 4.1. The deflected shape chosen for the present analysis is, therefore, of the following form:

$$W = \cos\frac{a_1\pi x}{\ell}\sum A_{1j}\cos b_j\frac{\pi y}{b} + \cos\frac{a_2\pi x}{\ell}\sum A_{2j}\cos b_j\frac{\pi y}{b} \qquad 4.15$$

Taking appropriate derivatives of w and substituting in equation 4.14, we obtain the following equation.

$$\nabla^4 F_2 = E\left(\frac{a_1\pi}{\ell}\right)^2 \sum\sum A_{1i}\, A_{1j}$$
$$[Y_i' Y_j' \sin^2 \frac{a_1\pi x}{0} + Y_i Y_j'' \cos^2 \frac{a_1\pi x}{\ell}$$
$$+ E\left(\frac{\pi}{\ell}\right)^2 \sum\sum A_{1i}\, A_{2j}$$
$$[2a_1 a_2 \sin \frac{a_1\pi x}{\ell} \sin \frac{a_2\pi x}{\ell} Y_i' Y_j'$$
$$+ \cos \frac{a_1\pi x}{\ell} \cos \frac{a_2\pi x}{l} (a_1^2 Y_i Y_j'' + a_2^2 Y_i Y_j'')]$$
$$+ E\left(\frac{a_2\pi}{\ell}\right) \sum\sum A_{2i} A_{2j} [Y_i' Y_j' \sin \frac{a_2\pi x}{\ell}$$
$$+ Y_i Y_j'' \cos^2 \frac{a_2\pi x}{\ell}] \qquad 4.16$$

Assuming

$$F_2 = F_{2A} + F_{2B} + F_{2CD} \qquad 4.17$$

Equation 4.16 can be subdivided into the following three equations.

$$\nabla^4 F_{2A} = E \left(\frac{a_1 \pi}{\ell}\right)^2 \sum \sum A_{1i} A_{1j} \left[Y_i' Y_j' \sin^2 \frac{a_1 \pi x}{\ell} + Y_i Y_j'' \cos^2 \frac{a_1 \pi x}{\ell} \right] \qquad 4.18(a)$$

$$\nabla^4 F_{2CD} = E \left(\frac{\pi}{\ell}\right)^4 \sum \sum A_{1i} A_{2j} \left[2 a_1 a_2 \sin \frac{a_1 \pi x}{\ell} \sin \frac{a_2 \pi x}{\ell} Y_i' Y_j' + \cos \frac{a_1 \pi x}{\ell} \cos \frac{a_2 \pi x}{l} \left(a_1^2 Y_i Y_j'' + a_2^2 Y_i Y_j'' \right) \right]$$

4.18(b)

$$\nabla^4 F_{2B} = E \left(\frac{a_2 \pi}{\ell}\right) \sum \sum A_{2i} A_{2j} \left[Y_i' Y_j' \sin \frac{a_2 \pi x}{\ell} + Y_i Y_j'' \cos^2 \frac{a_2 \pi x}{\ell} \right]$$

4.18(c)

Each of the above equations can be solved independently. The solutions of these equations are outlined in appendix A. The boundary conditions at the loaded and unloaded edges of the plate have been satisfied during the solution of each of these equations. It may be noted that the stress function F_{2A} relates to

the single term solution, F_{2B} relates to the second harmonic and F_{2CD} correspond to the cross or the coupling terms. The final equations from the solutions given in appendix A for F_{2A}, F_{2B} and F_{2CD} are given on the following pages.

Final Equation for F2A

$$F_{2A} = F_{21A} + F_{22A} \cos \frac{2\pi a_1}{\ell} x$$

$$F_{21A} = \sum \sum A_{1i} A_{1j} \cos b_i \frac{\pi y}{b} \cos b_j \frac{\pi y}{b} \qquad 4.19$$

$$F_{22A} = \left(\frac{E}{2}\right)\left(\frac{\pi a_1}{\rho}\right)^2\left(\frac{\pi}{b}\right)^2 \sum \sum A_{1i} A_{1j} f_{22Aij}(y)$$

where

$$f_{22Aij} = \gamma_{A_1} \cosh \frac{2\pi a_1}{\ell} y + \gamma_{A_2} \frac{y}{b} \sinh \frac{2\pi a_1}{\ell} y$$
$$+ k_1 \cos \frac{(b_j + b_i)\pi}{b} y + k_2 \cos \frac{(b_j - b_i)\pi}{b} y$$

The coefficients are given by the following equations in appendix A.

γ_{A1}	is	given	by	equation A.26
γ_{A2}	is	given	by	equation A.27
k_1	is	given	by	equation A.22
k_2	is	given	by	equation A.23

Final Equation for F2B

$$F_{2B} = F_{21B} + F_{22B} \cos \frac{2\pi a_2}{l} x$$

$$F_{21B} = \sum \sum A_{2i} A_{2j} \cos b_i \frac{\pi y}{b} \cos b_j \frac{\pi y}{b} \qquad 4.20$$

$$F_{22B} = \left(\frac{E}{2}\right)\left(\frac{\pi a}{\rho}\right)^2\left(\frac{\pi}{b}\right)^2 \sum \sum A_{2i} A_{2j} f_{22B_{ij}}(y)$$

where

$$f_{22B_{ij}} = \gamma_{B1} \cosh \frac{2\pi a}{l} y + \gamma_{B2} \frac{y}{b} \sinh \frac{2\pi a_2}{l} y + K_3 \cos\left(b_j + b_j\right)\frac{\pi y}{b} + K_4 \cos\left(b_j - b_j\right)\frac{\pi y}{b}$$

The coefficients are given by the following equations in appendix A.

γ_{B1} is given by equation A.34

γ_{B2} is given by equation A.35

K_3 is given by equation A.36

K_4 is given by equation A.37

Final Equation for F2CD

$$F_{2CD} = F_{2C} \cos\left(a_1 - a_2\right)\frac{\pi x}{l} + F_{2D} \cos\left(a_1 + a_2\right)\frac{\pi x}{l}$$

$$F_{2C} = \left(\frac{E}{2}\right)\left(\frac{\pi}{l}\right)^2\left(\frac{\pi}{b}\right)^2 \sum\sum A_{1i}\ A_{2j}\ f_{2C_{ij}}(y)$$

$$F_{2D} = \left(\frac{E}{2}\right)\left(\frac{\pi}{l}\right)^2\left(\frac{\pi}{b}\right)^2 \sum\sum A_{1i}\ A_{2j}\ f_{2D_{ij}}(y)$$

4.21

$$f_{2C_{ij}} = \gamma_{C1} \cosh(a_2 - a_1)\frac{\pi y}{l} + \gamma_{C2}\left(\frac{y}{b}\right)\sinh(a_2 - a_1)\frac{\pi y}{b}$$
$$+ k_5 \cos(b_j + b_i)\frac{\pi y}{b} + k_6 \cos(b_j - b_i)\frac{\pi y}{b}$$

$$f_{2D_{ij}} = \gamma_{D1} \cosh(a_2 + a_1)\frac{\pi y}{l} + \gamma_{D2}\left(\frac{y}{b}\right)\sinh(a_2 + a_1)\frac{\pi y}{b}$$
$$+ k_7 \cos(b_j + b_i)\frac{\pi y}{b} + k_8 \cos(b_j - b_i)\frac{\pi y}{b}$$

The coefficients are given by the following equations in appendix A.

γ_{C1} is given by equation A.40

γ_{C2} is given by equation A.41

γ_{D1} is given by equation A.42

γ_{D2} is given by equation A.43

K_5 is given by equation A.44

K_6 is given by equation A.45

K_7 is given by equation A.46

K_8 is given by equation A.47

4.5.1.3 Stresses in System 3

Figure 4.3 shows a typical finite element grid to solve for the stresses in a perforated plate for which loads are applied at nodal points around the hole edge. These nodal loads are calculated from stress systems 2 for each combination of A_{ij} A_{mn} at some unit value. The procedure for the evaluation of nodal loads from the stress distribution at the hole edge are given in standard finite element books. Since the present finite element analysis utilises eight noded isoparametric elements, the procedure given by Cook [5] is used to calculate the nodal loads. These loads are applied at the hole boundary to compute the stresses in the plate by the finite element method. The nodal stresses obtained as a result of the finite element analysis are used to get a functional representation by a bicubic spline surface fit. The stresses in system 3 are thus given by :

$$\delta x_3 = \sum \sum A_{ij} \; A_{mn} \; S_{3x}$$

$$\delta y_3 = \sum \sum A_{ij} \; A_{mn} \; S_{3y} \qquad 4.22$$

$$\tau xy = \sum \sum A_{ij} \; A_{mn} \; S_{3T}$$

where

$$S_{3x} = \sum\sum C_{xij}\, M_i(x)\, N_j(y)$$

$$S_{3y} = \sum\sum C_{yij}\, M_i(x)\, N_j(y)$$

$$S_{3T} = \sum\sum C_{Tij}\, M_i(x)\, N_j(y)$$

4.5.2 Minimisation of the Total Strain Energy

4.5.2.1 Strain-Energy Due to-Mid-Plane Stresses

Strain energy in a plate due to mid-plane stresses given by equation 2.19 is re-written below:-

$$U_M = \frac{t}{2E}\iint\left\{\left[\frac{\partial^2 F}{\partial x^2} + \frac{\partial^2 F}{\partial y^2}\right]^2 - 2(1+\vartheta)\left[\frac{\partial^2 F}{\partial x^2}\frac{\partial^2 F}{\partial y^2} - \left(\frac{\partial^2 F}{\partial x \partial y}\right)^2\right]\right\} dx\, dy$$

where $\sigma_x = \partial^2 F/\partial y^2$, $\sigma_y = \partial^2 F/\partial x^2$ and $\tau_{xy} = -\partial^2 F/\partial x \partial y$ comprise of stresses in the three systems discussed in section 4.4. Equations 4.12, 4.13 and 4.22 are the mathematical representation of the direct and shear stress components in the three stress systems. Using the appropriate deflection and stress equations the strain energy can be derived. The derivation is given in appendix B.

The final equation for the strain energy, equation B5 (Appendix B) is re-written below:-

$$U_M = \frac{t}{2E}\iint\Big[\sum\sum\sum\sum A_{1i}A_{1j}A_{1m}A_{1n}\psi_A +$$

$$\sum\sum\sum\sum A_{1i}A_{1j}A_{1m}A_{2n}\psi_B +$$

$$\sum\sum\sum\sum A_{1i}A_{1j}A_{2m}A_{2n}\psi_C +$$

$$\sum\sum\sum\sum A_{1i}A_{2j}A_{1m}A_{2n}\psi_D +$$

$$\sum\sum\sum\sum A_{1i}A_{2j}A_{2m}A_{2n}\psi_E +$$

$$\sum\sum\sum\sum A_{2i}A_{2j}A_{2m}A_{2n}\psi_F +$$

$$\sum\sum A_{1i}A_{1j}\psi_G +$$

$$\sum\sum A_{1i}A_{2j}\psi_H +$$

$$\sum\sum A_{2i}A_{2j}\psi_K \Big]\, dx\, dy$$

where ψ_A to ψ_K are given by equation (Appendix C)

For the specific case of taking two terms along the loaded direction i.e., putting $b_j = 1,3$ and $i,j,m,n = 1,2$ in above expression, we get a fourth order equation in A.

Since the equations contain bicubic spline function, the integration has to be performed for each spline panel (see figure 4.5 for a typical spline grid). The limits of integration for these panel are discussed in section. For the panel P11, containing a quarter of the hole the limits of integration are given by equation 4.8 and for other panels the integration limits are dependent on the interior knot positions.

The integration has been done numerically by Gaussian quadrature technique using NAG routine E02 DAF. It is obvious that, after integration and adding energy all spline panels, we obtain U_M which is a function of quadratic, cubic and quadruple in A_{11}, A_{12}, A_{21} and A_{22} or their combinations.

4.5.2.2 Strain Energy Due to Bending and Twisting

Strain energy due to bending and twisting given by equation 4.4 is applicable in the post-buckling solution. For a specific case of $b_j = 1,3$, $i,j,m,n=1,2$ the integration of this equation panelwise and summation of the energy contribution of all panel will result in an expression for U_B which is a function of the product of A_{ij} and A_{mn}.

4.5.3 Principle of-Minimum Strain Energy

Total strain energy in plate is the combination of strain energy due to bending and twisting and strain energy due to in-plane stresses.

$$U = U_B + U_M$$

By applying the principle of minimum strain energy the coefficients A_{1j}, A_{2j} in the deflection function can be evaluated. The information about the out-of-plane deflections corresponding to a prescribed edge compression are used in the appropriate equations to evaluate the internal stresses in a plate.

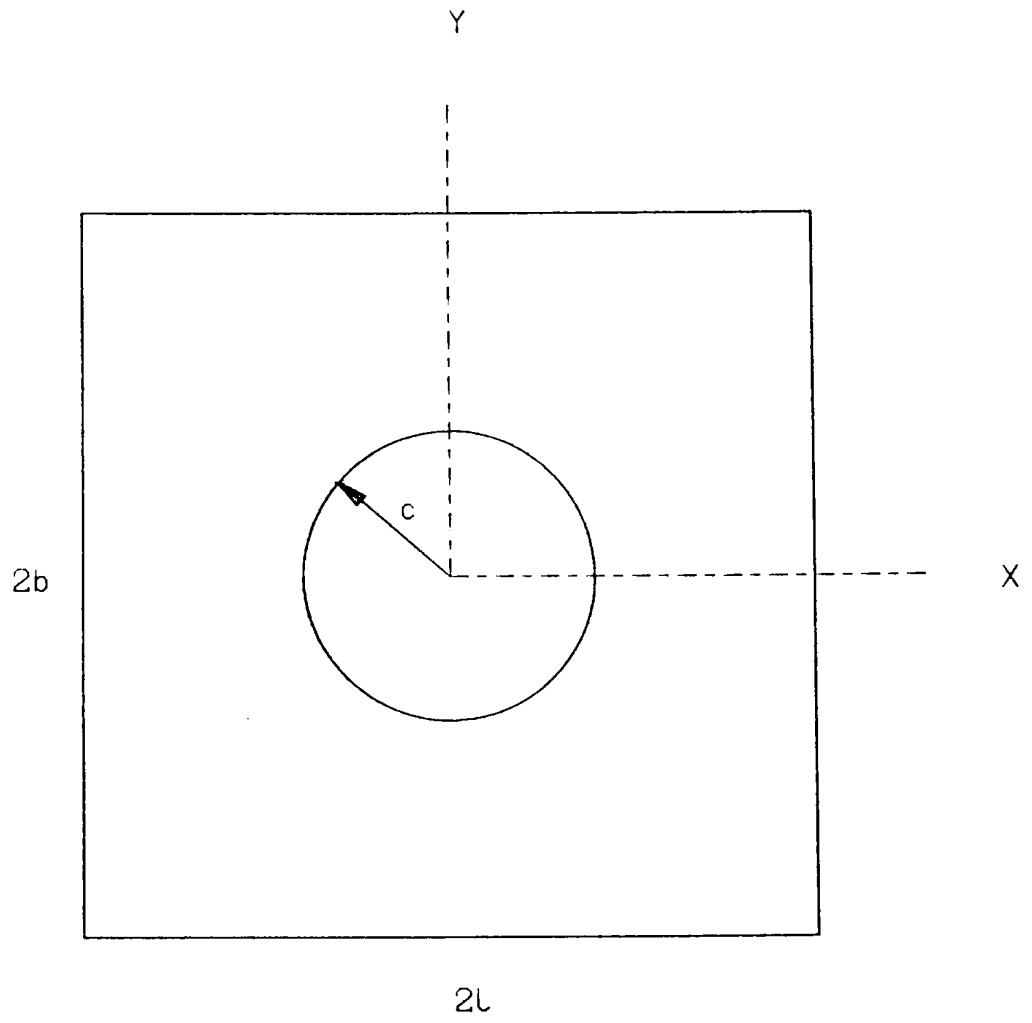

FIGURE 4·1 A TYPICAL PLATE WITH CIRCULAR HOLE

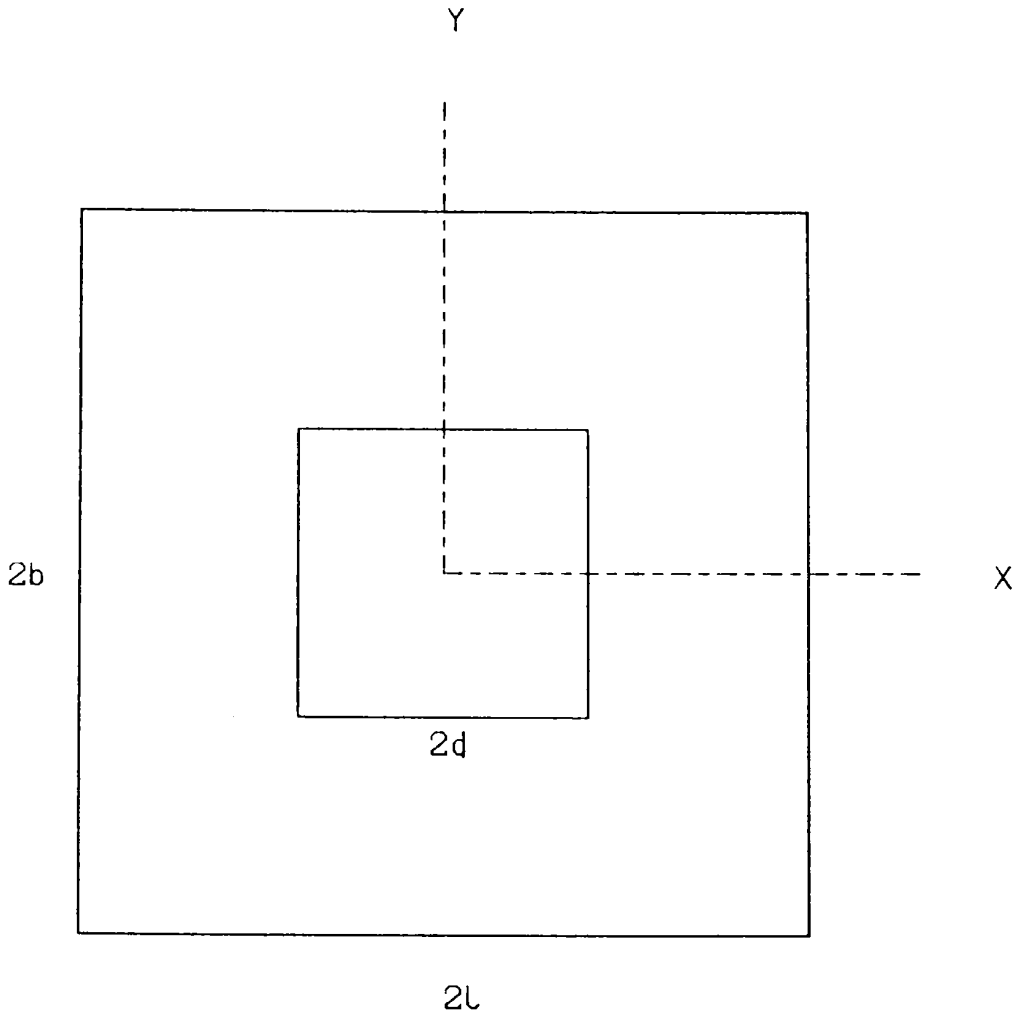

FIGURE 4·2 A TYPICAL PLATE WITH SQUARE HOLE

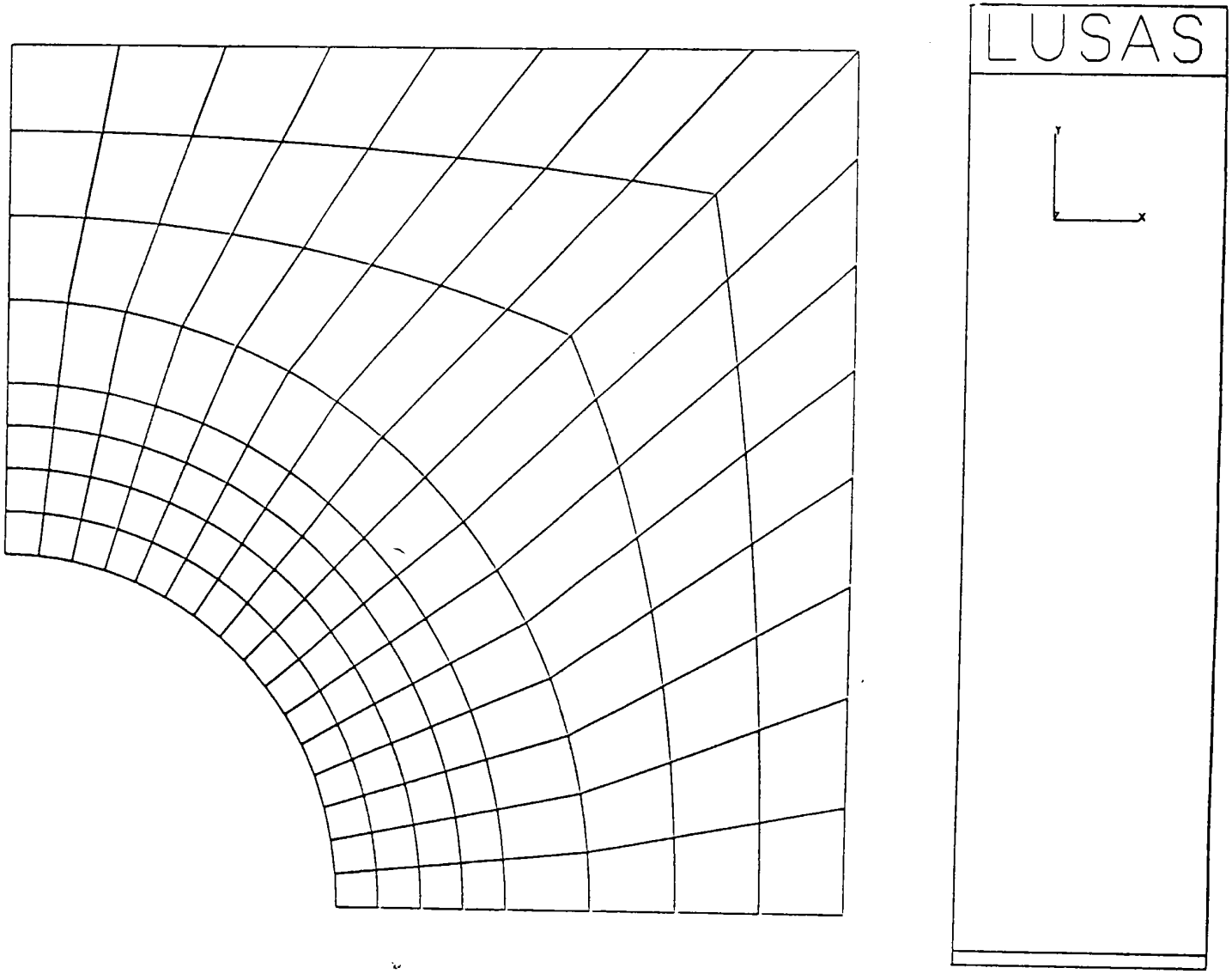

FIGURE 4.3 A TYPICAL FINITE ELEMENT MESH - PLATE WITH CIRCULAR HOLE

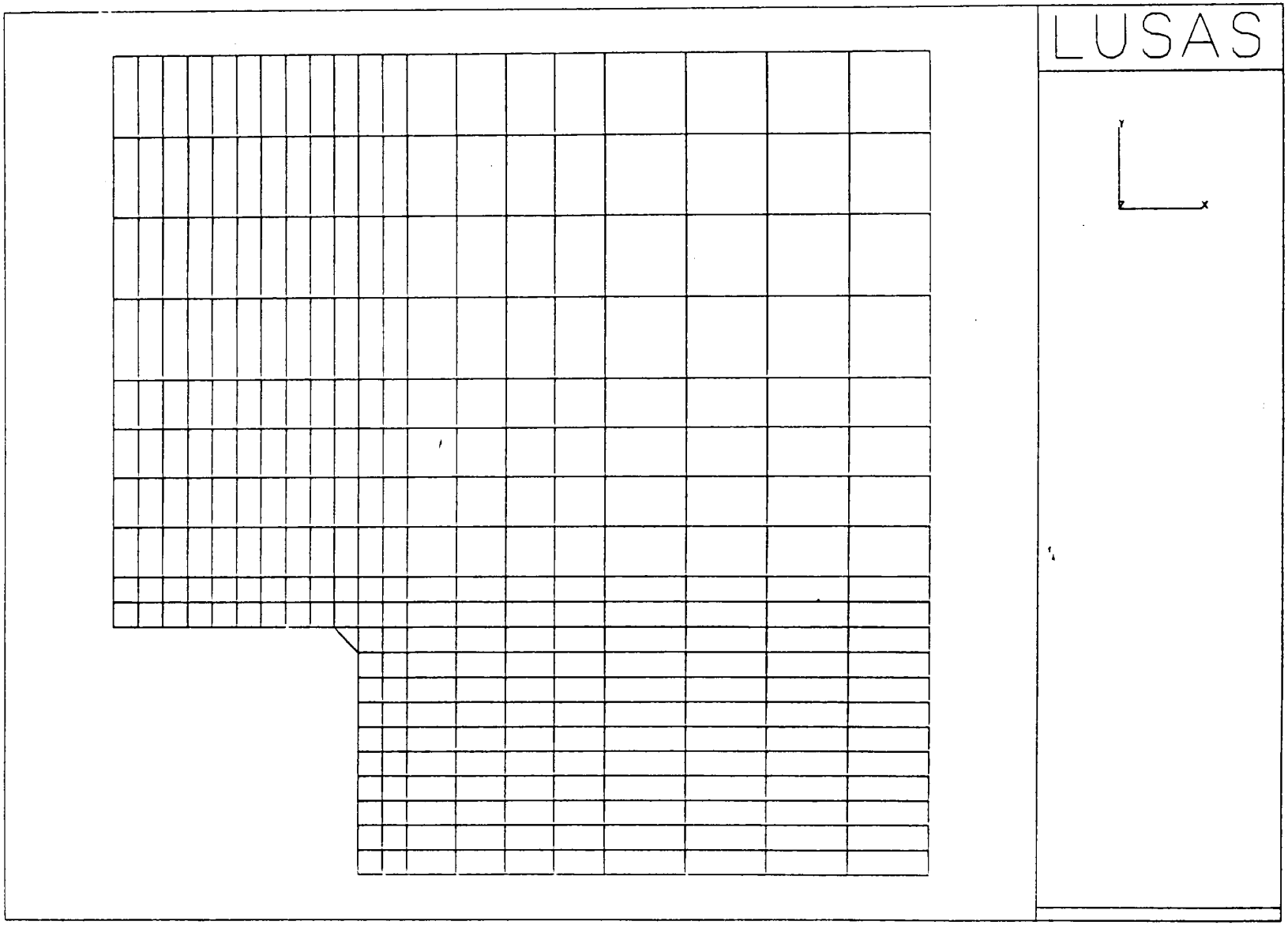

FIGURE 4.4 A TYPICAL FINITE ELEMENT MESH - PLATE WITH SQUARE CUTOUT

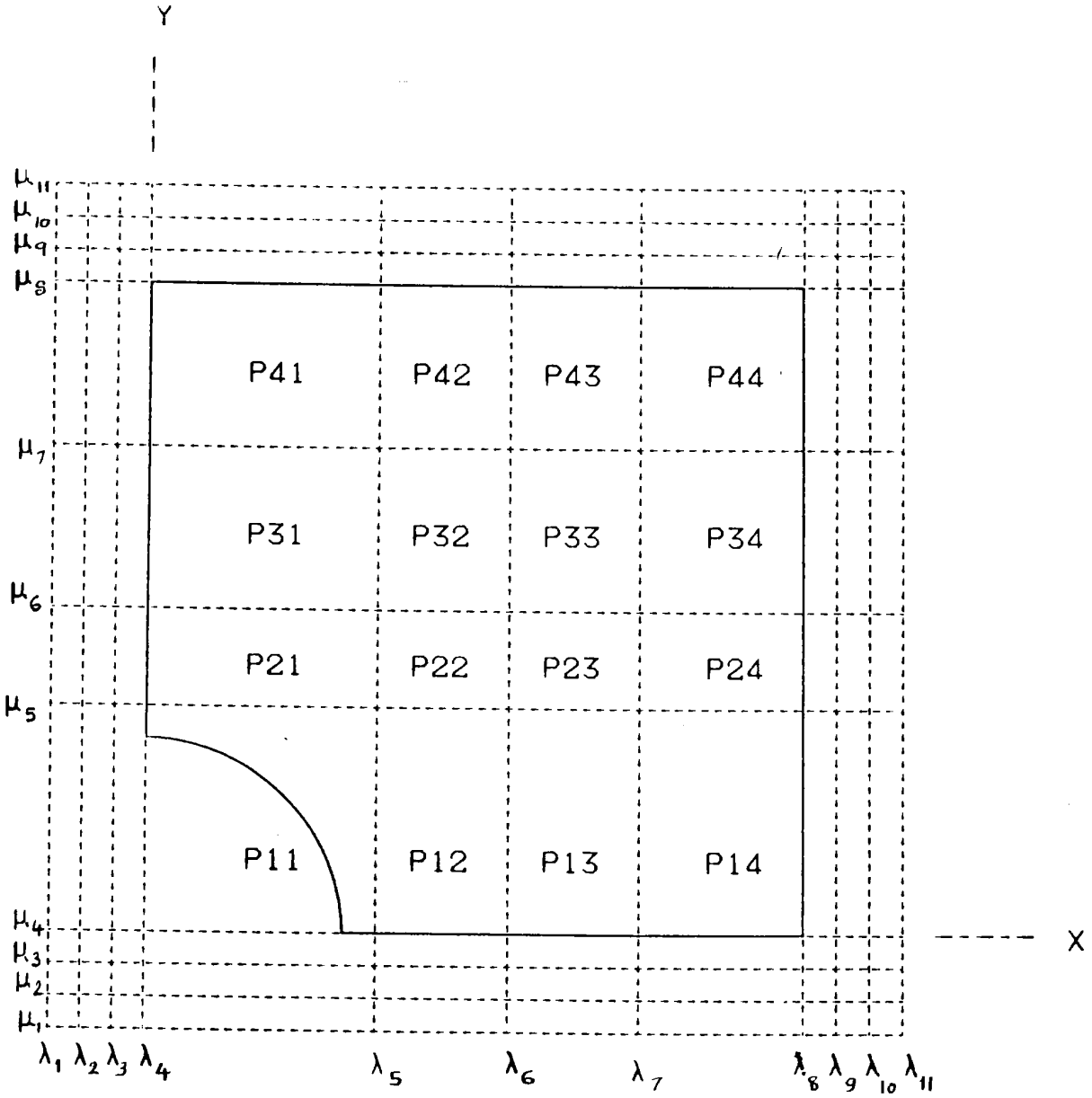

FIGURE 4·5 A TYPICAL SPLINE GRID FOR QUARTER PLATE

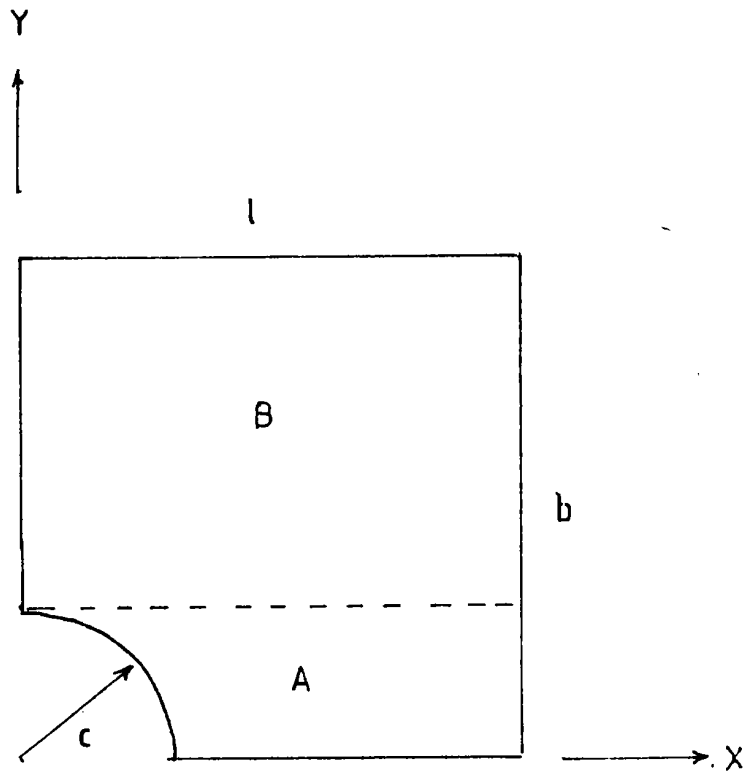

FIGURE 4.6 A TYPICAL PLATE FOR DEFINING INTEGRATION LIMITS

CHAPTER FIVE

EXPERIMENTAL INVESTIGATIONS

EXPERIMENTAL INVESTIGATION

5.1 Introduction

An experimental investigation was carried out to obtain information on the buckling and post-buckling behaviour of plates with circular and square cutouts. The experimental work was conducted through one Msc. project [29]. The general purpose of the investigation was to examine the behaviour of perforated plates under in-plane compressive loading and obtain experimental results on deflections and internal stresses to authenticate the validity of the theoretical analysis given in chapter three and four. The test rig was designed and manufactured at the College of Aeronautics. The rig was designed to test the plates under the same loading and boundary conditions as assumed during the theoretical analysis, which are:-

(a) The loaded edges are simply supported but are held straight during the loading process, i.e. a uniform displacement of the loaded edges.

(b) The unloaded edge are simply supported with no restraint in the plane of the plate.

(c) Zero shear stresses on all edges.

5.2 The Test Equipment

The test equipment consists of : -

- The Test Rig
- The Loading Machine
- The Strain Recording Equipment

5.2.1 The Test Rig

The design of the test rig and the test specimen was constrained by the size of the loading machine. Figure 5.1 shows a photograph of the experimental setup. The mild steel test rig comprises of a heavy fixed base and strong vertical support and a loading head (see figure 5.6.1) and was designed with a purpose to achieve maximum accuracy of the measured deflections and strains.

In order to achieve the simple support boundary conditions of the unloaded edges with no in-plane restrains, the unloaded edges were supported by the knife edge support arrangements. The vertical knife edges were designed with adjustment facilities for testing plates of

different thicknesses. The knife edges were made from mild steel of dimensions 10"x13/8"x1/2" and were machined to a small radius and hardened (figure 5.6.3). These were then fixed to a 13"x11"x1/2" supporting plate. To ensure horizontal movement of the knife edges, 1/2"x3/8" slots were machined in the supporting plate as shown in figure 5.6.4. The knife edges and supporting plates were attached to the vertical supports as shown in the plan view of the test rig in figure 5.6.2. Each of the two vertical supports was made from two mild steel 1/2" thick angle section bars of dimensions 3"x3"x24". A 3"x3"x1/2" mild steel plate was welded to each of the vertical support at the lower end in order to attach these supports to the base (see figure 5.6.5).

The base consisted of a mild steel plate machined to 18"x11"x1" with four 9/16" holes tapped to receive the vertical supports. Four 9/16" holes were also tapped in the centre line to house the roller assembly. The drawing of the base plate is shown in figure 5.6.6.

The loading head of the test rig consisted of two mild steel plates of dimensions 11 3/4"x5"x1/2", one plate to attach the loading head of the machine by means of 3/16" screws and the other to house a roller assembly (figure 5.6.6). The two plates were joined by means of four 3/8"

cap head screws.

In order to achieve the simple support boundary conditions at the loaded edges, the plate specimen were supported by two roller assemblies which consisted of cylindrical rollers supported by the needle rollers in a housing block. Each of the 10" long cylindrical roller of $1\frac{1}{4}$" diameter was machined from mild steel and hardened. A flat surface was machined along the whole length of the roller and a 1/4"x1/4" groove was machined along the flat surface. Centring strips of dimensions 10"x1/4"x1/4" containing 1/16"x1/16" central slots as shown in figure 5.6.8 were fitted in the groove to allow the specimen plates to be located in the centre of the roller. The cylindrical rollers were surrounded by nineteen needle rollers of 1/8" diameter and 10" in length. The needle rollers were made of mild steel and hardened. The rollers were polished and lubricated to reduce friction and to achieve free rotation. The cylindrical and needle rollers were installed in the housing block of dimension 10"x3"x3". The dimensions of the roller assembly block are shown in figure 5.6.9. Mild steel L-shaped strips of 1/8" thickness were screwed to the edges of the housing block to house the needle rollers. The edges of these strips were chamfered to 30 degrees angle for providing rotational space of the specimen plate. Two 3"x3"x1/8"

support plates were installed on the sides of the roller assembly. The detailed drawings of the cylindrical and needle rollers, the L-shaped strips and the support plate are given in figure 5.6.7 and the roller assembly arrangements are shown in figure 5.6.10

The fixed base with a roller assembly, two vertical supports and the loading head with a roller assembly were then assembled to form the complete test rig. The dimensions of the rig and manufacturing drawings are shown from figures 5.6.1 to 5.6.10.

5.2.2 The Loading Machine

INSTRON 1195 testing machine of maximum loading capacity of 10,000 lbf. was used during the tests. Though the loading is the uniform displacement type, the applied load corresponding to each incremental displacement was measured through load cells of the machine containing load transducers.

5.2.3 The strain Recording Arrangements

Two types of TML strain gauges, one of foil gauge series F-FLA-6 and the other of series F-FCA-6 were used

to measure strains. The former gauges which measure unidirectional strains were installed on the specimen plates to estimate the buckling load whereas the latter, which were two gauge rosette type, were used to record strains to investigate the internal stress variations in the perforated plate. The 'three wire technique' was used to connect the strain gauges into a wheatstone bridge circuit which compensates for changes in resistance in the leads from the bridge circuit to the gauges (figure 5.7). The wheatstone bridge circuit was connected to the data logger and the strain output was pointed on a paper roll.

5.3 Test Specimens

Test specimens of square plates with a circular or a square cutout (figures 5.2 & 5.3) made from mild steel and aluminium sheets of thickness 1.22 mm and dimensions 254 x 254 mm (b/t = 208) were manufactured. Ten plates, five with a circular and five with a square cutout, were tested to observe load ~ delection behaviour. Tests were conducted on plates with various cutout sizes ranging from c/b (cutout size/plate width ratio) of 0.2 - 0.6 to obtain data for the load and out-of-plane deflections. Two plates with c/b=0.5 were used to measure strains at

various locations. To take advantage of the symmetry, strain gauges were installed on 1/4 of each plate as shown in figures 5.4 and 5.5. Initial imperfections were measured on all the plates by the method described in the next section. Tensile tests were conducted on the test specimen to evaluate the material properties. The specimen plates and the tensile test specimen were made from the same sheet of material.

5.4 The Test Procedure

5.4.1 Tests to Investigate Load ~ Deflection Behaviour

Dial gauges were used to measure the out-of-plate deflections and the buckling loads were estimated from the strain measurements using the method described in the next paragraph. Following steps were taken prior to the application of the load to ensure accuracy of test results.

(a) The thickness of the plates was measured at various points with a micrometer in order to obtain an average value. A slight variation of thickness was noticed at different locations of the plate.

(b) The edges of the plate were checked for squareness and the hole contour was checked for uniformity and smoothness.

(c) The initial imperfections were estimated by placing the specimen on a flat surface and checking the initial deflections at various locations with the help of DC-LVDT position transducers. The output of the transducers was connected to a x-y plotter and the deflection curves were plotted at various sections of the plate. The initial imperfections were then calculated form the deflection curves which were found to be varying from 0.053 to 0.258 times plate thickness.

(d) The test specimen were placed on the bottom rollers and its exact vertical positioning was ensured. The knife edges were then positioned on the unloaded edges so as to ensure free in-plane but zero lateral movement of the plate. The loading head, which was initially fixed to the loading machine, was gradually lowered in order to align the plate upper edge to the centring strip slot in the roller assembly. A small fraction of the estimated buckling load was applied on the specimen and then released so that the specimen is

properly settled in its supports.

(e) The dial gauges were attached to a stand having a magnet base and the assembly was placed on the base plate of the test rig. The dial gauges were positioned on the hole edge and on diagonally opposite locations, half way between plate corner and its centre. For few plates the deflection measurements were also recorded at other locations by moving these gauges.

The incremental load was applied and deflection and strain measurements were taken at each increment till the plate collapsed which was noticed by the reversal of the load. The buckling loads were estimated from the variation of the membrane strain with load. The membrane strains were measured at some point on the plate. The average strain value from two opposite locations of strain gauges at that point gave the membrane strain. The estimation of the buckling load from the strain measurement was made by comparing pre- and post-buckling curves of load vs. membrane strain. This method has been suggested by Coan [52] and used by Ritchie [10]. The method described by Coan considered that buckling occurred at the load corresponding to the intersection of tangents to the pre- and post-buckling load ~ mid surface

strain curves. In this method only straight lines of best fit are required to be drawn through the pre- and post-buckling experimental plots. Figure 5.8 illustrates estimation of buckling load by the method described above.

5.3.2 Tests to Investigate Stress Variation

The investigation of the internal stress variation was carried out by performing tests on two steel plate specimen. One plate with a circular hole size of c/b=0.5 and the other with a square cutout of the same size were tested. Both the plates were extensively strain gauged. To take advantage of symmetry, strain gauges were installed on one quadrant of each plate. Forty strain gauges were installed on each of the plates, twenty on each side. The strain gauges were connected to data logger by the 'three wire technique'. The incremental load was applied and the strain measurements were taken for each increment. The applied load was increased up to about twice the critical load to allow the plate to stay in the elastic range for any possible re-use.

The experimental results to investigate the load - deflection behaviour and the variation of the internal

stresses at different applied loads have been presented and discussed in chapter six.

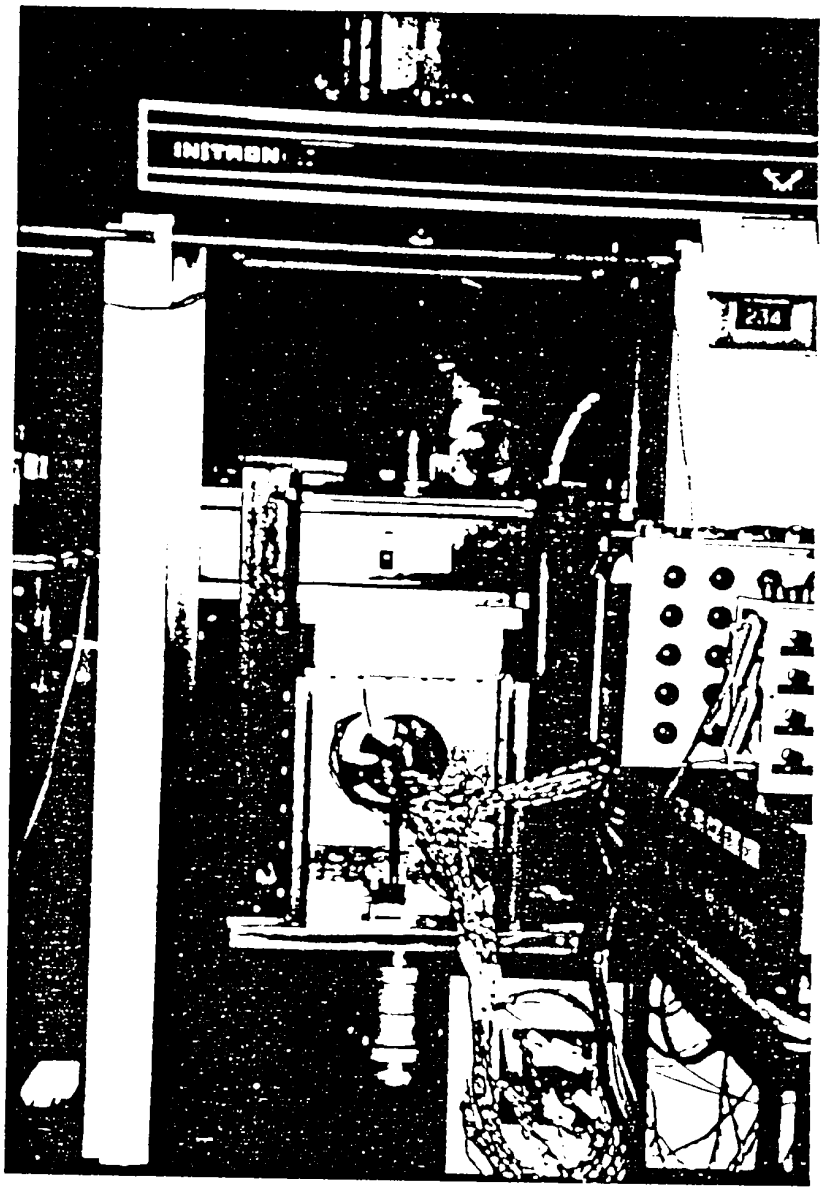

FIGURE 5.1 THE EXPERIMENTAL SETUP

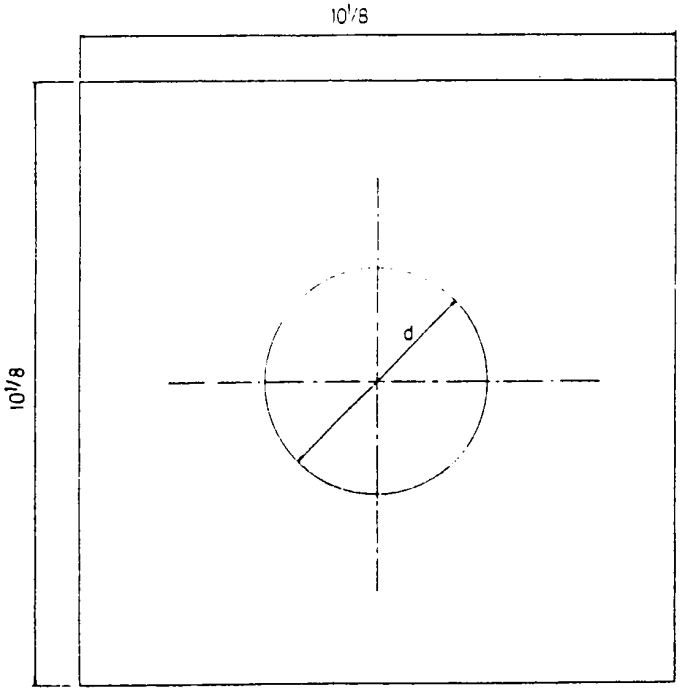

PLATE SPECIMEN THICKNESS t = 0.048 (1.22mm)

S.NO	MATERIAL	d	QTY
1	MILD STEEL	2	1
2	—〃—	3	1
3	—〃—	4	1
4	—〃—	5	1
5	—〃—	6	1
6	AL-L72	2	1
7	—〃—	3	1
8	—〃—	4	1
9	—〃—	5	1
10	—〃—	6	1

FIGURE 5.2 PLATE SPECIMEN WITH CIRCULAR HOLE

ALL DIMENSIONS IN INCHES

			FULL	TITLE:- SPECIMEN PLATE VARYING HOLE DIAMETERS
COLLEGE OF AERONAUTICS CRANFIELD INSTITUTE OF TECHNOLOGY CRANFIELD				3

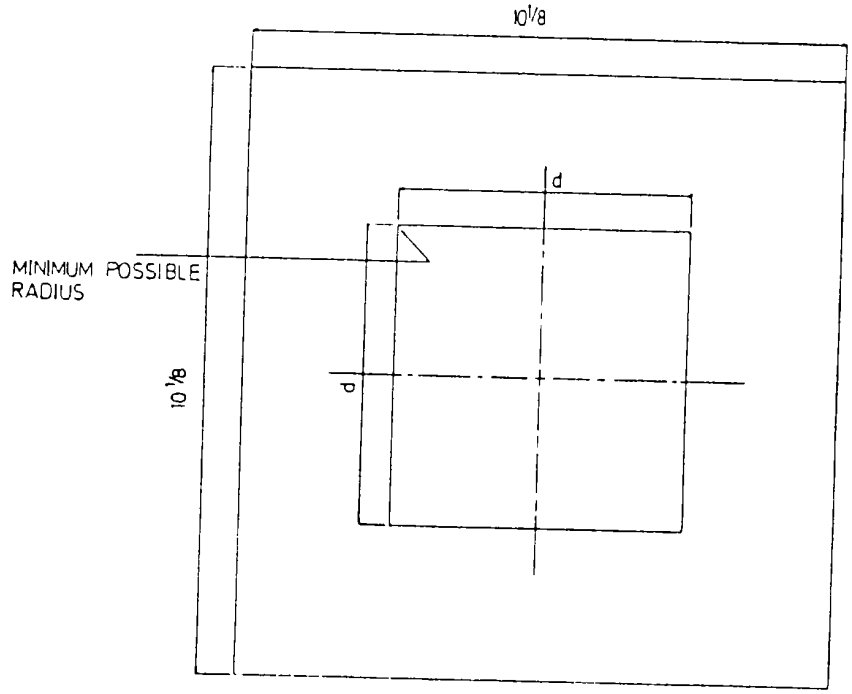

S.NO	MATERIAL	d	QTY
1	MILD STEEL	2	1
2	—"—	3	1
3	—"—	4	1
4	—"—	5	1
5	—"—	6	1
6	AL-L72	2	1
7	—"—	3	1
8	—"—	4	1
9	—"—	5	1
10	—"—	6	1

FIGURE 5.3 PLATE SPECIMEN WITH SQUARE CUTOUT

ALL DIMENSIONS IN INCHES

			FULL	TITLE:- SPECIMEN SQUARE PLATE - VARYING CUTOUTS
COLLEGE OF AERONAUTICS CRANFIELD INSTITUTE OF TECHNOLOGY CRANFIELD				3

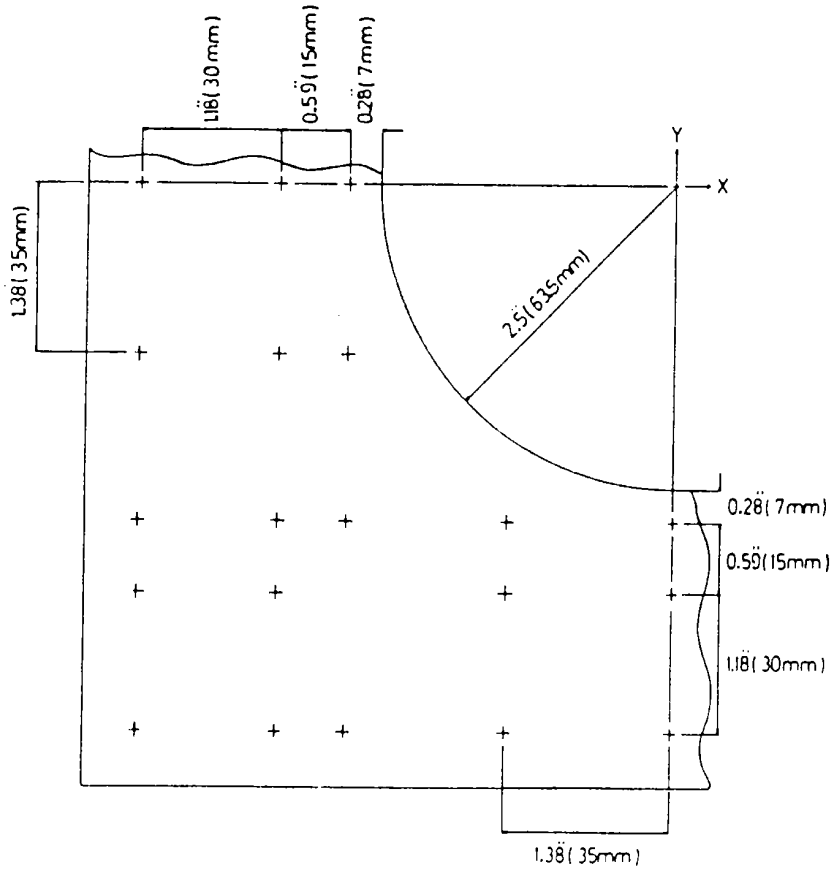

			SCALE 2:1	TITLE:-ARRANGEMENT OF STRAIN GAUGE ROSETTES - PLATE A
COLLEGE OF AERONAUTICS CRANFIELD INSTITUTE OF TECHNOLOGY CRANFIELD				DRAWING No. 2
				SHT 1 OF 2 SHEETS

FIGURE 5.4 STRAIN GAUGE LOCATIONS

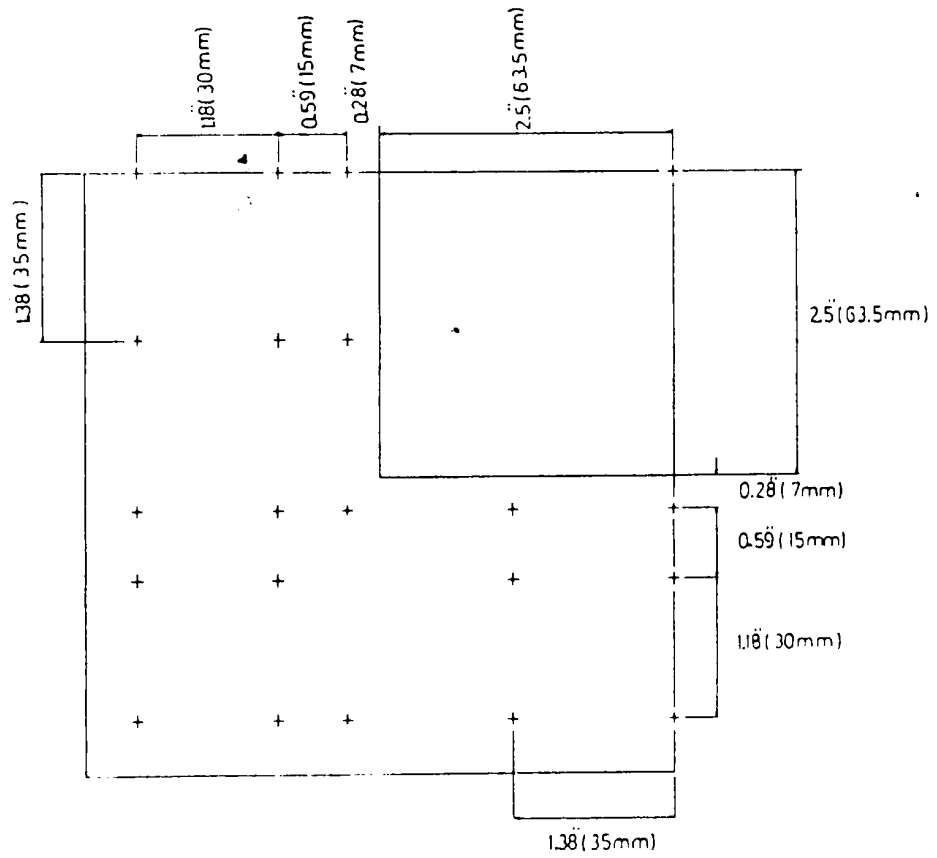

FIGURE 5.5 STRAIN GAUGE LOCATIONS

			SCALE 2:1	TITLE:-ARRANGEMENT OF STRAIN GAUGE ROSETTES - PLATE B
COLLEGE OF AERONAUTICS CRANFIELD INSTITUTE OF TECHNOLOGY CRANFIELD				DRAWING No. 2

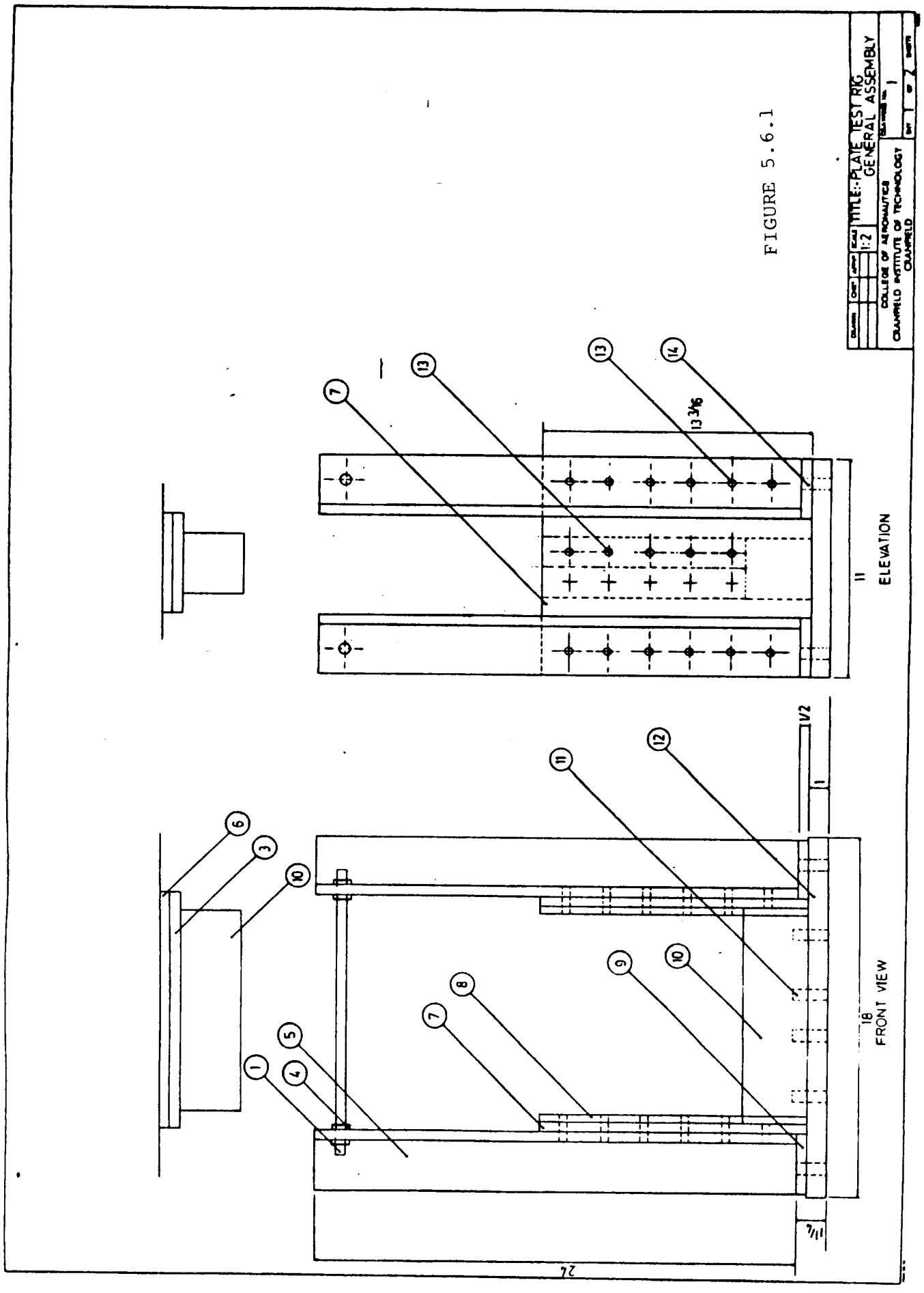
TITLE:- PLATE TEST RIG
GENERAL ASSEMBLY
COLLEGE OF AERONAUTICS
CRANFIELD INSTITUTE OF TECHNOLOGY
CRANFIELD
SCALE 1:2
ELEVATION
FRONT VIEW
13 3/16
11
18
27
7/11
1/2

FIGURE 5.6.1

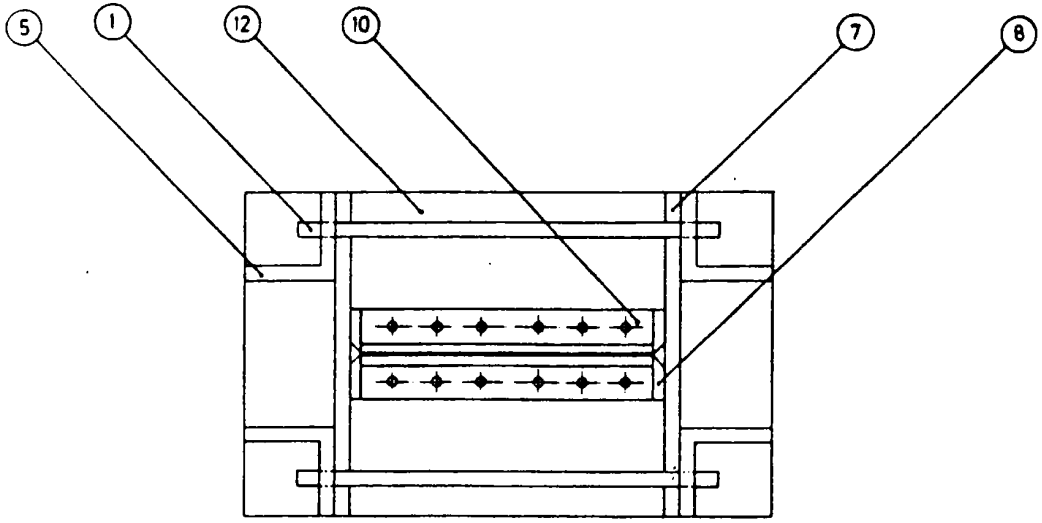

FIGURE 5.6.2

DRAWN	CHK'D	APP'D	SCALE 1:2	TITLE:- PLATE TEST RIG GENERAL ASSEMBLY

COLLEGE OF AERONAUTICS
CRANFIELD INSTITUTE OF TECHNOLOGY
CRANFIELD.

DRAWING No. 1

SHT 2 OF 2 SHEETS

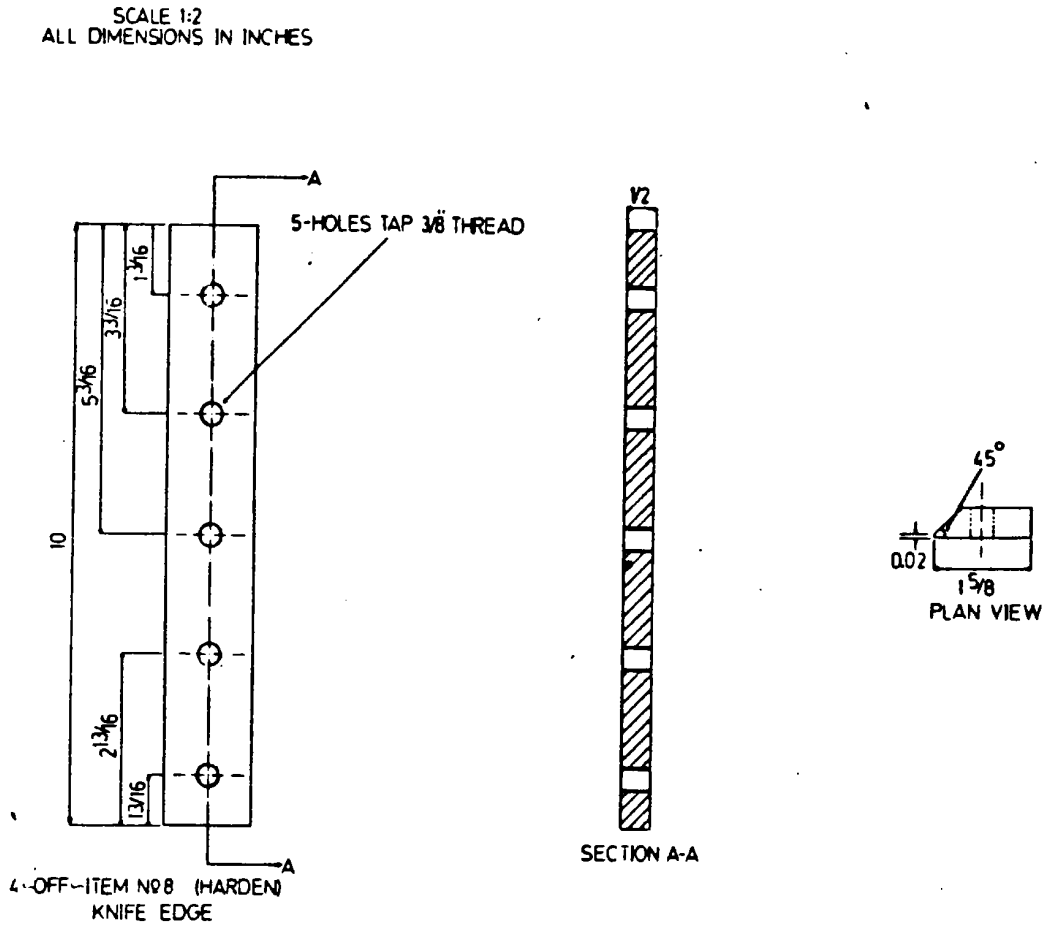
SCALE 1:2
ALL DIMENSIONS IN INCHES
A
5-HOLES TAP 3/8 THREAD
1-3/16
3-3/16
5-3/16
10
2-13/16
13/16
A
4-OFF-ITEM No 8 (HARDEN)
KNIFE EDGE
1/2
SECTION A-A
45°
0.02
1 5/8
PLAN VIEW

FIGURE 5.6.3

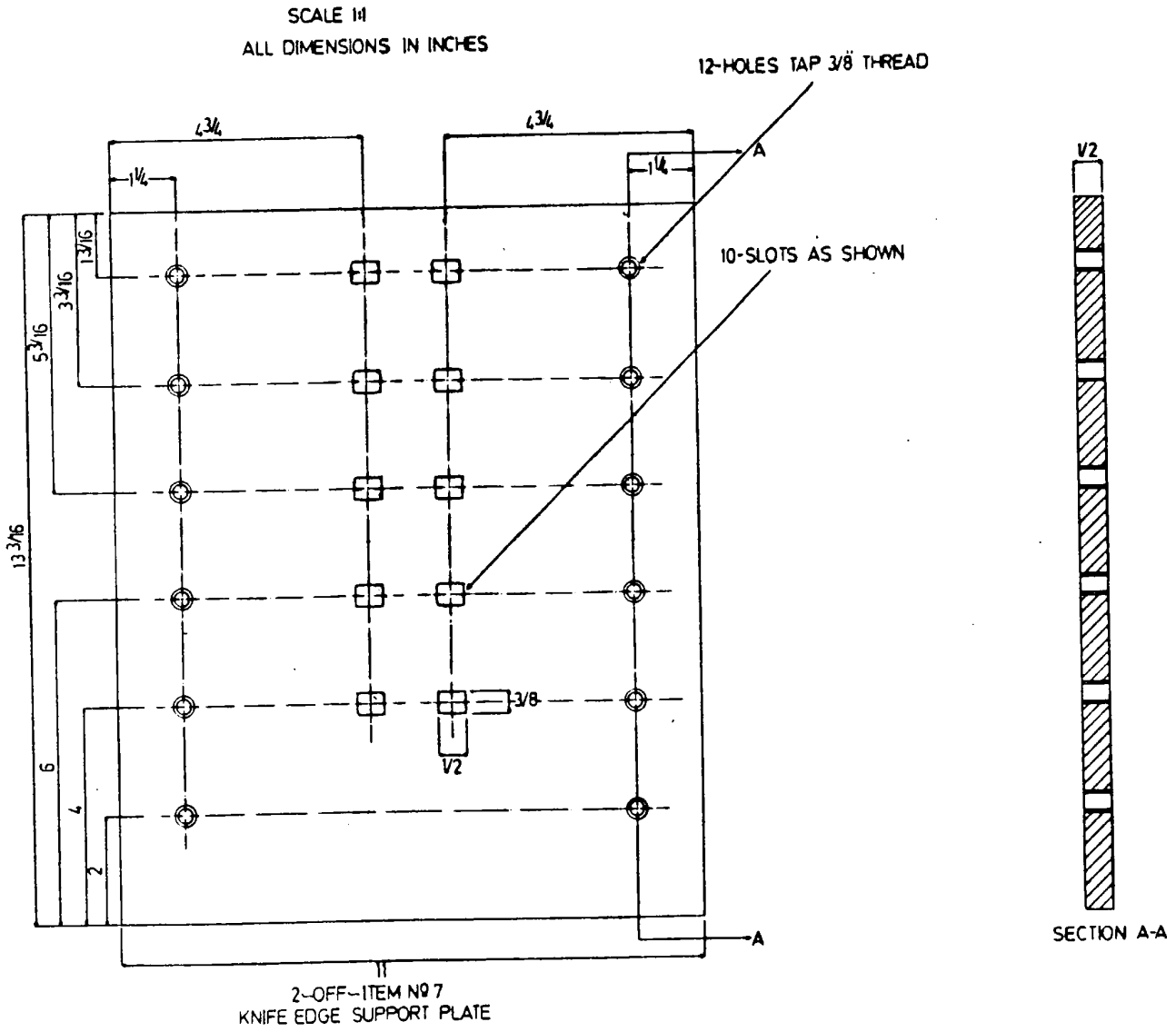
SCALE 1:1
ALL DIMENSIONS IN INCHES
12-HOLES TAP 3/8 THREAD
10-SLOTS AS SHOWN
4 3/4
4 3/4
1 1/4
1 1/4
A
A
1 3/16
3 3/16
5 3/16
13 3/16
6
4
2
3/8
V2
V2
SECTION A-A
2-OFF-ITEM NO 7
KNIFE EDGE SUPPORT PLATE

FIGURE 5.6.4

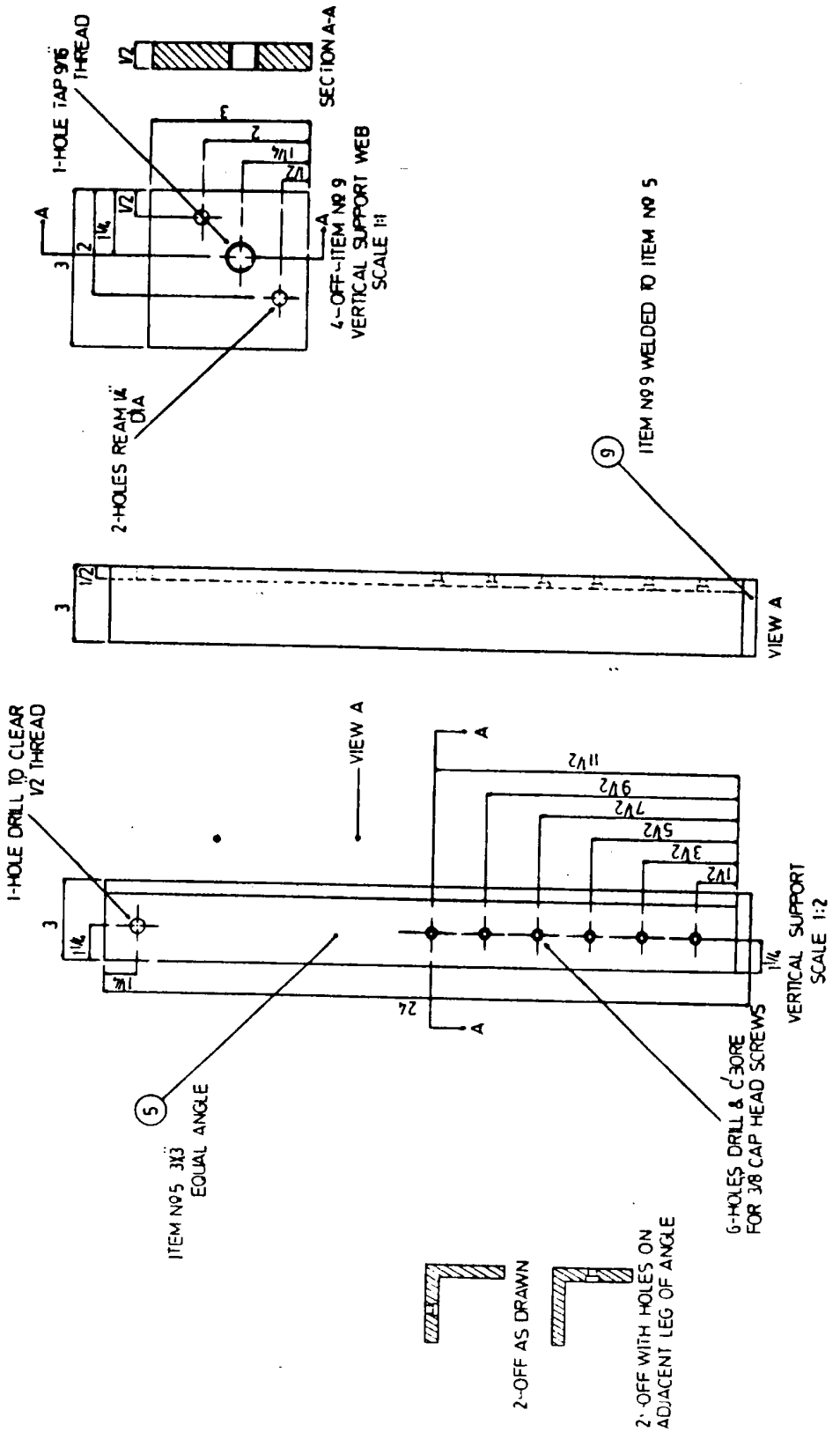
1-HOLE TAP 9/16 THREAD
SECTION A-A
4-OFF-ITEM NO 9
VERTICAL SUPPORT WEB
SCALE 1:1
2-HOLES REAM 1/4" DIA
ITEM NO 9 WELDED TO ITEM NO 5
VIEW A
1-HOLE DRILL TO CLEAR 1/2" THREAD
VIEW A
ITEM NO 5 3X3 EQUAL ANGLE
6-HOLES DRILL & C'BORE FOR 3/8 CAP HEAD SCREWS
VERTICAL SUPPORT
SCALE 1:2
2-OFF AS DRAWN
2-OFF WITH HOLES ON ADJACENT LEG OF ANGLE

FIGURE 5.6.5

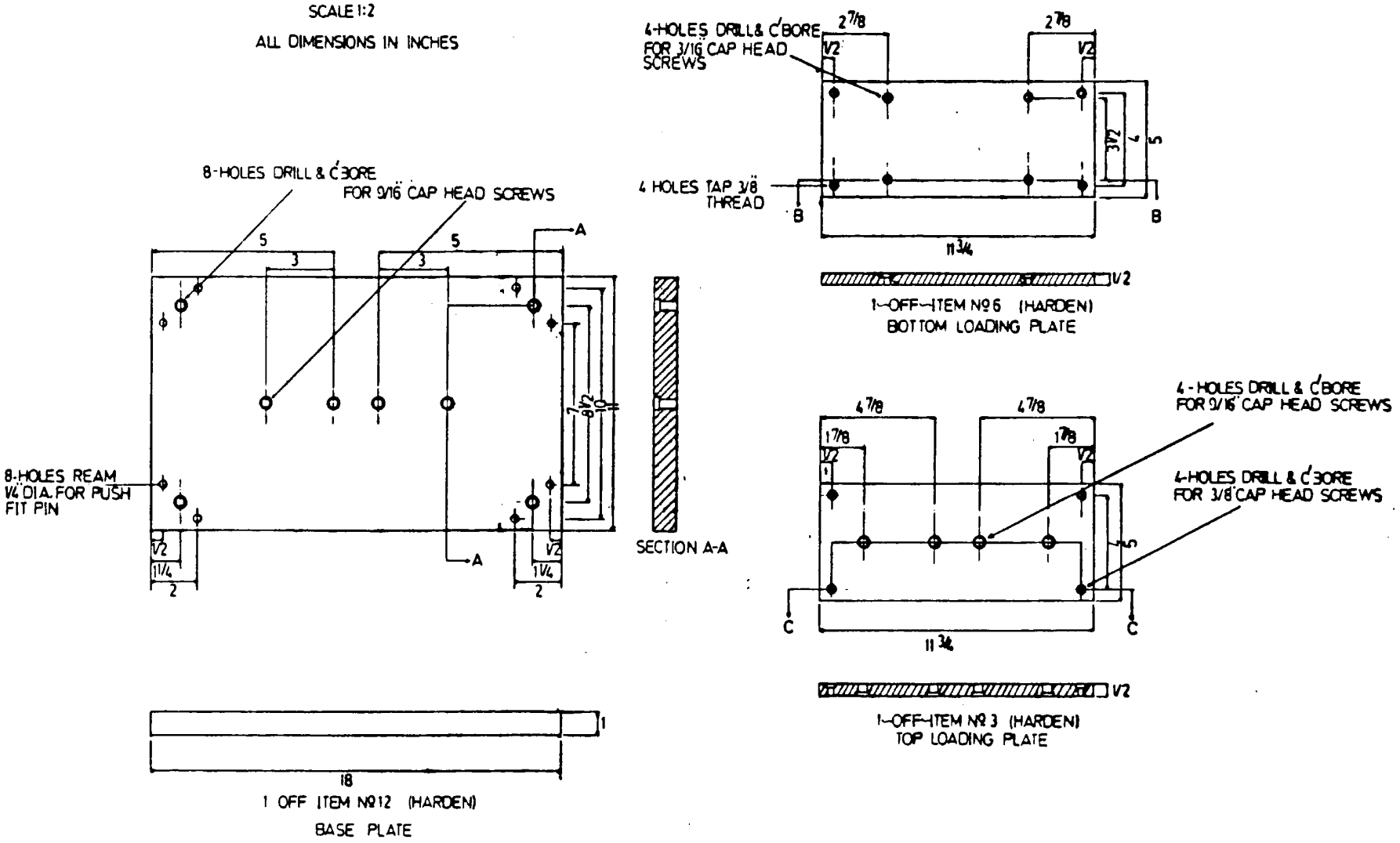
SCALE 1:2
ALL DIMENSIONS IN INCHES
8-HOLES DRILL & C'BORE FOR 9/16 CAP HEAD SCREWS
8-HOLES REAM 1/4 DIA FOR PUSH FIT PIN
SECTION A-A
1 OFF ITEM NO 12 (HARDEN)
BASE PLATE
4-HOLES DRILL & C'BORE FOR 3/16 CAP HEAD SCREWS
4 HOLES TAP 3/8 THREAD
1-OFF-ITEM NO 6 (HARDEN)
BOTTOM LOADING PLATE
4 - HOLES DRILL & C'BORE FOR 9/16 CAP HEAD SCREWS
4-HOLES DRILL & C'BORE FOR 3/8 CAP HEAD SCREWS
1-OFF-ITEM NO 3 (HARDEN)
TOP LOADING PLATE

FIGURE 5.6.6

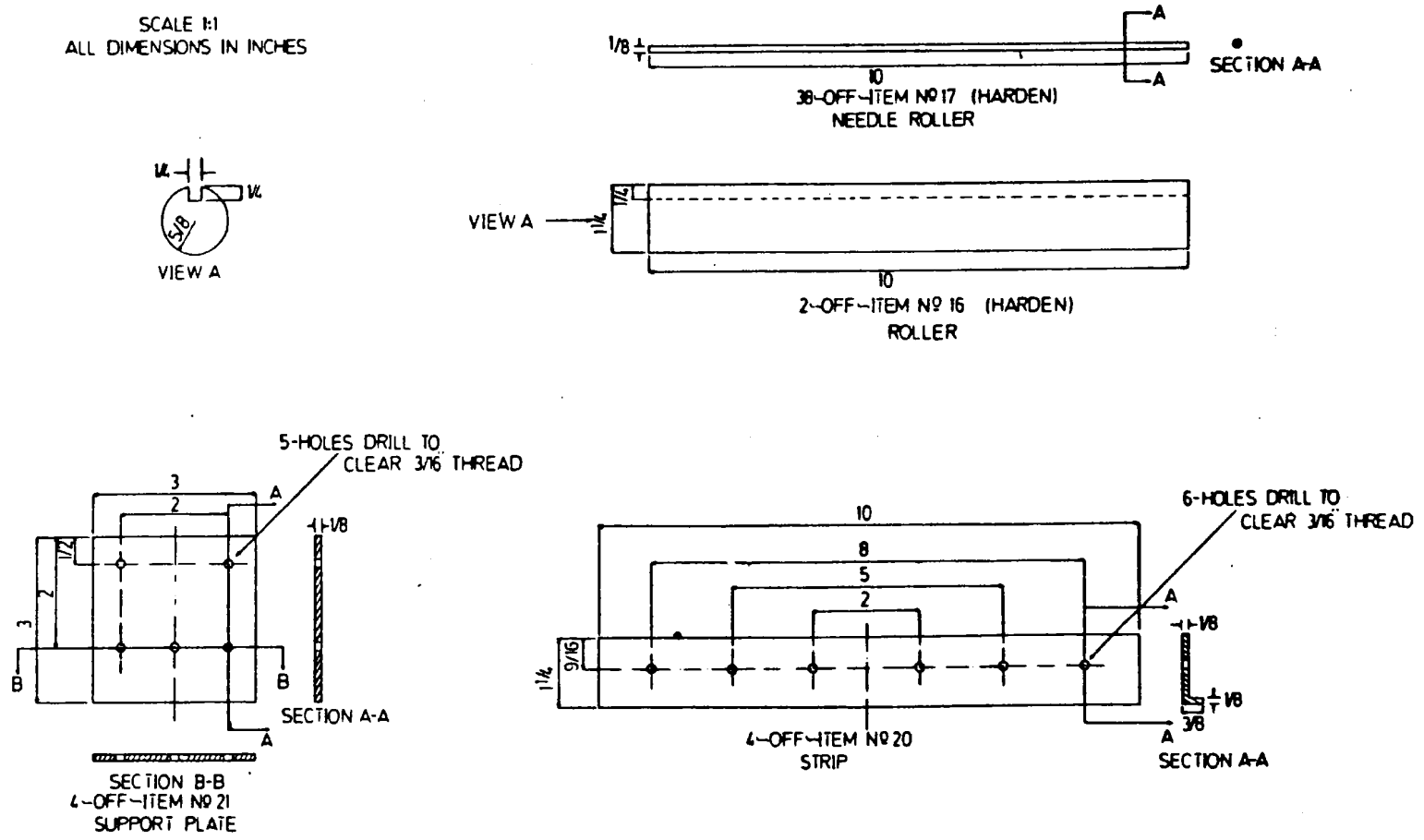
SCALE 1:1
ALL DIMENSIONS IN INCHES
VIEW A
38-OFF-ITEM Nº 17 (HARDEN)
NEEDLE ROLLER
SECTION A-A
VIEW A
2-OFF-ITEM Nº 16 (HARDEN)
ROLLER
5-HOLES DRILL TO
CLEAR 3/16 THREAD
SECTION A-A
SECTION B-B
4-OFF-ITEM Nº 21
SUPPORT PLATE
6-HOLES DRILL TO
CLEAR 3/16 THREAD
4-OFF-ITEM Nº 20
STRIP
SECTION A-A

FIGURE 5.6.7

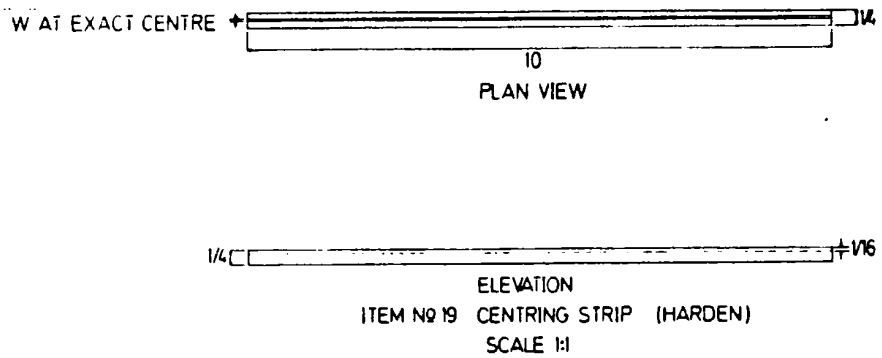

QTY	W GAUGE
TWO	22
TWO	20
TWO	18
TWO	16

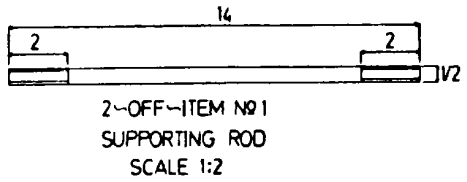

FIGURE 5.6.8

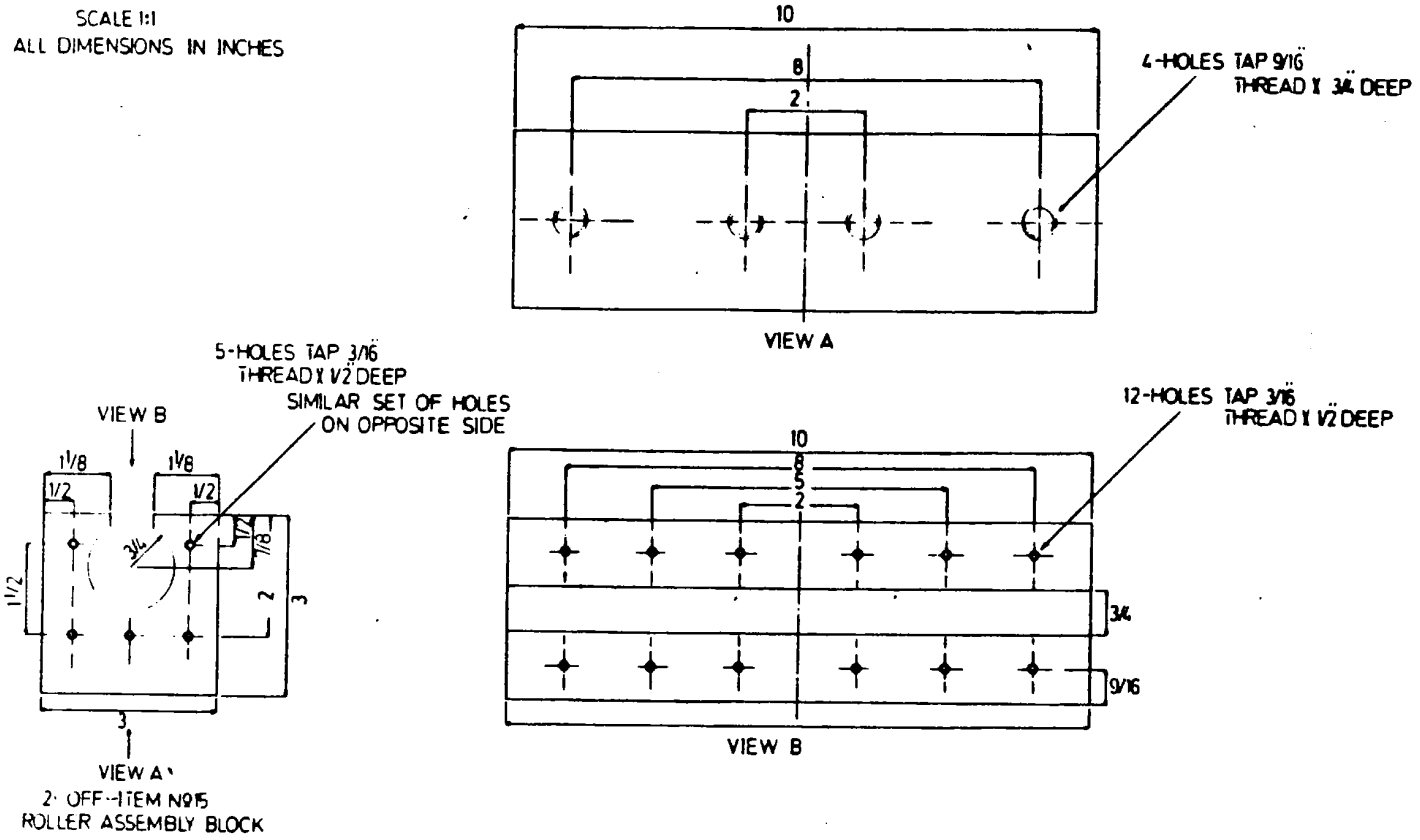
SCALE 1:1
ALL DIMENSIONS IN INCHES
10
8
2
4-HOLES TAP 9/16
THREAD X 3/4 DEEP
VIEW A
5-HOLES TAP 3/16
THREAD X 1/2 DEEP
SIMILAR SET OF HOLES
ON OPPOSITE SIDE
VIEW B
1 1/8
1 1/8
1/2
1/2
3/4
1/2
7/8
1 1/2
2
3
3
VIEW A
2 OFF-ITEM NO 15
ROLLER ASSEMBLY BLOCK
12-HOLES TAP 3/16
THREAD X 1/2 DEEP
10
8
5
2
3/4
9/16
VIEW B

FIGURE 5.6.9

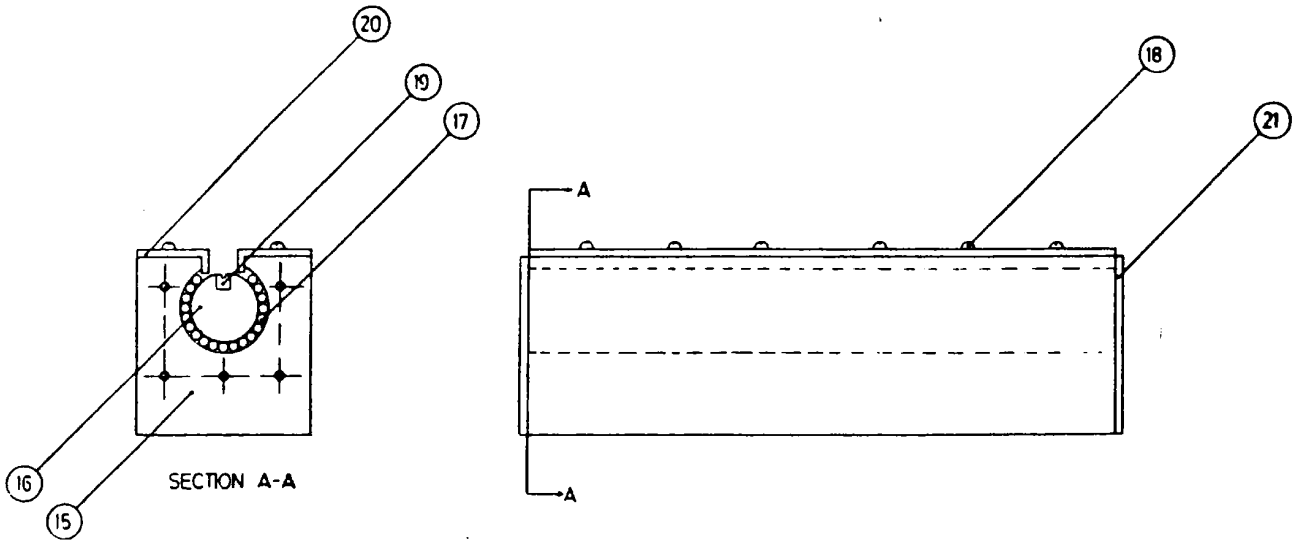

FIGURE 5.6.10

			FULL	TITLE:- GENERAL ASSEMBLY OF SUB-ASSEMBLY NO 10
COLLEGE OF AERONAUTICS CRANFIELD INSTITUTE OF TECHNOLOGY CRANFIELD.				2

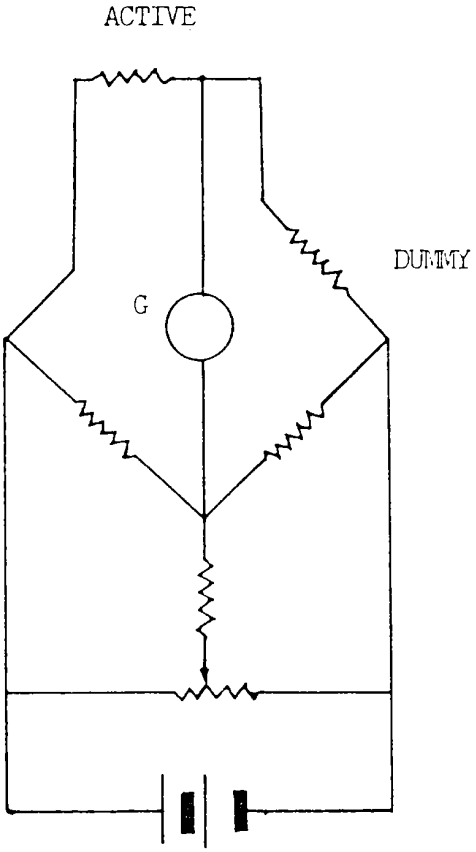

FIGURE 3.7 THE THREE WIRE TECHNIQUE

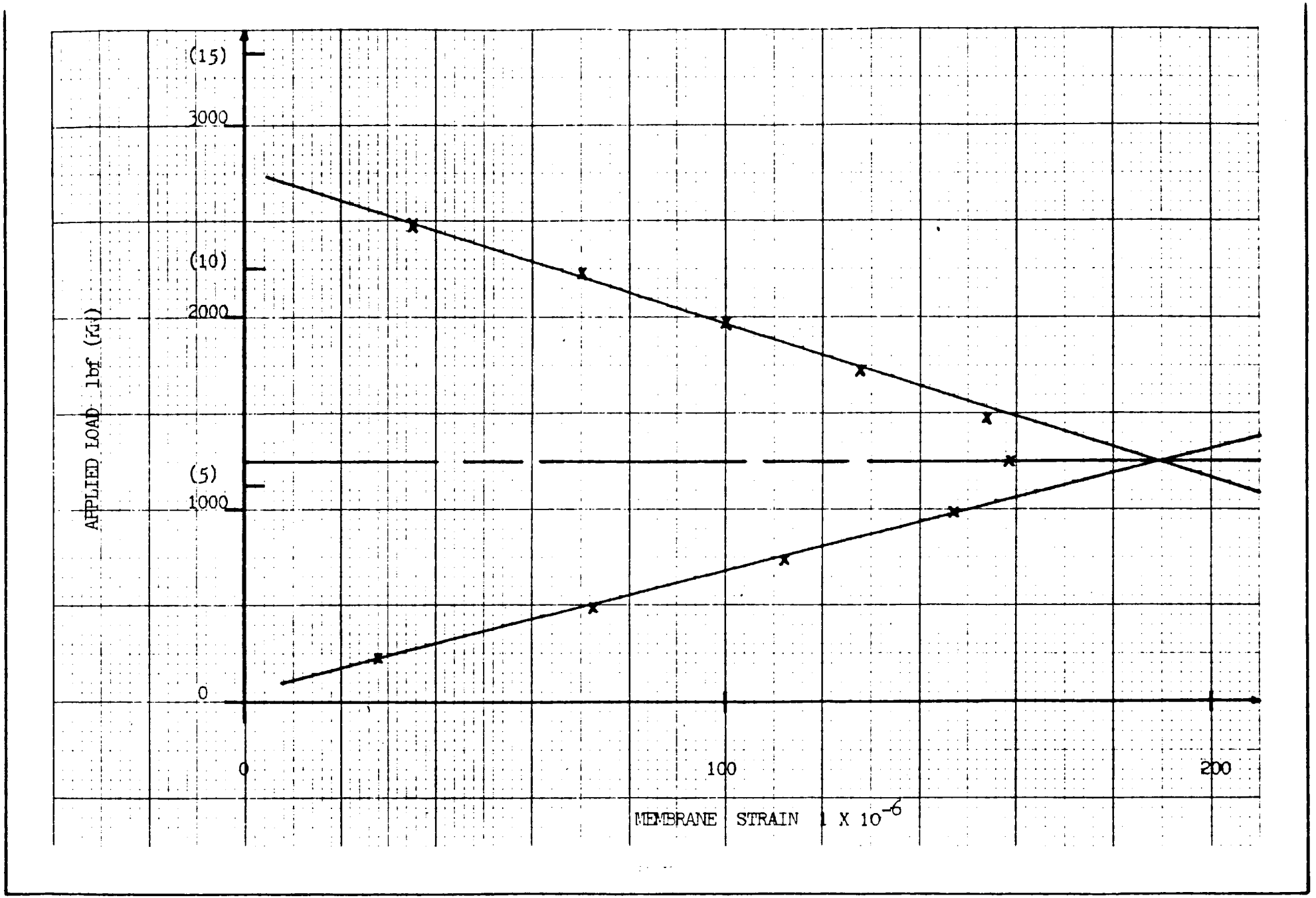

FIGURE 5.8 ESTIMATION OF THE EXPERIMENTAL BUCKLING LOAD

CHAPTER SIX

PRESENTATION OF RESULTS AND DISCUSSION

PRESENTATION OF RESULTS AND DISCUSSION

The theoretical analysis described in chapter four has been applied on square plates with centrally located circular and square cutouts. The results thus obtained on the displacements and internal stress distribution in these plates and their comparison with the theoretical and experimental results of other investigators [10,11 & 29] are described in this chapter. The results are presented and discussed under the following headings.

6.1 Buckling Results

6.2 Post-Buckling Results

- 6.2.1 Load ~ Out-of-plane deflections
- 6.2.2 Load ~ edge compression
- 6.2.3 Internal stress distributions

The detailed breakdown of the presentation, showing the figure and page numbers of each type of result is tabulated as shown in table 6-1. All the results presented are for simply supported square plates subjected to in-plane compressive loading. The cutout sizes considered range from c/b=0.2 to 0.5; these being the most commonly used sizes inthe practical situations.

6.1 Buckling Results

The theoretical analysis described in chapter four, sections 4.4, is used to obtain the buckling results of simply supported square plates with centrally located circular and square cutouts. For plates with a circular hole the results are presented for the two types of loading, i.e. the uniform displacement loading and the uniform stress loading. For plates with a square cutout the results are presented for the case of uniform displacement loading only. The results are plotted for K/K_u vs. c/b , where K and K_u are the buckling coefficients for the perforated and the unperforated plates respectively, c is the hole radius and b is the half plate width. The buckling coefficients have been calculated using the following equation :-

$$\delta_{cr} = K \frac{\pi^2 E}{12(1-\nu^2)} \left(\frac{t}{b}\right)^2$$

σ_{cr} is the average stress at any section parallel to the loaded edge corresponding to the applied load/displacement at the time of buckling. When a perforated plate is subjected to uniform edge compression the stresses vary along the loaded edge. The stress σ_x corresponding to the

critical edge displacement is integrated along the y-axis, at any section in the plate, to evaluate the critical stress per unit width which is substituted in the above equation to obtain the buckling coefficient.

The experimental buckling load has been estimated by the method described in section 5.3.1. This method which was first described by Coan [52] considered that the buckling occurred at the intersection of the tangents to the pre- and post-buckling load ~ mid surface strain curves.

6.1.1 Buckling Results of Plates with Circular Holes

The variation of the buckling coefficient with the hole size for a simply supported square plate with a centrally located circular hole is presented in figure 6.1. The theoretical results plotted for the two types of loading show a different pattern of curves, similar to those presented by the other investigators [10,12].

For the case of uniform stress loading the buckling coefficient decreases with the increase in hole size. The loaded edges of a perforated plate in this case are unrestrained and the in-plane distortions are non uniform. The variations in the edge displacements is

proportional to the hole size, and thus the critical loads becomes smaller as the hole size is increased. For plates subjected to the uniform displacement loading, the loaded edges are constrained to be held straight which results in a non uniform stress variation along the loaded edge. For plates with larger cutout sizes the stresses at the loaded edges are higher towards the corners and are lower towards the centre. For a perforated plate with c/b=0.5 the pre-buckling stress σ_x at the centre of the loaded edge is almost negligible as can be seen in figures 6.71 and 6.72. A plate with a larger hole size can be represented by a simplified model of two strips. Most of the load is carried by these strips whose width d depends on the plate dimensions and the hole size and is given by d=b-c, where b is the length of the side of the plate and c is the radius of the hole as illustrated in figure 6.6.1. It has been shown [12] that the critical load increases as the width of these strips becomes small. Therefore, for plates under the uniform displacement loading the buckling load increases with the increase in the cutout size. The experimental results shown in figure 6.1 show a trend which is similar to the theoretical curve, thus validating the above argument.

The buckling results have been compared with the other investigators. The theoretical and experimental results

presented by Ritchie [10] are compared with the author's theoretical results in figure 6.2. The variation of the buckling load for plates under the uniform stress loading is the same for both the investigations. For plates under uniform displacement loading, variation of the buckling load is almost identical for smaller holes, up to about c/b=0.35, beyond which the author's buckling loads give a more conservative prediction. One of the reasons for this difference is the type of elements used to evaluate the pre-buckling stresses. The constant strain triangular finite elements used in ref. 10 is reported [11] to exhibit a relatively poor representation of the in-plane stresses than the eight noded isoparametric elements used by the author. The subsequent spline representation of these stresses, which has been used in the current analysis, ensures continuity of stress functions up to second derivative. Furthermore, the buckled shape chosen by the author allows for changes along the loaded direction compared to a single term solution used in ref. 10. During the buckling analysis it was observed that by including a second harmonic along the x-direction, i.e. a second x term in the deflection function (equation 4.1), the eigenvalue reduced considerably for larger hole sizes. In addition to the theoretical comparisons, figure 6.2 also shows the experimental results of ref. 10. Though there is a scatter in the experimental results for

the plates with the same hole size, the general trend of increasing buckling load with the hole size can be clearly seen from this figure.

The variation of the buckling load with the hole size for a uniform displacement loading presented by Azizian [11], Kawai and Ohtsubo [12] and Ritchie [10] are plotted along with the author's results in figure 6.3. The results presented by Azizian give a lower prediction of the buckling loads for all hole sizes as compared to the author and the other two investigators. The main reason for this difference is the methods used to constrain the loaded edges to remain straight during the application of the load. In the finite element evaluation of pre-buckling stresses by the author, uniform compression of the loaded edges is ensured by applying uniform displacement at the nodes and restraining in-plane distortion of these nodes. Azizian [11] constrained the loaded edges to remain straight in the plane of the plate by introducing very stiff, two degrees of freedom, shear elements connecting adjacent nodes. This method of restraining the loaded edges cannot possibly secure the edges to remain absolutely straight and nodes towards the middle of the edge are likely to distort as the load is increased. This is confirmed by the fact that the curve representing the buckling load presented by Azizian [11]

lie between the buckling curves of the two loading cases. the uniform displacement and uniform stress loading, presented by the author (fig. 6.1).

6.1.2 Buckling Results for Plates with Square Cutouts

The variation of the author's theoretical buckling loads with the cutout size has been compared with the experimental results of Baig [29] in figure 6.4. The comparison is similar to the plates with a circular hole. The author's theoretical results has also been compared with theoretical results presented by Azizian [11] in figure 6.5. It is observed that the buckling results of Azizian [11] are lower than the author's results as was the case for the circular holes.

The pre-buckling stress distribution for a plate with a square cutout evaluated for the uniform displacement loading is similar to that of a plate with a circular hole except near the edge of the cutout, where local stresses are higher for the circular case. Consequently, the buckling loads of the plates with a square cutout exhibit an identical behaviour to plates with a circular hole of the same nominal size. This is particularly true for smaller size cutouts. For larger cutouts, however,

the buckling loads for plates with a square cutout were found to be higher than plates with a circular hole of the same dimension (c/b) as shown in figure 6.6. The reason for this difference is attributed to the cutout geometry and its effects on the pre-buckling stress distributions in the plate.

6.1.3 Overview of the Buckling Behaviour of Perforated Plates

For a perforated plate the non-dimensional buckling coefficient K, defined by equation 6.1, depends on the loading and boundary conditions at the plate edges and also on the ratio of the size of the cutout to the side of the plate. The study of the figures 6.1 to 6.6 clearly show that for square perforated plates subjected to uniform edge compression the value of K decreases only by a small percentage for smaller cutout size($c/b < 0.35$) and then increases for larger cutout sizes. Similar trend has also been observed in the experimental investigations. Because of the practical limitations and the initial imperfections the estimation of the experimental buckling loads may not be very accurate. This is demonstrated by the scatter in the experimental buckling loads presented in reference 10 for different plates of the

same dimensions and hole size. However, the trend of increasing buckling loads with the hole size can be clearly observed for both circular and square holes for current theoretical and experimental results and those presented by other investigators.

6.2 Post-Buckling Results

The behaviour of a plate with regards to displacements and stresses, their relationship with each other and with the applied loading are obviously the important parameters to be investigated in any post-buckling analysis. The slope at any point in the load ~ edge compression curve is a measure of the plate's axial stiffness. The purpose of investigating the load ~ out-of-plane deflection behaviour and the comparison between the theoretical and experimental results is to establish the accuracy to which these deflections are predicted. The internal stress variations are examined to find out how the stress distributions vary with increase in the applied load and also to predict the ultimate load carrying capacity of a plate.

The theoretical post-buckling analysis described in chapter four, section 4.5, has been used to investigate

the behaviour of simply supported square plates with cutouts when subjected to loads beyond its critical point. The eigenvectors found in buckling analysis are used to define the buckled shape at the start of the analysis. The post-buckling solution has been found for the following cases :-

(a) The buckled shape does not change from the initial buckling mode, but only its magnitude changes. This case will be referred to as a "single term solution".

(b) The buckled shape changes along the 'Y' axis, but remains fixed along the 'X' axis.

(c) The buckled shape changes along the 'X' axis,but remains fixed along the 'Y' axis.

(d) The buckled shape is allowed to change in both the directions. This case will be referred to as a "multiterm solution".

Though the solutions have been found for all the cases mentioned above, the results are presented for case (a) and (d), i.e. for single and multiterm solutions only.

The theoretical and experimental post-buckling results and their comparison with the results of other researchers are described under the following three sub-headings :-

. Out-of-plane deflection behaviour.

. In-plane displacement behaviour.

. Internal stress distribution.

6.2.1 Load ~ Out-of-Plane Deflections

A proper study of the post-buckling behaviour of a plate depends on the ability of the theoretical analysis to accurately predict the out-of-plane deflections. The values of the coefficients A_{ij} in the deflection function used in the current analysis (equation 4.1) shall determine the magnitude and shape of the deflection. The evaluation of the out-of-plane deflections involves computation of deflection coefficients for each increment of the applied edge displacements which can then be substituted in equation 4.1 to find deflection at any point in the plate for that displacement.

Experimentally the deflections are easily measurable by dial gauges or deflection transducers and can be conveniently plotted on the plotter directly linked to the measuring system.

The load ~ deflection plots for square plates with circular and square cutouts are shown in figures 6.7 to 6.14. The non-dimensionalised load P/P_{cu} is plotted against w/t, where w is the out-of-plane deflection at points shown in the diagrams and t is the plate thickness. The applied load P is computed by integrating stresses at the loaded edge corresponding to a prescribed edge displacement. P_{cu} is the critical load of an unperforated plate. The theoretical analysis assumes the plate to be perfectly flat, and the deflections remain zero until the applied load equals the buckling load. Because of the initial imperfections the experimental deflections are recorded from the onset of loading and can be observed from the load ~ deflection curves. In the experimental setup all the edges are simply supported with unloaded edges free to wave in-plane. The knife edge supports provide an good simulation of the simply support boundary conditions, but the roller assembly attached to the loading head and the base had its limitations which influenced the experimental results.

6.2.1.1 Out-of-Plane Deflections for Plates with a Circular Hole

Figures 6.7 to 6.10 show plots of load ~ deflection for

a range of plates with circular hole sizes of c/b = 0.2, 0.3, 0.4 and 0.5. The experimental deflections below the critical point indicate the effect of local imperfections. At higher loads the theoretical deflections are in good agreement with the experimental ones; particularly at locations away from the edges. In all these graphs the point near the edge of the hole on the centre line, i.e. point No. 1, show a closer agreement between the theoretical and experimental deflections. A small difference between the experimental and the theoretical deflections at these points is attributed to the approximation used in the assumed deflection function given by equation 4.1. Though the deflection function used in the multi-term theoretical analysis consist of two terms along and two terms across the loaded direction, truncation of the remaining terms in the series has contributed towards small errors in the theoretical deflections.

At other points closer to the edges, i.e. points 2 and 3, the comparison is not as good as for the points closer to the centre of the plate. The load ~ deflection behaviour of plate with hole size c/b = 0.5 shows that for two diagonally opposite locations, points 2 and 3 in figure 6.10, the experimental deflections are different. The deflections at these points should ideally be the same as seen from the theoretical curve. The difference

between the measured deflections at these points is because of the inconsistency in the boundary conditions at the two loaded edges. In spite of the smoothness of the needle rollers, the roller assembly cannot possibly generate a frictionless surface. Besides, there is a small offset between the pivot point and edge of the plate (fig. 5.6.10) in the roller assembly.

An interesting feature observed during the deflection measurements is that a change in the wave form was noticed for plate with hole size of c/b=0.4, prior to collapse, as shown in figure 6.9. This phenomenon has been experienced generally for larger hole sizes both for the circular holes [10,29] and the square cutouts [29].

6.2.1.2 Out-of-Plane Deflection of Plates with Square cutouts

Load ~ deflection behaviour of plates with a square cut-out is illustrated in figures 6.11 to 6.14 and is similar to that of the plates with a circular hole. The deflection plots reveal that, like the circular holes, the theoretical curves and experimental data points were in closer agreement at the centre point in the plate, i.e. at point no. 1 for all hole sizes. For diagonally

opposite points near the loaded edges the experimental deflections are not the same. The experimental results of plate with hole size c/b=0.5 show a change in the wave form prior to collapse.

The results tend to agree more closely at higher loads both for circular and square cutouts. This is because the effect of initial deflections present in the plates used for experimental work diminishes as the load and consequently deflections start to increase.

6.2.2 Load ~ Edge Displacements

The relationship between load and edge compression is a measure of the plate stiffness. The slope of load displacement curve is constant prior to the bifurcation point. The plate loses its stiffness after buckling. The loss in stiffness is measured by the ratio of slopes of the load ~ displacement curves after and prior to buckling. If the buckled shape is assumed to remain unchanged from its initial buckling mode, this ratio is constant and is 0.408 for a simply supported unperforated plate with sides free to wave in-plane. If the buckled shape is allowed to change, the load ~ displacement curve is non-linear and the plate continues to lose its stiffness

with increase in the applied load.

Figures 6.15 and 6.16 illustrate the load displacement behaviour of plates with a circular and square cutout respectively. In both these graphs the curve of an unperforated plate is drawn as for reference. All the results shown are for a multiterm solution. The critical load and displacement of an unperforated plate, 'P_{cu}' and 'U_{cu}', are used to non-dimesionalise applied displacement and the corresponding end load. Since at Pcu the displacement of the perforated plates vary with the hole size, the plate stiffness prior to buckling is different for each type of plate; the stiffness reducing with increasing hole size. The nonlinear load displacement curve in the post-buckling region indicate constantly reducing plate stiffness with increase in the applied displacement. The slope of these curves reduce more rapidly with the increase in the hole size for plates with a circular as well as square cutout. The edge compression could not be measured during the experimental work and, therefore, the accuracy of the theoretical analysis vis-a-vis experimental results can only be judged from the deflection behaviour and internal stress variation.

6.2.3 Internal Stress Distribution

The variation of the internal stress distribution in thin plates in the post-buckling region has not been investigated extensively or has not been published with the exception of few. Ritchie [10] presented the theoretical and experimental post-buckling stress distribution in plates with circular hole which, to the author's knowledge, is the only comprehensive published information available on the variation of stresses in a perforated plate. His results cover square and rectangular plates with a centrally located circular hole. His theoretical post-buckling analysis is limited to a fixed buckled shape. The current research extends the analysis to cater for changes in the post-buckled shape. The stress variation in plates with a circular as well as square cutout has been investigated for the different cutout sizes and at different sections as stated below:

(a) For plates with a circular hole the stresses are plotted at the minimum section and at the loaded edge for hole sizes of c/b = 0.2, 0.3, 0.4 and 0.5.

(b) For plates with a square cutout the stresses are plotted at the minimum section, near the hole

edge and near the loaded edge for hole sizes c/b = 0.2, 0.3, 0.4 and 0.5.

The non-dimensionalised stress $P_{cu}\ \sigma_x bt/P_{cu}$ plotted against y/b. σ_x is the stress in the x-direction at any load, P_{cu} is the critical load of an unperforated plate and b and t are the plate dimensions. The stresses are plotted for different levels of applied displacements U. The experimental stresses are presented in reference 10 and 29 for different values of the applied loads P and, therefore, theoretical curves are also plotted for the same values of P for a direct comparison.

The non-uniform pre-buckling stresses in a perforated plate are redistributed as the applied load is increased beyond its critical point. The theoretical stress distribution is obtained by superimposing the three stress systems described in chapter four. At a desired load level the stresses in system 1, which are independent of out-of-plane deflections, are evaluated by multiplying the B-spline functions by appropriate load factor. At each point in the plate these stresses vary linearly with changed applied loads. The stresses in systems 2 and 3 depend on the deflection parameters which are obtained after minimisation of the total strain energy. The stresses in these systems are, therefore, evaluated after

determining these deflection parameters at any load level. The three stress systems are then superimposed to get the final stresses. The process is repeated at each load obtained by a small increment to the previous load.

6.2.3.1 Stress Variation for Plates with Circular Hole

The author's theoretical stress distribution has been compared with the experimental results of ref. 10 and ref. 29. The stress variation for a plate with size c/b=0.2 is presented from figures 6.21 to 6.24 at the minimum section and from figures 6.25 to 6.28 at the loaded edge. These figures show stresses at different loads both for single and multiterm solutions. At the minimum section the concentration of stresses are at the hole edge for loads prior to or just after buckling. In this situation, since there is no or very little deflection, the effect of change in the buckled shape is insignificant. Therefore, very little difference is observed between the two solutions. At higher loads the effect of change in the buckled shape is noticeable from the difference between single and multiterm solutions in figures 6.23, 6.24, 6.27, 6.28, 6.31 and 6.32.

Consider figure 6.32 which compares the author's theoretical stress distribution with the experimental results of reference 10 for the plate with a circular hole of size c/b=0.2. The applied load in this case is 2.03 times the critical load of an unperforated plate. The curve pattern shows a reduction in stress level from a higher value at the edge of the hole to a minimum at y/b=0.27 and then a sharp rise towards the plate edge. The comparison between the two types of solutions, single and multiterm, show that the stresses are relatively higher towards the edges for a multiterm solution. Since the stress distributions in a plate are correlated to the deflected shape, the difference in the stress variations for the two types of solution is obvious. The comparison of theoretical stresses at the minimum section with the experimental results of ref. 10 in figures 6.29 to 6.32 show good agreement between the experimental and theoretical results at all load levels; thus verifying the validity of the current theoretical analysis.

The distribution of stresses at the loaded edge for the plate with hole size c/b=0.2 is illustrated from figures 6.25 to 6.28. The stress variation along the edge at loads prior to buckling is non uniform. As the load is increased the stresses start to grow towards the edges and become relatively smaller in the middle. The pattern

of stresses at applied edge displacement few times the critical displacement is observed to be similar to a plate without hole.

The theoretical stress variation for a plate with hole size c/b=0.3 is shown from figures 6.33 to 6.36 at the minimum section and from 6.37 to 6.40 at the loaded edge. The comparison of internal stress distribution with the experimental results of ref. 10 is shown in figures 6.41 - 6.43. The experimental results in these cases are lower than the theoretical predictions but the general pattern of stress distribution is identical to the other hole sizes.

In the absence of any experimental results for plates of hole size c/b=0.4 only theoretical results are presented. These have been shown from figures 6.44 to 6.47 at the minimum section and from figures 6.48 to 6.52 at the loaded edge. The redistribution of stresses after buckling and their general pattern is similar to other plates.

The results for a plate with circular hole size c/b=0.5 are presented from figures 6.53 to 6.81 at two sections, the minimum section and the loaded edge. Some of these figures also show comparisons between the present

theoretical results and the experimental results of reference 10 and 29. Consider figures 6.53 to 6.58 where the theoretical stresses are presented at the minimum section. It is obvious from these figures that the changes in the buckled shape had considerable effects on stress distribution at higher loads as was observed for other size holes, but the effect is more significant for the plate under discussion, i.e. for c/b = 0.5. From this observation we can infer that allowing for changes in the buckled shape improved the post-buckling results more significantly for larger holes. Another important point which these curves reveal is that the multiterm solution gave a more conservative prediction of the peak stresses than the single term solution. Since the difference between the two types of solution has been caused by the out-of-plane deflections, the functional representation of deflections is important in any post-buckling analysis.

The stresses at the minimum section have also been compared with the experimental results of reference 29 shown from figures 6.65 to 6.70 and those of reference 10 shown from figures 6.78 to 6.81. The pre-buckling stresses lie below the theoretical curves (figures 6.65 and 6.66) except for a point near the unloaded edge. This is primarily due to the effects of local imperfections.

The experimental post-buckling stresses lie below theoretical curves at all loads, but the difference reduces with the increased applied load. In addition to the effects of local imperfections which have more influence on deflections and stresses at lower loads, the main reasons for the discrepancy between theoretical and experimental stress distribution are attributed to the truncated terms of the deflection function used in the theoretical analysis and practical limitations in achieving ideal boundary conditions during experimental investigations. Both theoretical and experimental results show a similar trend of redistribution of stresses with change in the applied load.

The author's theoretical stresses at the loaded edge have also been compared with the experimental results of reference 29 shown from figures 6.71 to 6.77. The pre-buckling stresses are almost zero at the middle of the loaded edge. The experimental pre-buckling stress values are lower than the theoretical stresses except a point near the plate corner. This is caused by the inability of the roller assembly to achieve simply support boundary conditions at the loaded edge. This effect has been noticed at all loads and it was observed that the yielding of plate material had first occurred at the top two corners of the plate. In spite of this discrepancy

the comparison between the theoretical and experimental results at the loaded edge show a similar trend of stress distributions.

6.2.3.2 Stress Variations for Plates-with Square Cutout

The internal stress variation for plates with a square cutout are presented from figures 6.82 to 6.113 for the cutout sizes of c/b= 0.2,0.3,0.4 and 0.5. The stresses are presented in these figures at the minimum section and at sections AA and section BB as shown in each of these figures. The comparisons of the stress variation between the plates with a circular and a square cutout of the same size reveal that the stress distribution follow a similar trend for both the shapes of cutouts. It is, therefore, not intended to discuss each type of plate with a square cutout. From the examinations of the stress plots few observations are, however, made about the stress distributions in plates with a square cutout. These are discussed as follows.

The redistribution of stresses at the centre section of the plate (referred as the minimum section in fig. 6.82-87,6.93-99,6.103-108 and 6.111-113) follow the same trend as that of plates with a circular hole except for localised stresses near the hole edge. Therefore the comments

written for the circular case are applicable here.

For plate with a square cutout the stresses are also plotted at section AA. The fluctuation of the theoretical curves at section AA, observed in figures 6.88, 6.89, 6.101, 6.102, and 6.110, is due to the limitation of B-spline surface fitting to obtain a proper fit in the case of an abrupt discontinuity.

Comparisons have been made with the experimental stresses for the plate with cutout size of c/b=0.5 at the minimum section, the intermediate section (AA) and near the loaded edge (BB). Figures 6.114 to 6.117 show the comparison at the minimum section. The stresses do not compare well at the lower loads of P/P_{cu}=1.33 and 1.67. The experimental stresses in these cases are relatively higher than the theoretical stresses towards the unloaded edges, possibly because of the initial deflections and the effects of experimental boundary conditions at the plate edges. The comparison of stresses in figure 6.117, for P/P_{cu}=2.03 is, however, better than the other two cases. The effects of initial imperfections are less dominant in this case and the stress distribution in the plate is due to large deflections caused by the increased loads. Similar trend of behaviour is observed at other sections. The comparison of stresses at the intermediate

section shown in figures 6.118 to 6.121 are reasonably good except at the location near the unloaded edge (i.e. at y/b=0.9). In all these graphs the stresses at this point are consistently higher than the theoretical stresses. This is due to the limitations of the experimental setup to achieve ideal boundary conditions at the plate edges. Figures 6.122 to 6.125 illustrate pattern of behaviour near the loaded edge. The experimental stresses in this case also tend to rise towards the edges with a greater slope than the theoretical stresses for the same reasons as mentioned for the other sections.

6.2.3.3 General Discussion on Internal Stress Variations

The comparison of stress variation between theoretical and experimental results show a close agreement for all plates investigated i.e. plates with all sizes containing circular and square cutouts; at different sections in the plate and at all load levels. The differences observed between the theoretical and experimental stresses, particularly at lower loads are attributed to the limitations of both theoretical analysis and experimental set-up. Experimental membrane stresses are calculated from the measured strains, the accuracy of which depends on the gradient of the strain field over the gauge area and on the magnitude of the strain. For higher strains, the

constant measurement error becomes proportionately small. This is one of the reason of better comparison between the theoretical and experimental results at higher loads. The second reason is the influence of the initial imperfections on the stresses in the plate at loads in the vicinity of or just above the critical loads. At higher loads the effects of initial imperfections on stresses decrease and because of the increase in the magnitude of deflections, the membrane stresses due the stretching of the middle surface start to dominate. One of the primary reasons for the discrepancy is the boundary conditions under which the two types of results are obtained, i.e. the ideal boundary conditions used during theoretical analysis and experimental difficulties to simulate these conditions. Another important factor is that the deflected shape obtained as a result of theoretical analysis is not the same as the actual shape formed during the tests. The deflection function used in the theoretical analysis does not accurately represent the experimental deflected shape. The size of the cutout alters pattern of the stress curve, but the redistribution of stresses in the post-buckling region show a similar trend for all sizes and shapes of cutouts, both for the theoretical and experimental investigations, which confirms applicability of the theoretical analysis to formulate stresses for plates with cutouts.

TABLE 6-1

PRESENTATION OF RESULTS

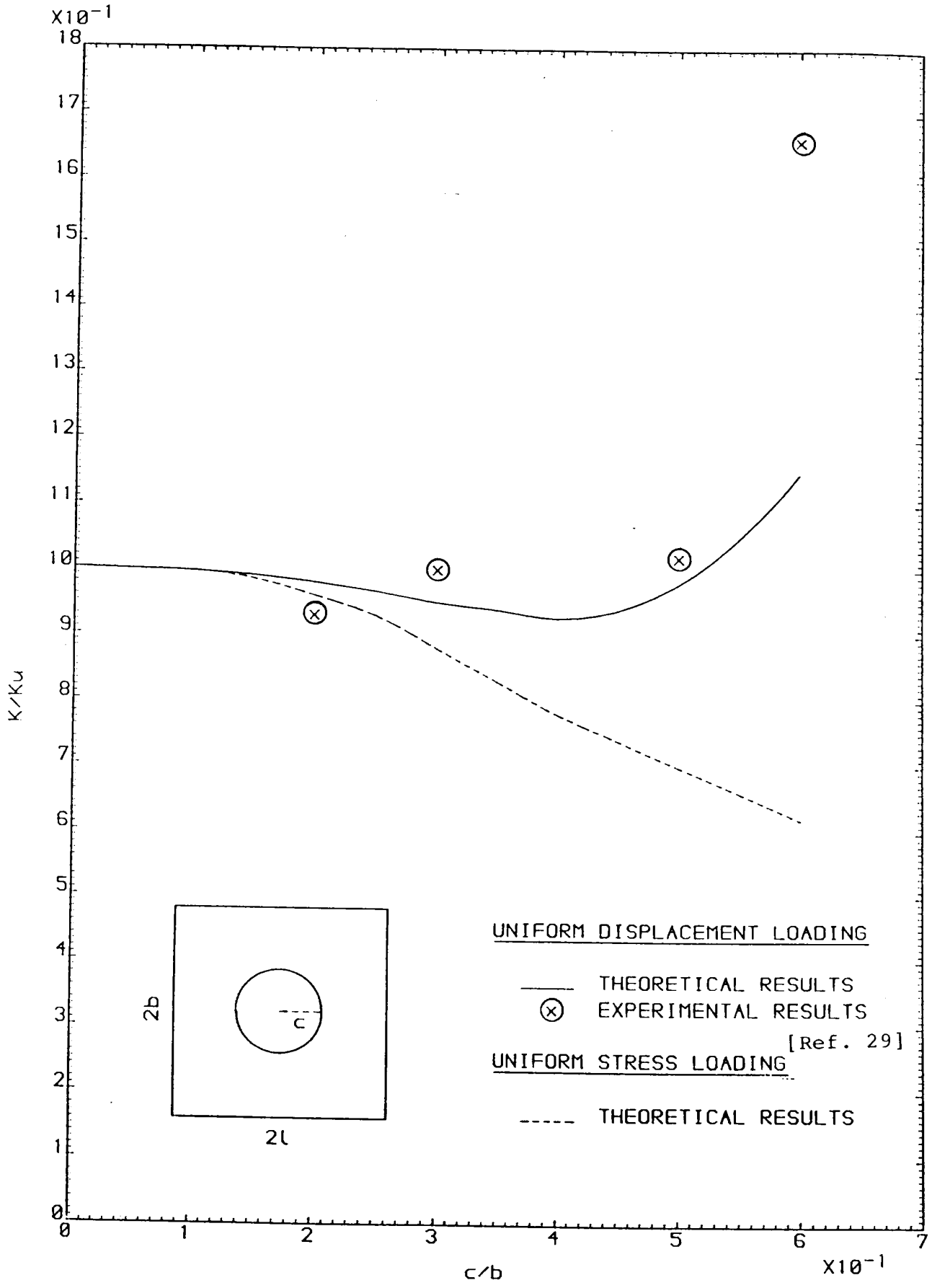

FIGURE 6·1 VARIATION OF BUCKLING COEFFICIENT WITH THE HOLE SIZE

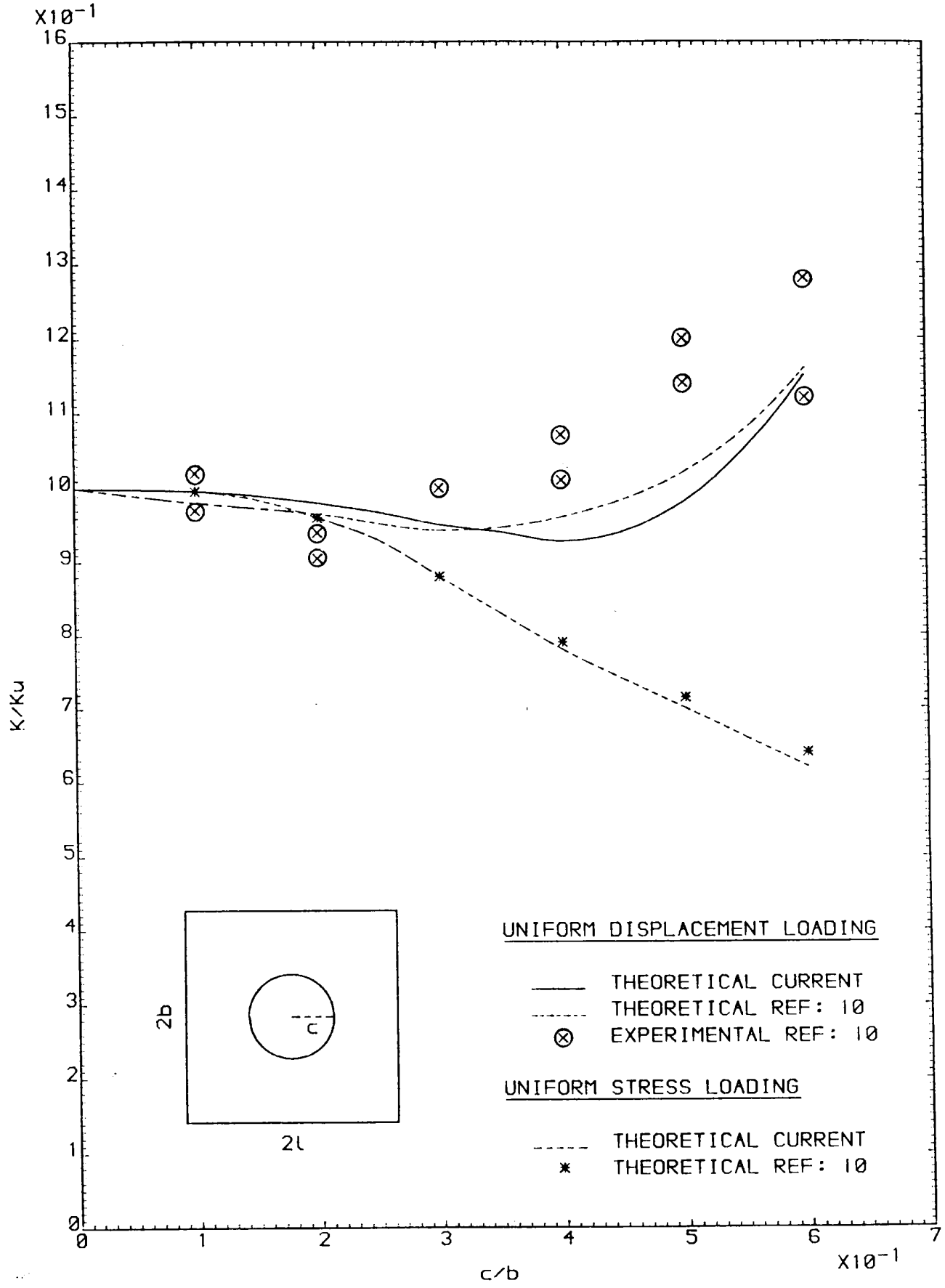

FIGURE 6.2 COMPARISON OF BUCKLING RESULTS WITH REFERENCE 10

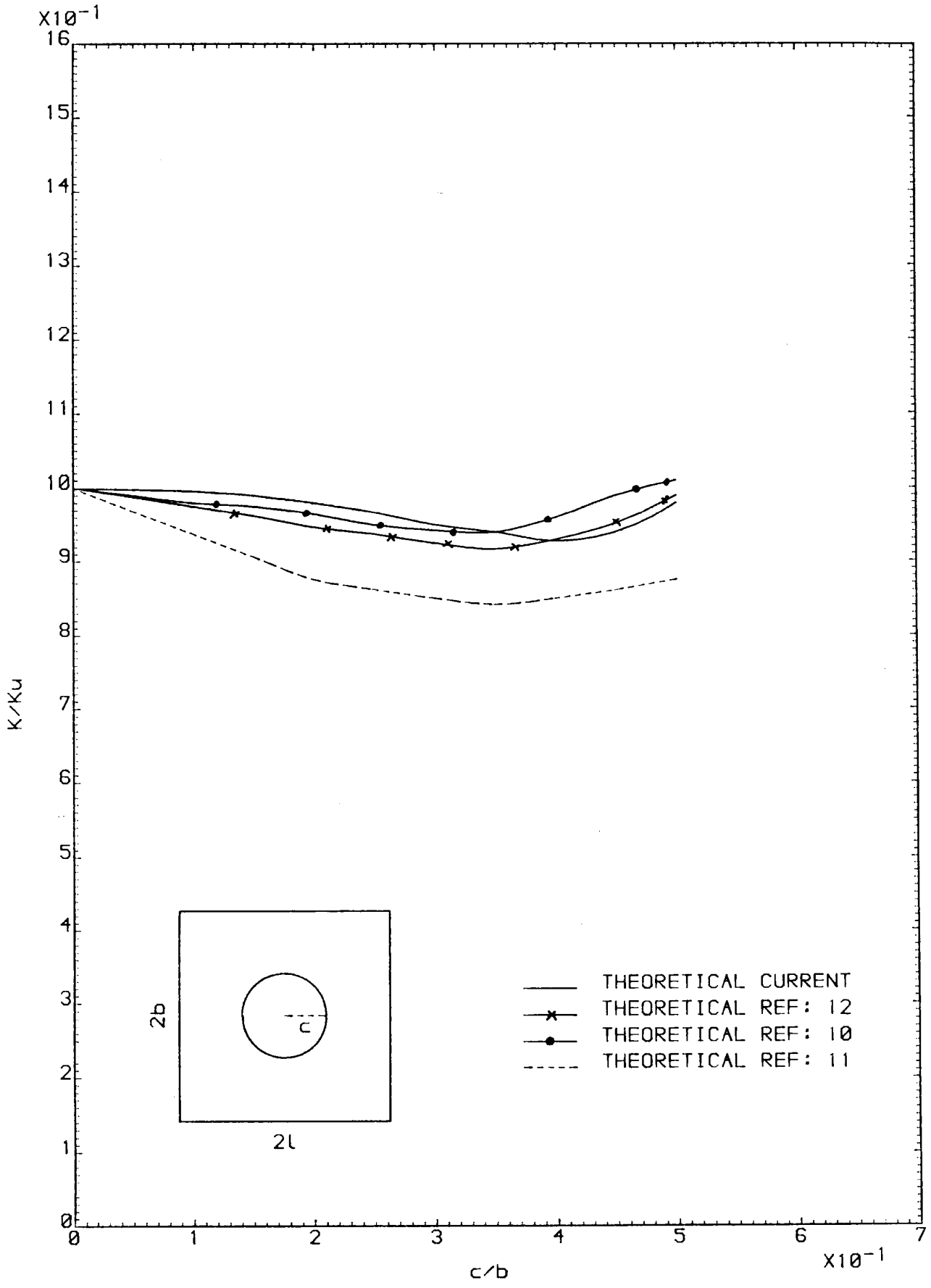

FIGURE 6.3 COMPARISON OF BUCKLING RESULTS WITH OTHER INVESTIGATORS

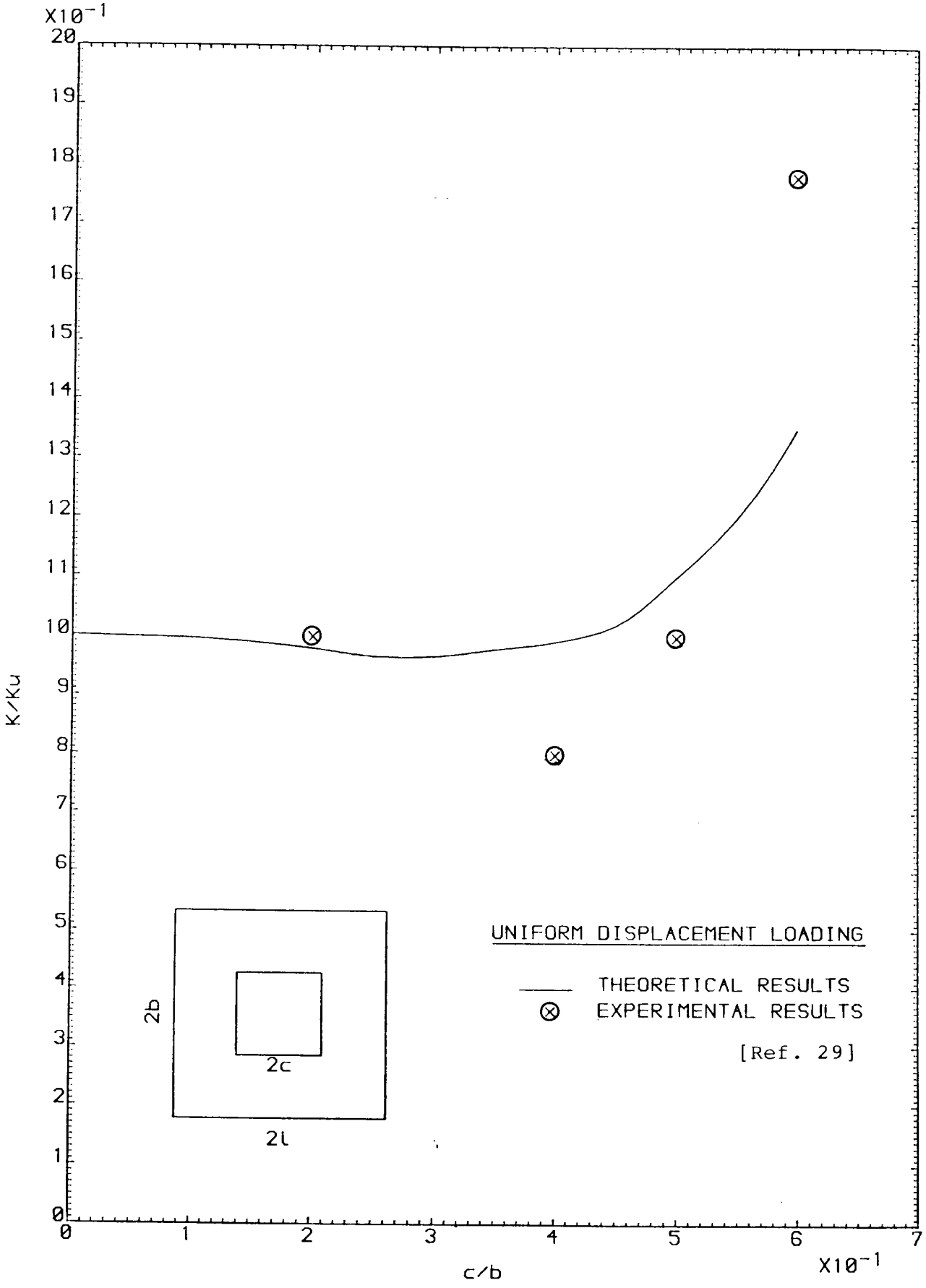

FIGURE 6·4 VARIATION OF BUCKLING COEFFICIENT WITH THE HOLE SIZE

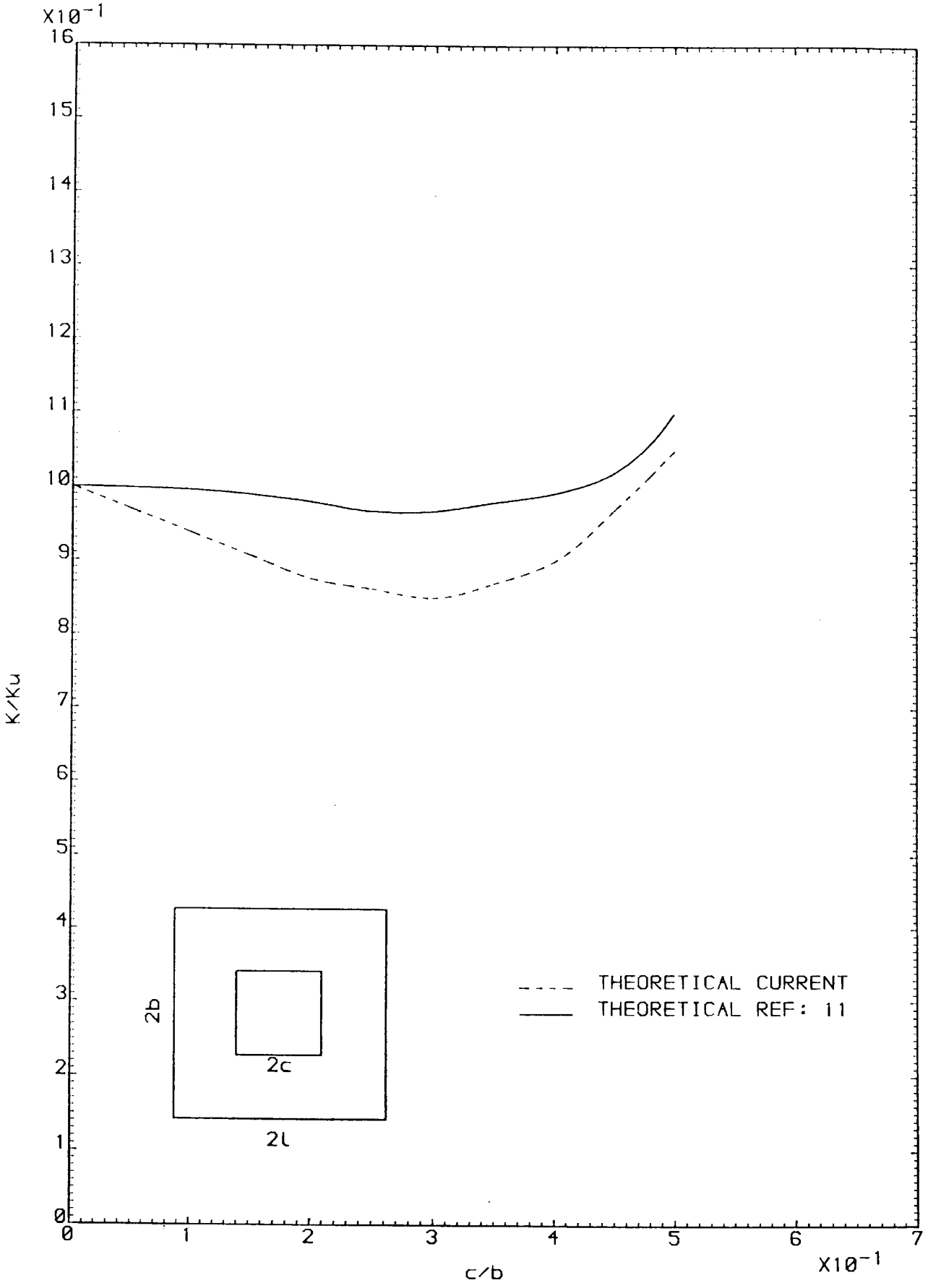

FIGURE 6·5 COMPARISON OF BUCKLING RESULTS WITH REFERENCE 11

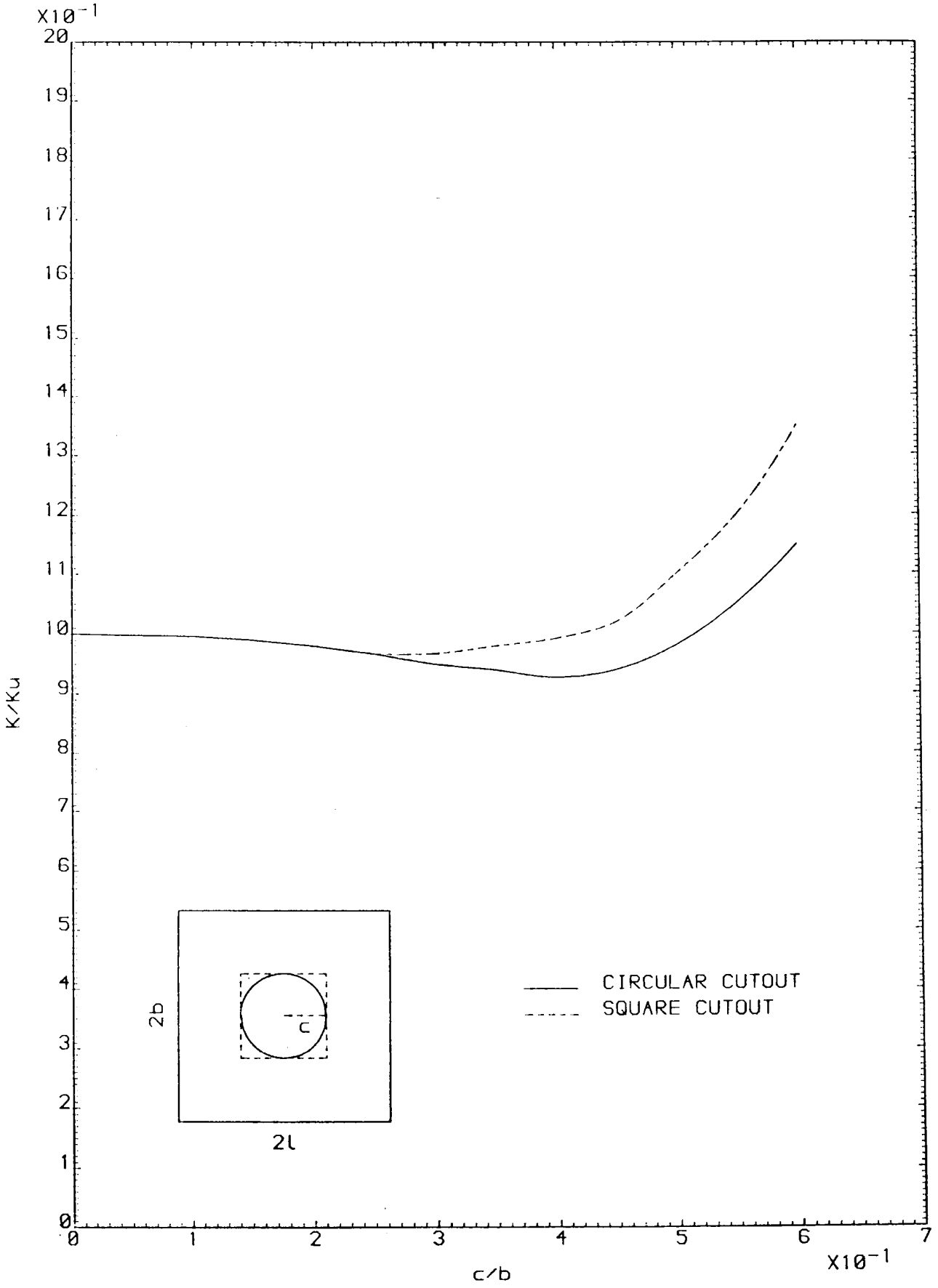

FIGURE 6·6 VARIATION OF BUCKLING COEFFICIENT WITH THE HOLE SIZE/SHAPE

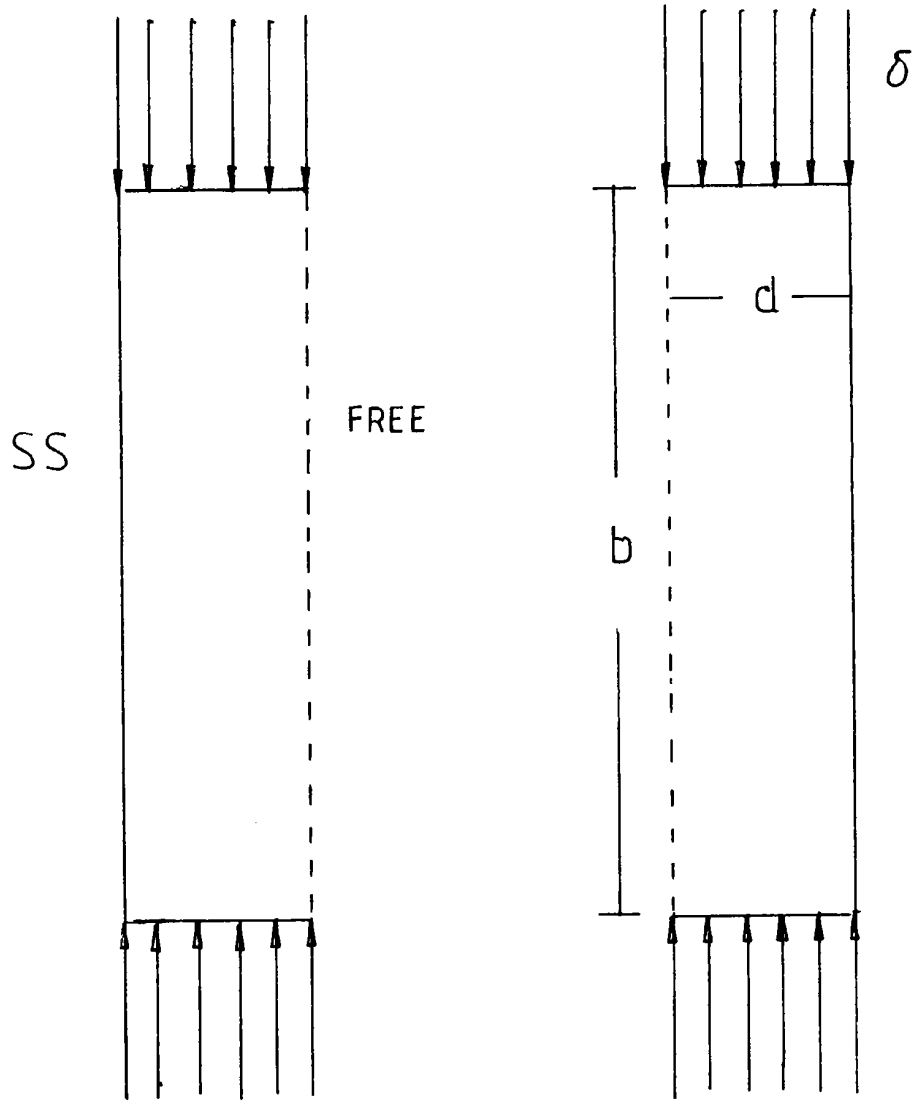

FIGURE 6.6.1 SIMPLIFIED MODEL OF BUCKLING PROBLEM OF A SQUARE PLATE WITH LARGER HOLE

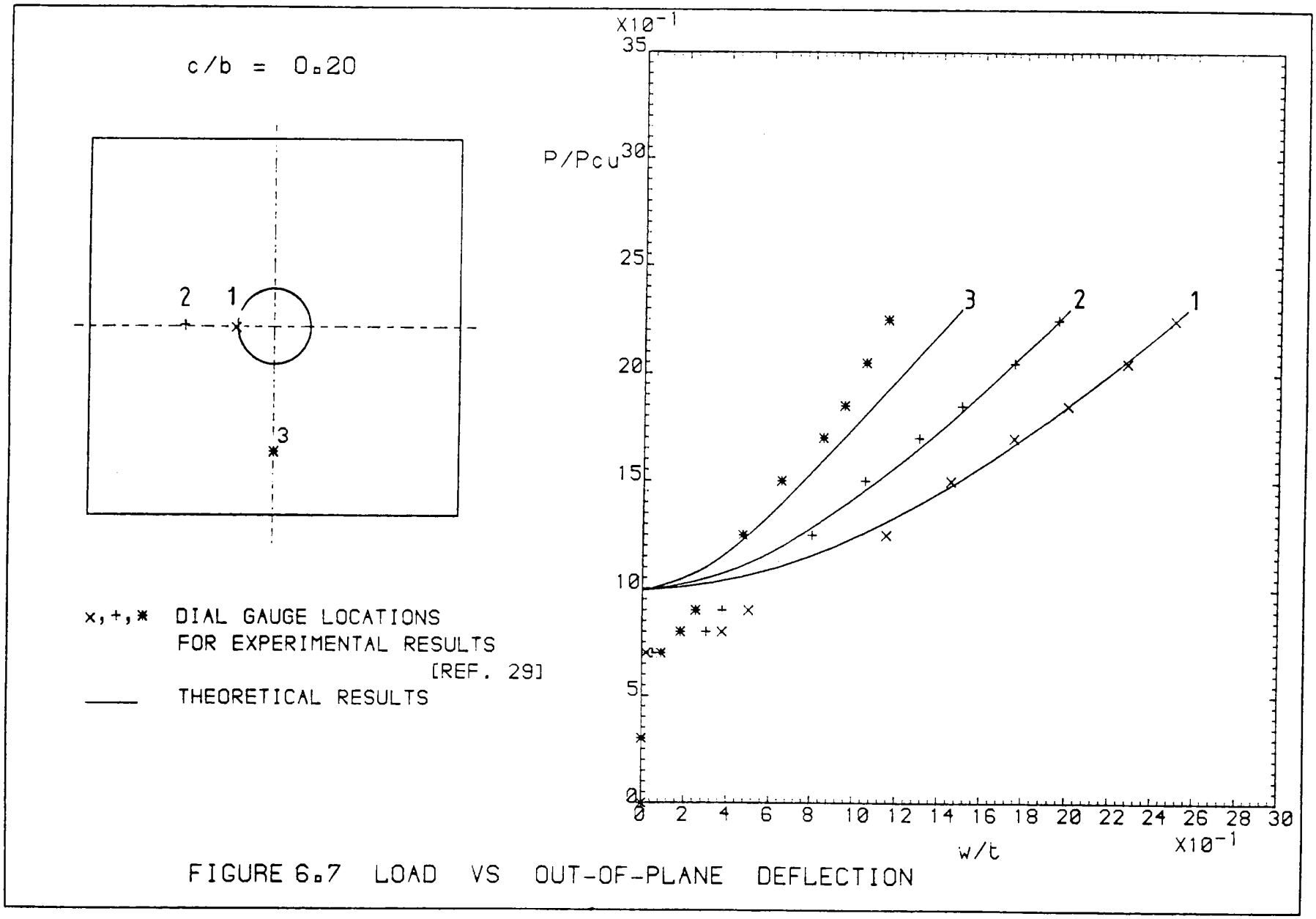

FIGURE 6.7 LOAD VS OUT-OF-PLANE DEFLECTION

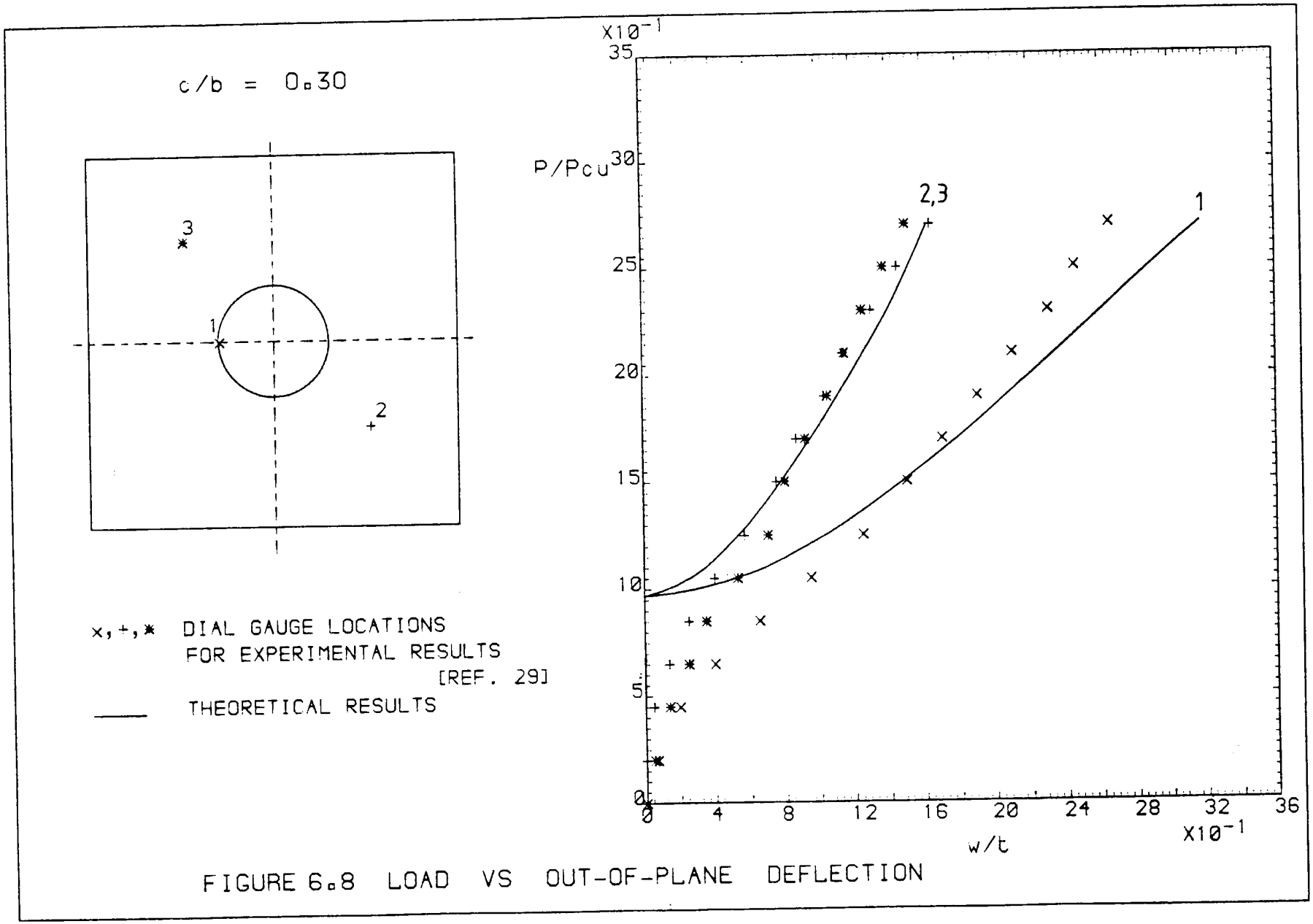

FIGURE 6.8 LOAD VS OUT-OF-PLANE DEFLECTION

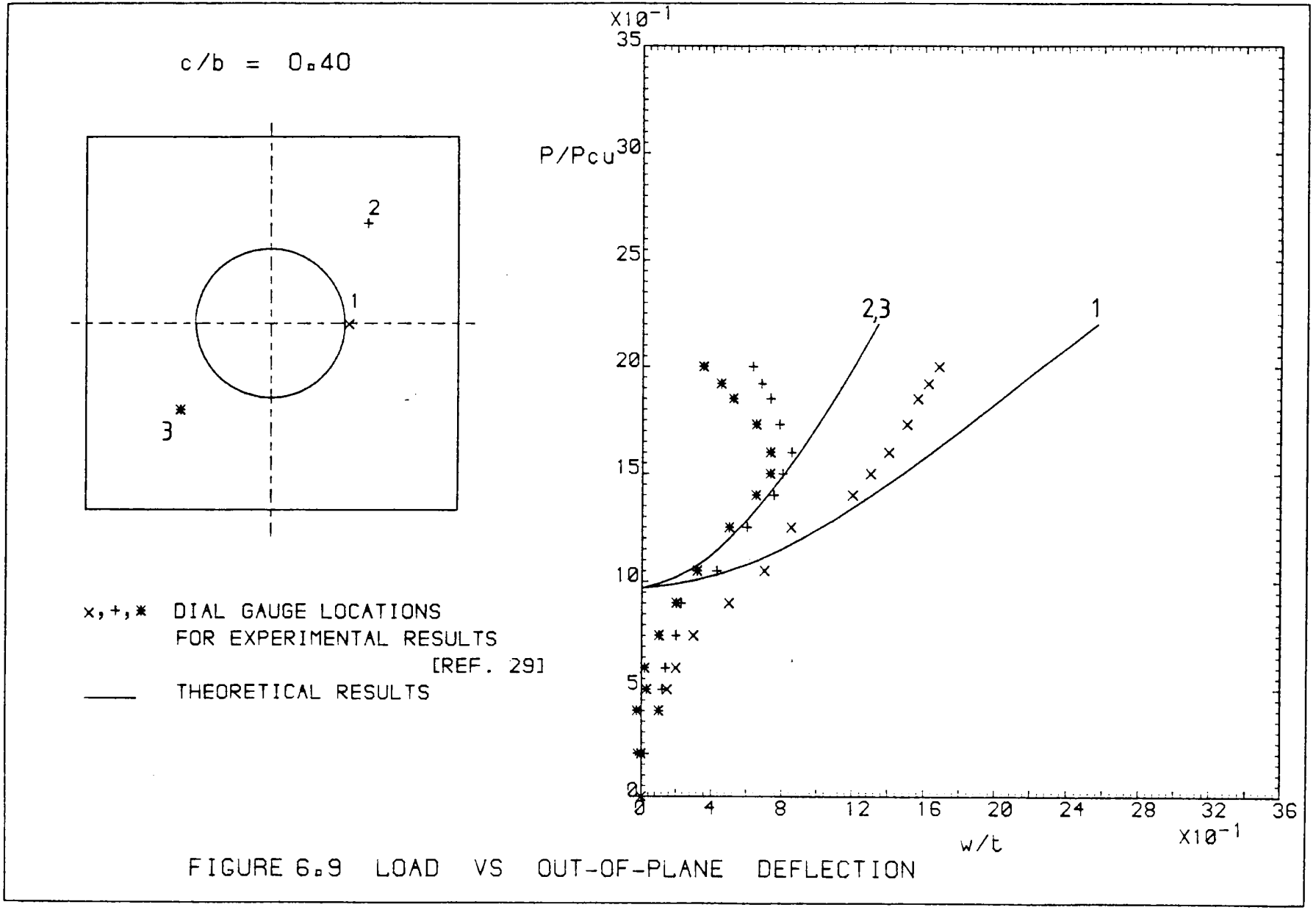

FIGURE 6.9 LOAD VS OUT-OF-PLANE DEFLECTION

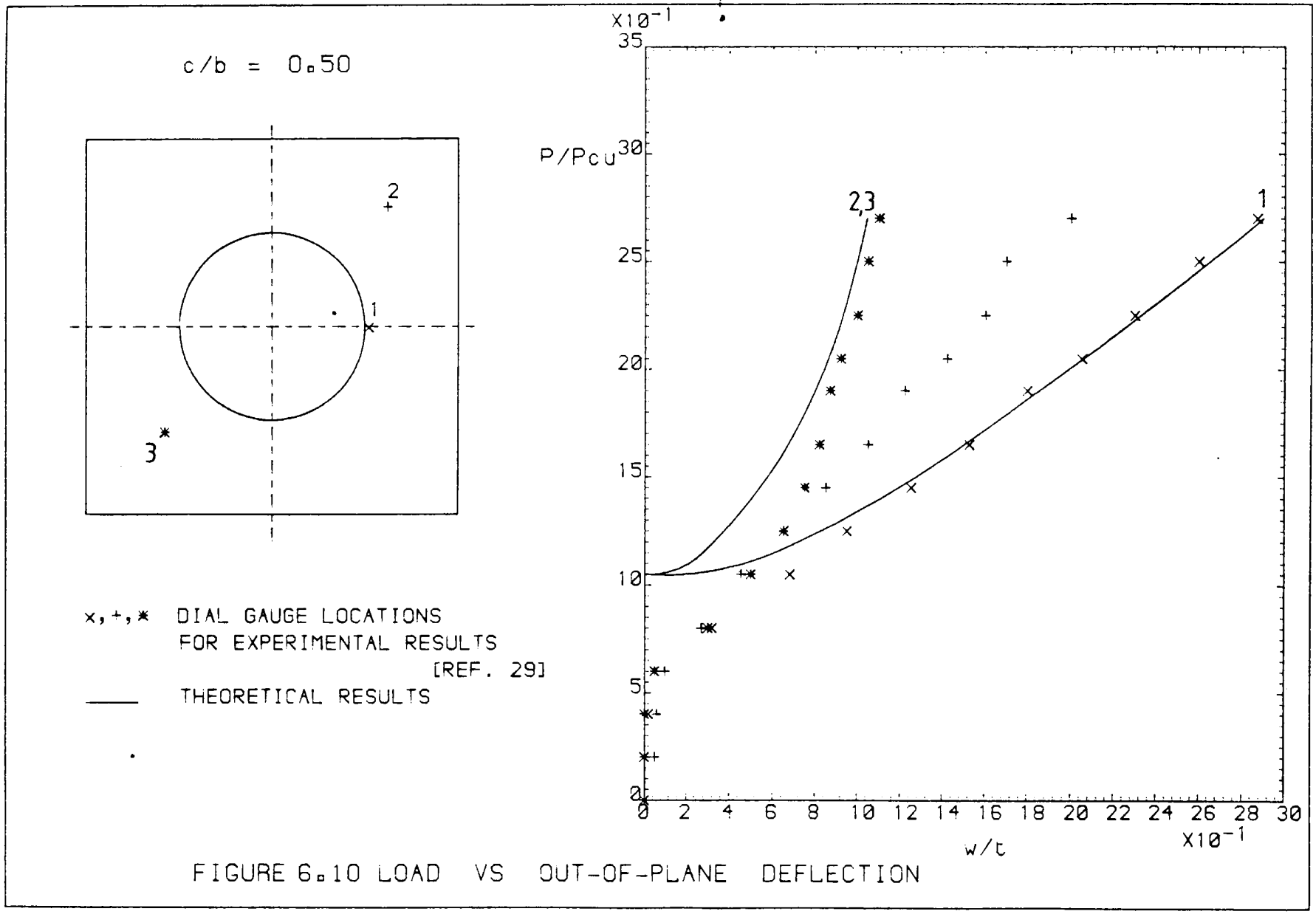

FIGURE 6.10 LOAD VS OUT-OF-PLANE DEFLECTION

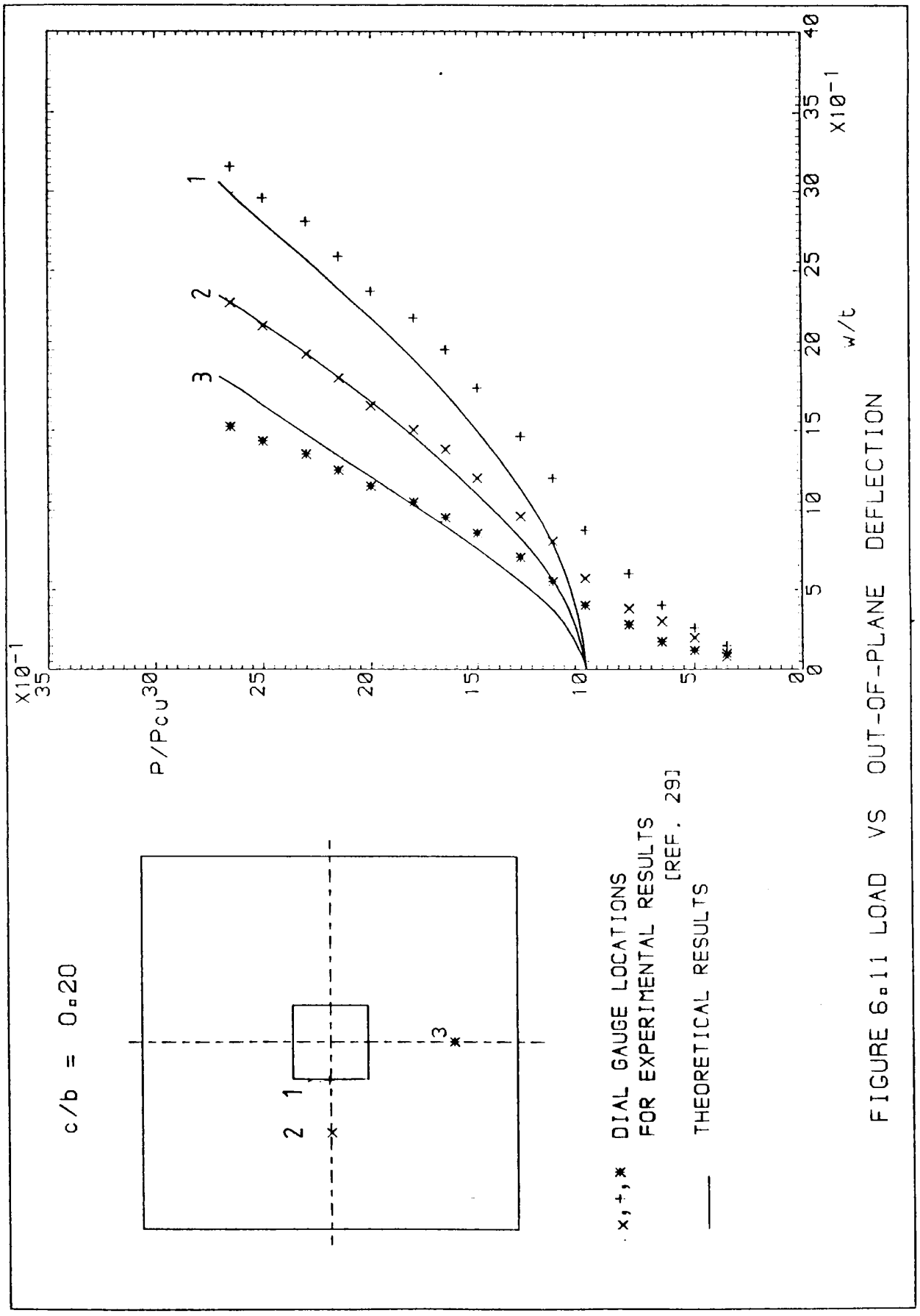

FIGURE 6.11 LOAD VS OUT-OF-PLANE DEFLECTION

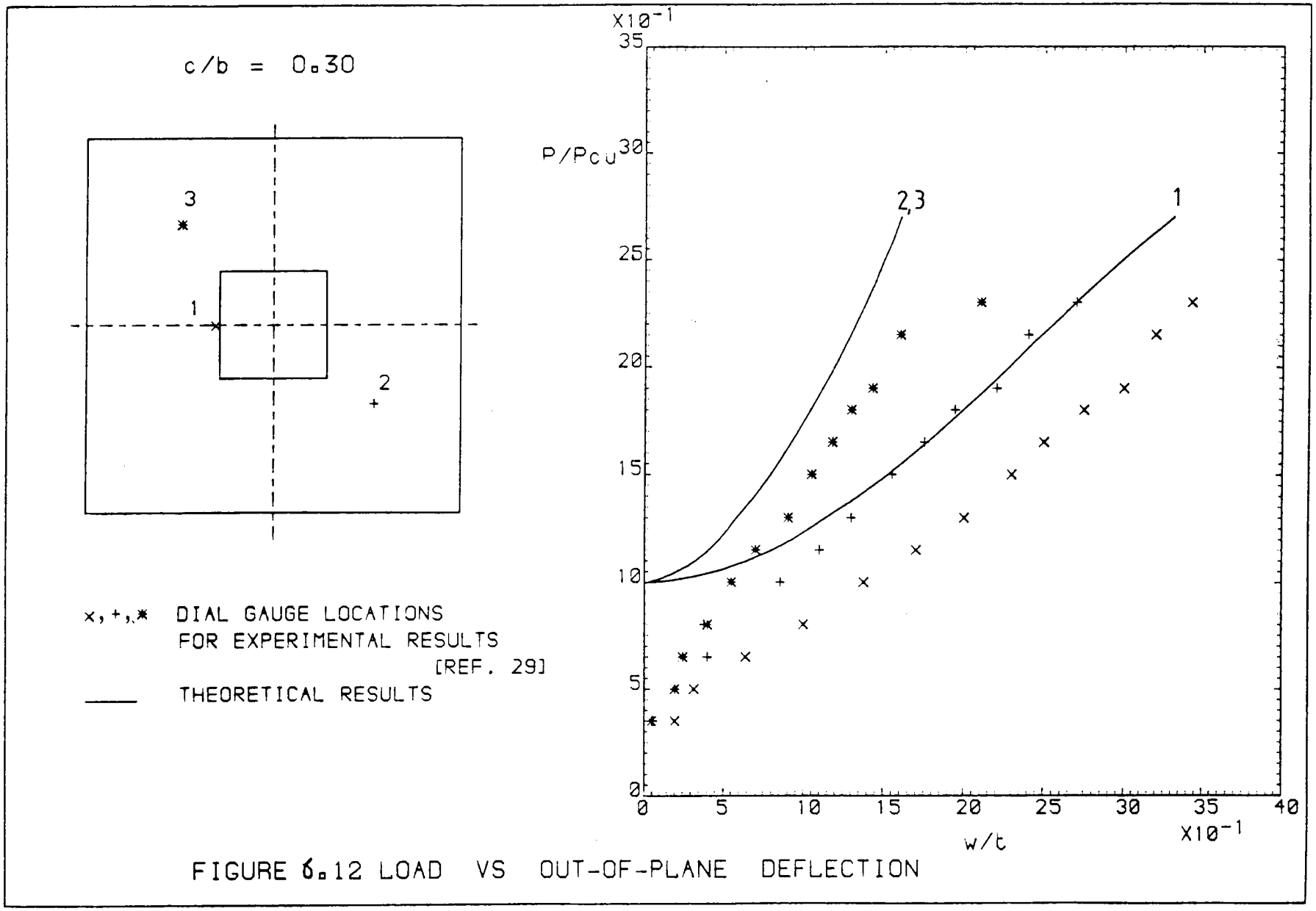

FIGURE 6.12 LOAD VS OUT-OF-PLANE DEFLECTION

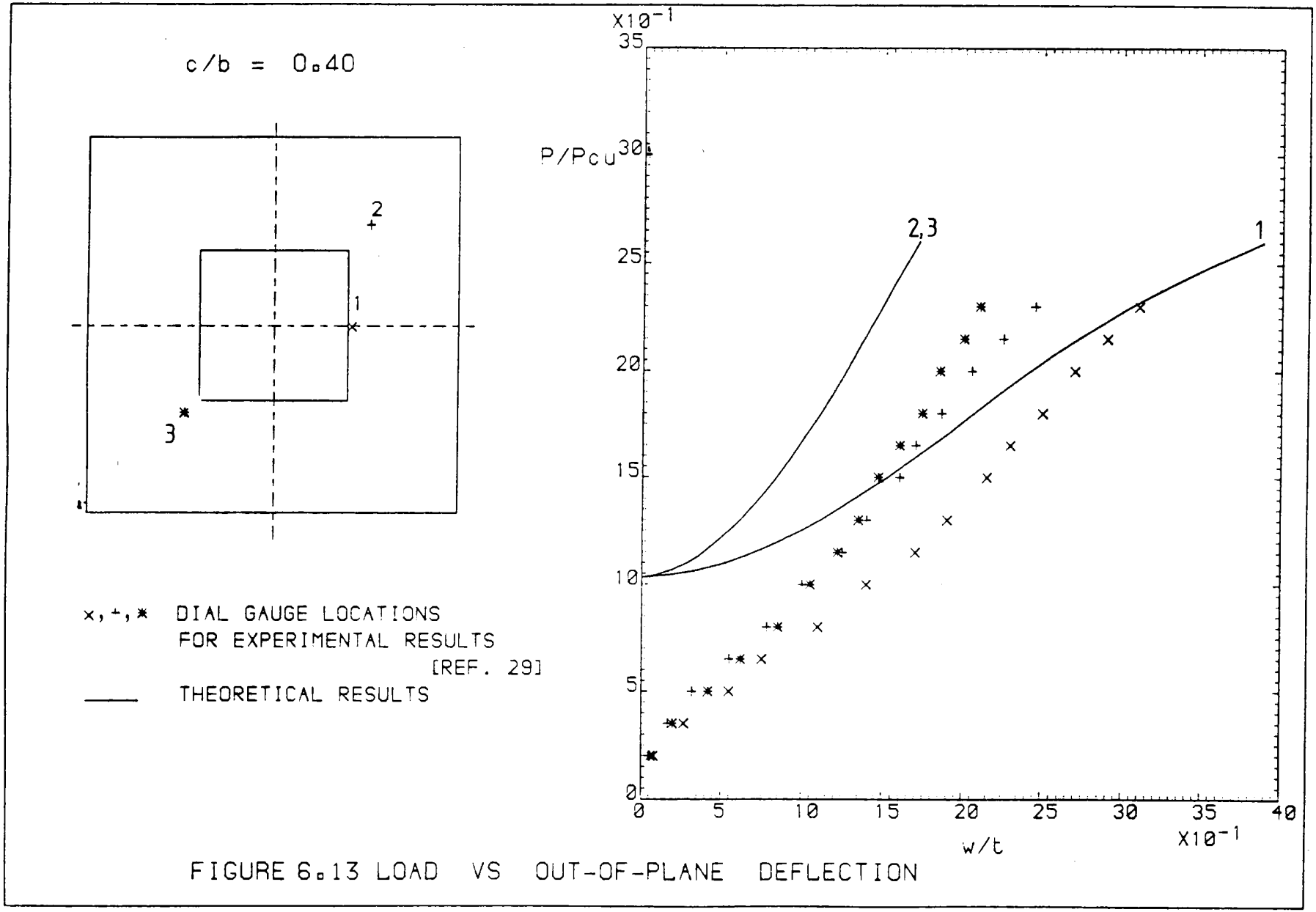

FIGURE 6.13 LOAD VS OUT-OF-PLANE DEFLECTION

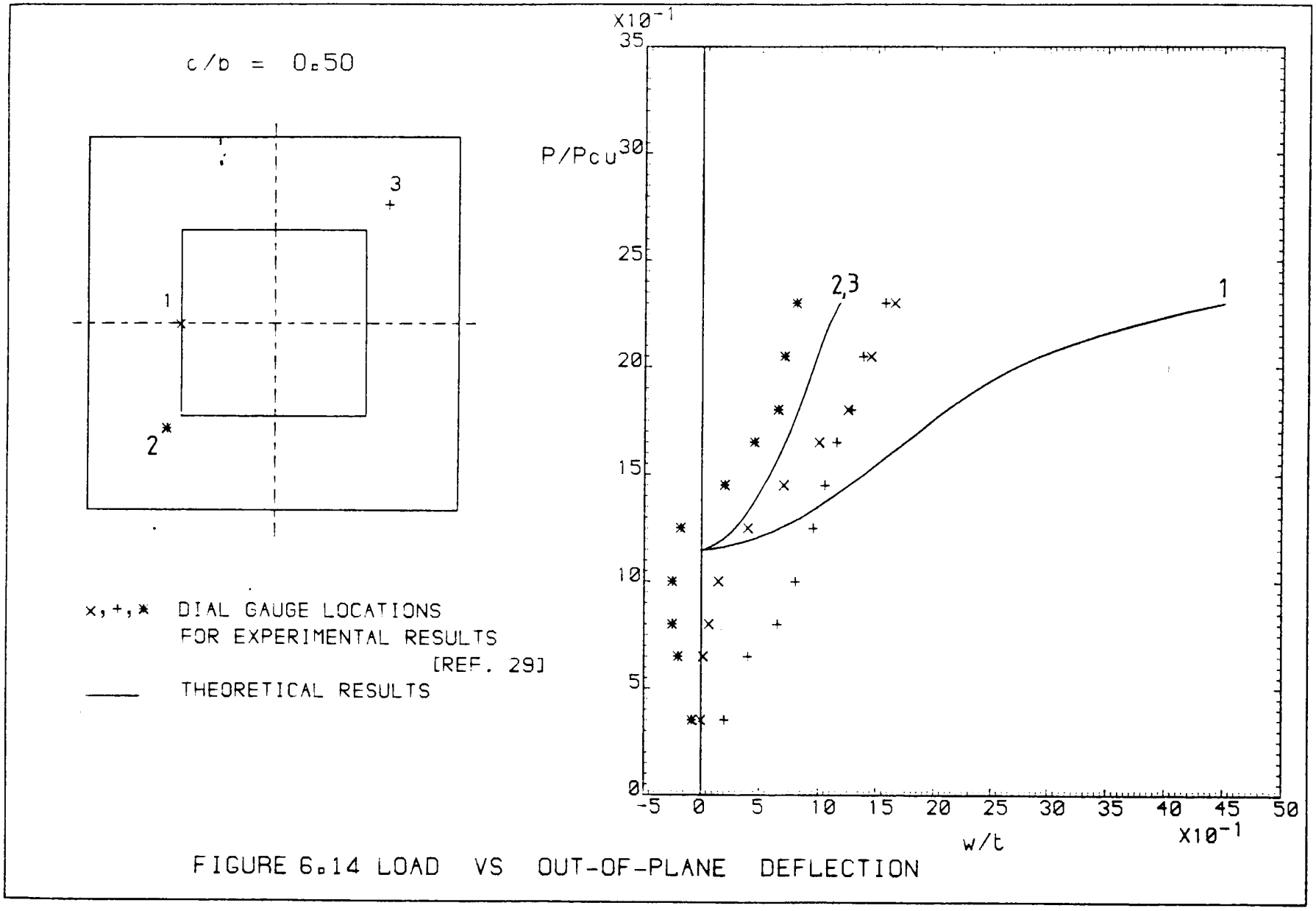

FIGURE 6.14 LOAD VS OUT-OF-PLANE DEFLECTION

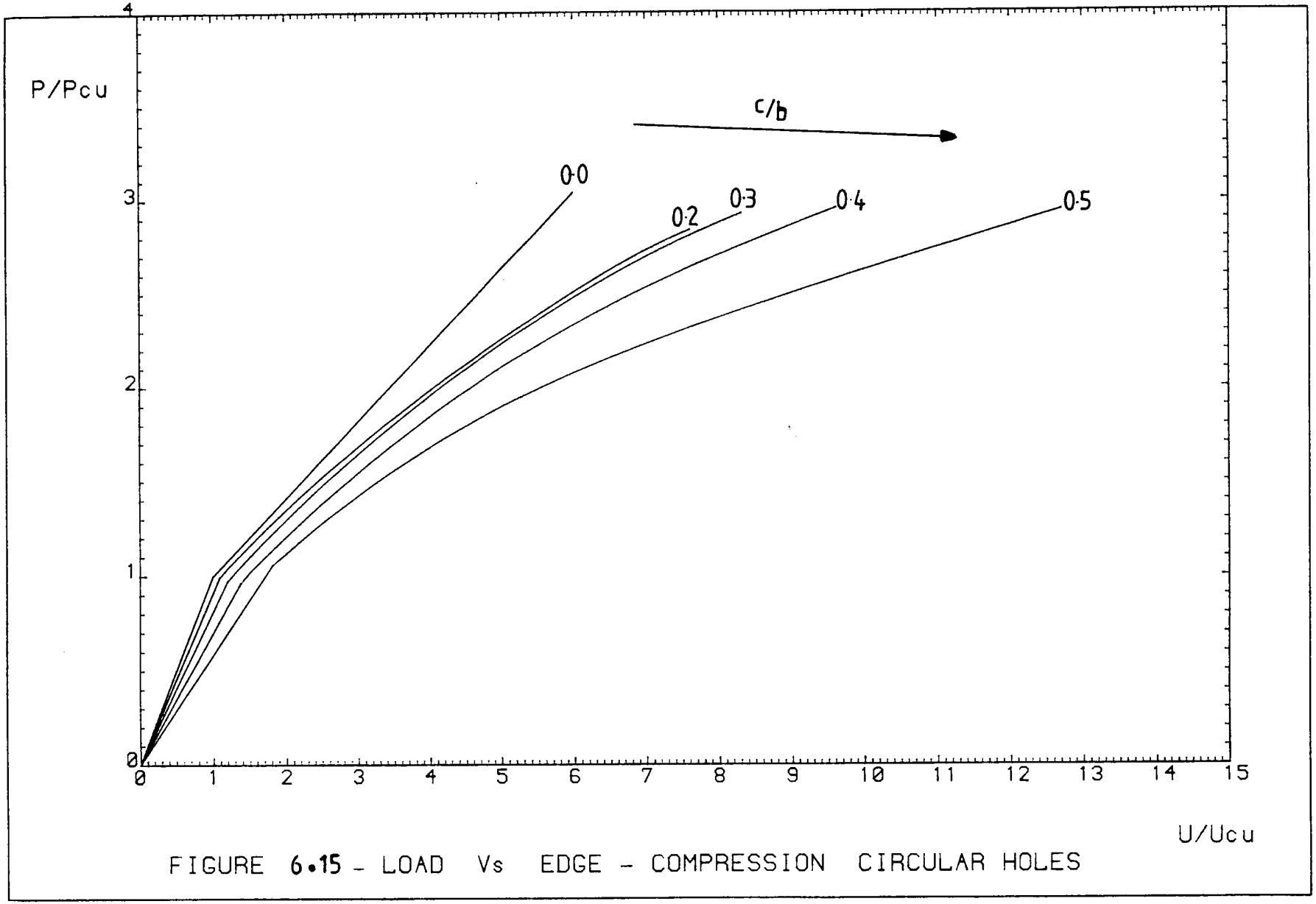

FIGURE 6.15 - LOAD Vs EDGE - COMPRESSION CIRCULAR HOLES

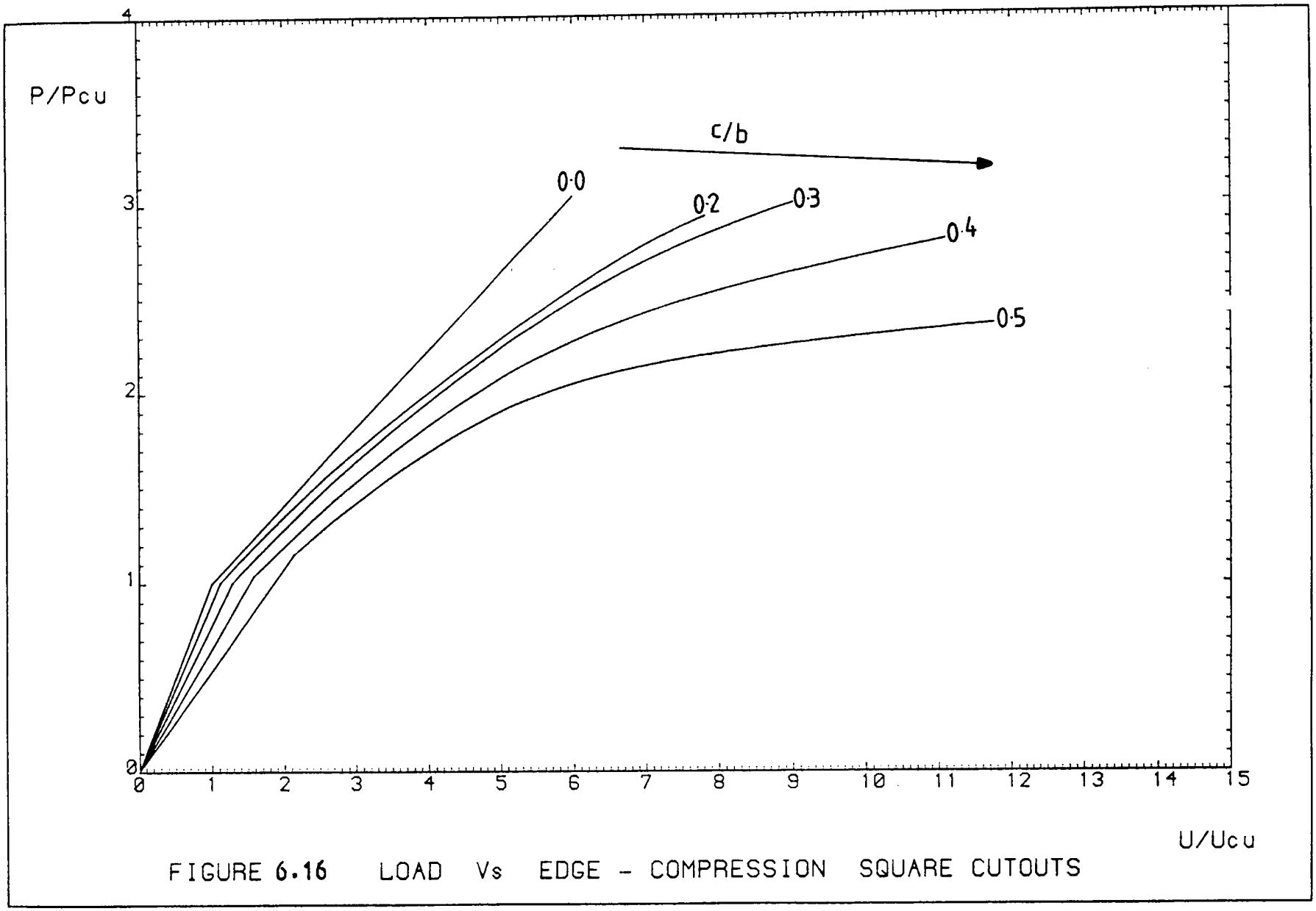

FIGURE 6.16 LOAD Vs EDGE - COMPRESSION SQUARE CUTOUTS

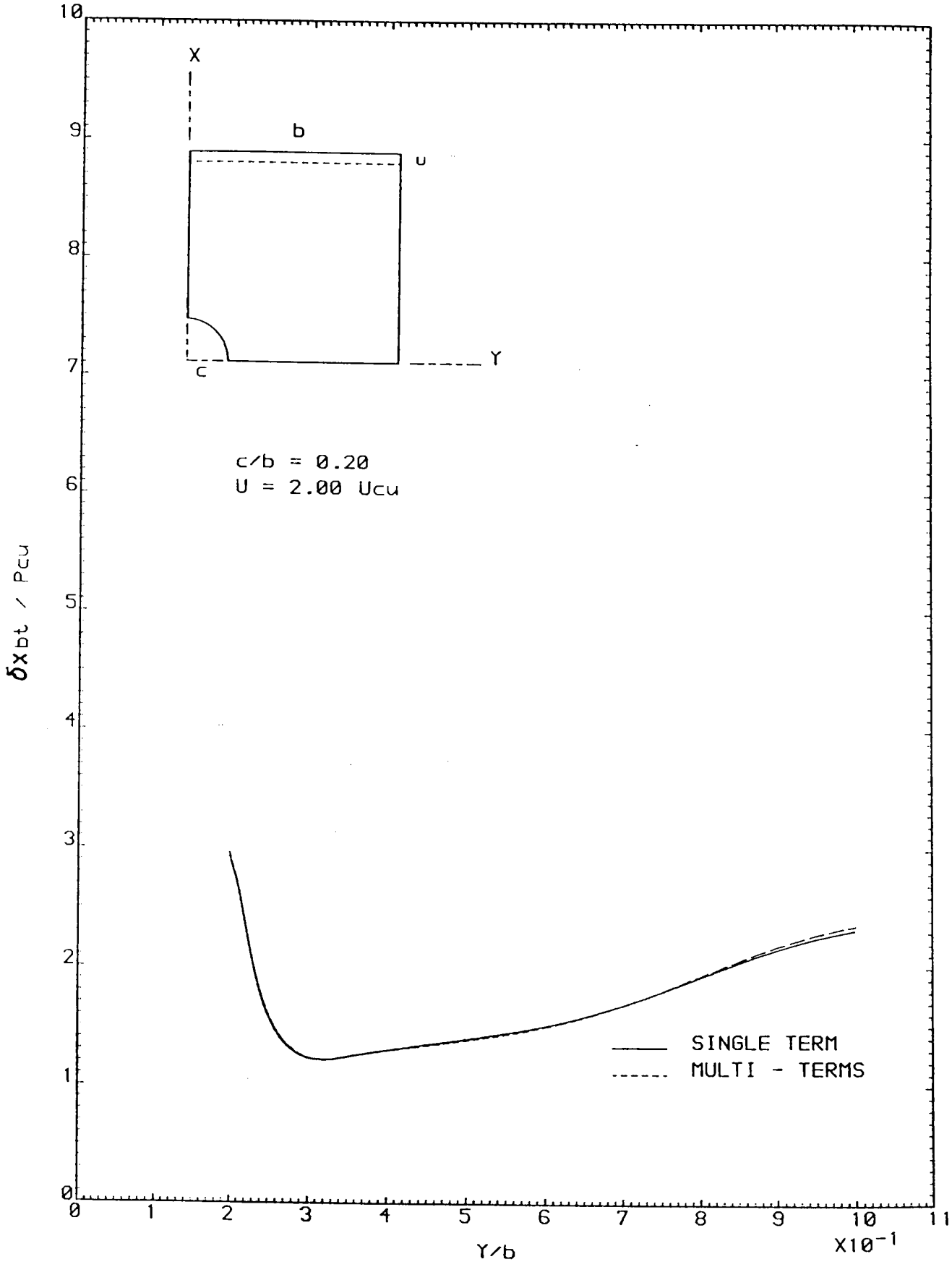

FIGURE 6·21 STRESSES AT THE MINIMUM SECTION

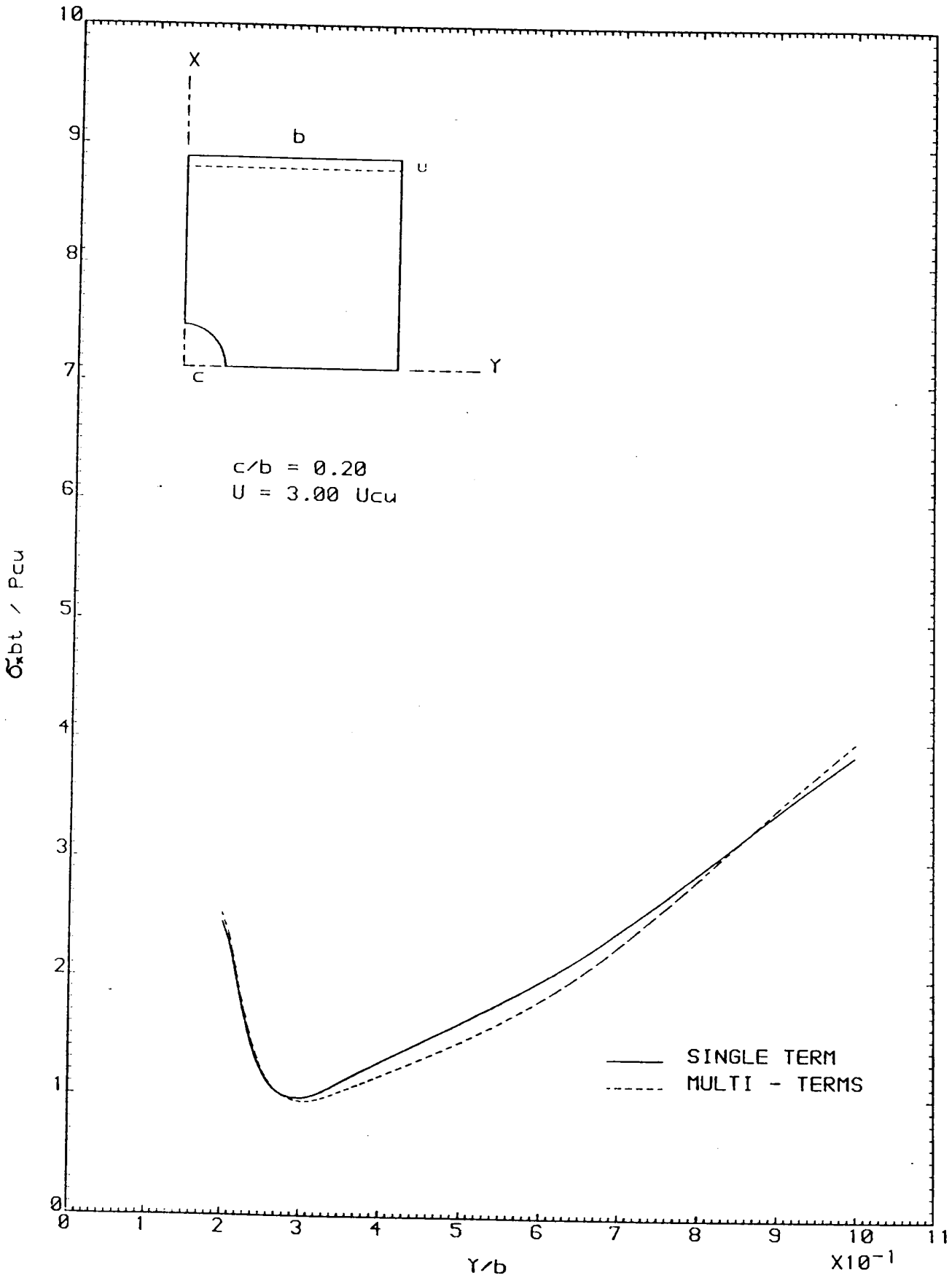

FIGURE 6·22 STRESSES AT THE MINIMUM SECTION

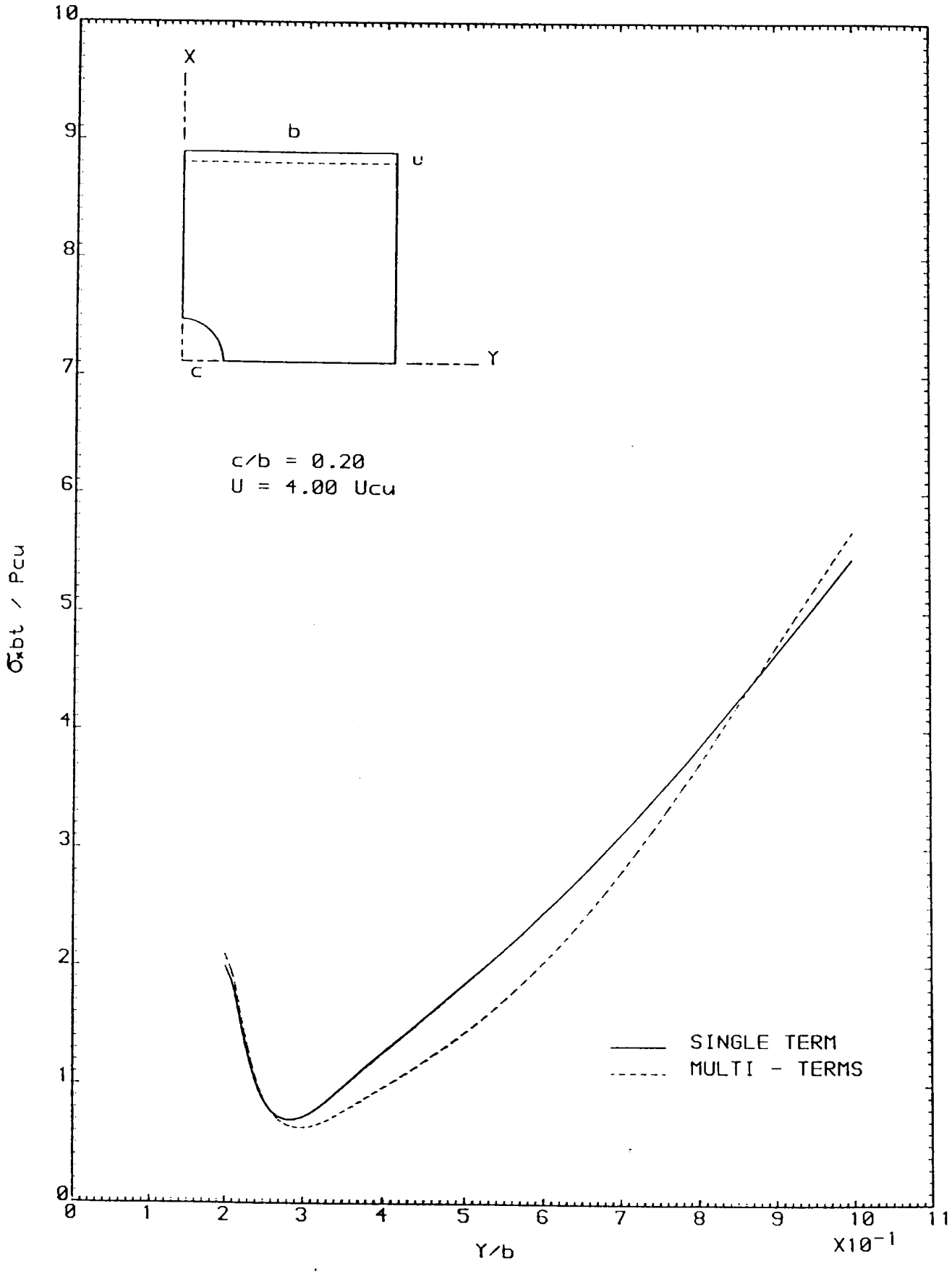

FIGURE 6·23 STRESSES AT THE MINIMUM SECTION

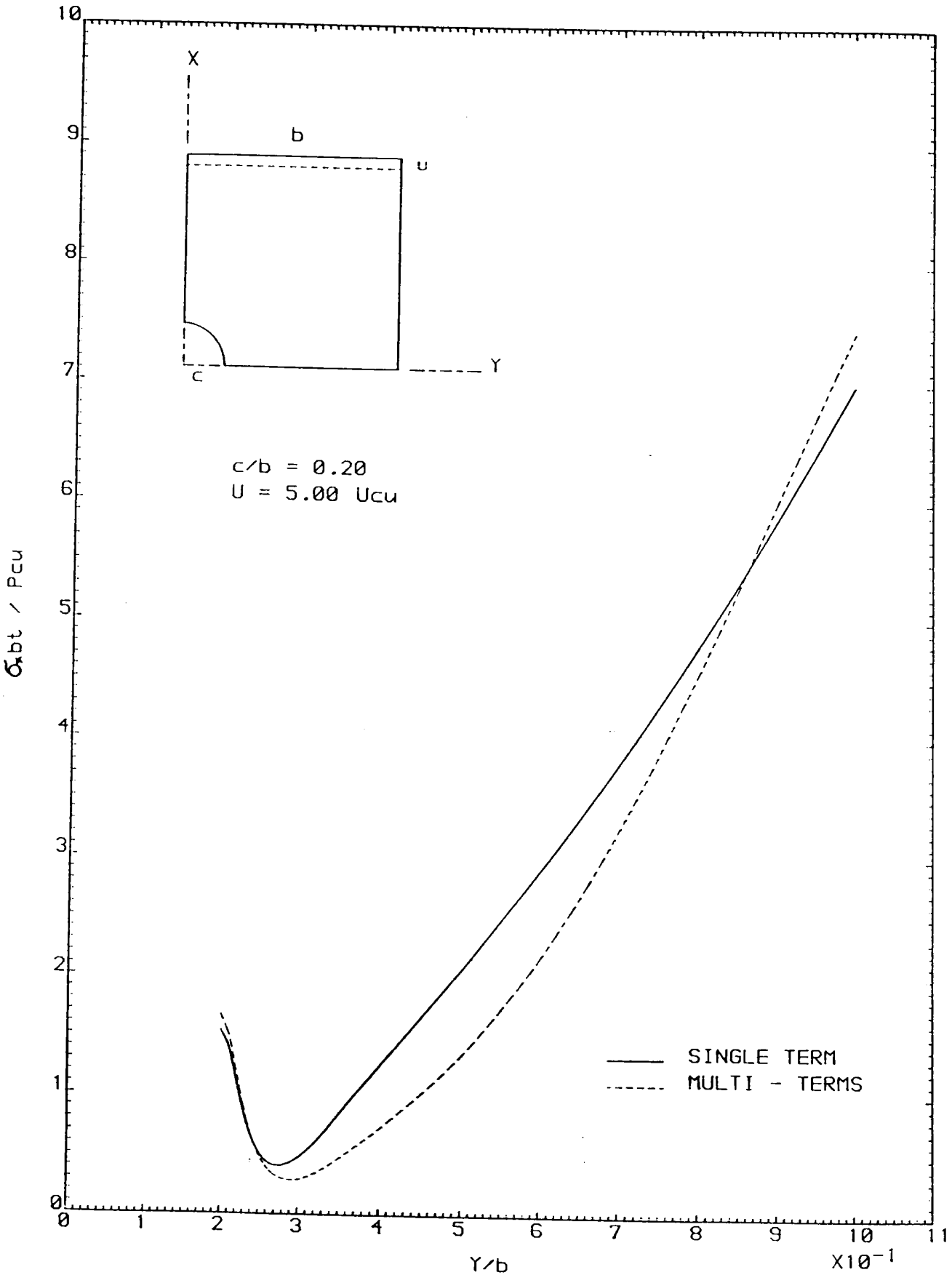

FIGURE 6·24 STRESSES AT THE MINIMUM SECTION

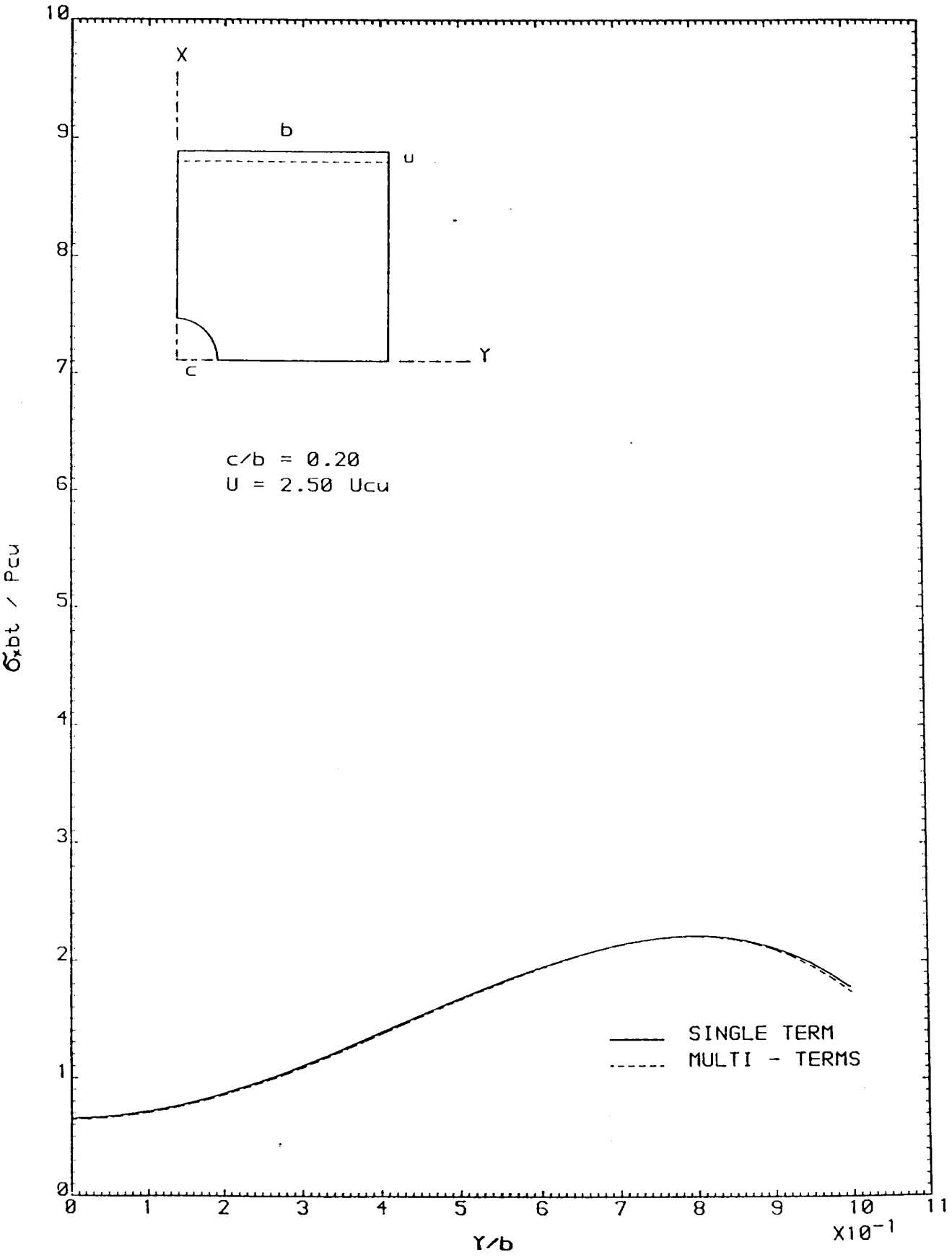

FIGURE 6·25 STRESSES AT THE LOADED EDGE

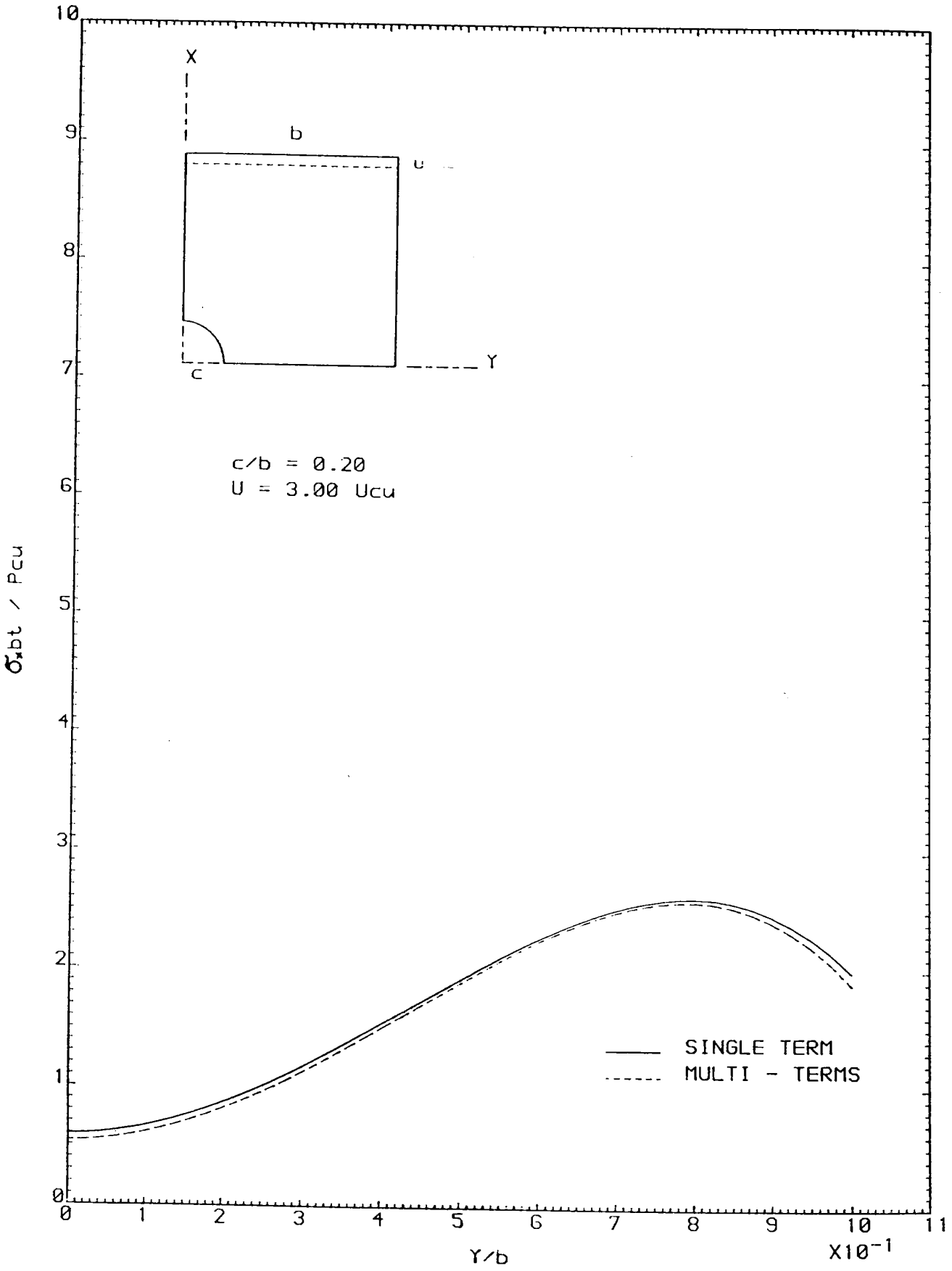

FIGURE 6·26 STRESSES AT THE LOADED EDGE

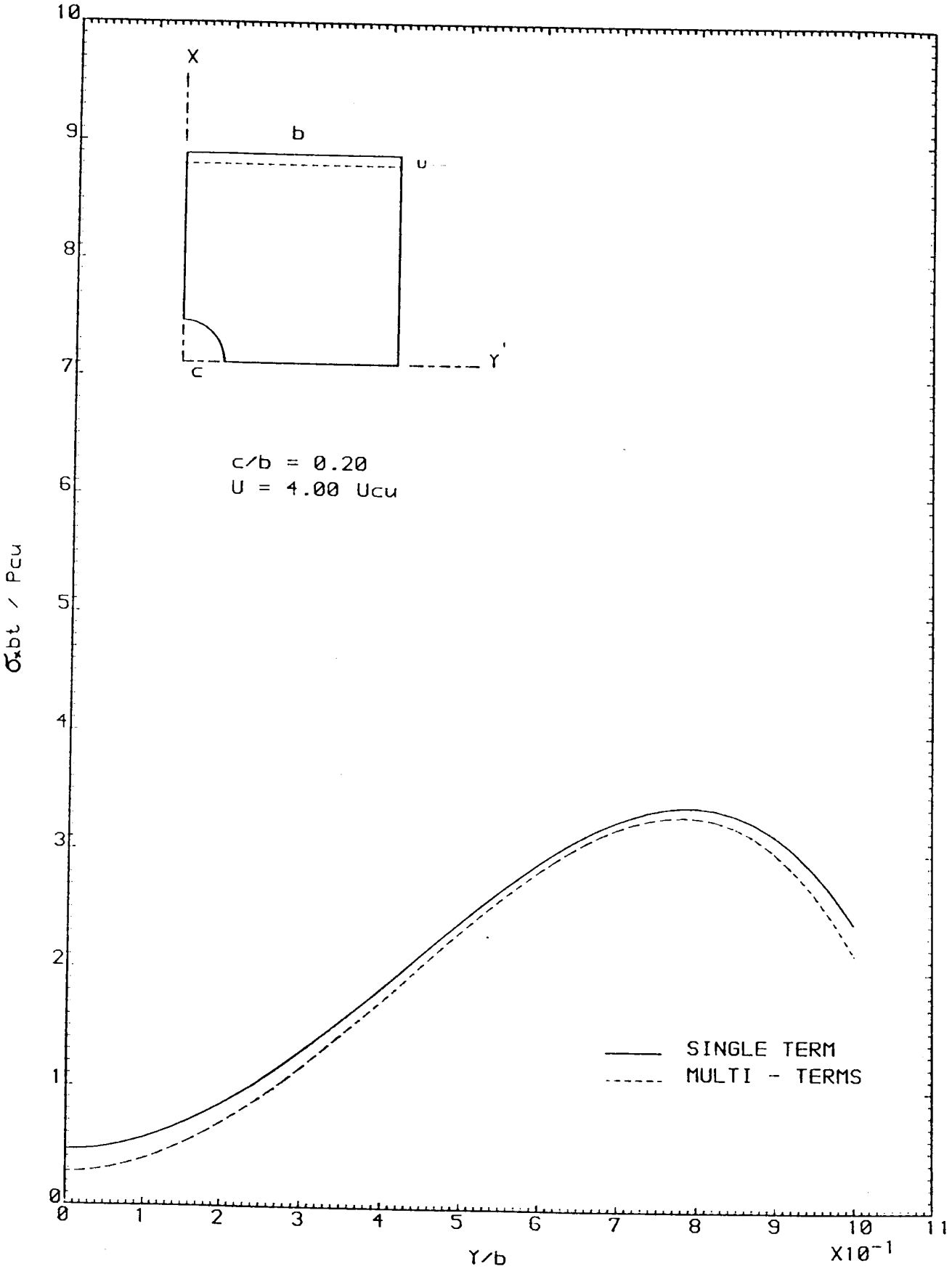

FIGURE 6·27 STRESSES AT THE LOADED EDGE

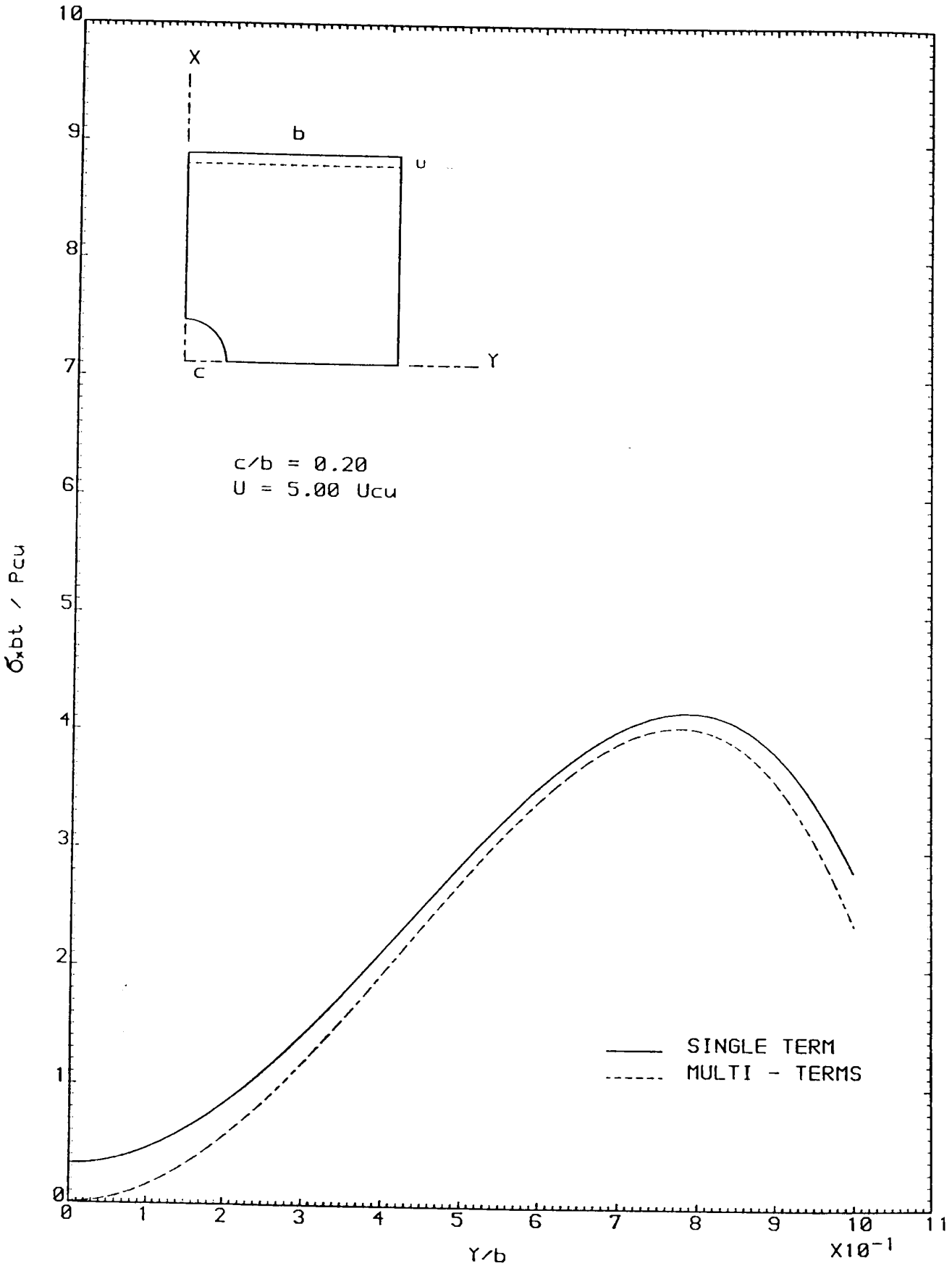

FIGURE 6·28 STRESSES AT THE LOADED EDGE

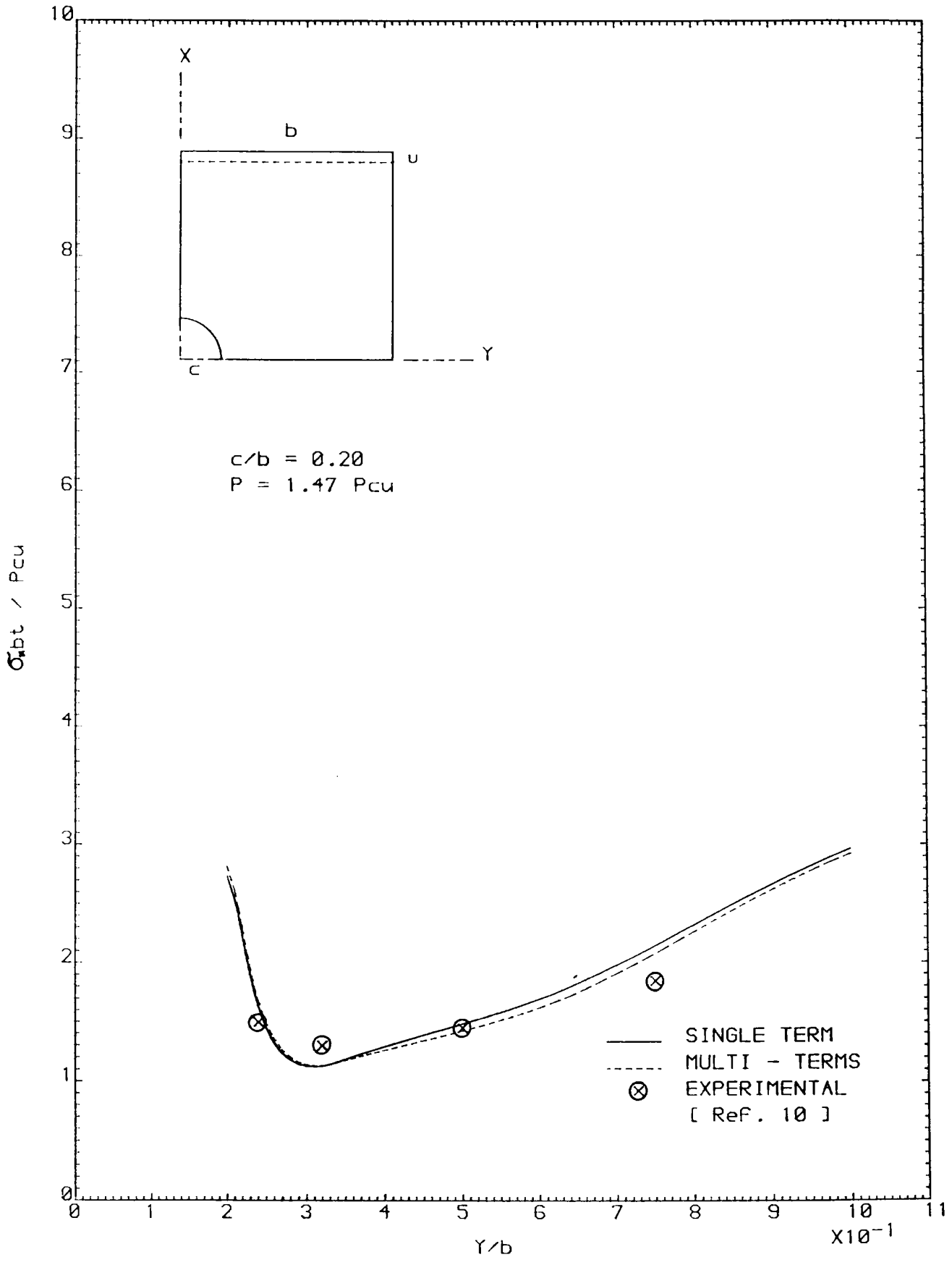

FIGURE 6·29 STRESSES AT THE MINIMUM SECTION

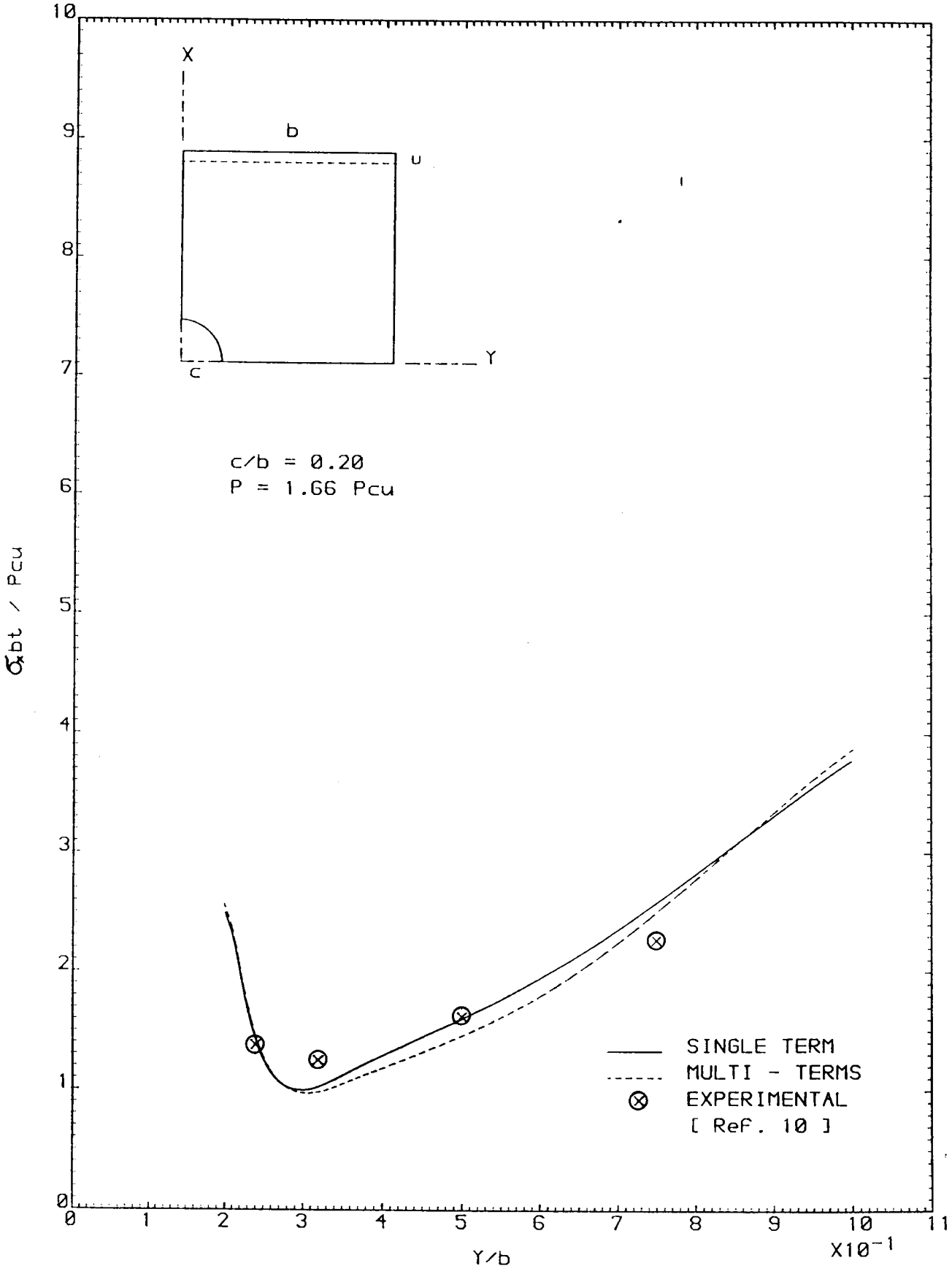

FIGURE 6·30 STRESSES AT THE MINIMUM SECTION

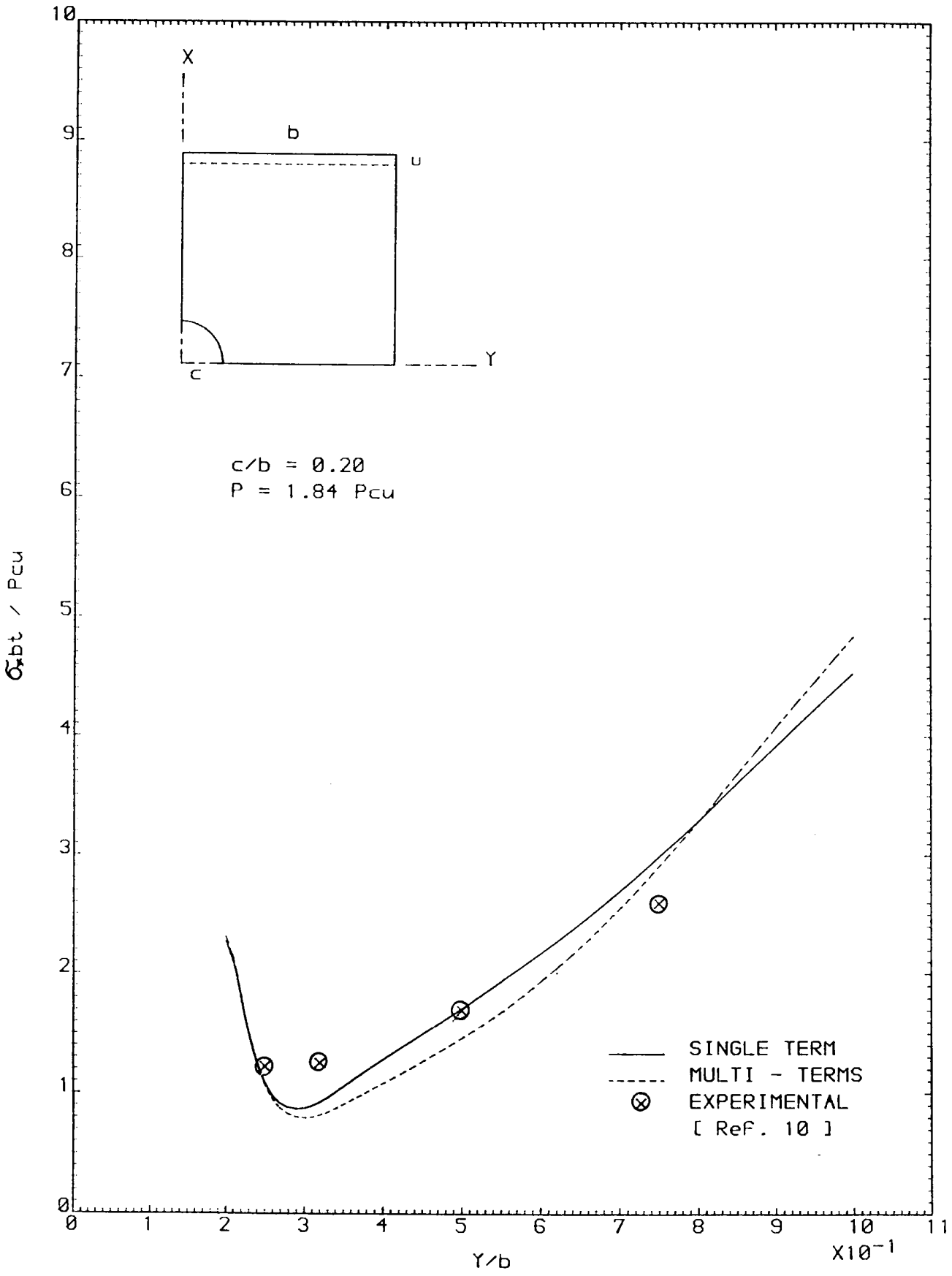

FIGURE 6·31 STRESSES AT THE MINIMUM SECTION

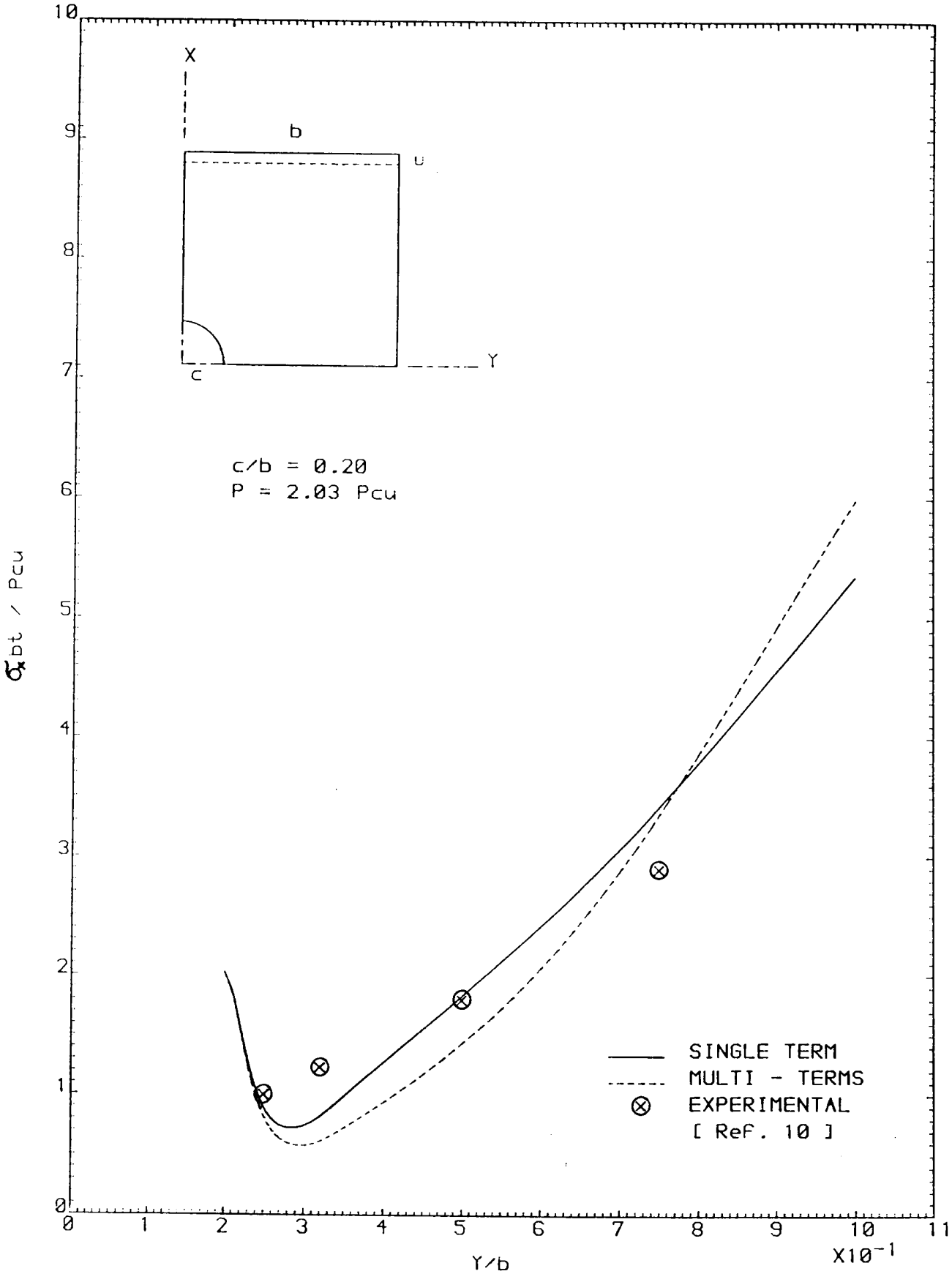

FIGURE 6·32 STRESSES AT THE MINIMUM SECTION

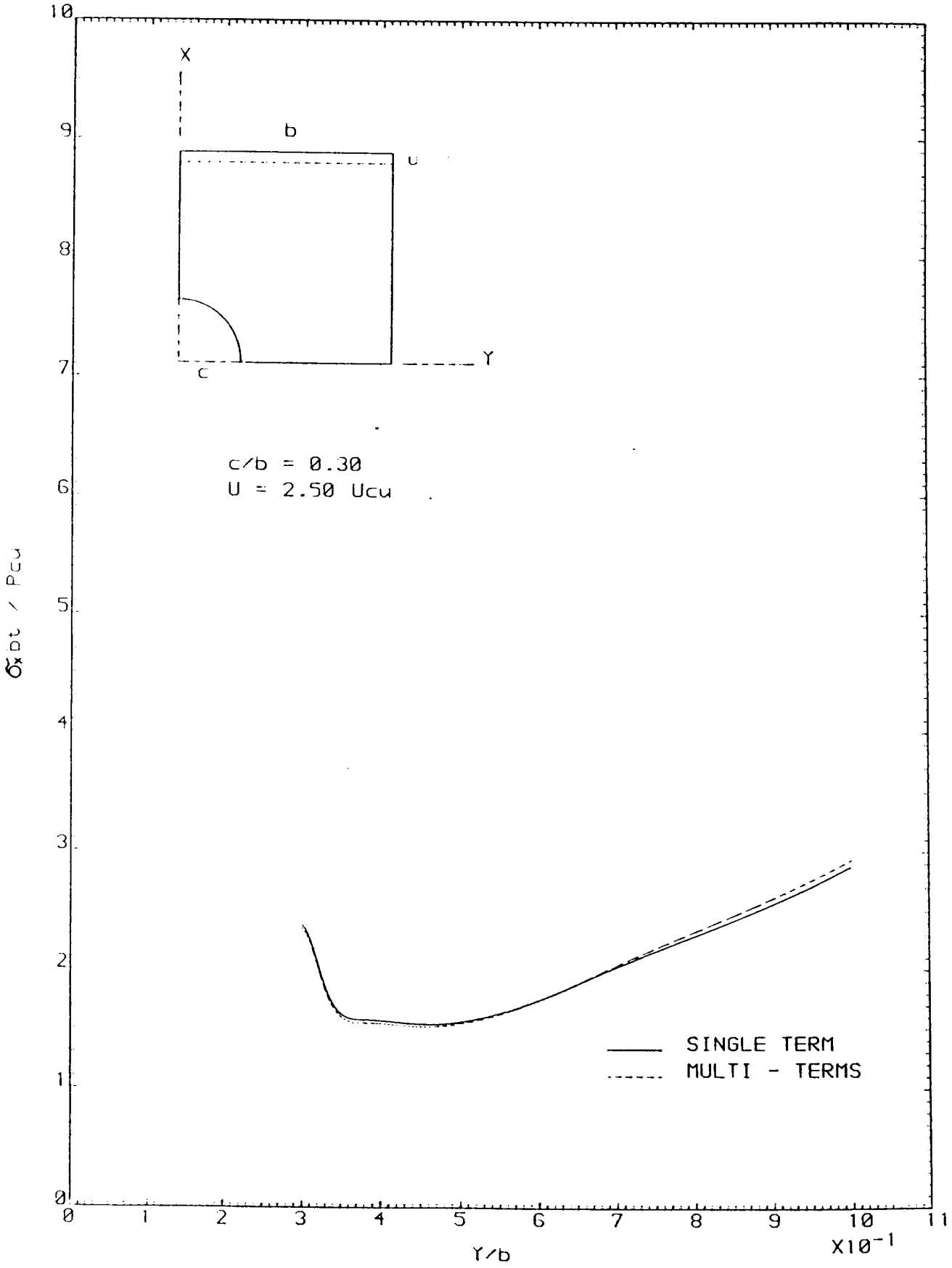

FIGURE 6·33 STRESSES AT THE MINIMUM SECTION

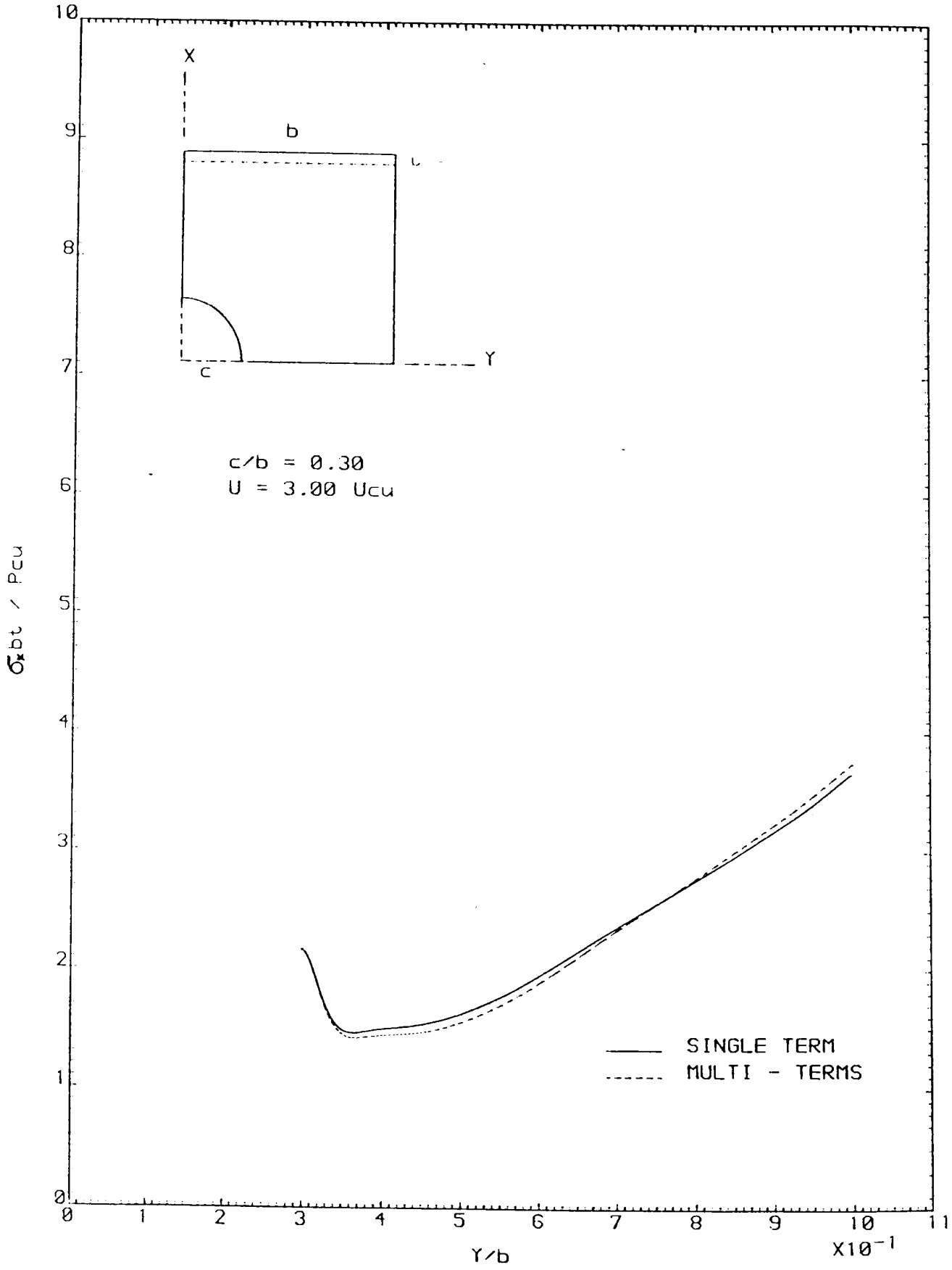

FIGURE 6.34 STRESSES AT THE MINIMUM SECTION

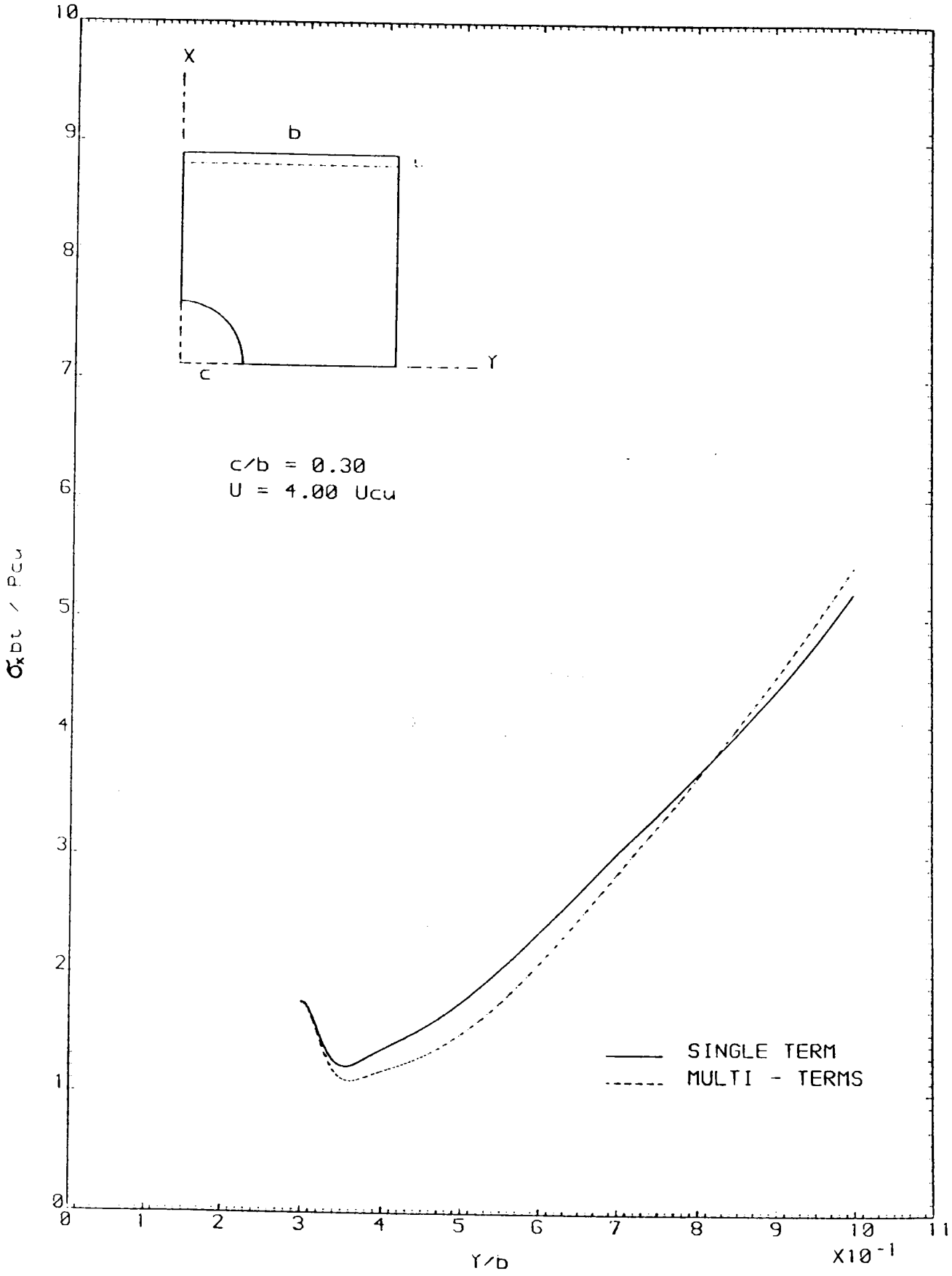

FIGURE 6·35 STRESSES AT THE MINIMUM SECTION

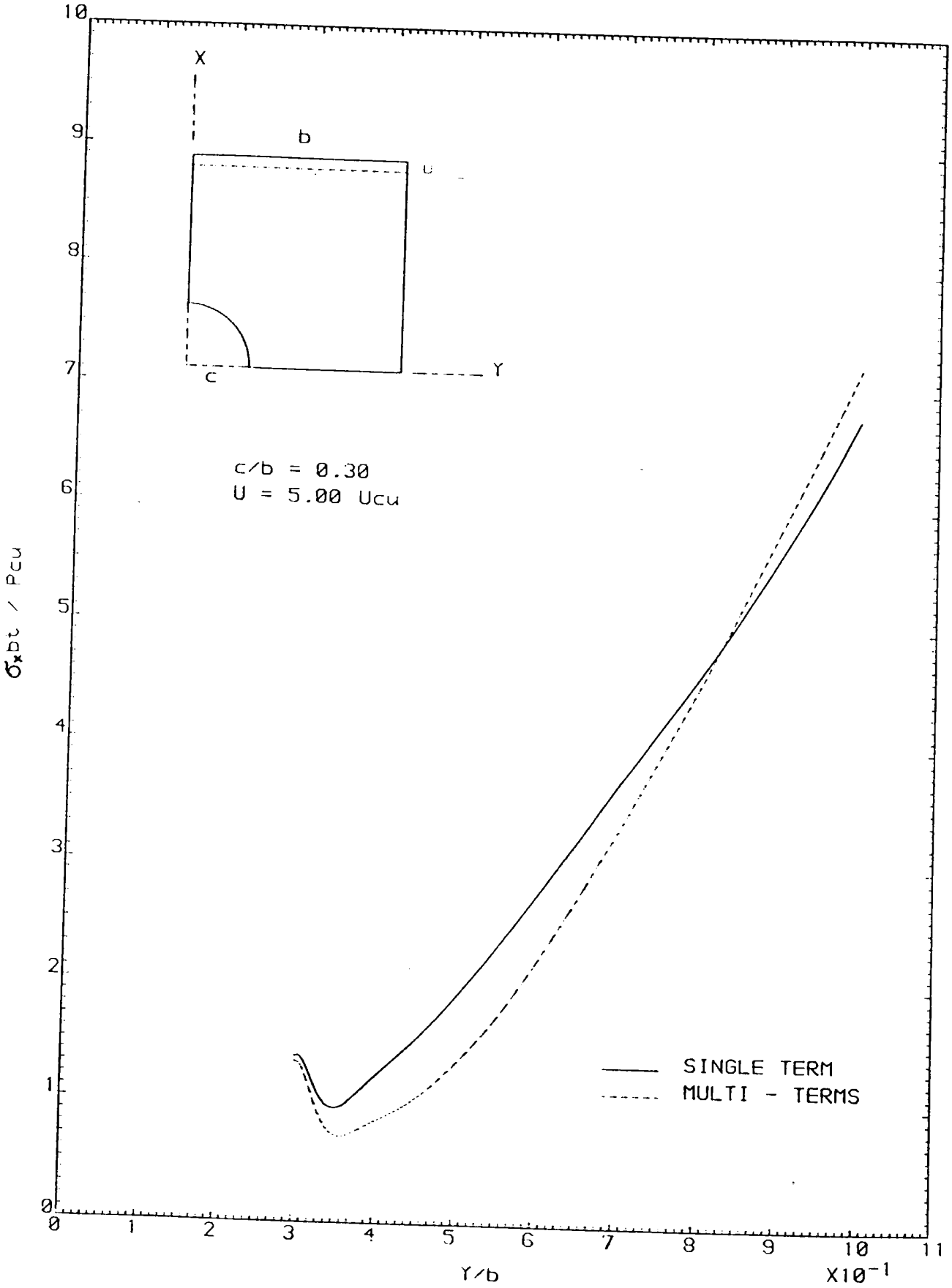

FIGURE 6·36 STRESSES AT THE MINIMUM SECTION

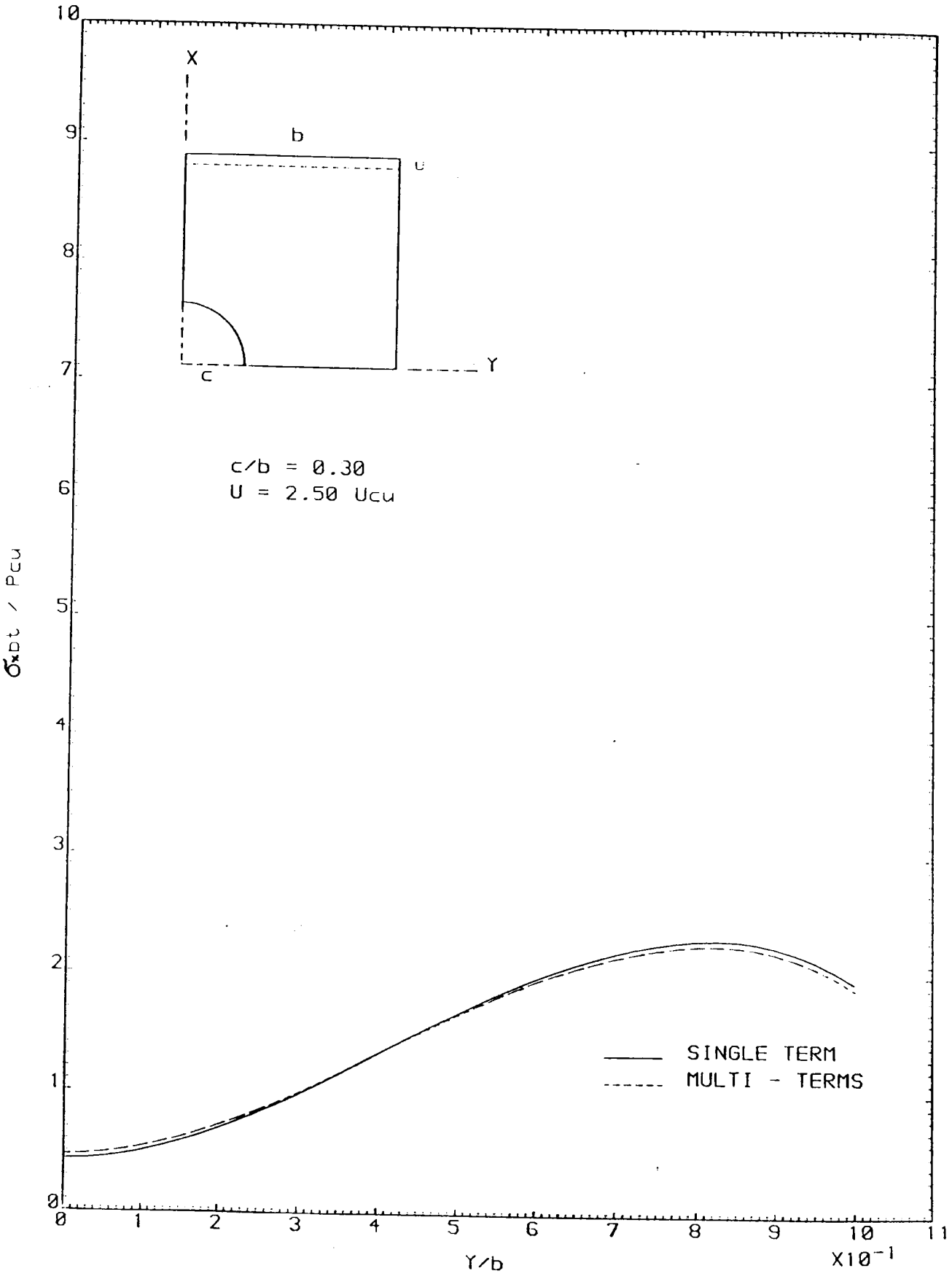

FIGURE 6·37 STRESSES AT THE LOADED EDGE

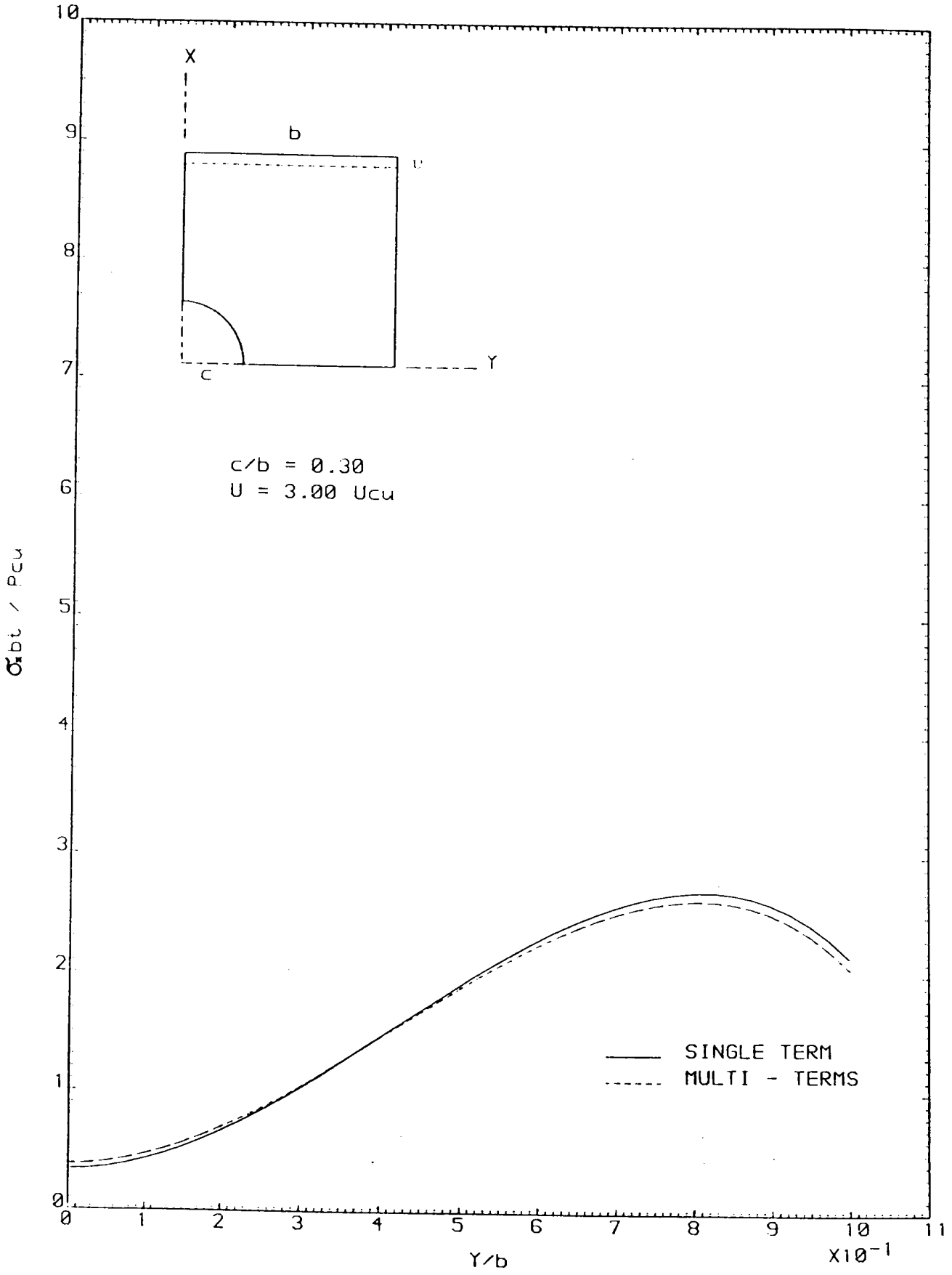

FIGURE 6·38 STRESSES AT THE LOADED EDGE

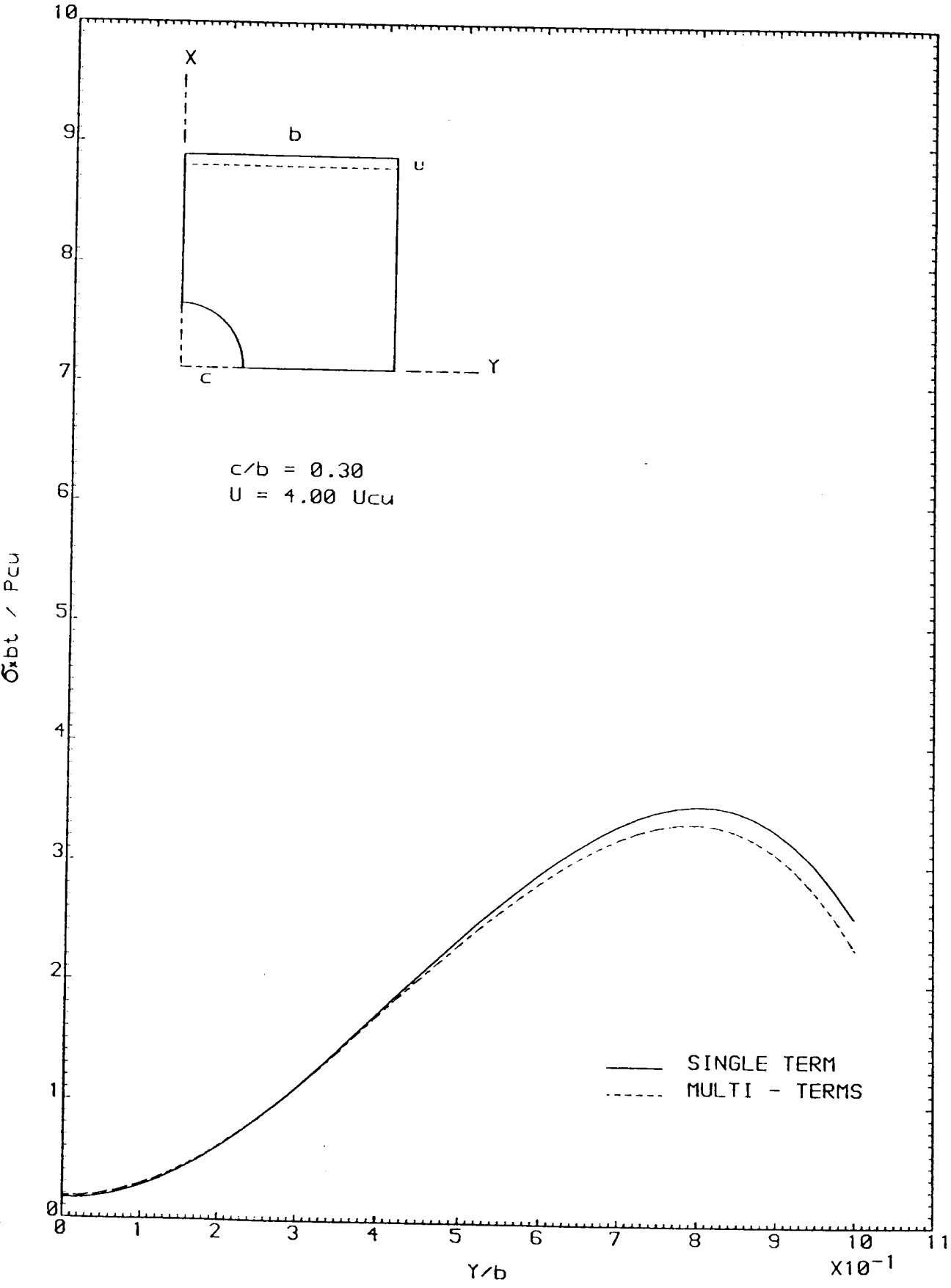

FIGURE 6·39 STRESSES AT THE LOADED EDGE

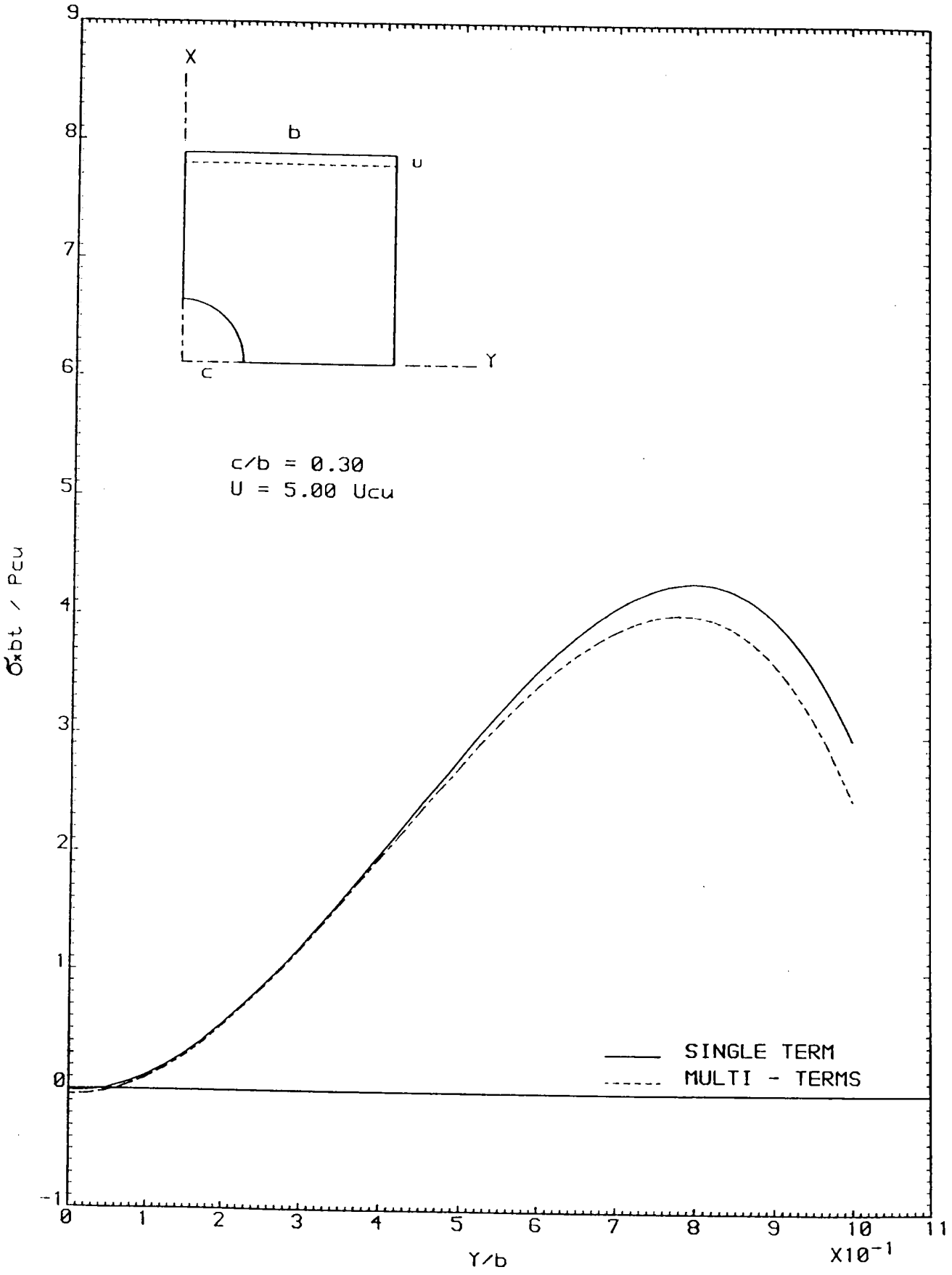

FIGURE 6·40 STRESSES AT THE LOADED EDGE

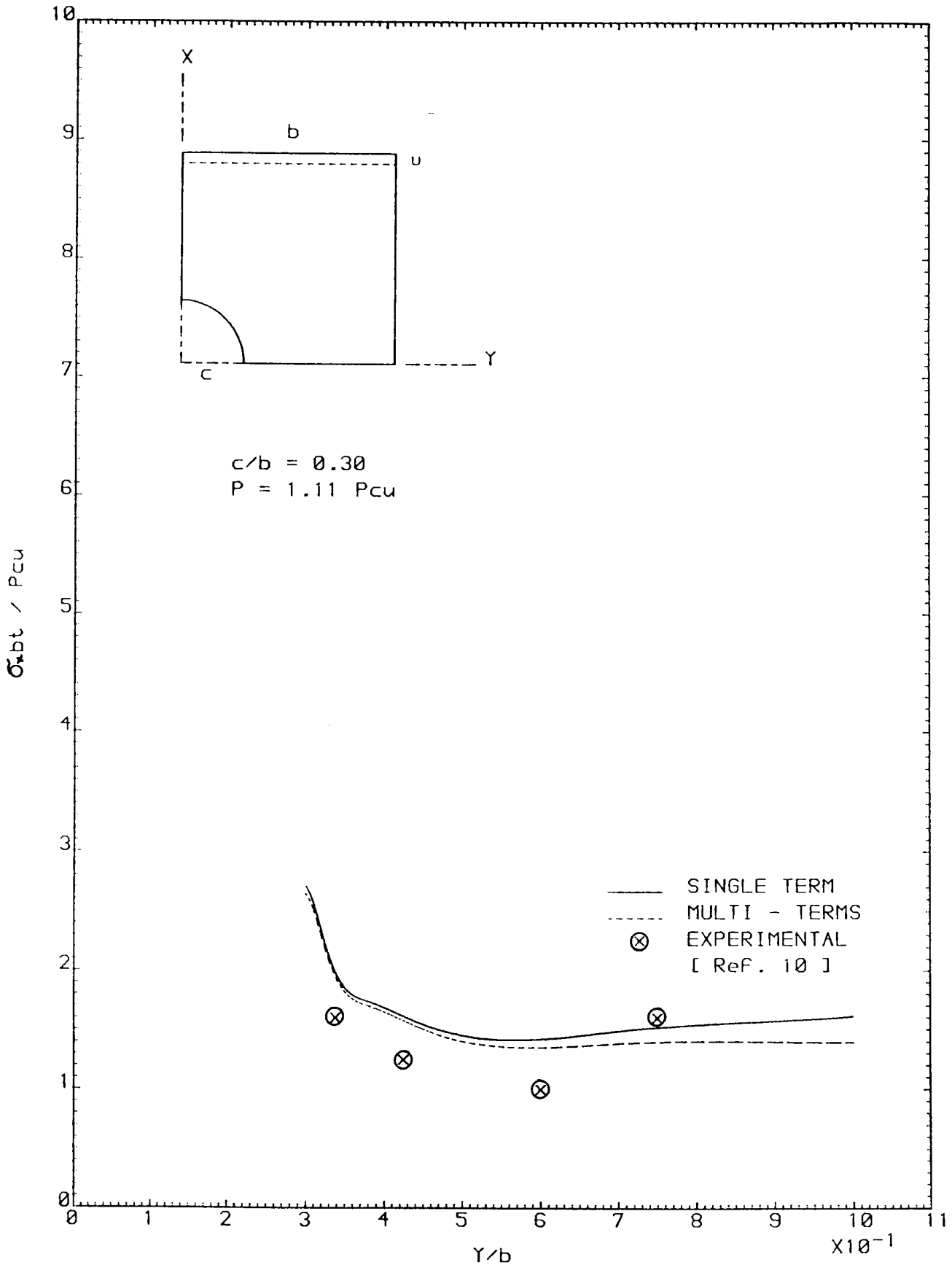

FIGURE 6·41 STRESSES AT THE MINIMUM SECTION

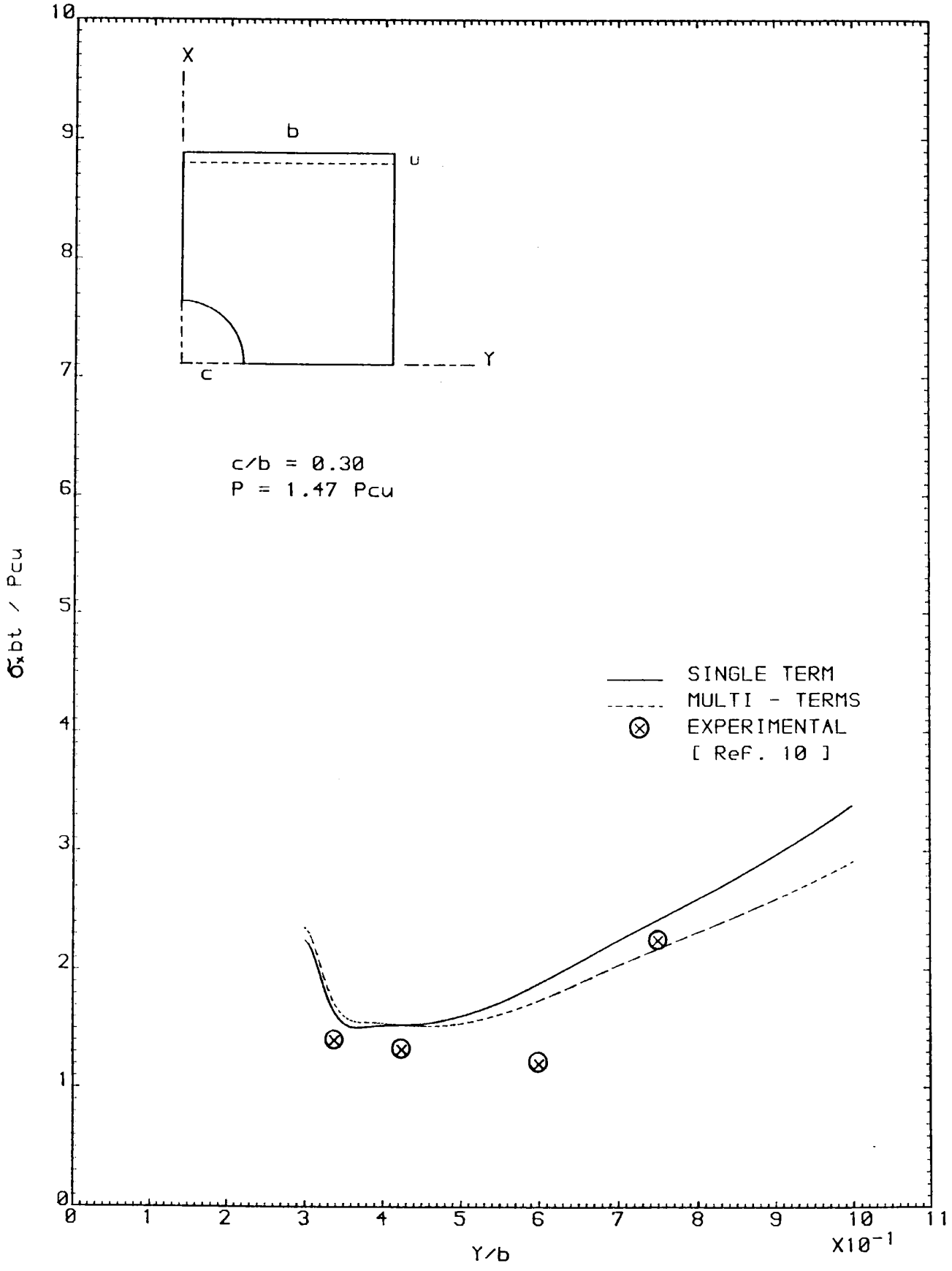

FIGURE 6·42 STRESSES AT THE MINIMUM SECTION

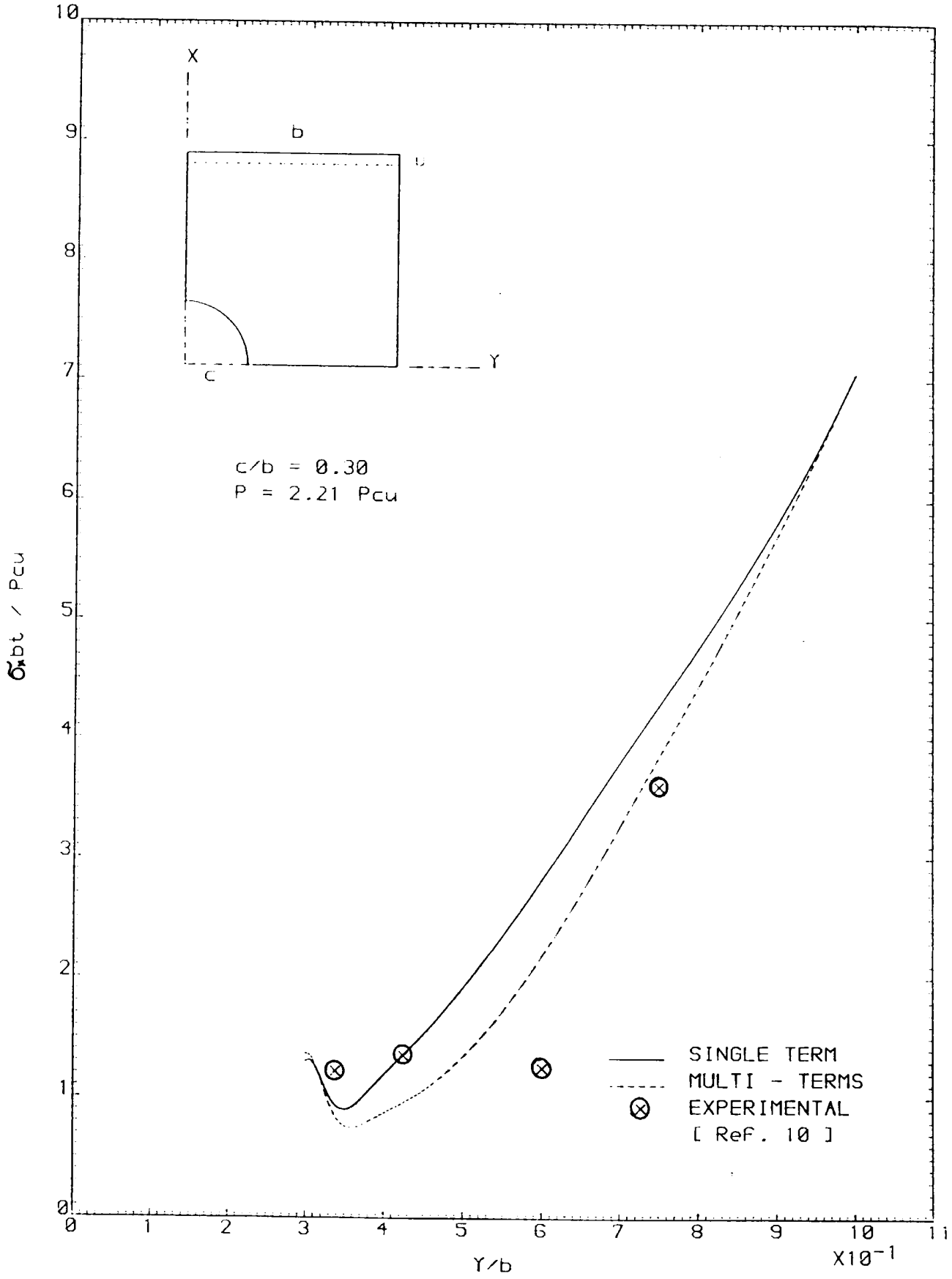

FIGURE 6·43 STRESSES AT THE MINIMUM SECTION

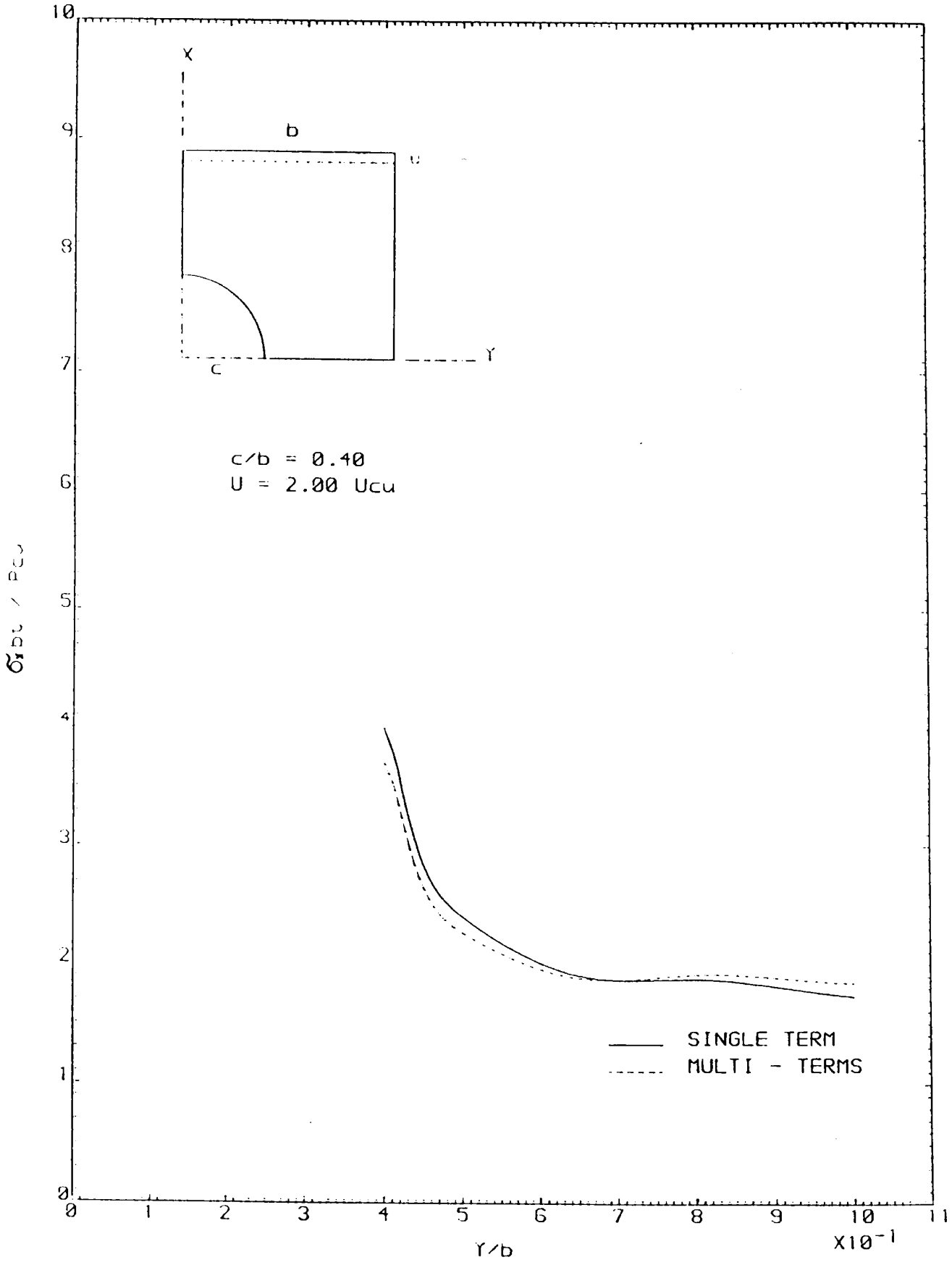

FIGURE 6·44 STRESSES AT THE MINIMUM SECTION

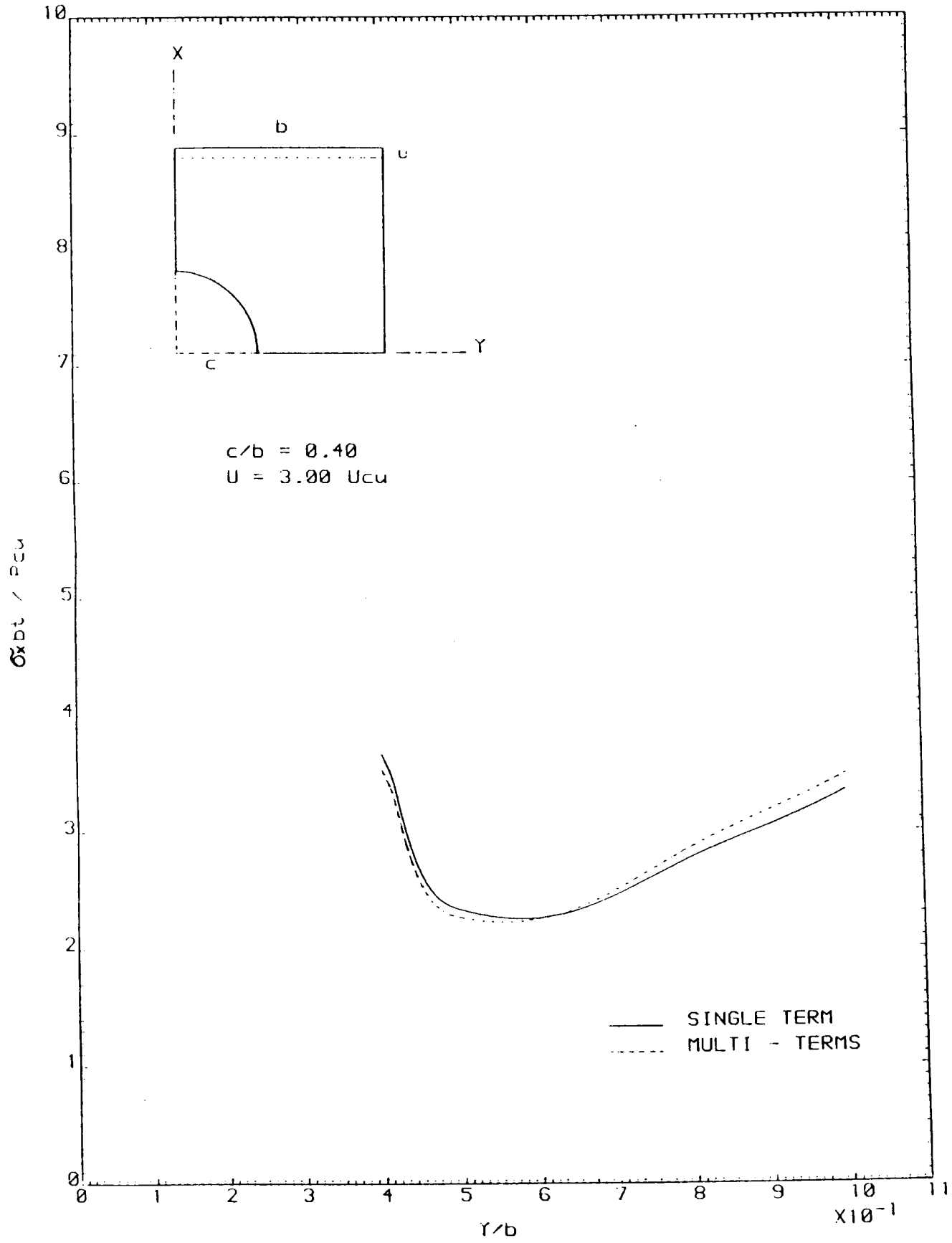

FIGURE 6·45 STRESSES AT THE MINIMUM SECTION

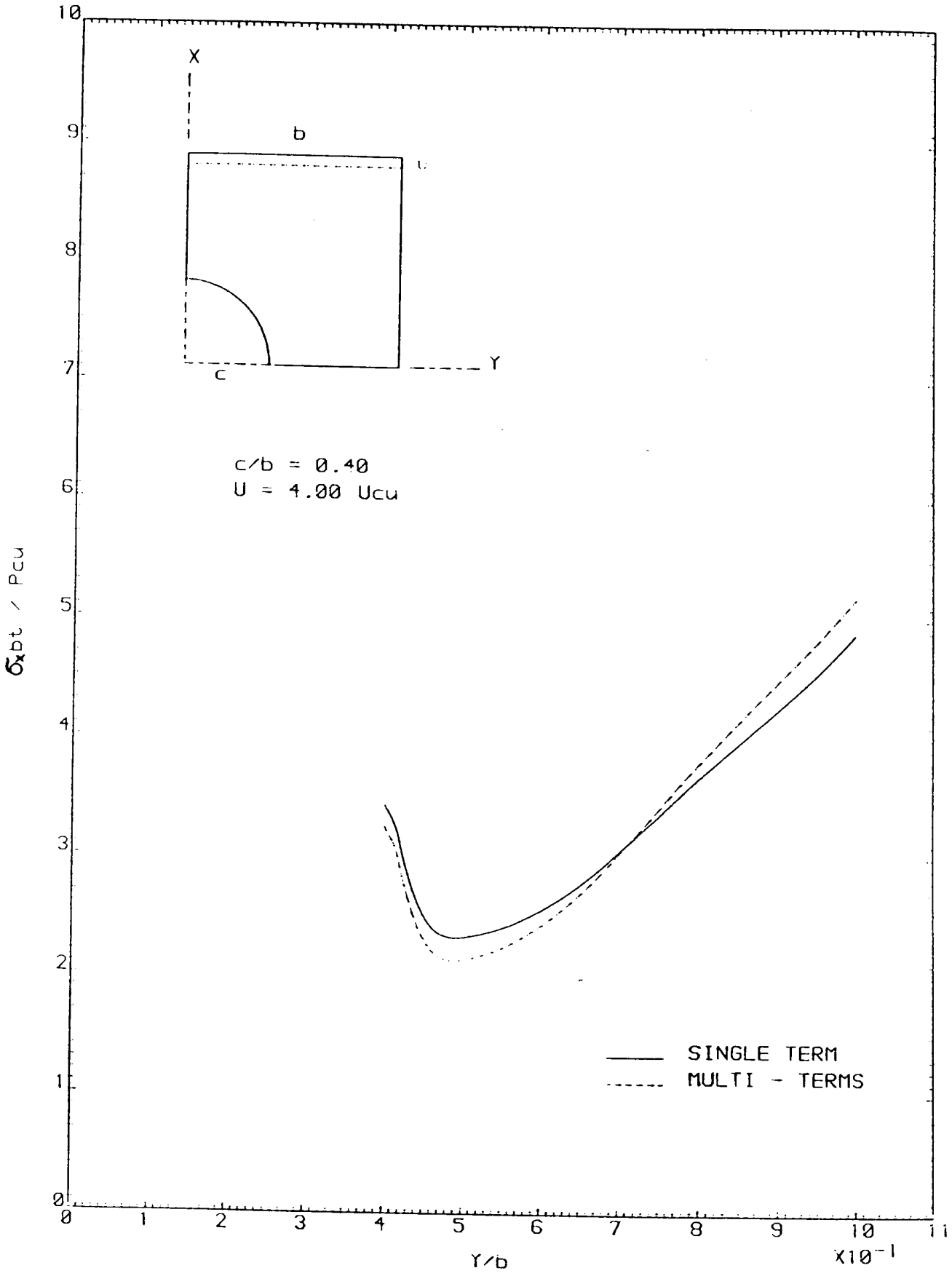

FIGURE 6·46 STRESSES AT THE MINIMUM SECTION

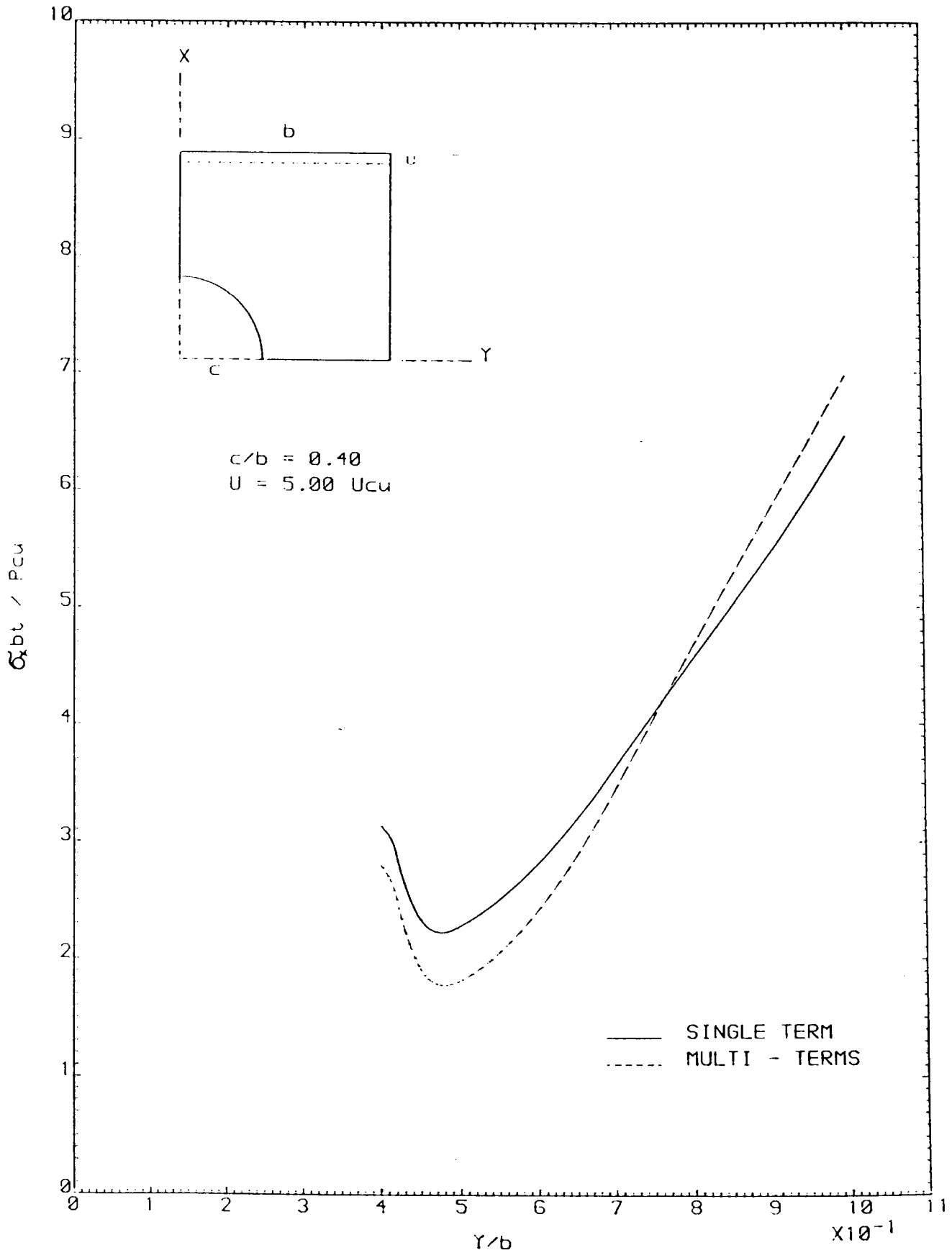

FIGURE 6·47 STRESSES AT THE MINIMUM SECTION

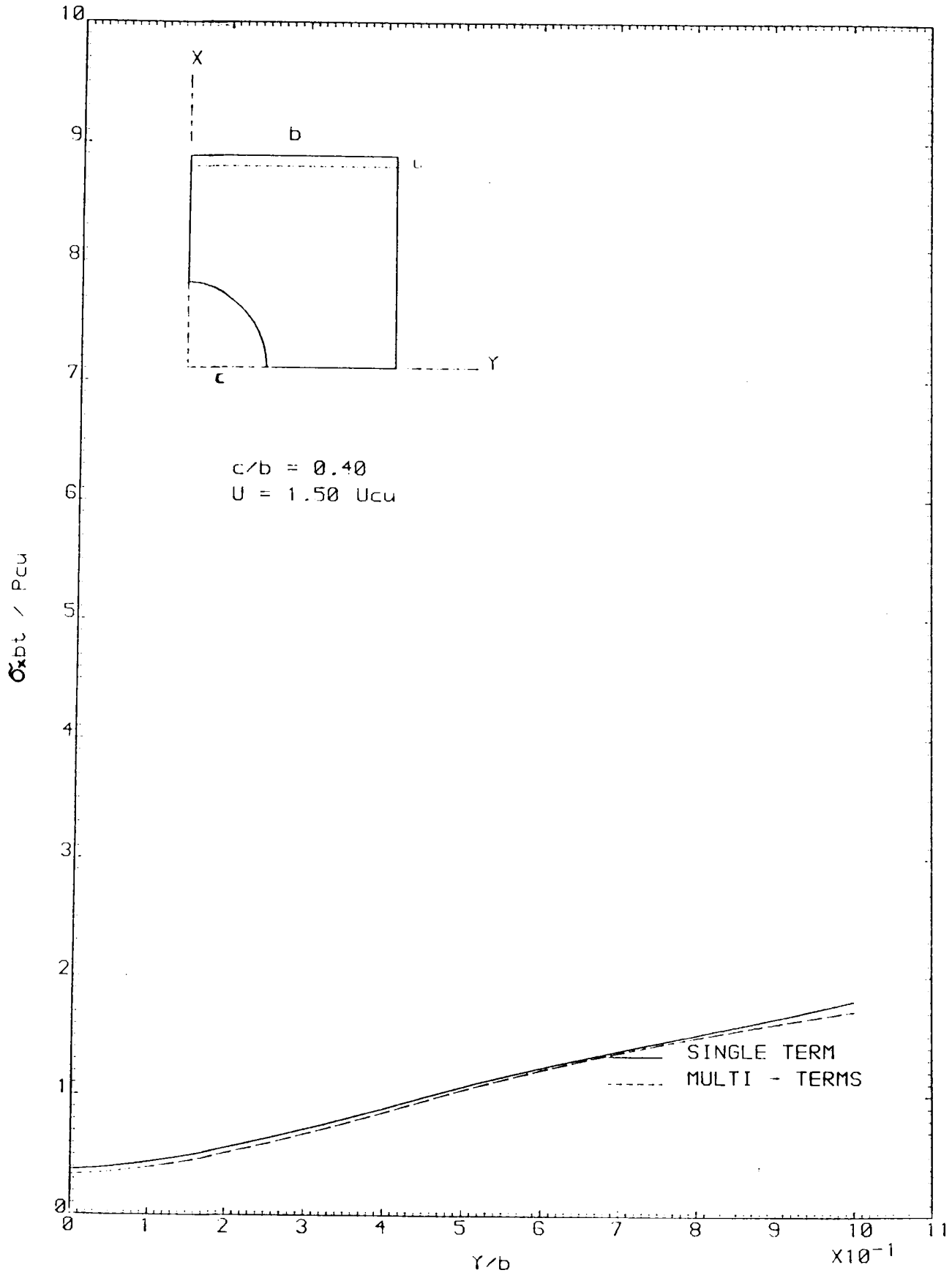

FIGURE 6·48 STRESSES AT THE LOADED EDGE

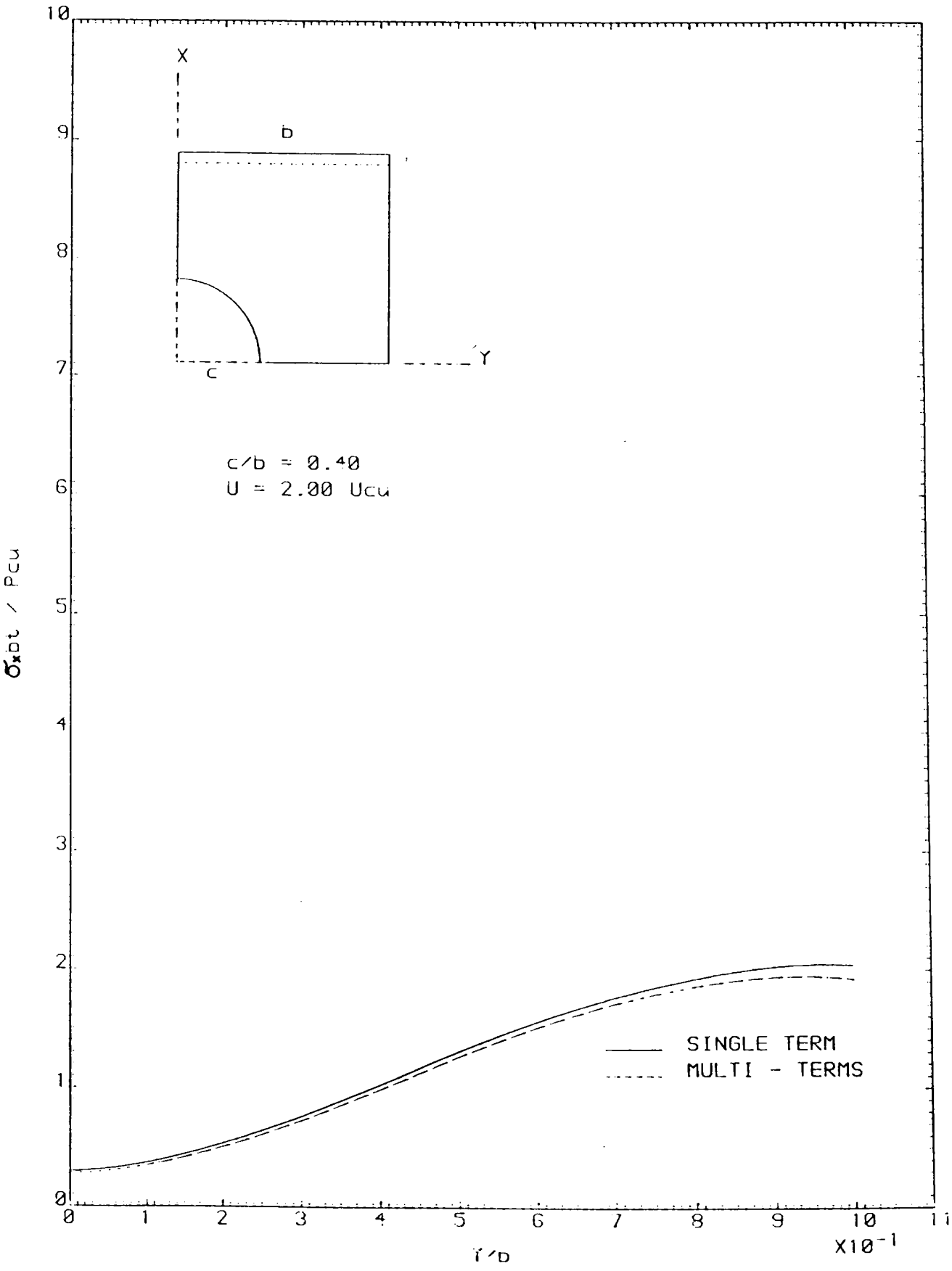

FIGURE 6·49 STRESSES AT THE LOADED EDGE

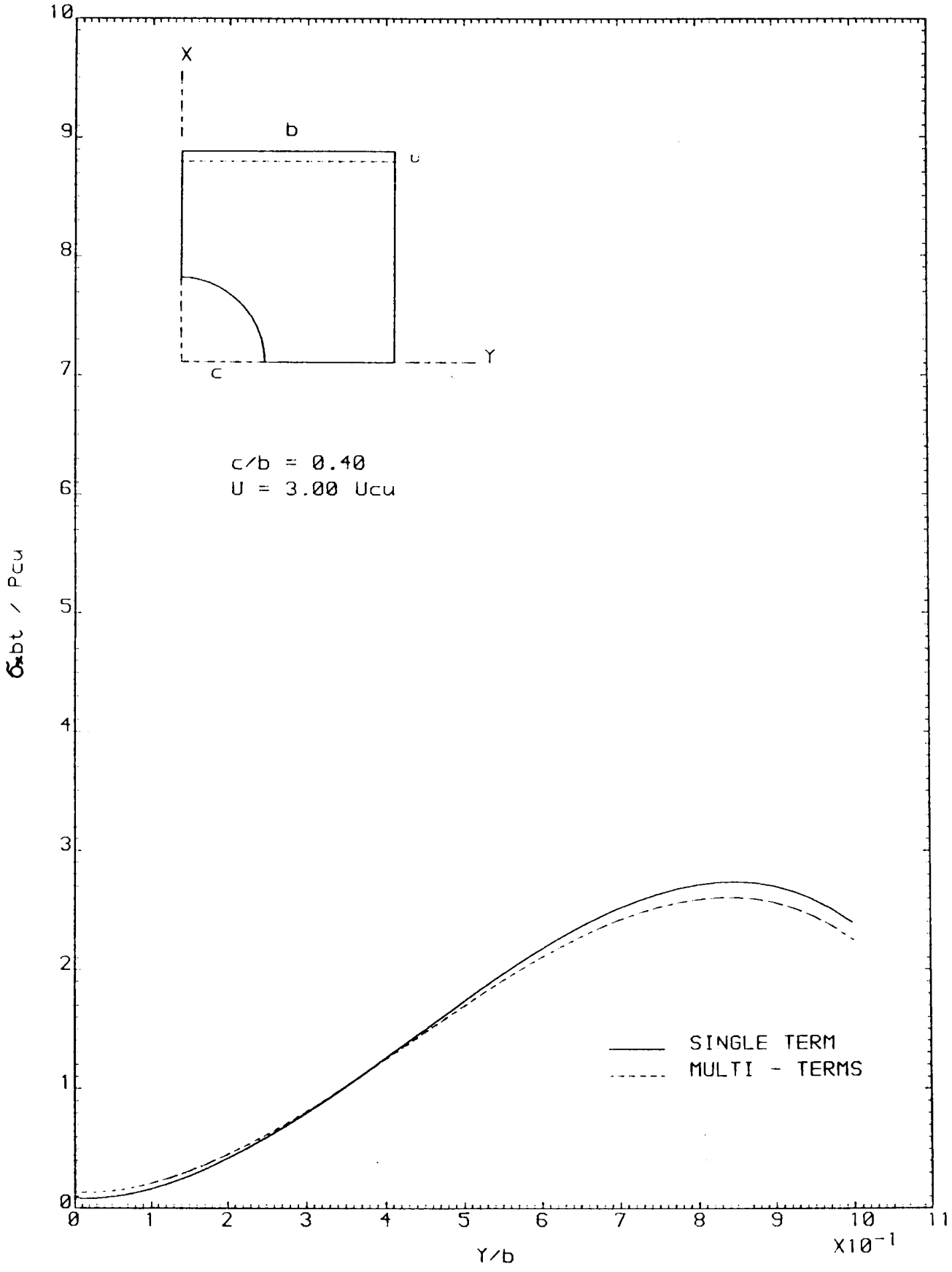

FIGURE 6·50 STRESSES AT THE LOADED EDGE

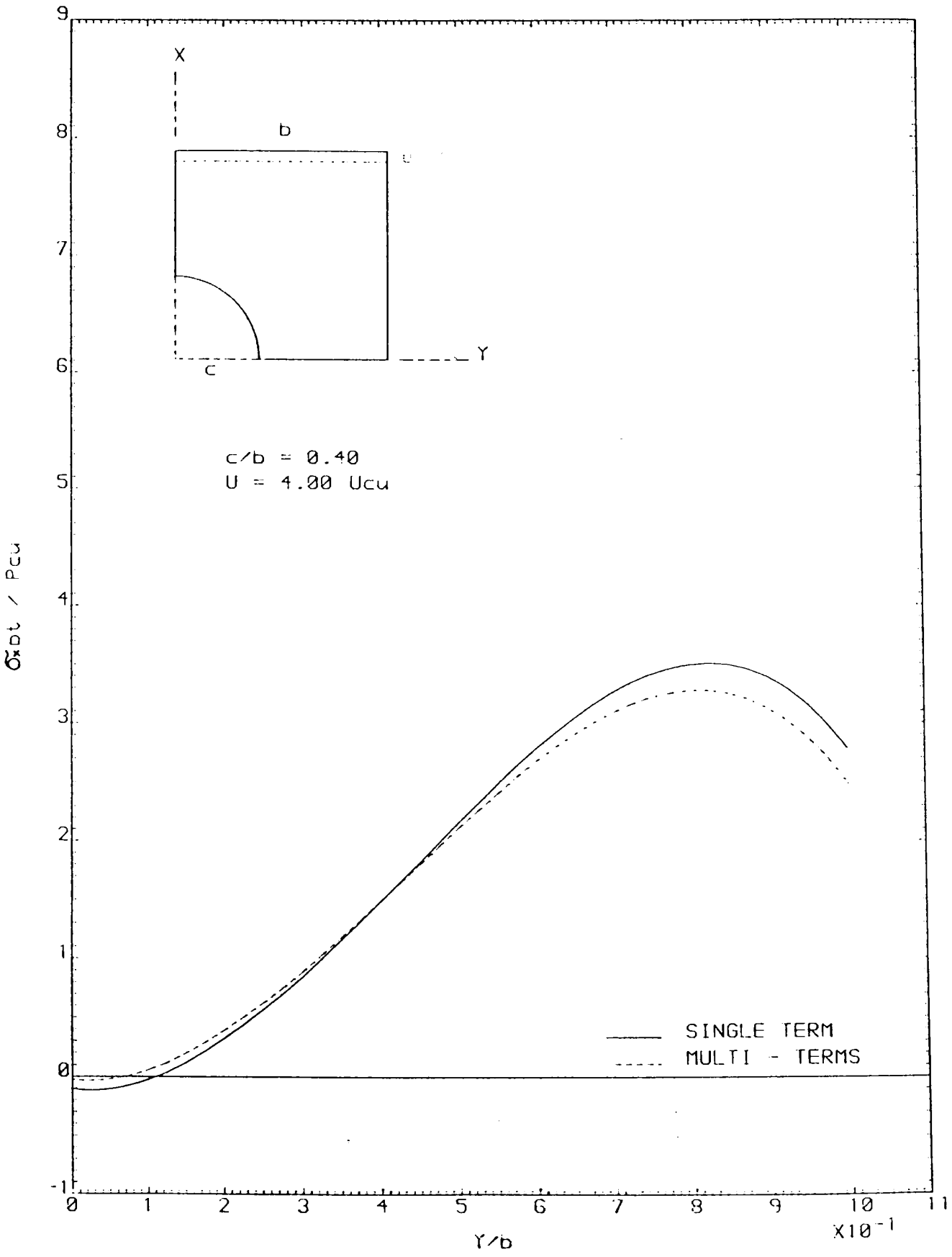

FIGURE 6·51 STRESSES AT THE LOADED EDGE

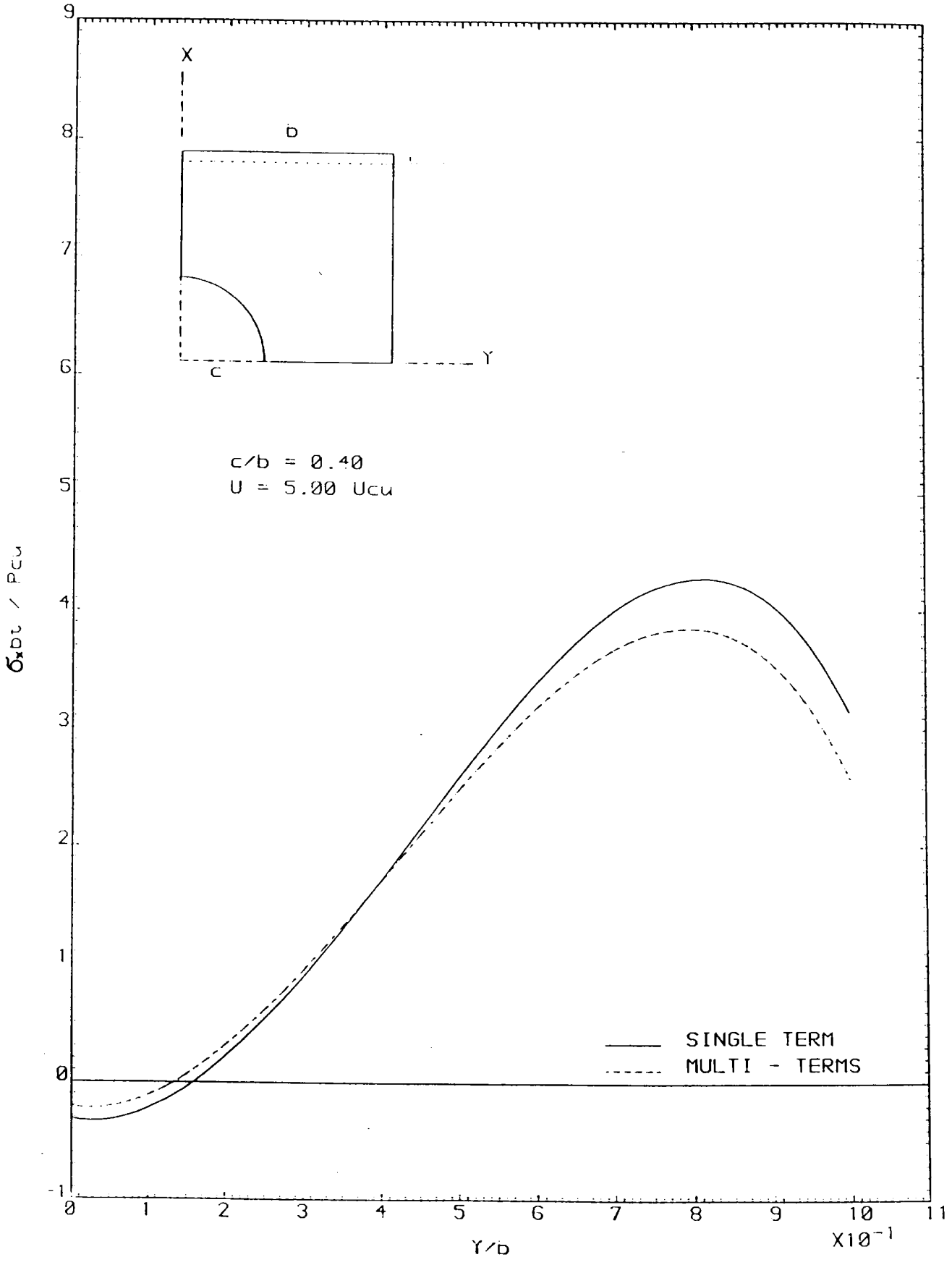

FIGURE 6·52 STRESSES AT THE LOADED EDGE

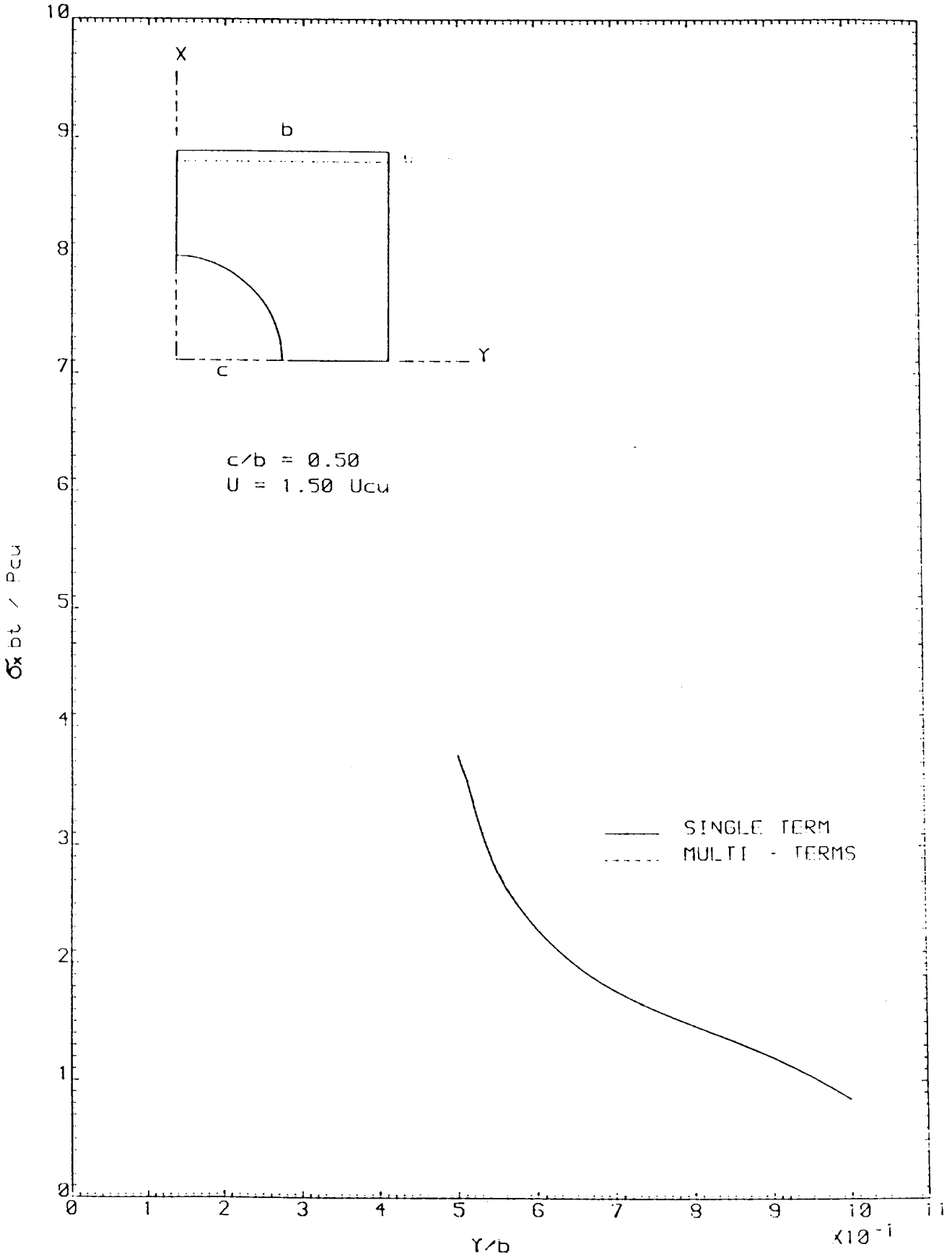

FIGURE 6·53 STRESSES AT THE MINIMUM SECTION

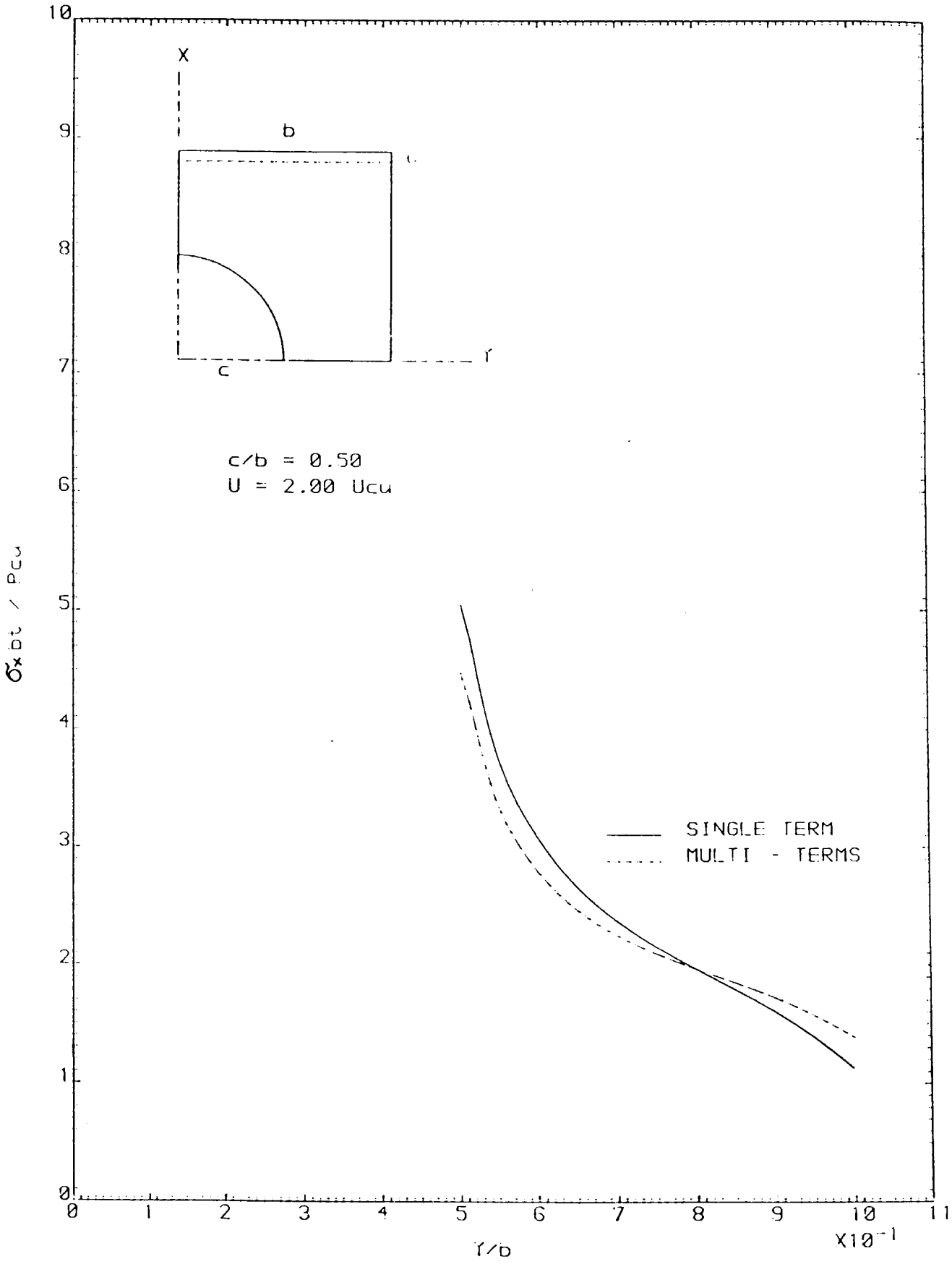

FIGURE 6·54 STRESSES AT THE MINIMUM SECTION

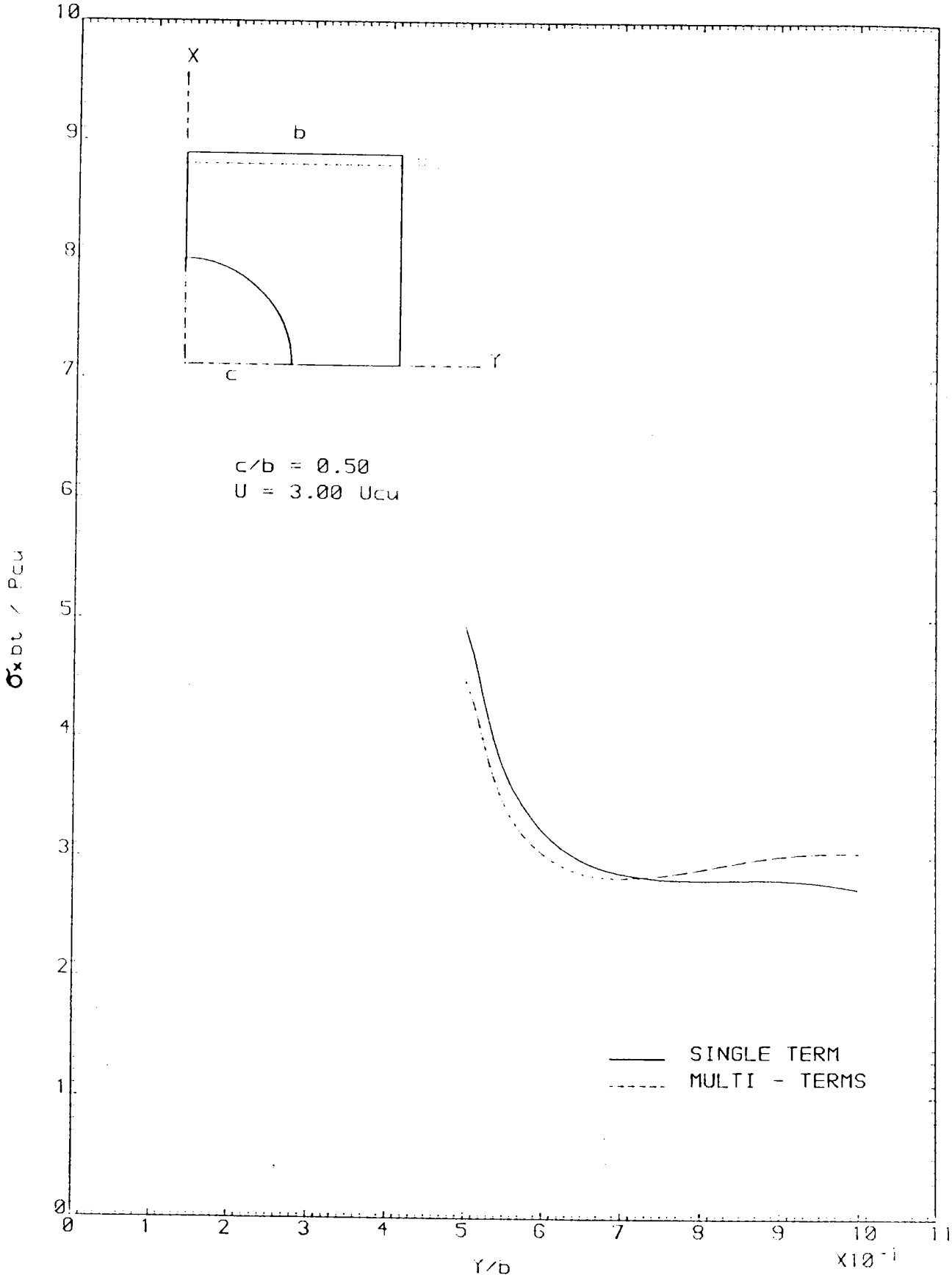

FIGURE 6·55 STRESSES AT THE MINIMUM SECTION

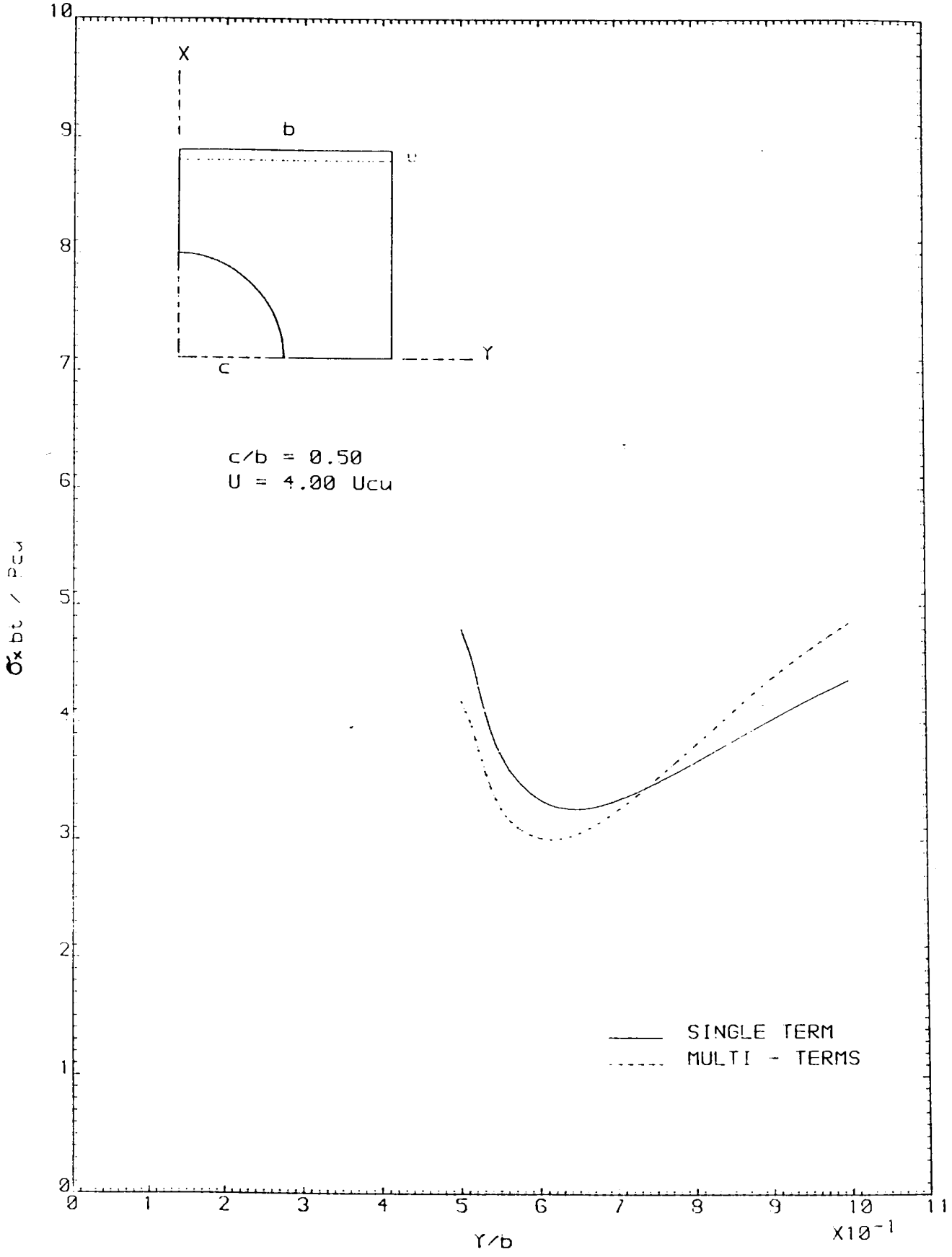

FIGURE 6·56 STRESSES AT THE MINIMUM SECTION

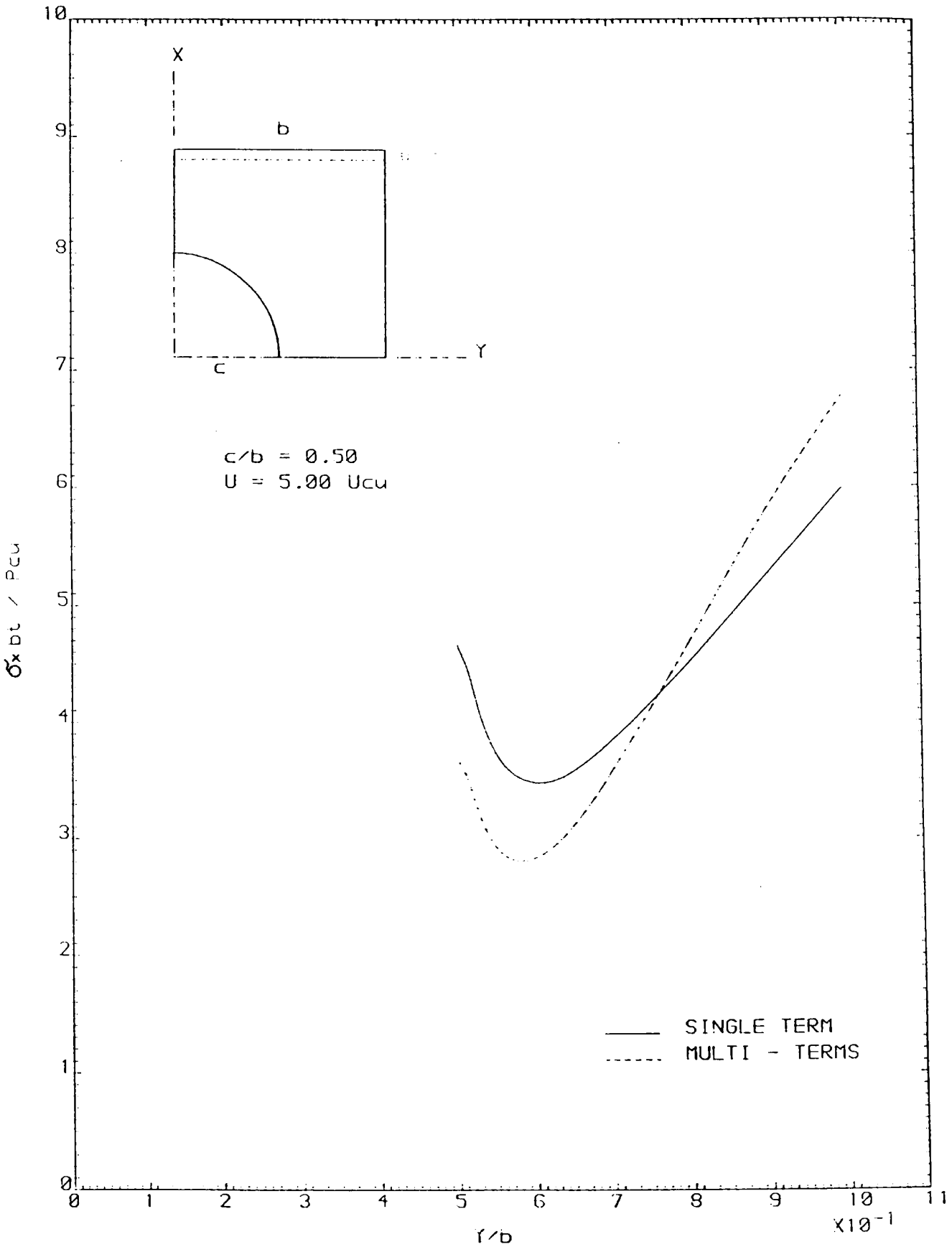

FIGURE 6·57 STRESSES AT THE MINIMUM SECTION

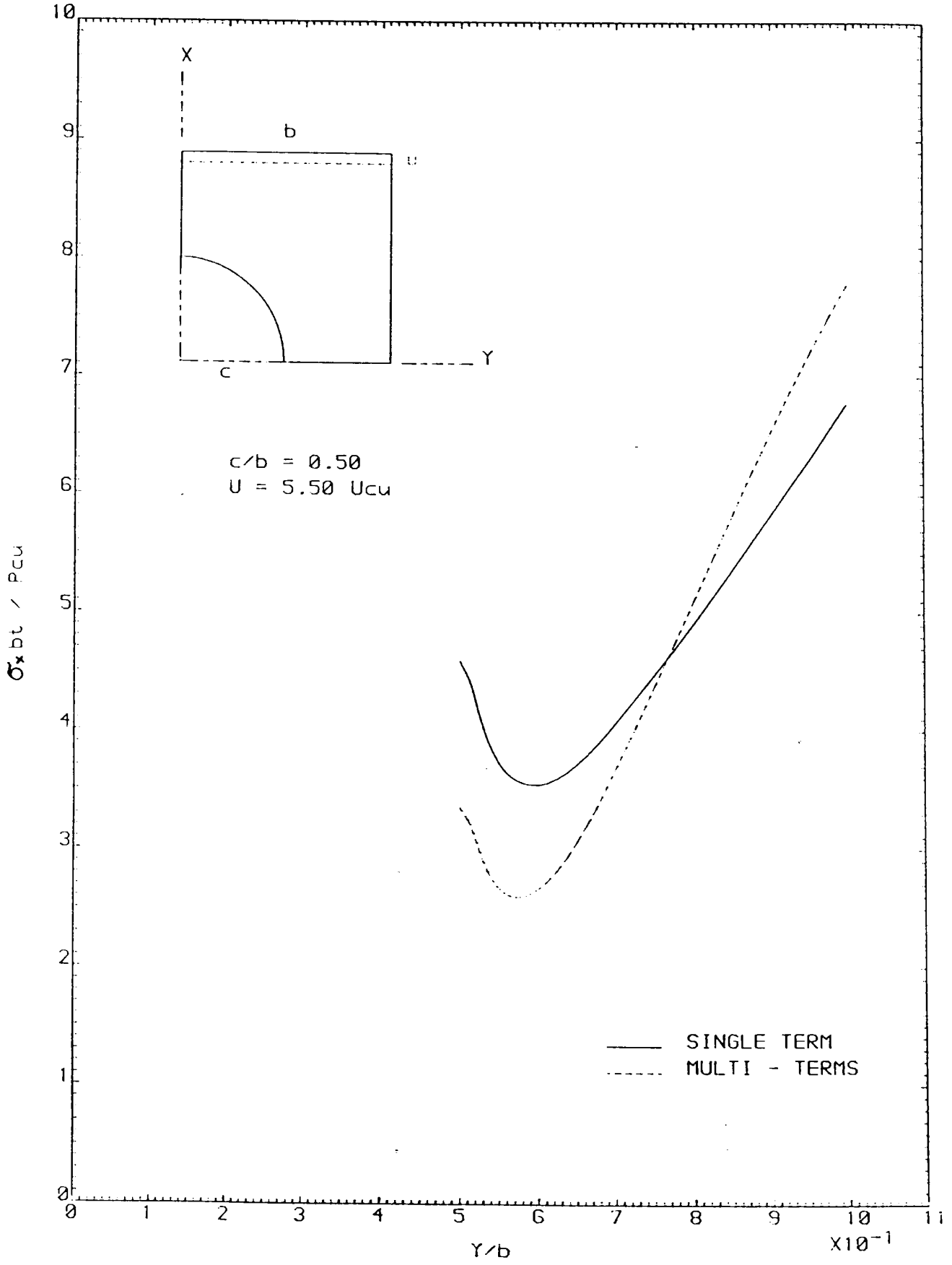

FIGURE 6·58 STRESSES AT THE MINIMUM SECTION

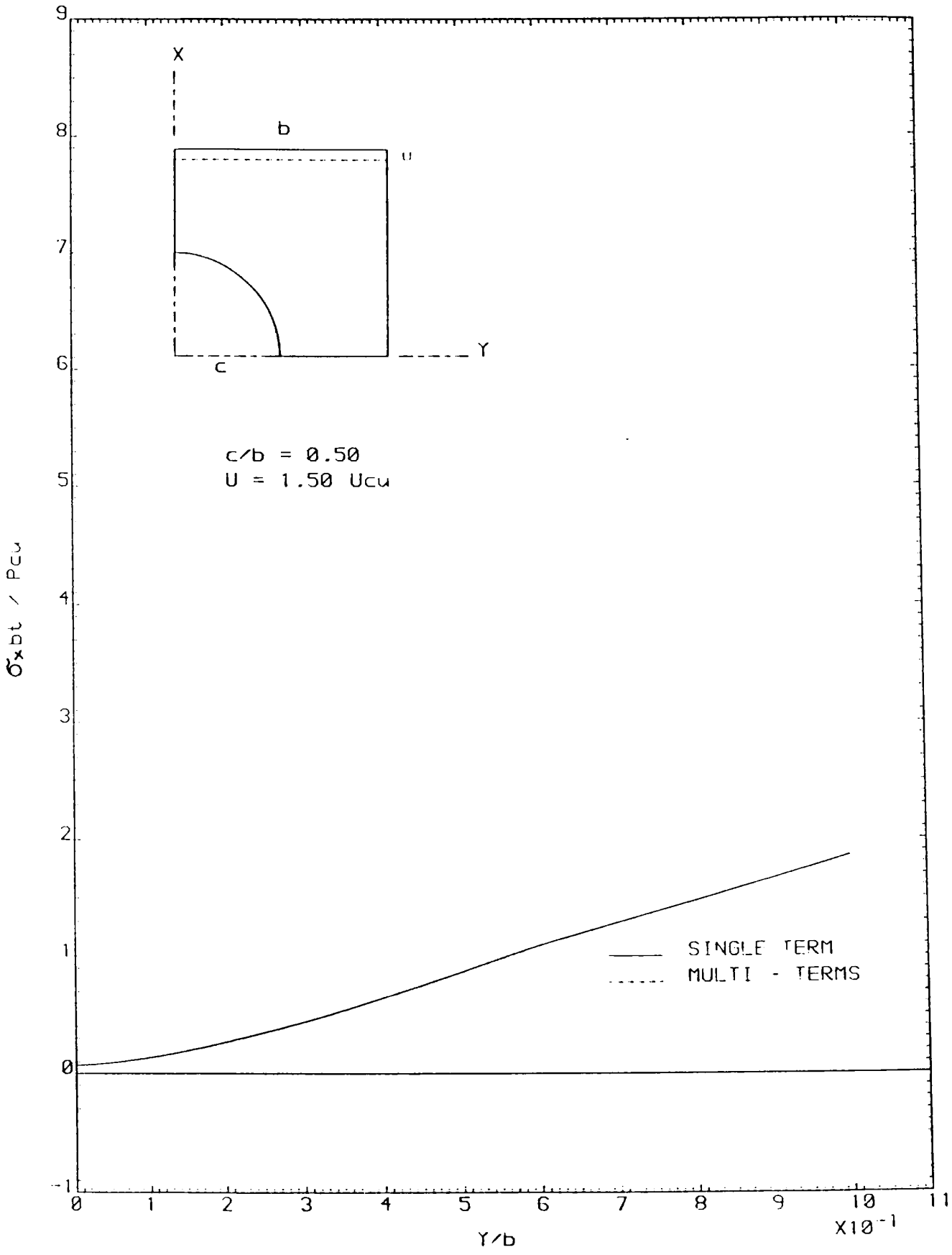

FIGURE 6·59 STRESSES AT THE LOADED EDGE

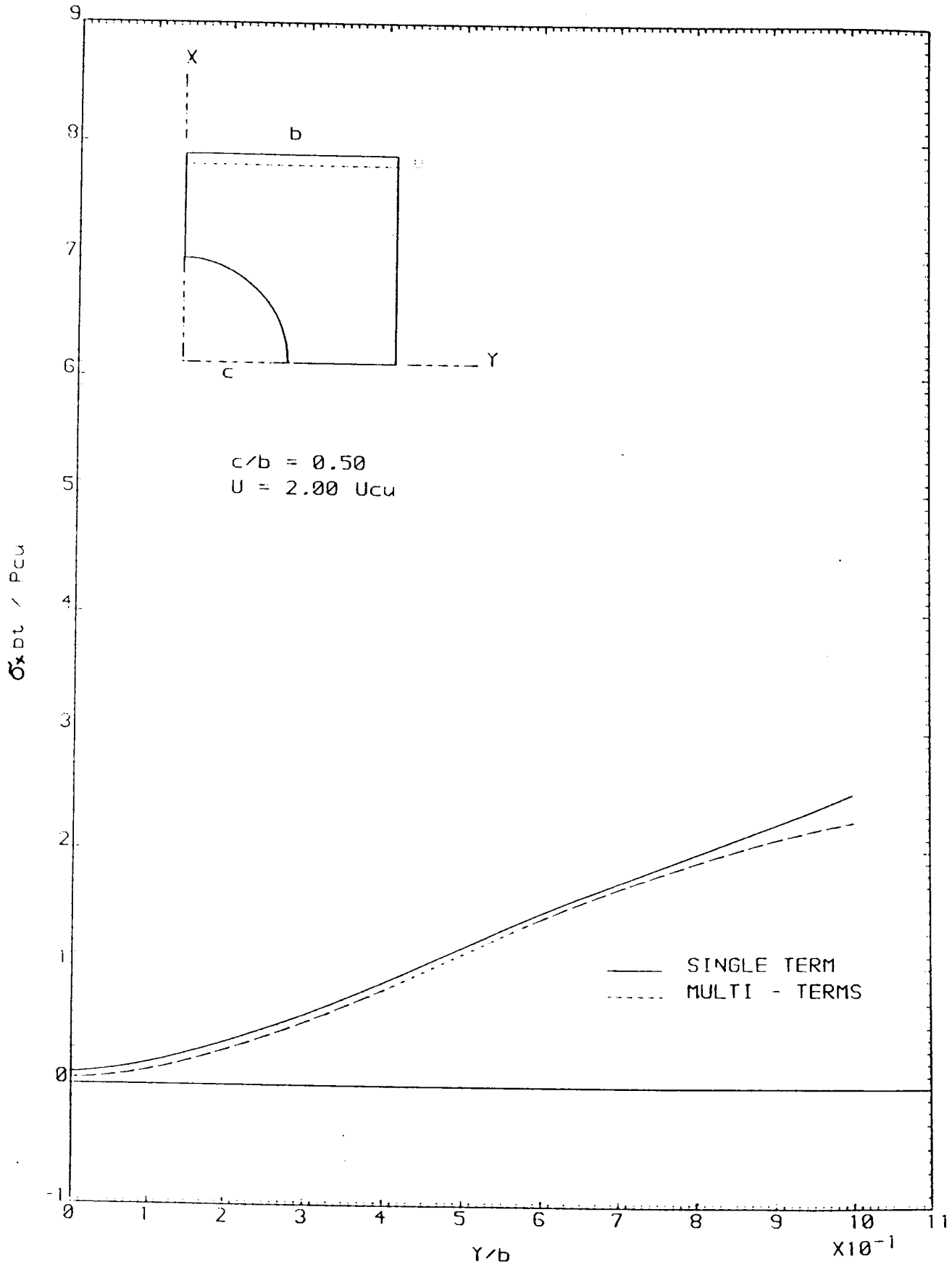

FIGURE 6·60 STRESSES AT THE LOADED EDGE

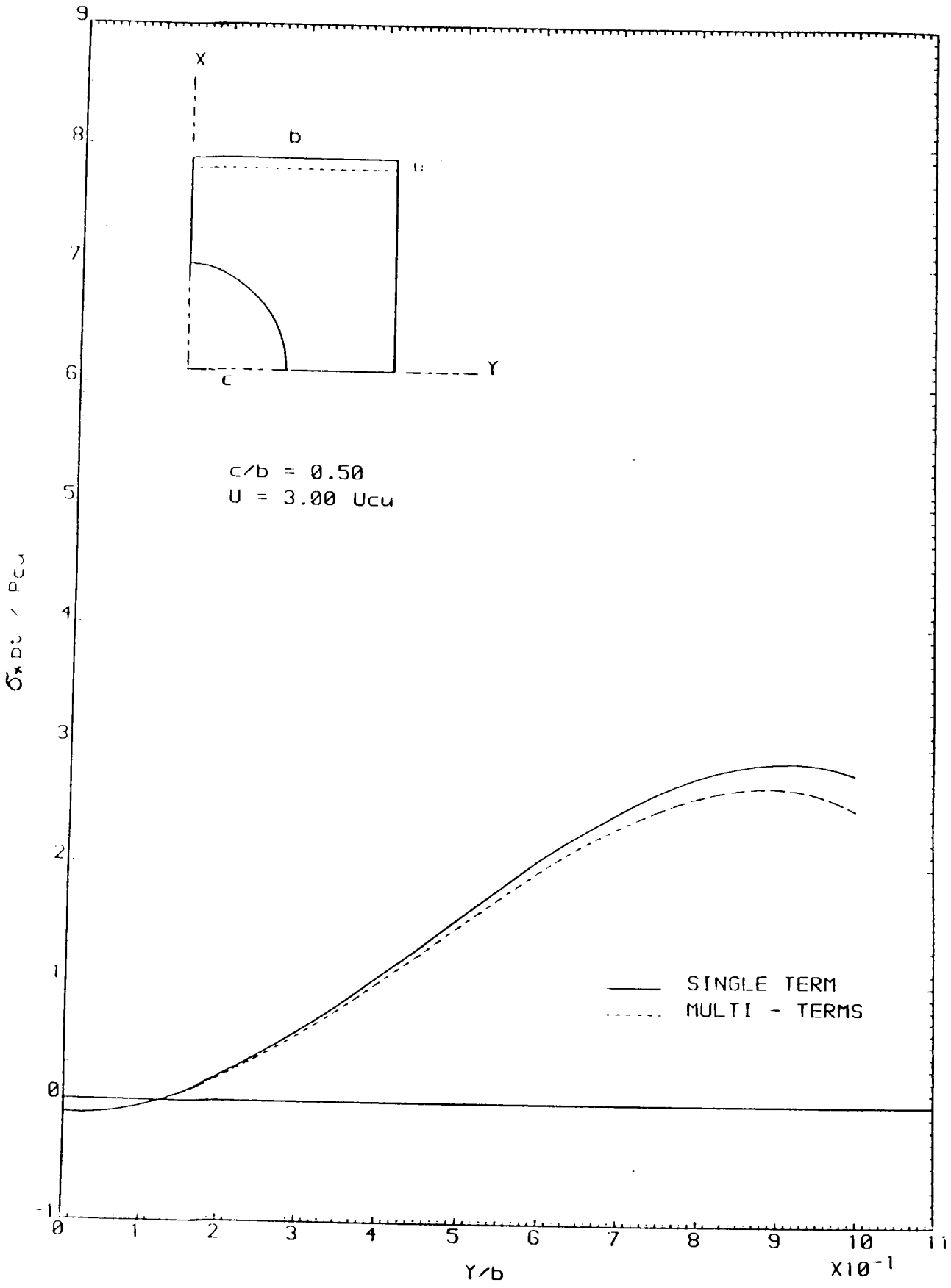

FIGURE 6·61 STRESSES AT THE LOADED EDGE

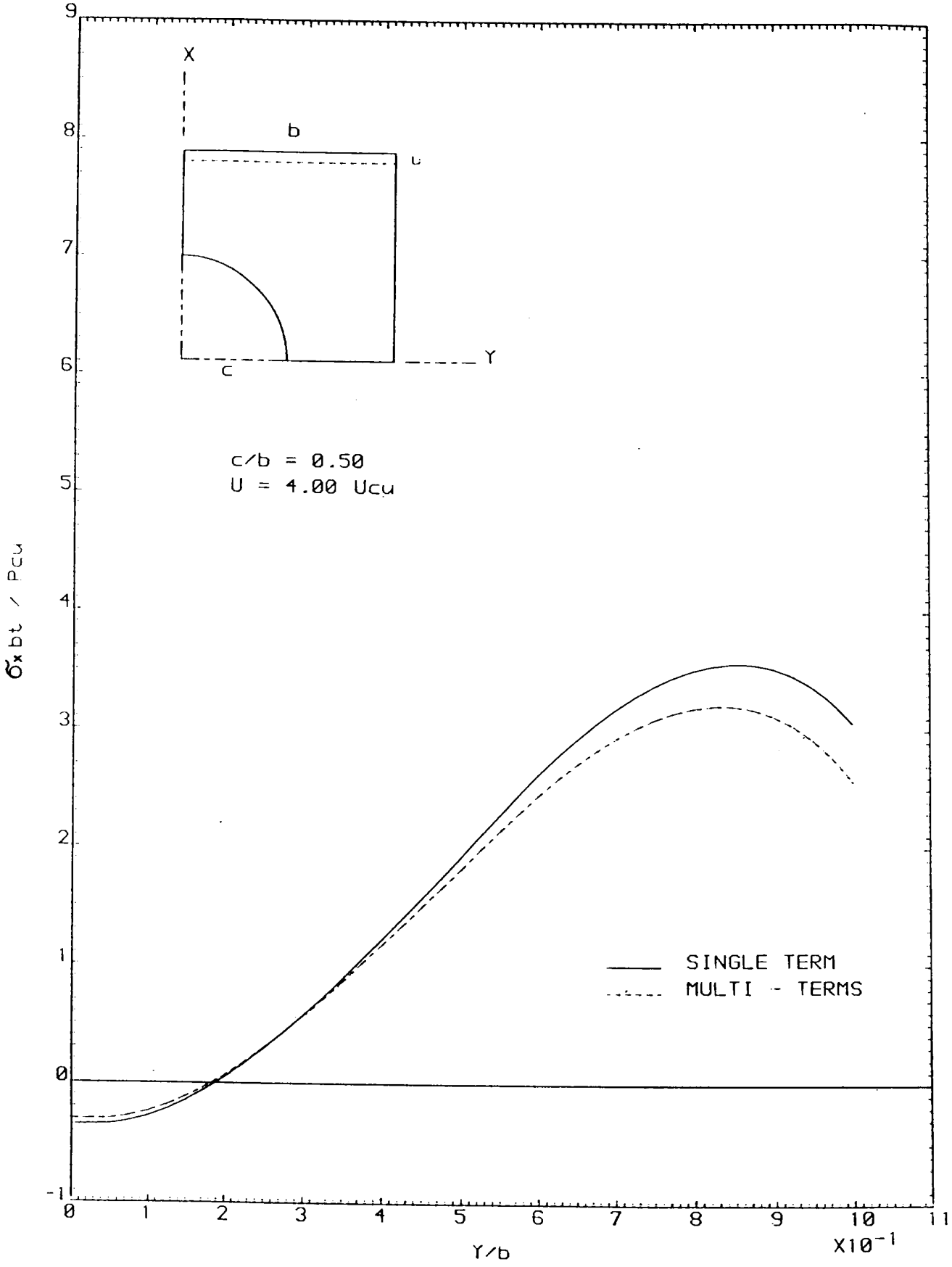

FIGURE 6·62 STRESSES AT THE LOADED EDGE

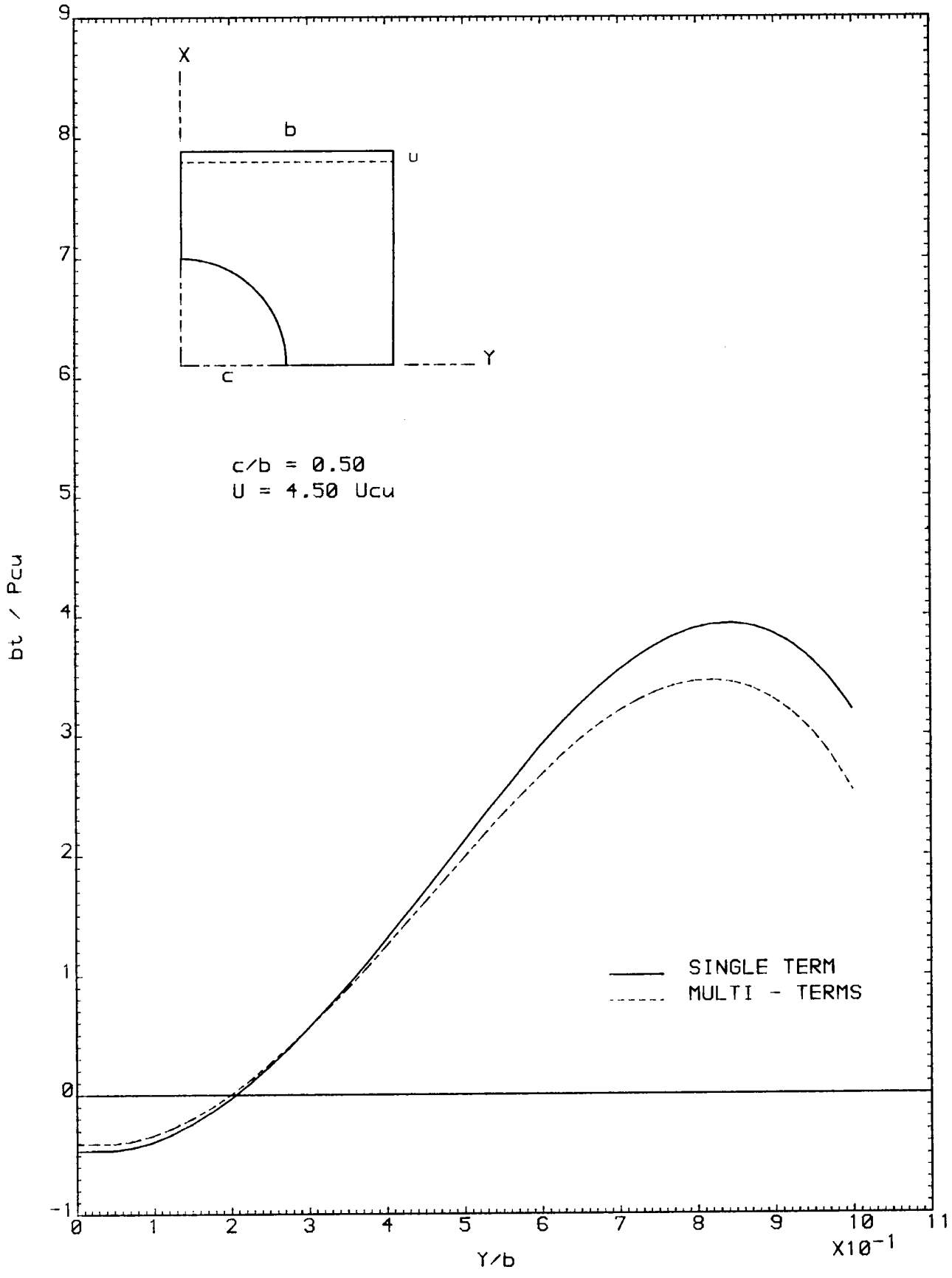

FIGURE 6.62 a STRESSES AT THE LOADED EDGE

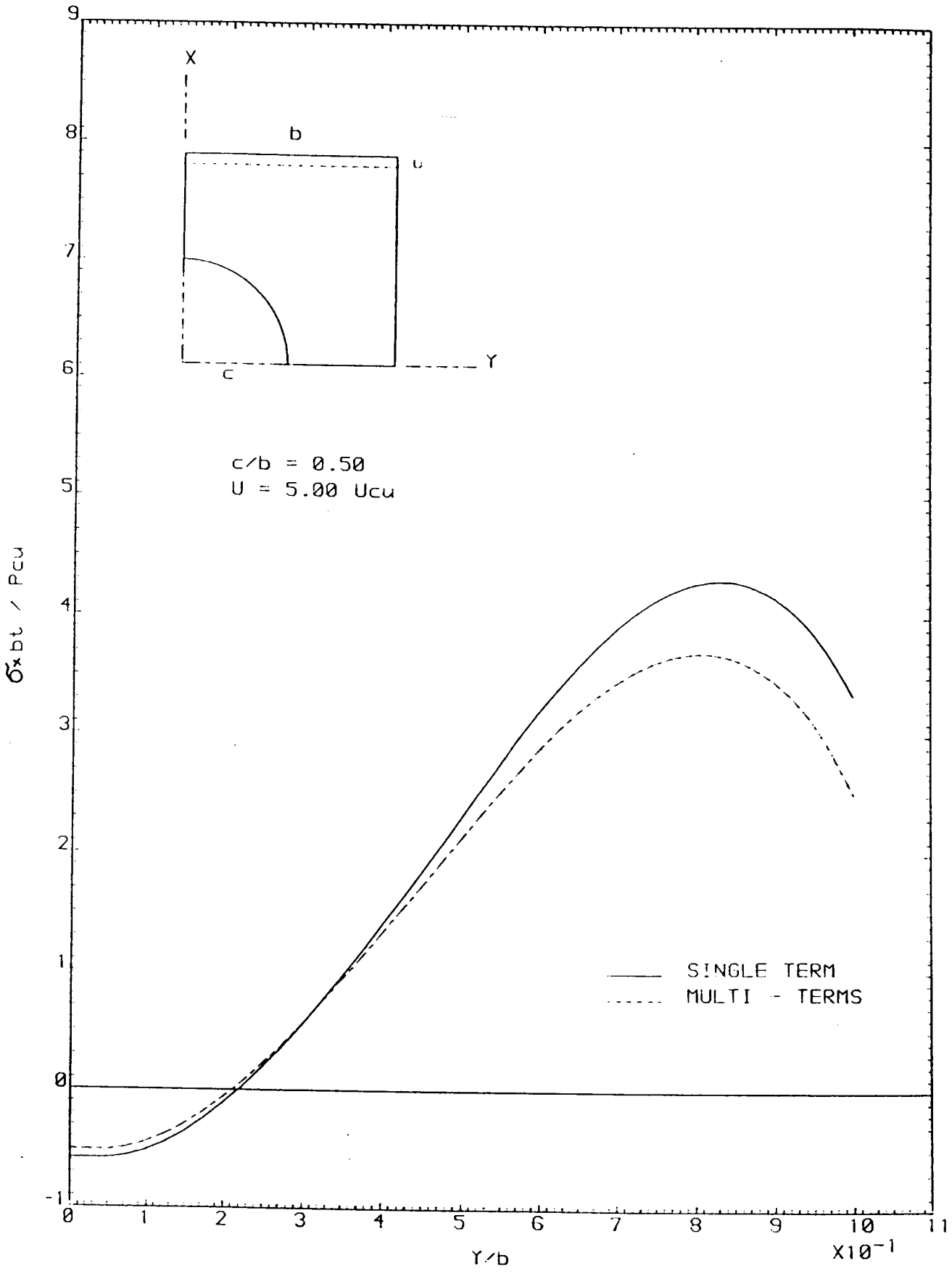

FIGURE 6·63 STRESSES AT THE LOADED EDGE

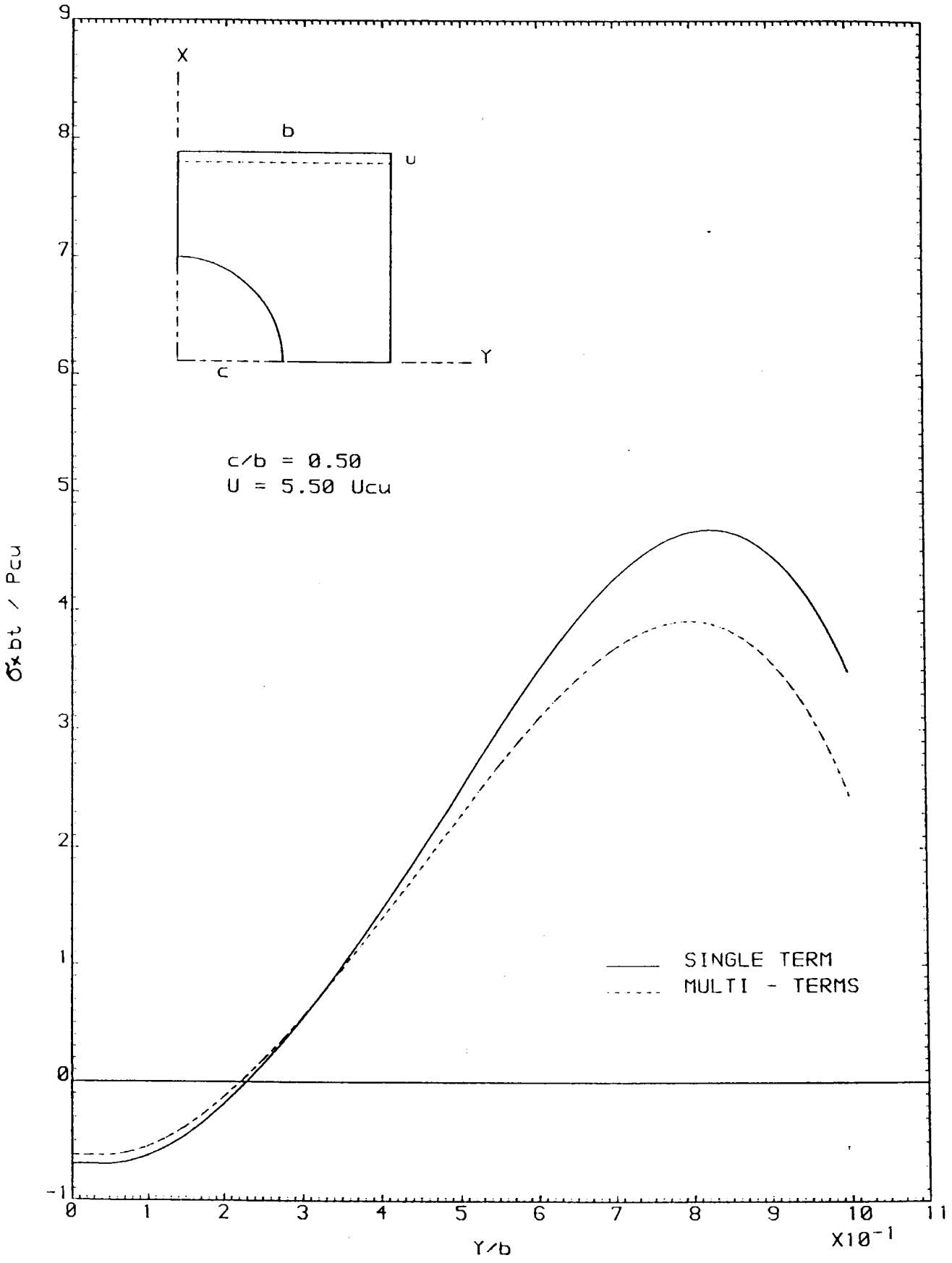

FIGURE 6·64 STRESSES AT THE LOADED EDGE

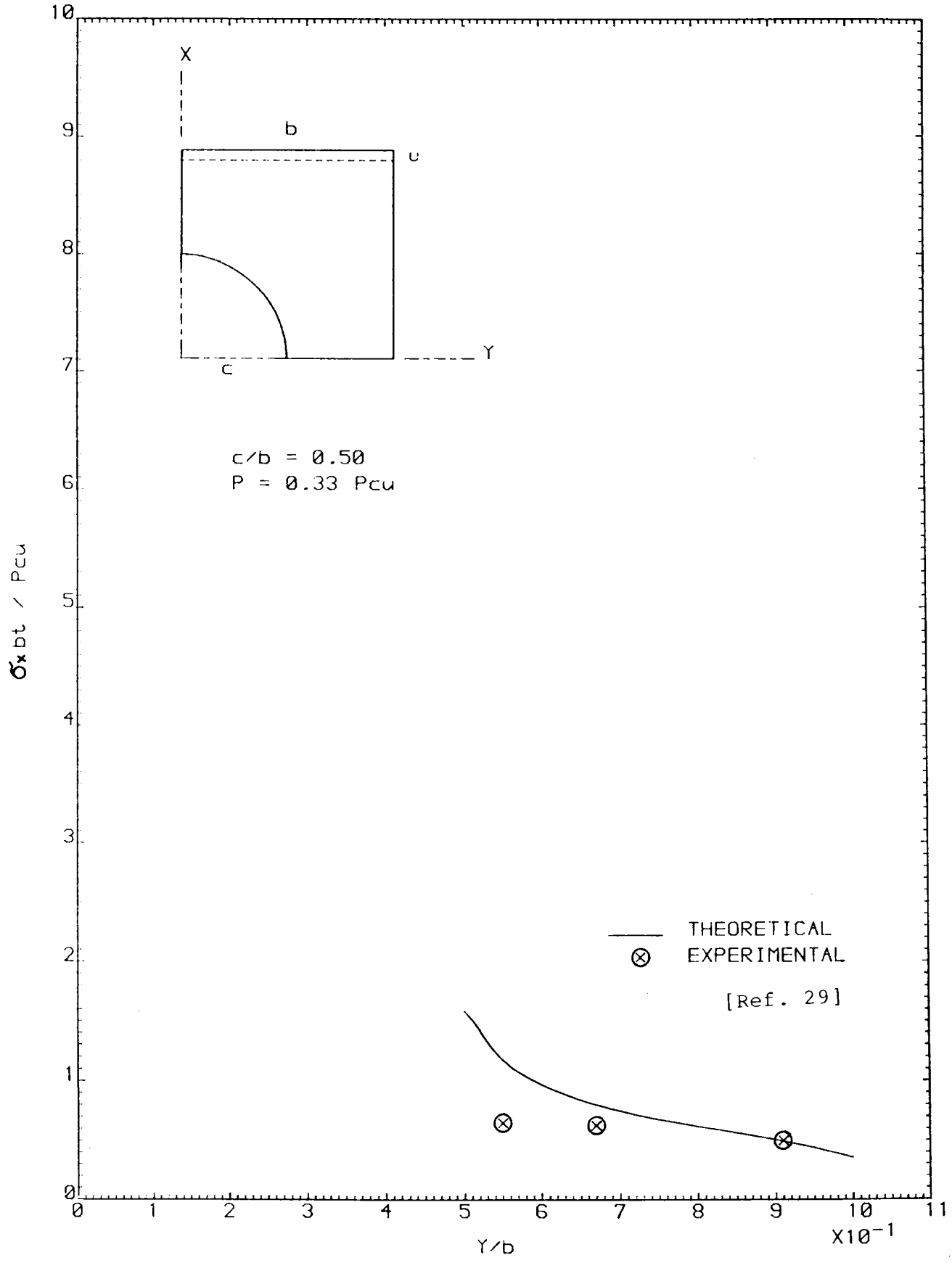

FIGURE 6·65 STRESSES AT THE MINIMUM SECTION

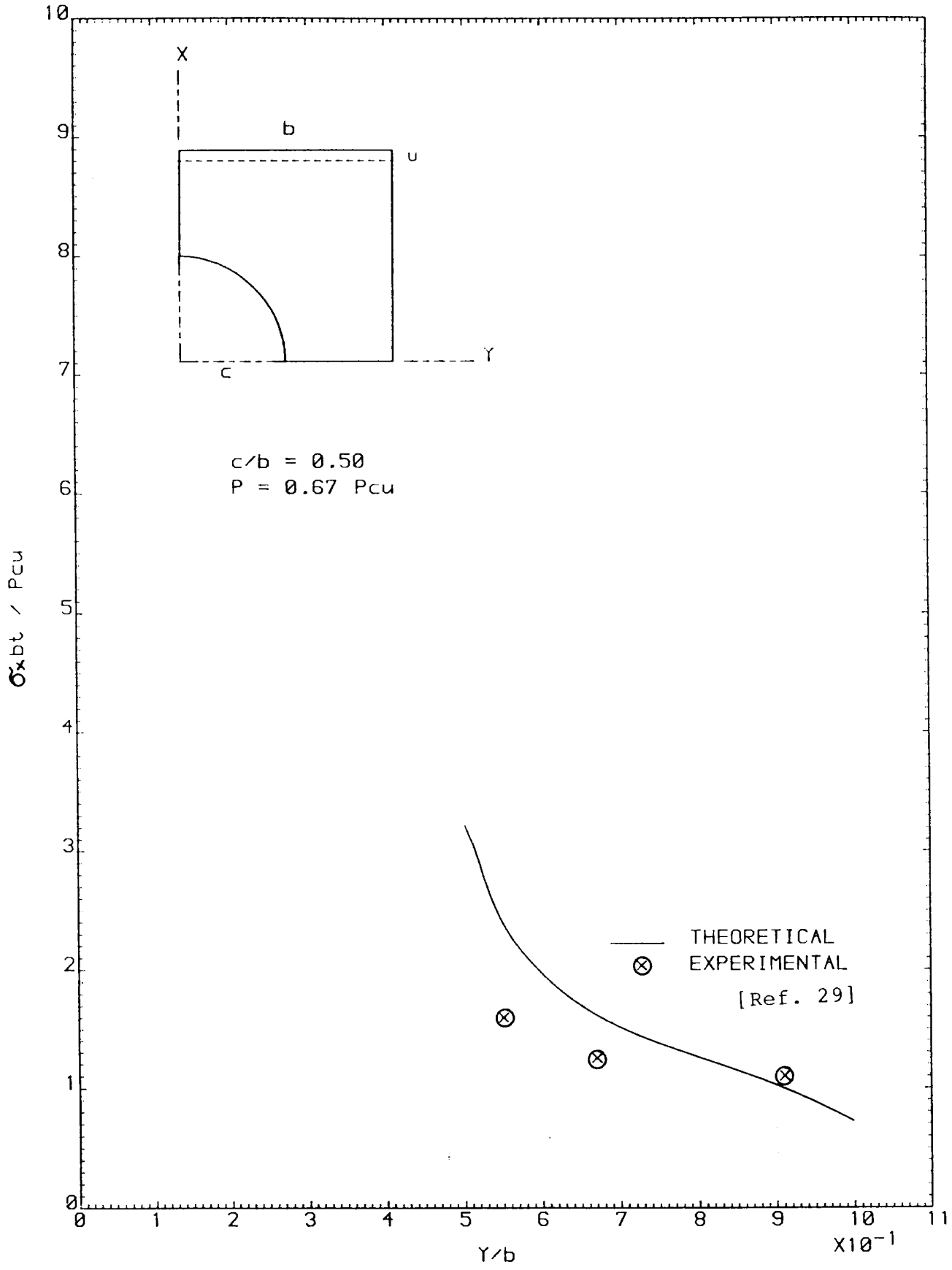

FIGURE 6·66 STRESSES AT THE MINIMUM SECTION

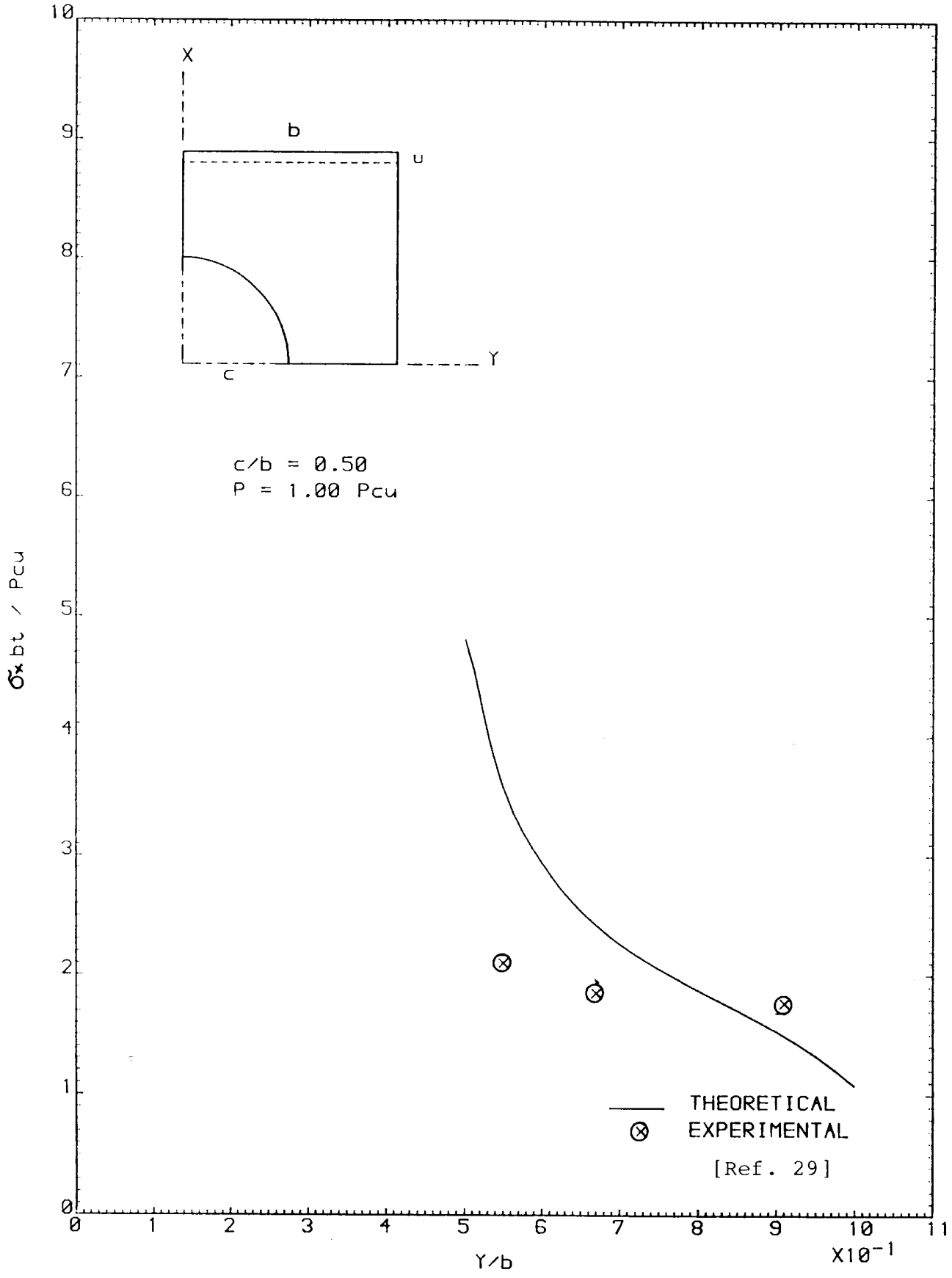

FIGURE 6·67 STRESSES AT THE MINIMUM SECTION

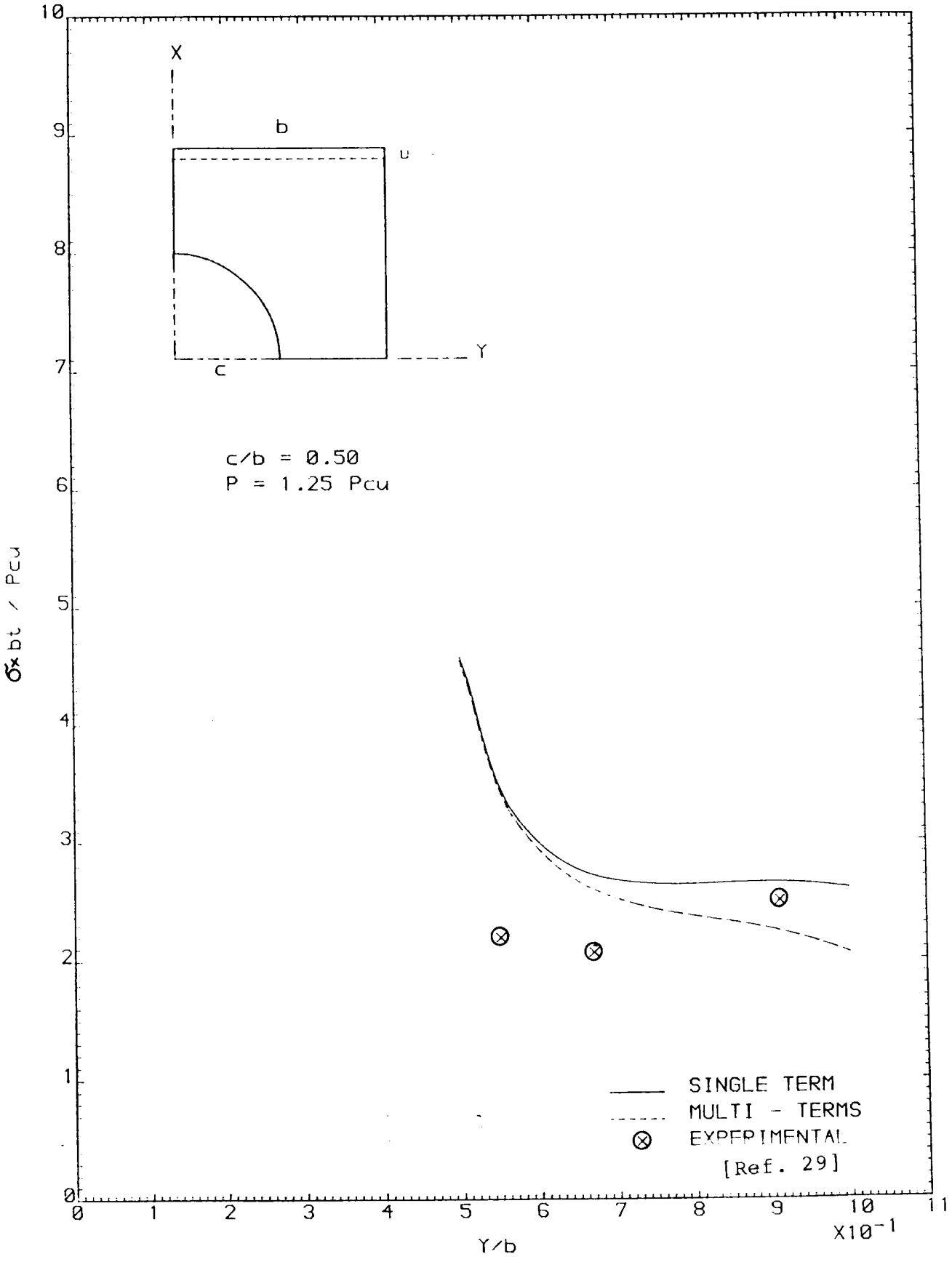

FIGURE 6·68 STRESSES AT THE MINIMUM SECTION

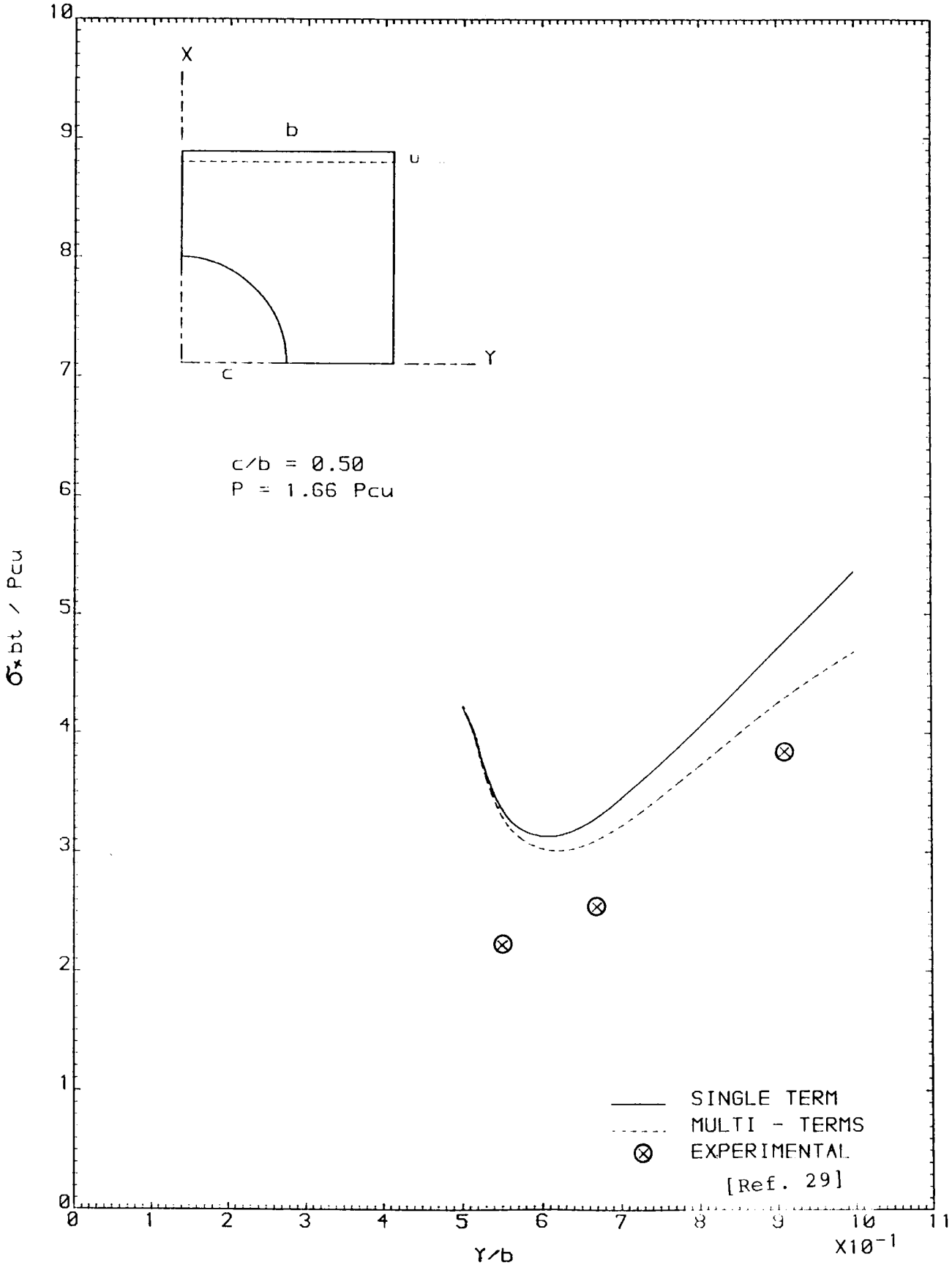

FIGURE 6·69 STRESSES AT THE MINIMUM SECTION

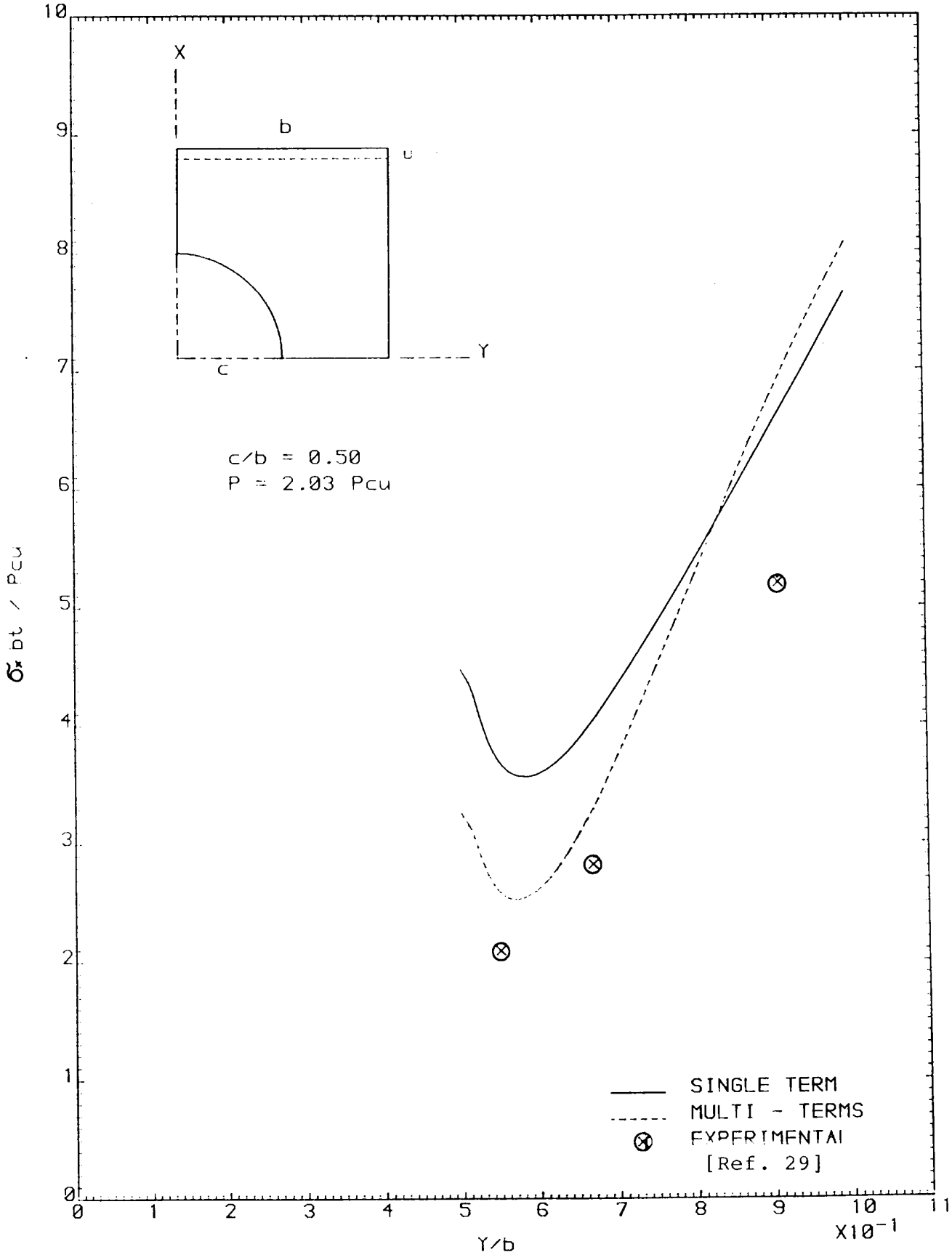

FIGURE 6·70 STRESSES AT THE MINIMUM SECTION

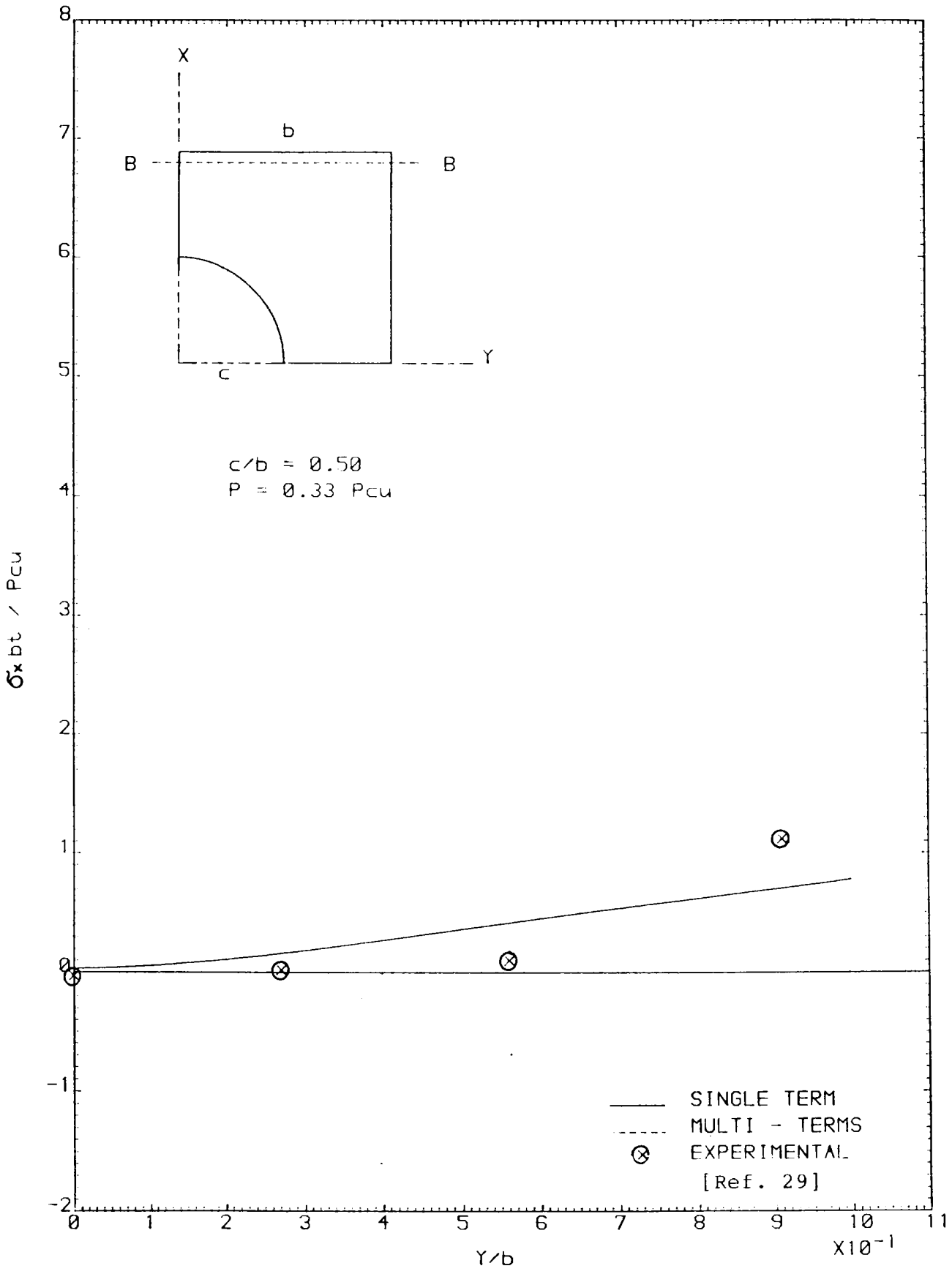

FIGURE 6·71 STRESSES AT SECTION B - B

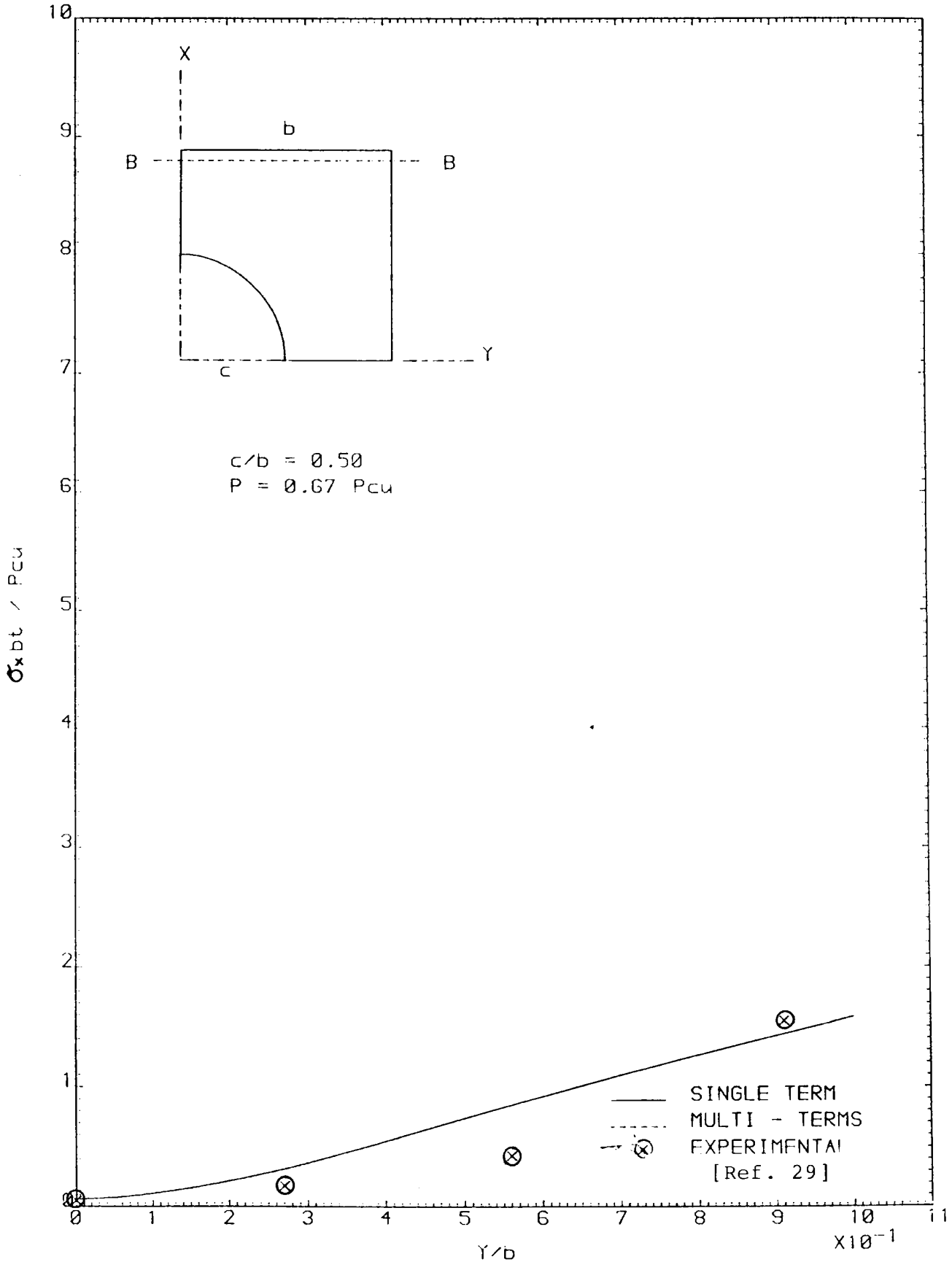

FIGURE 6·72 STRESSES AT SECTION B - B

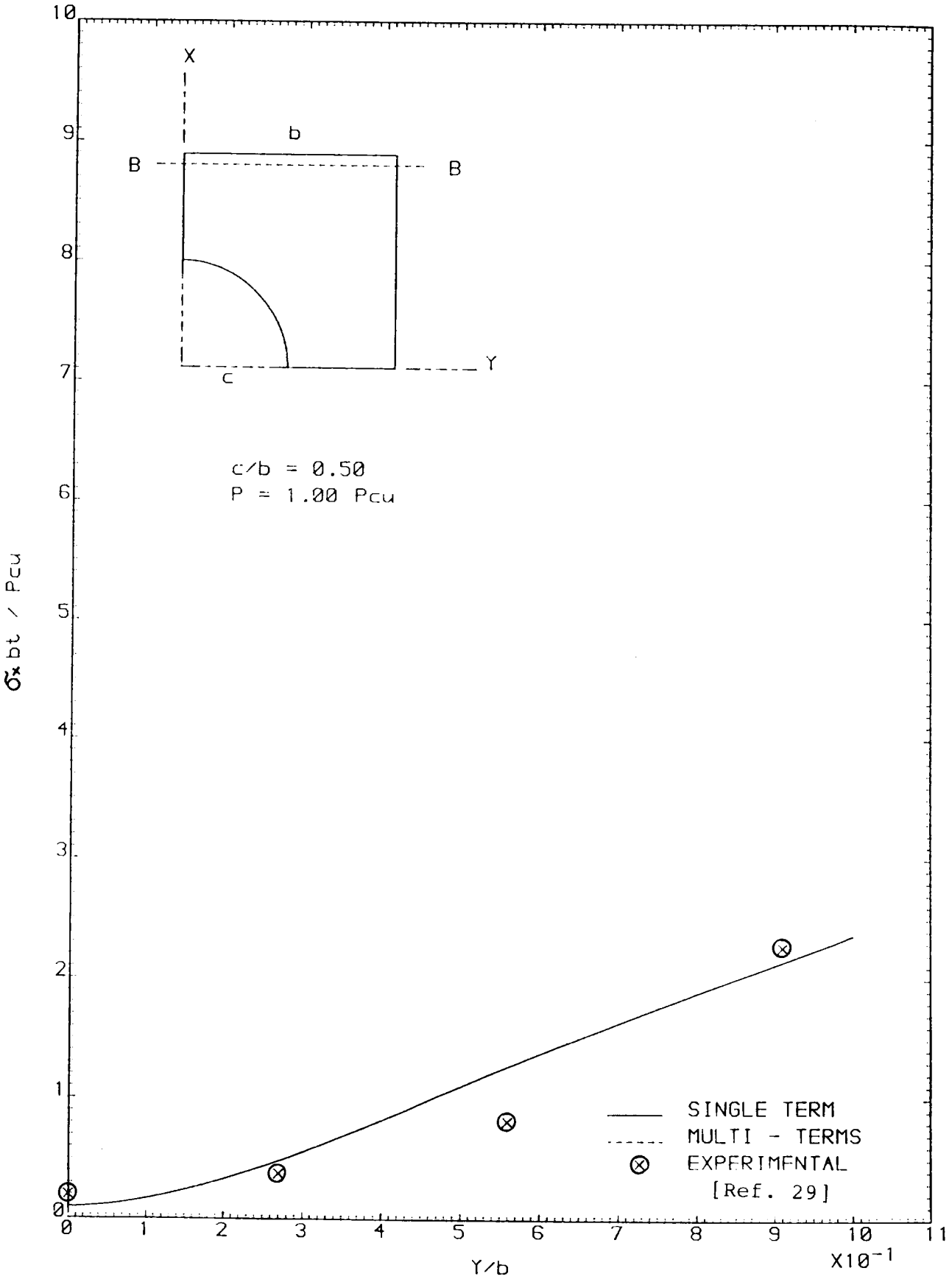

FIGURE 6·73 STRESSES AT SECTION B - B

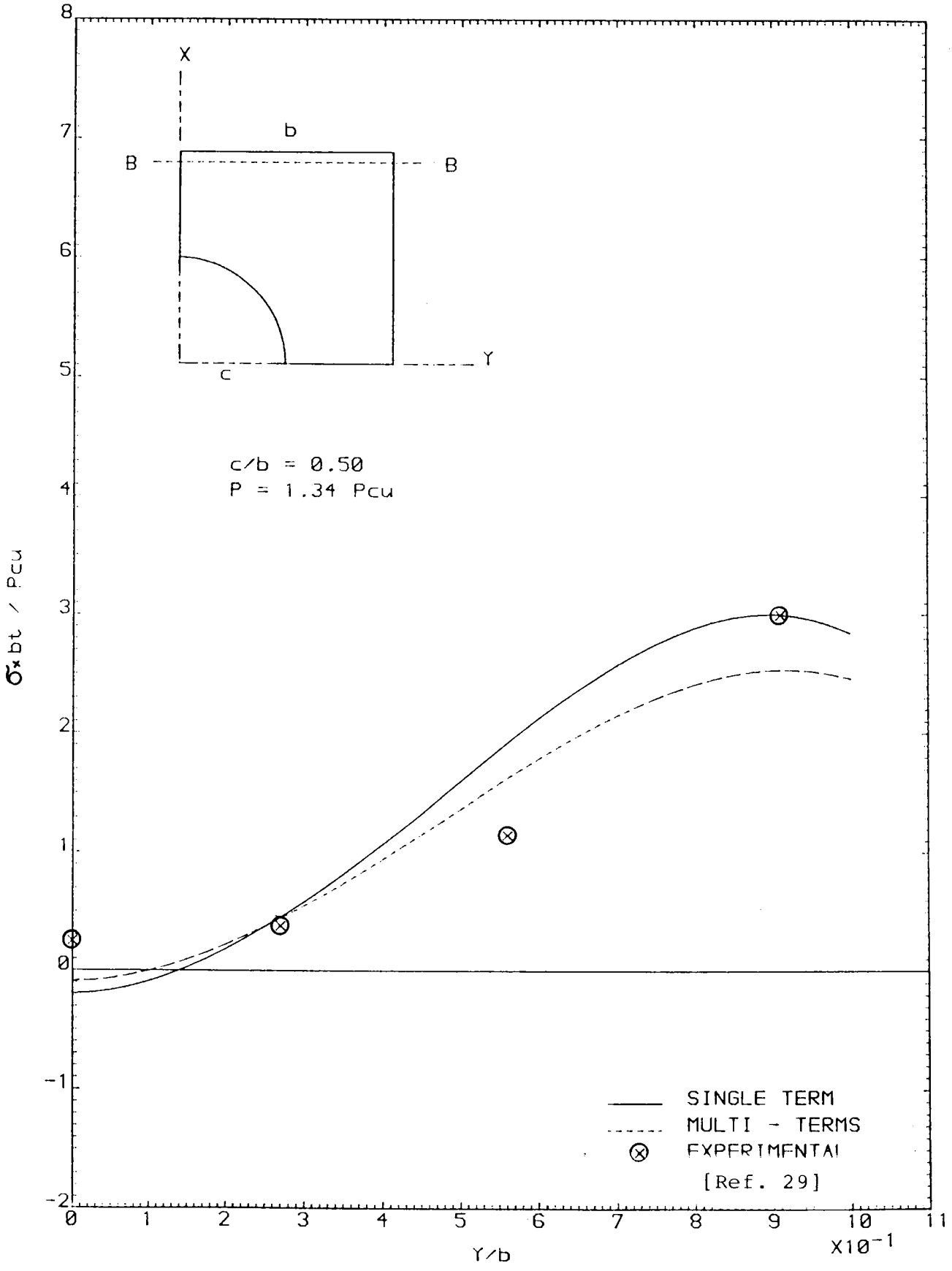

FIGURE 6·74 STRESSES AT SECTION B - B

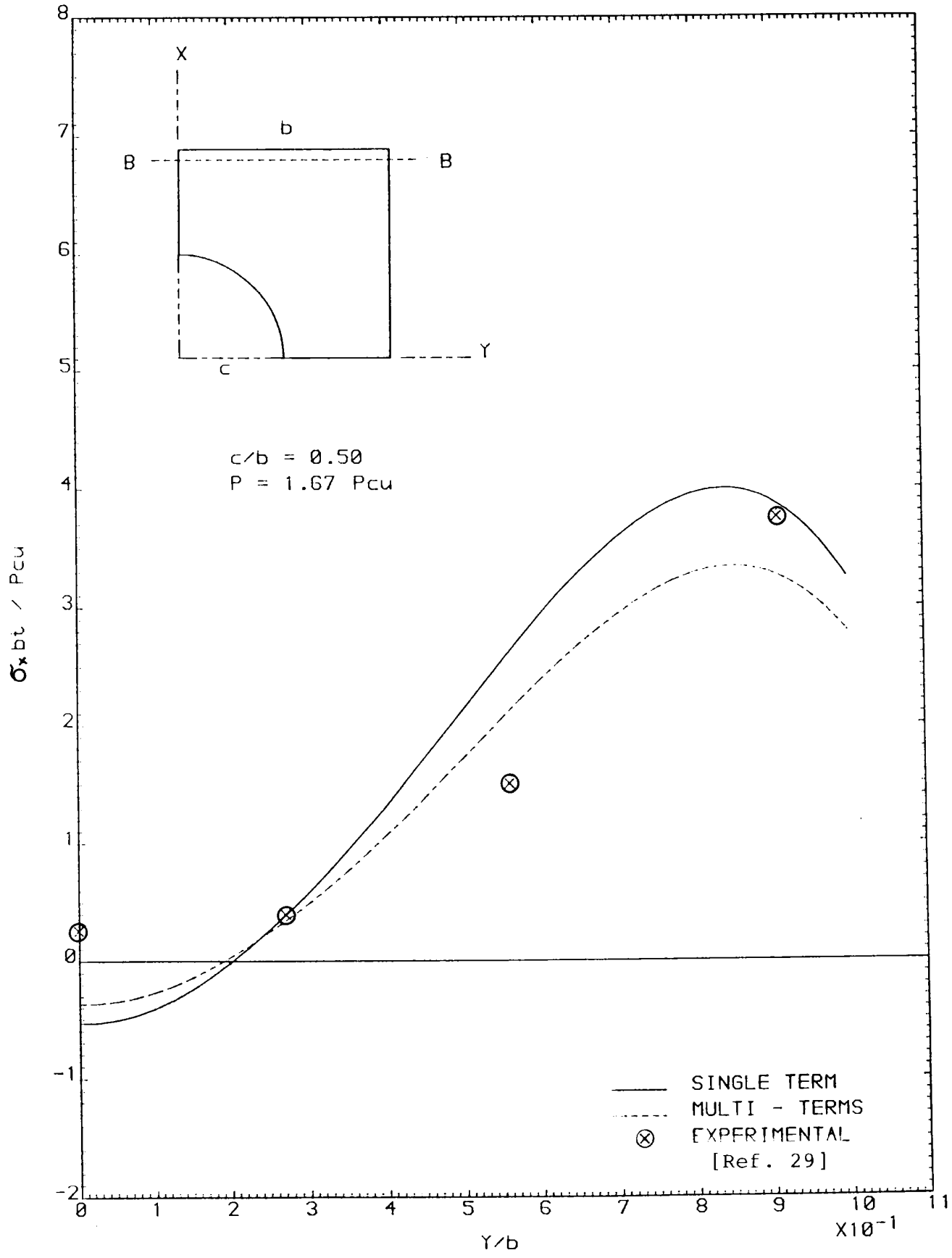

FIGURE 6·75 STRESSES AT SECTION B - B

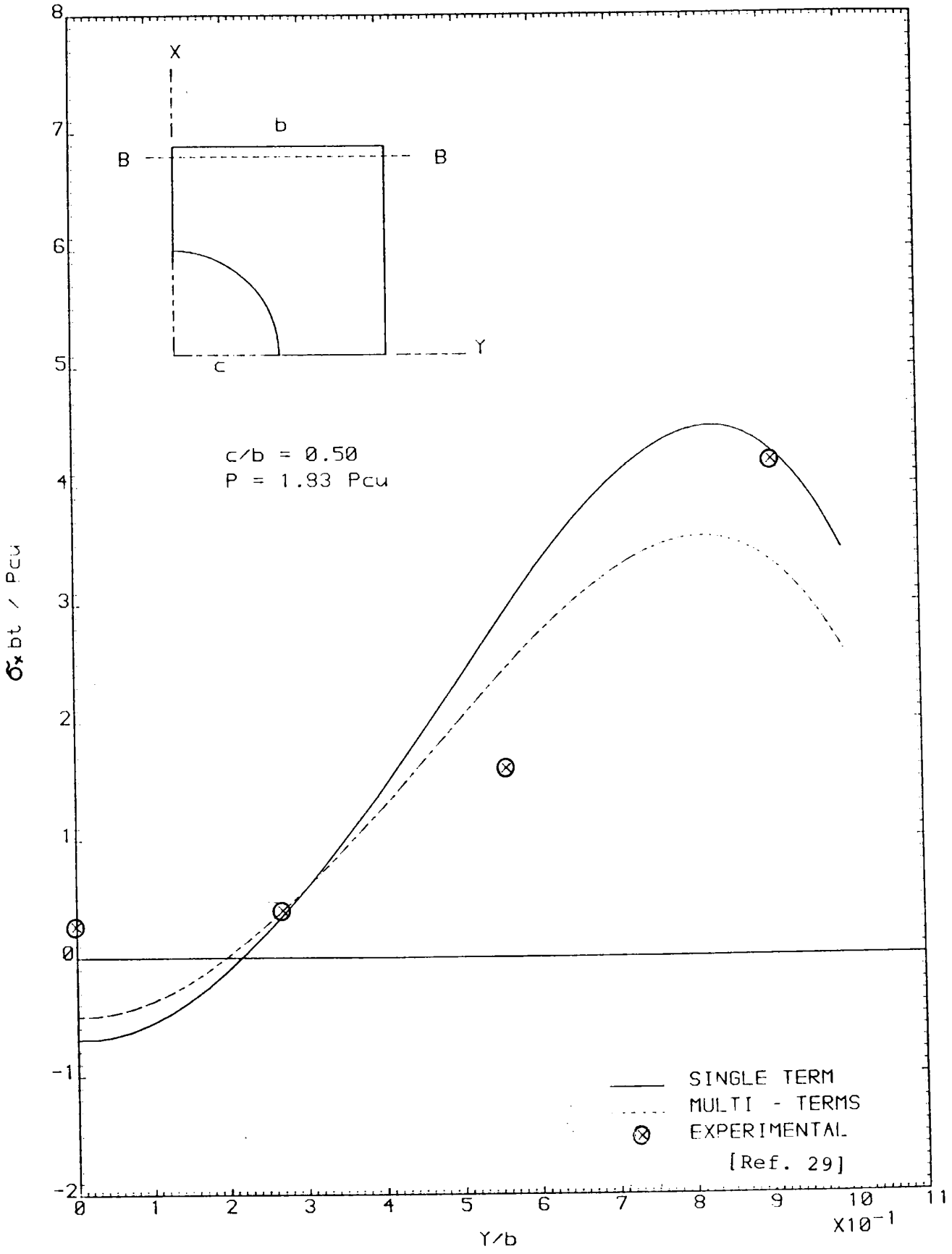

FIGURE 6·76 STRESSES AT SECTION B - B

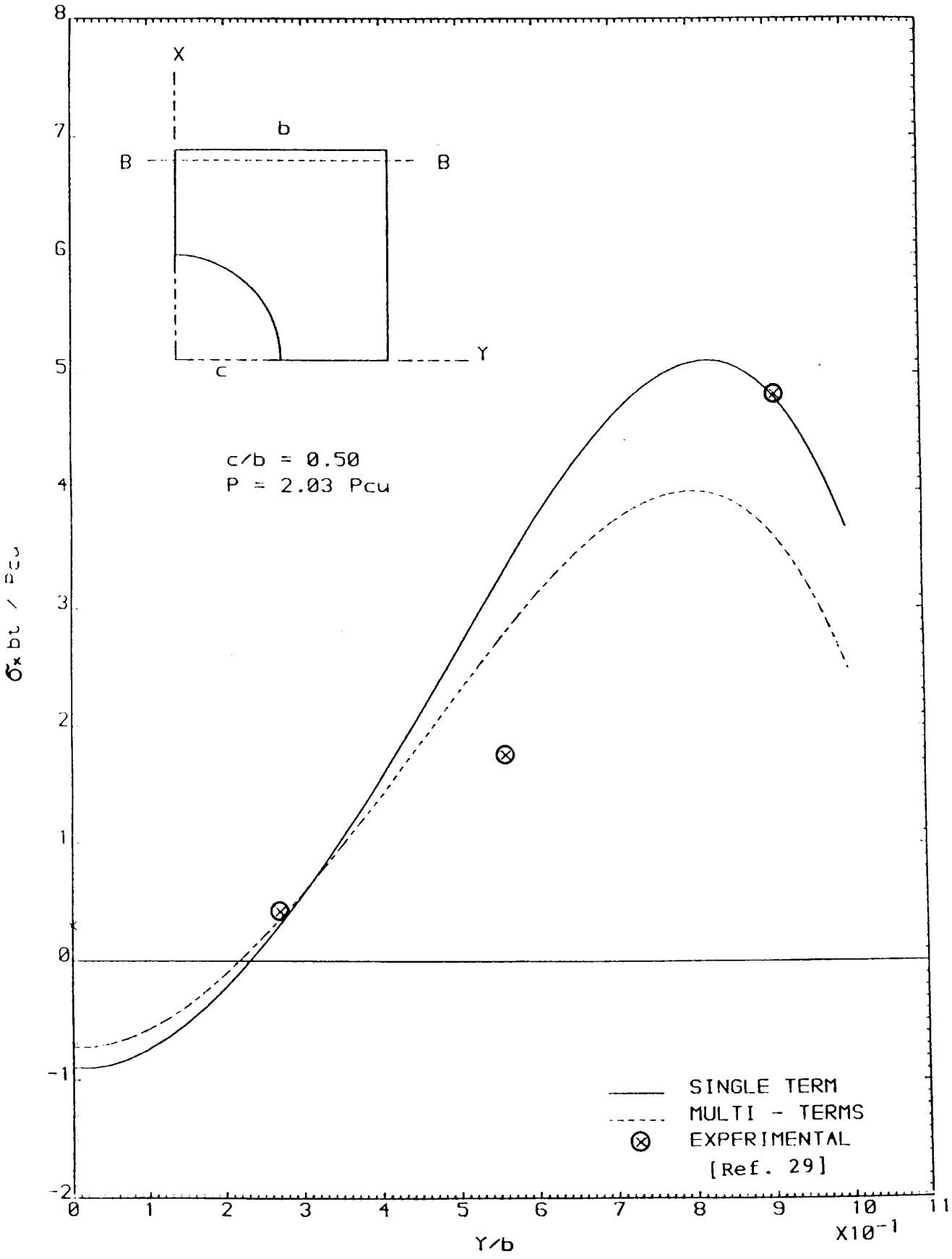

FIGURE 6·77 STRESSES AT SECTION B - B

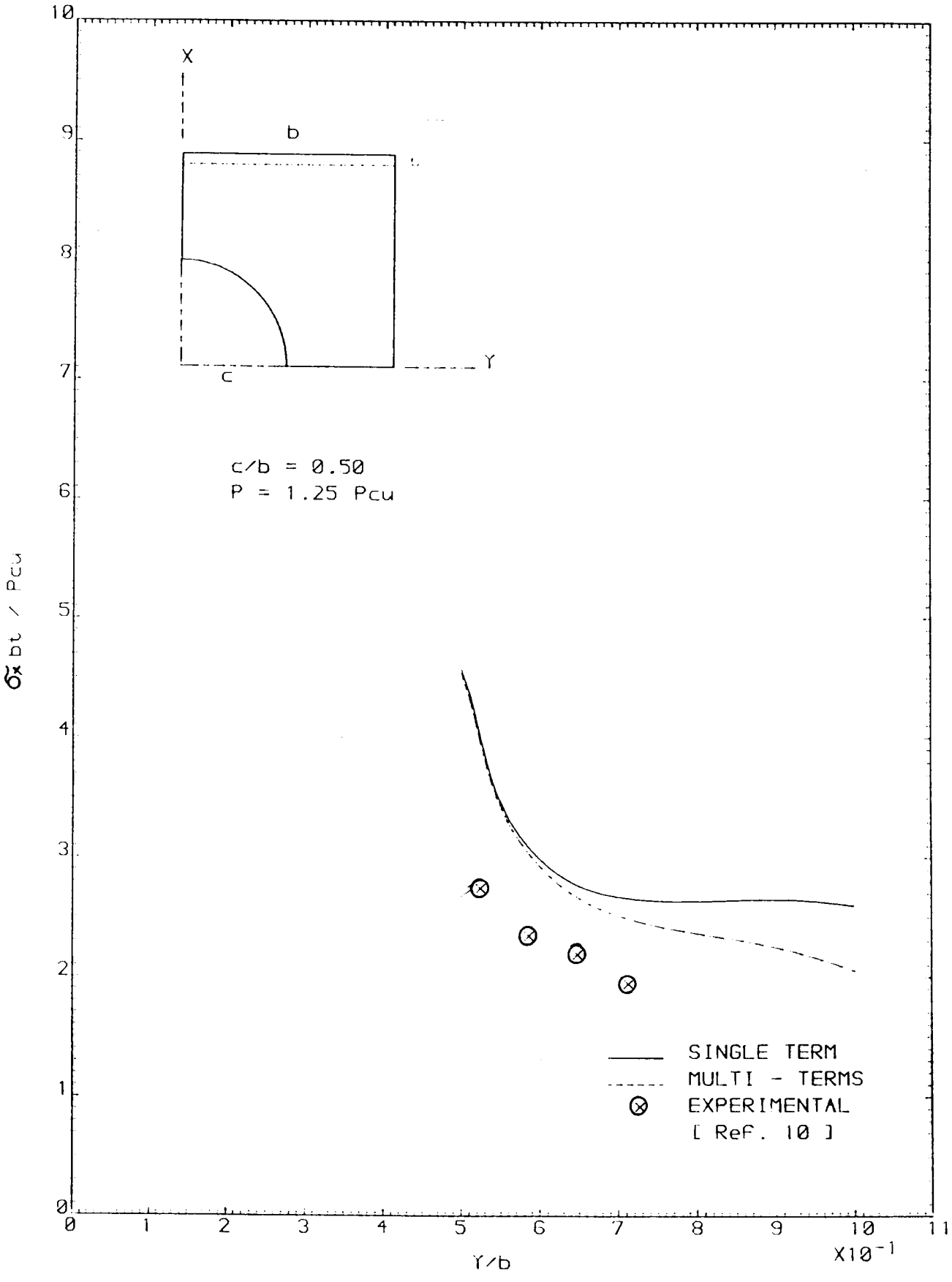

FIGURE 6·78 STRESSES AT THE MINIMUM SECTION

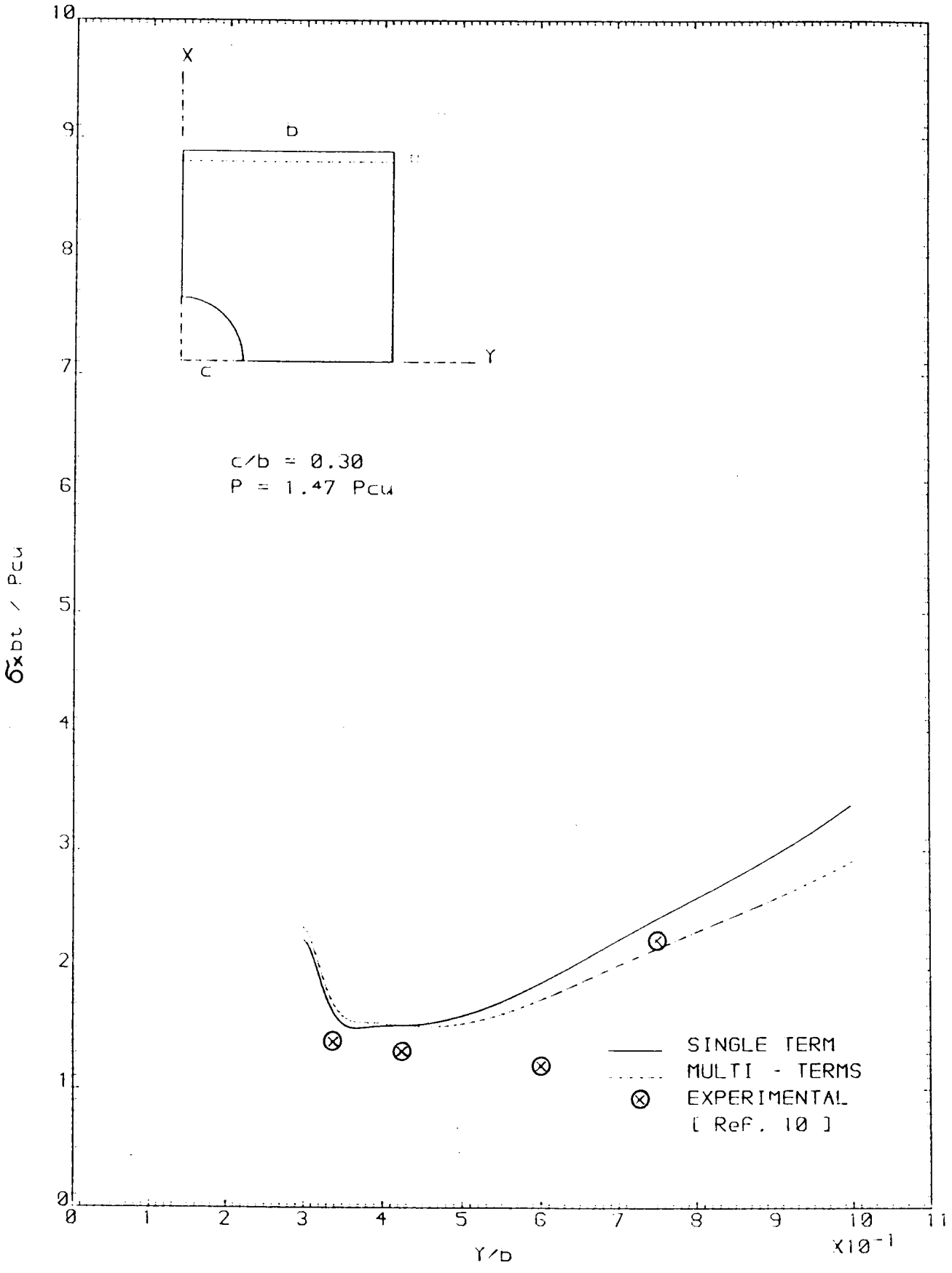

FIGURE 6·79 STRESSES AT THE MINIMUM SECTION

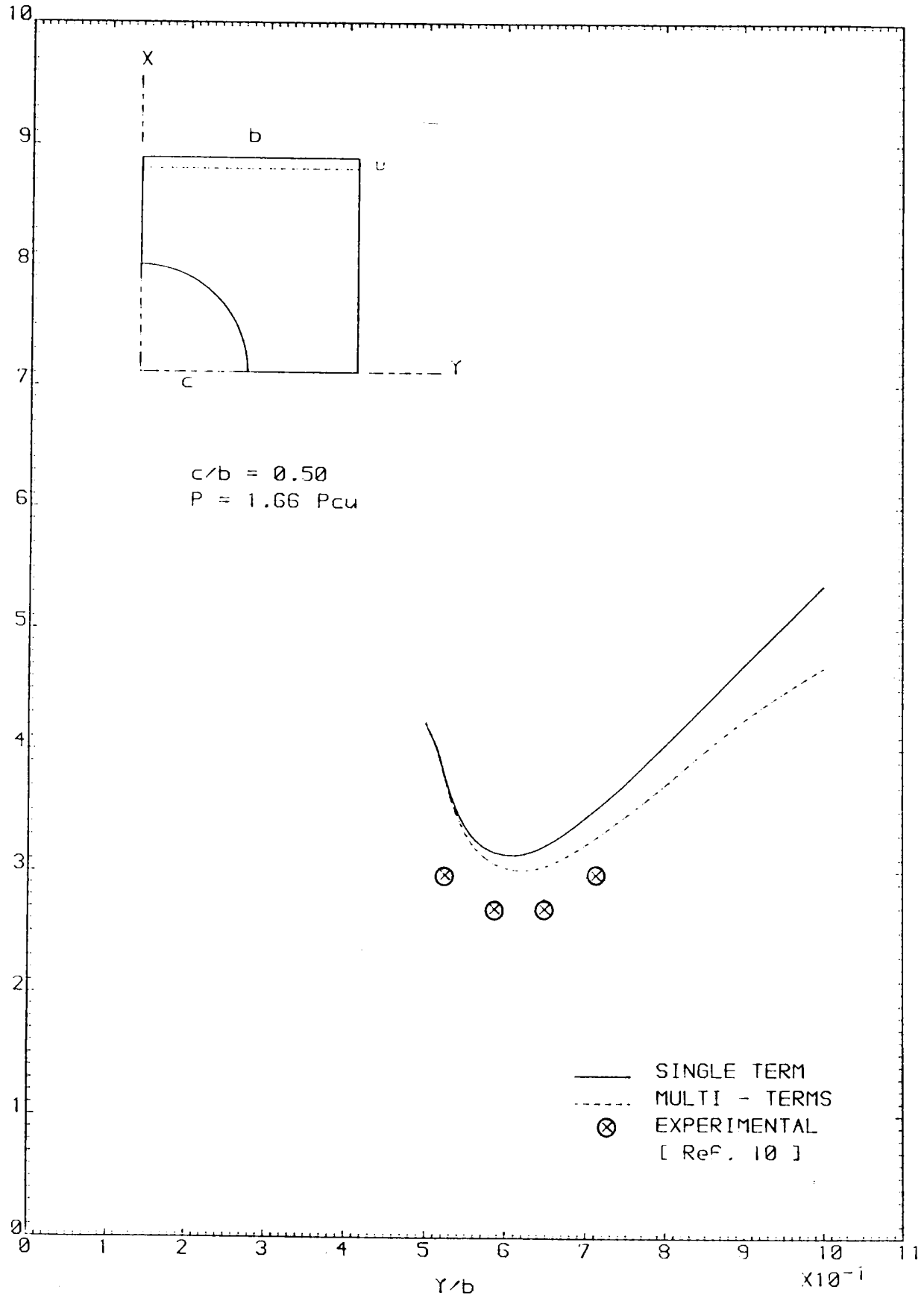

FIGURE 6·80 STRESSES AT THE MINIMUM SECTION

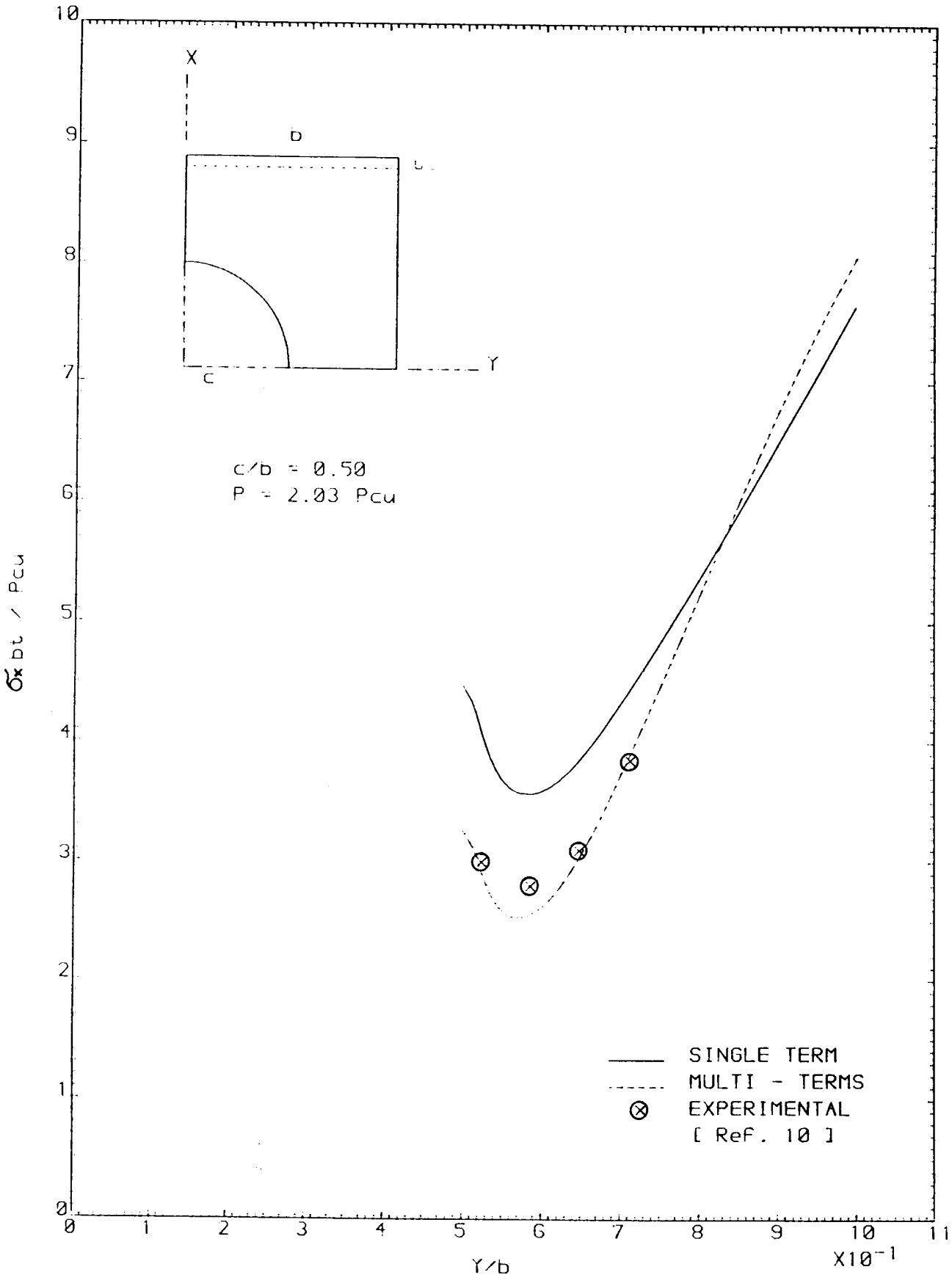

FIGURE 6-81 STRESSES AT THE MINIMUM SECTION

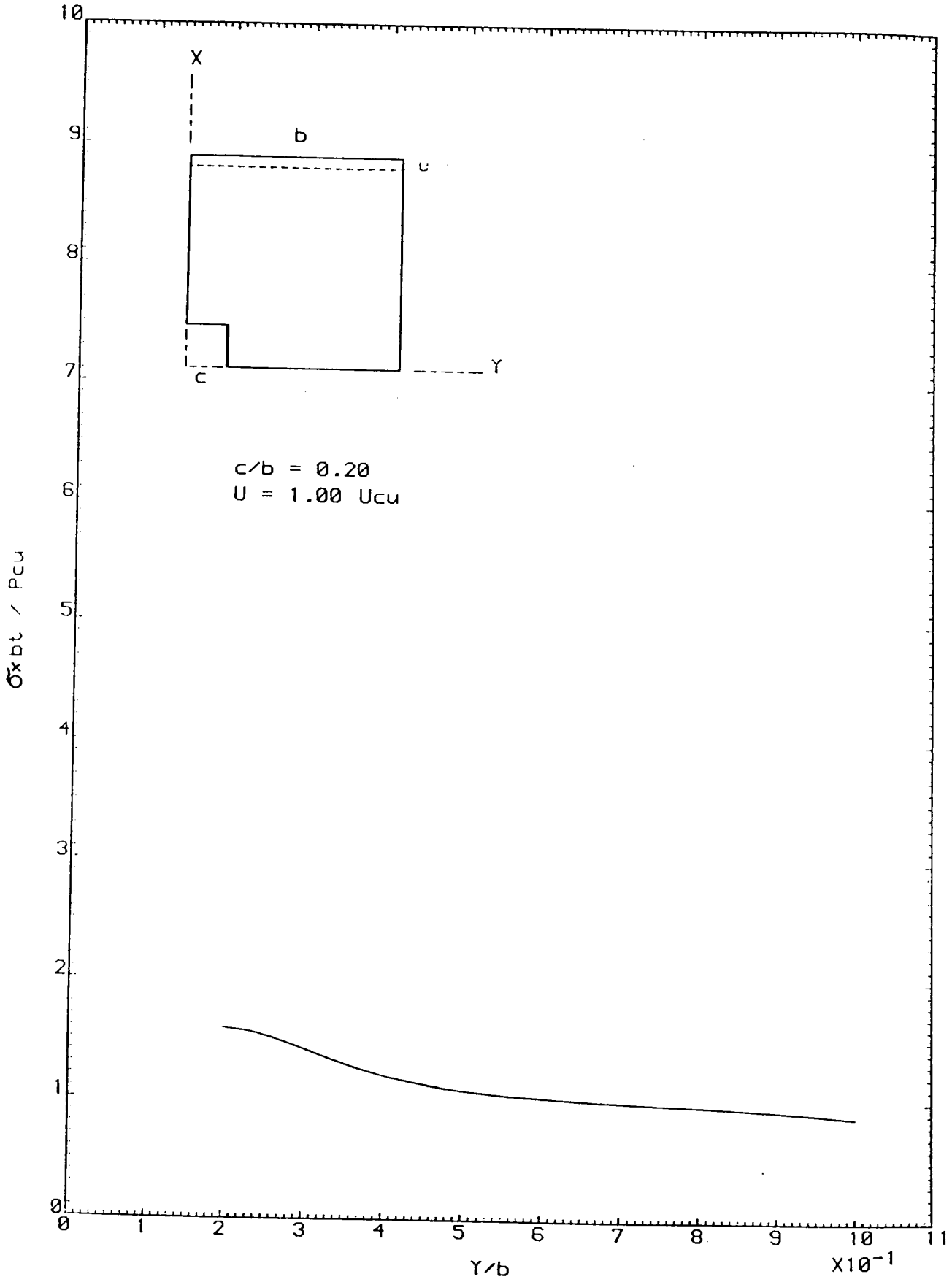

FIGURE 6·82 STRESSES AT THE MINIMUM SECTION

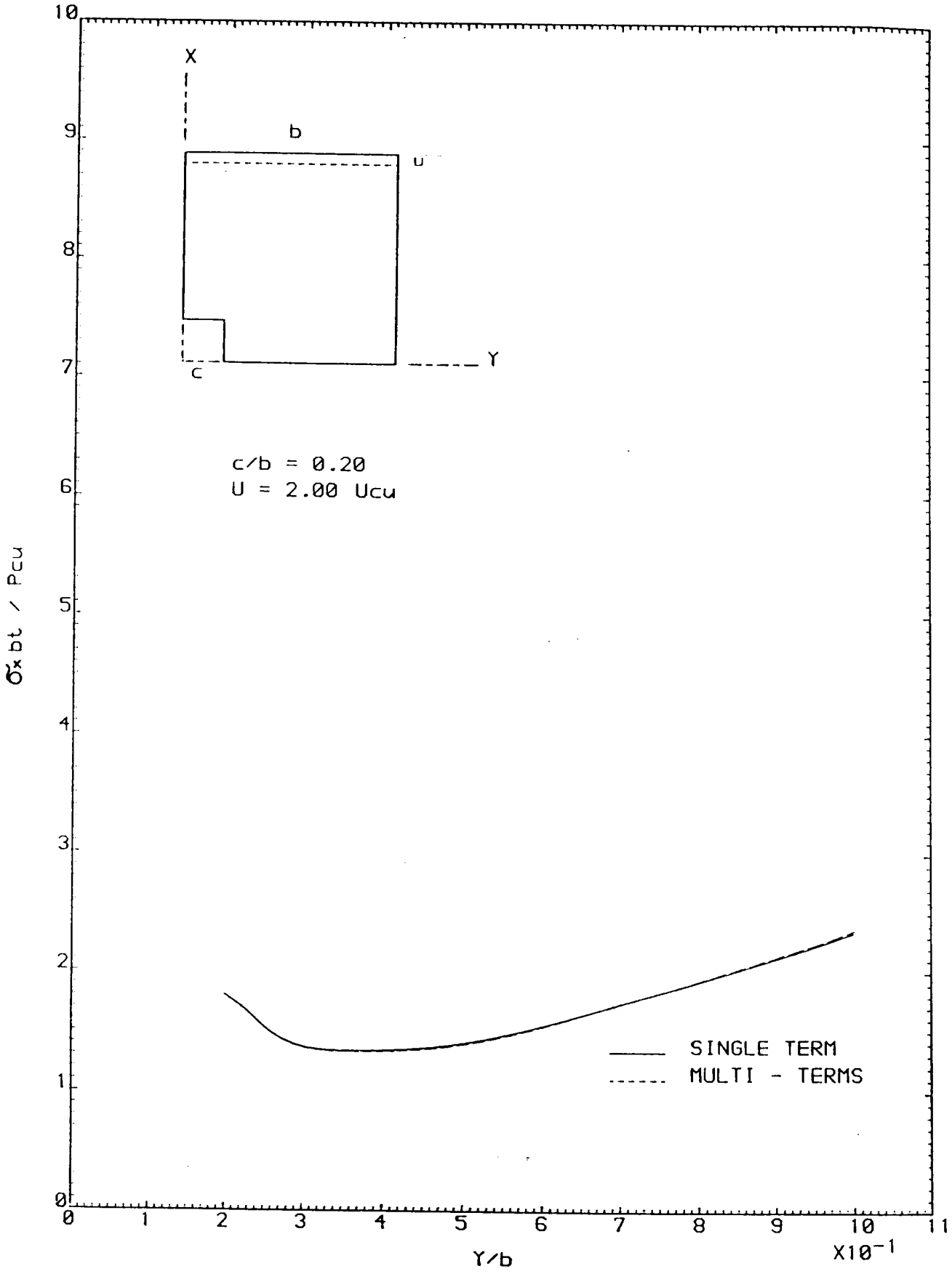

FIGURE 6·83 STRESSES AT THE MINIMUM SECTION

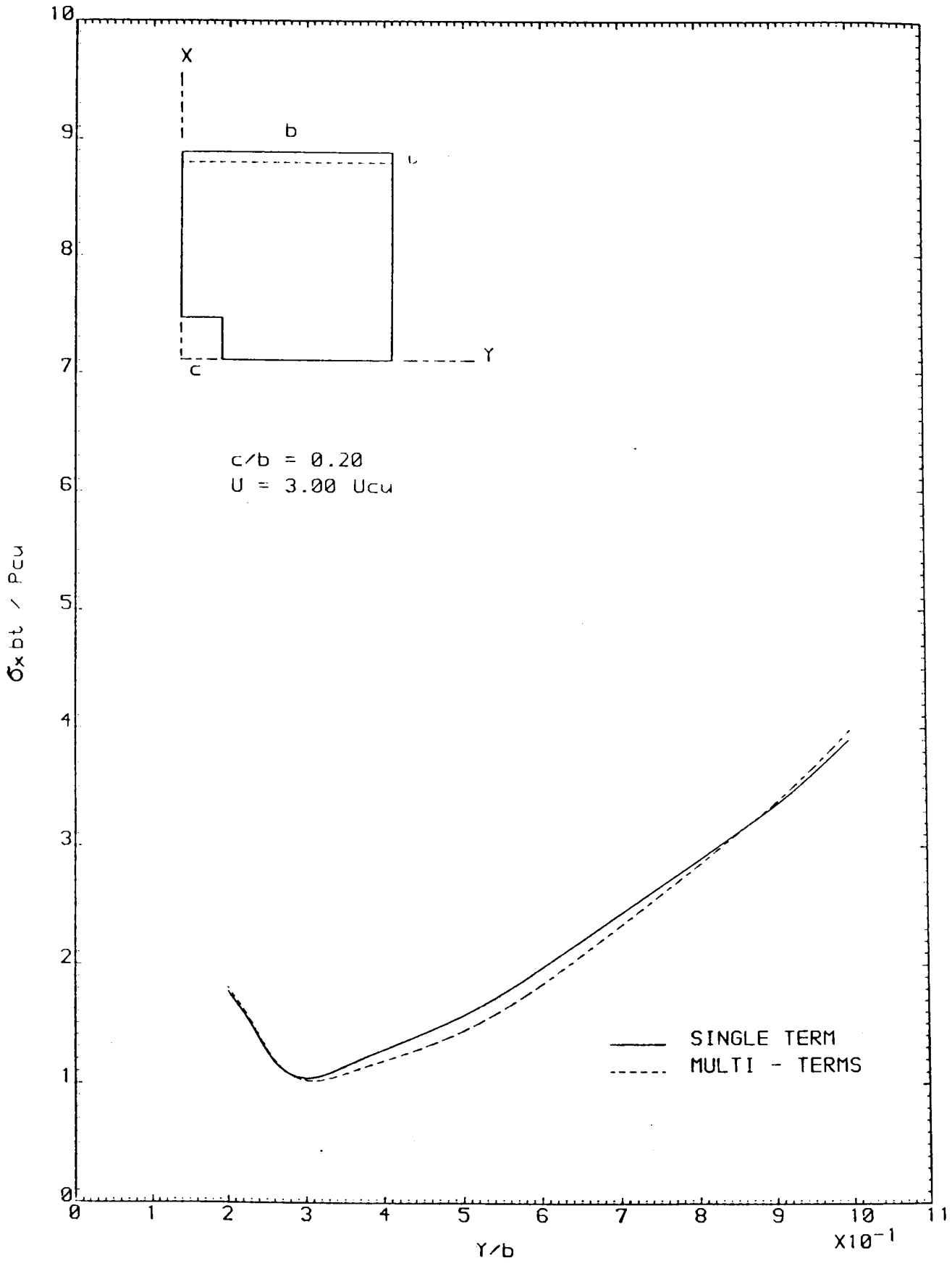

FIGURE 6·84 STRESSES AT THE MINIMUM SECTION

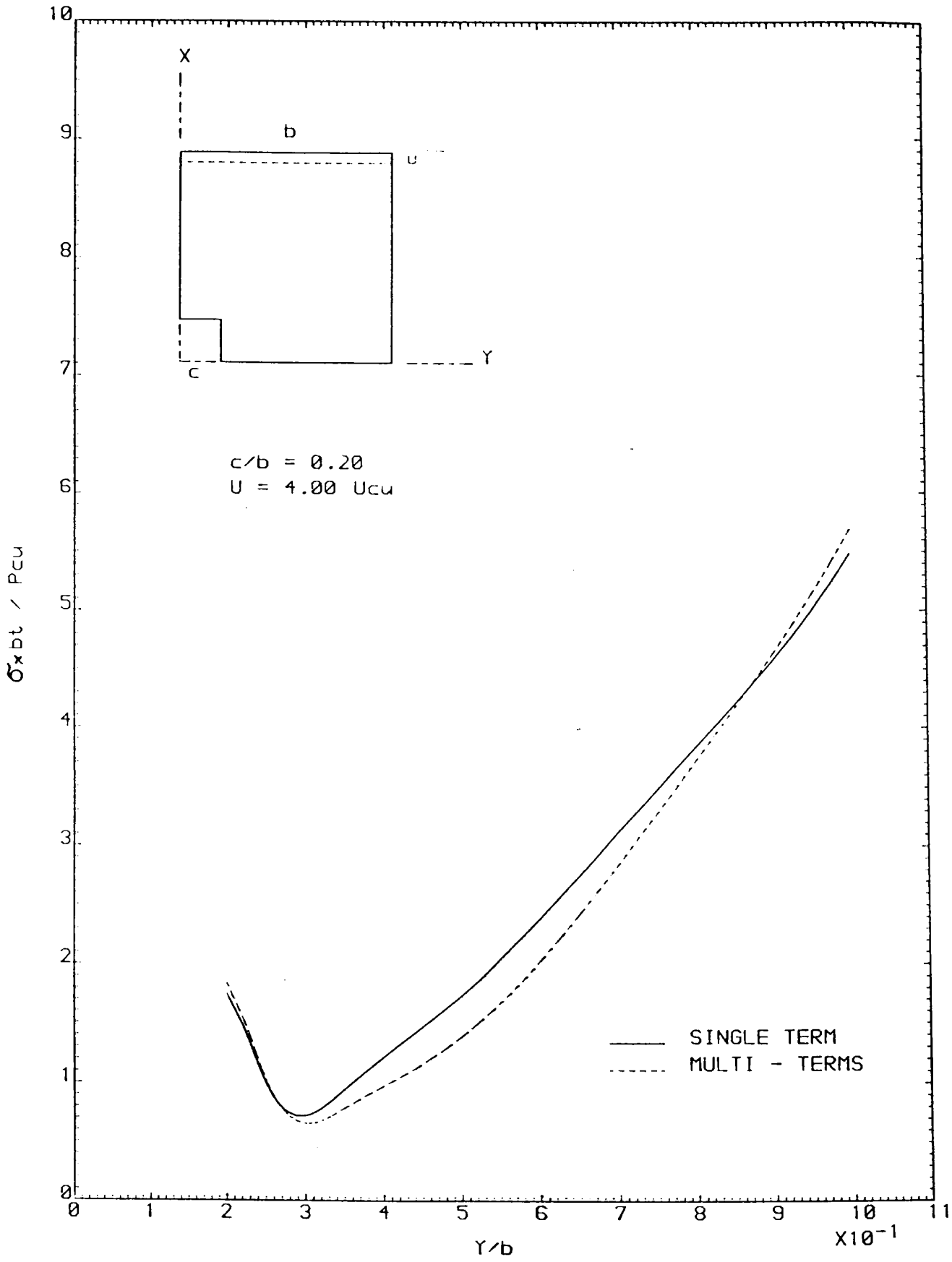

FIGURE 6·85 STRESSES AT THE MINIMUM SECTION

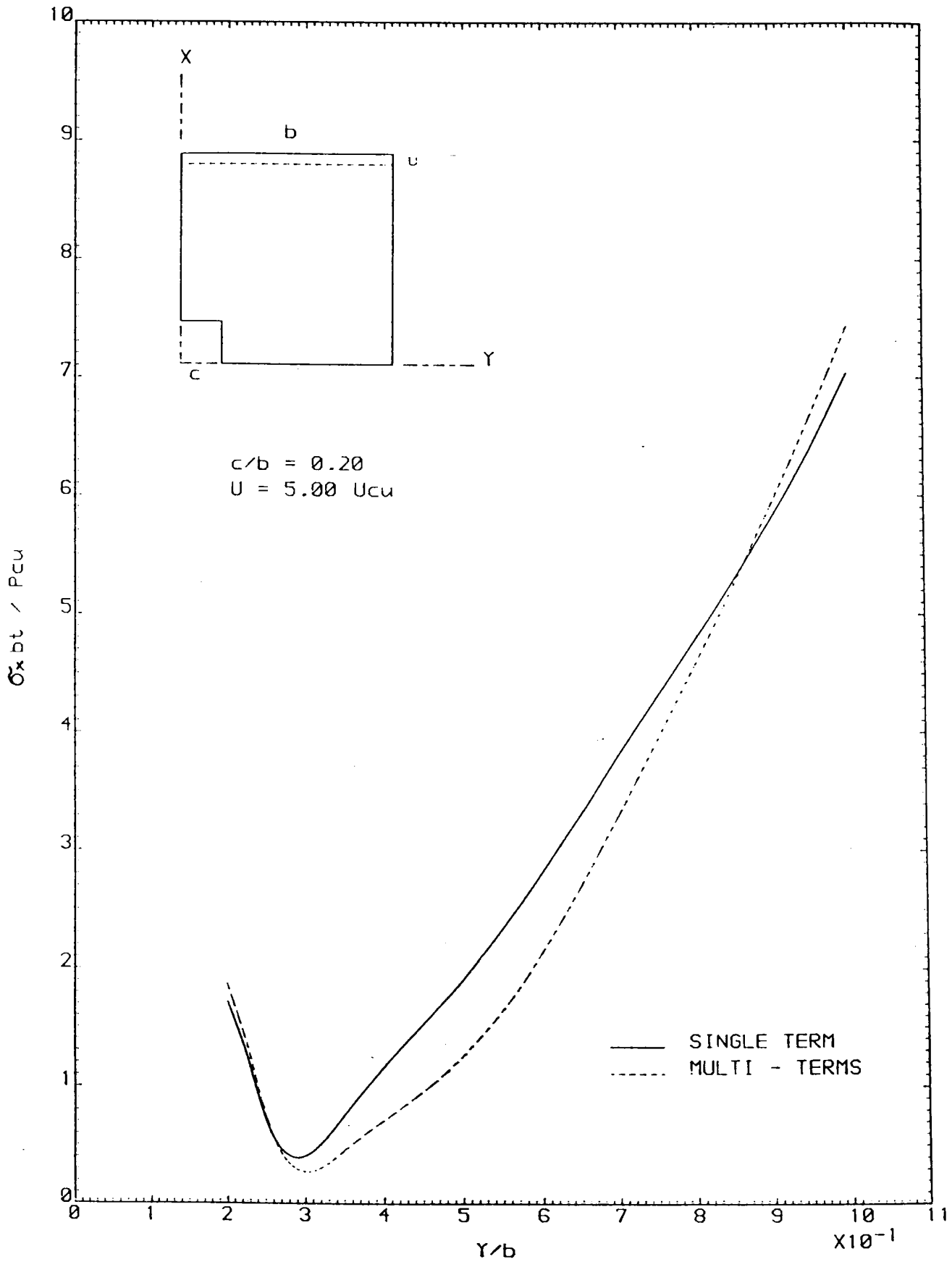

FIGURE 6·86 STRESSES AT THE MINIMUM SECTION

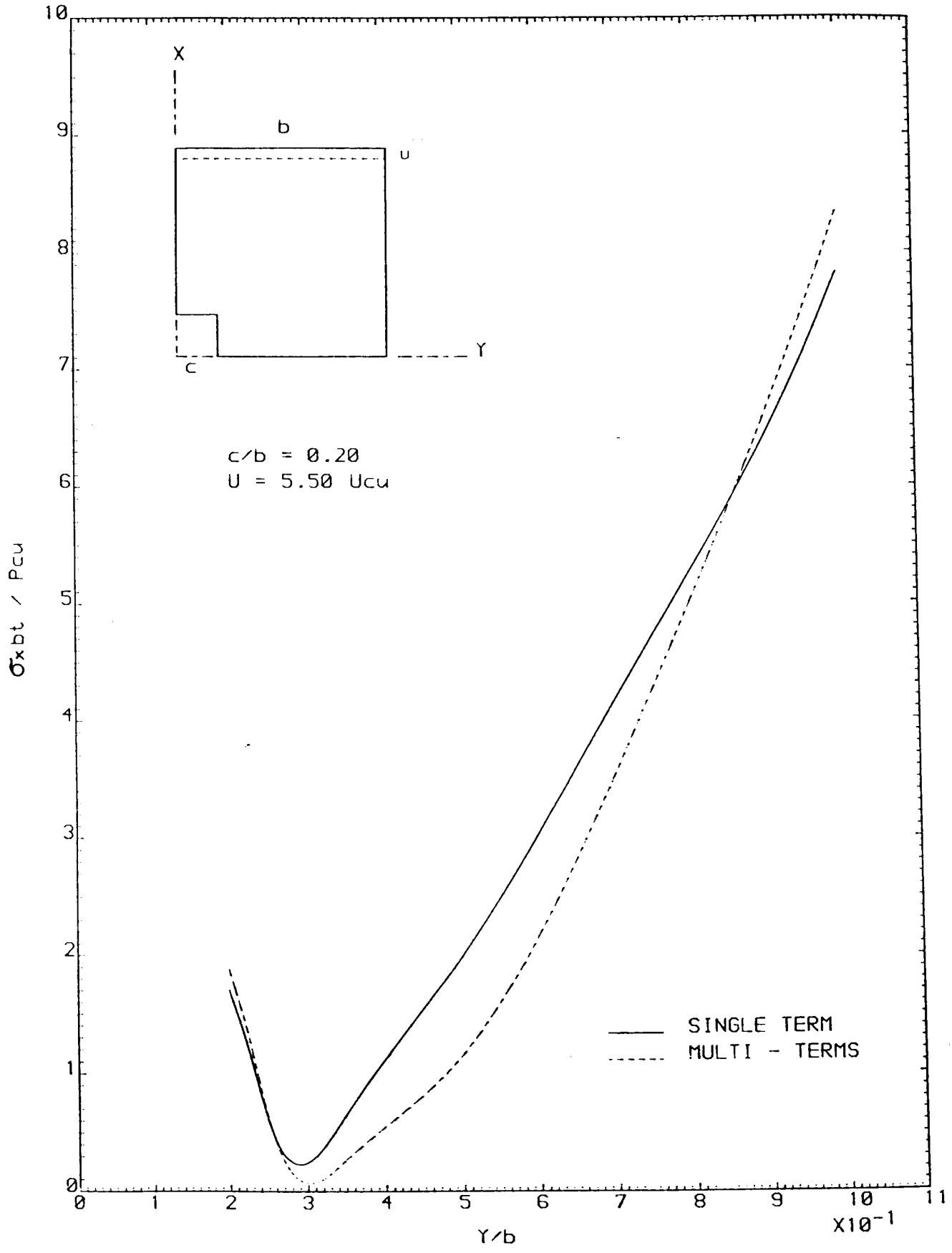

FIGURE 6·87 STRESSES AT THE MINIMUM SECTION

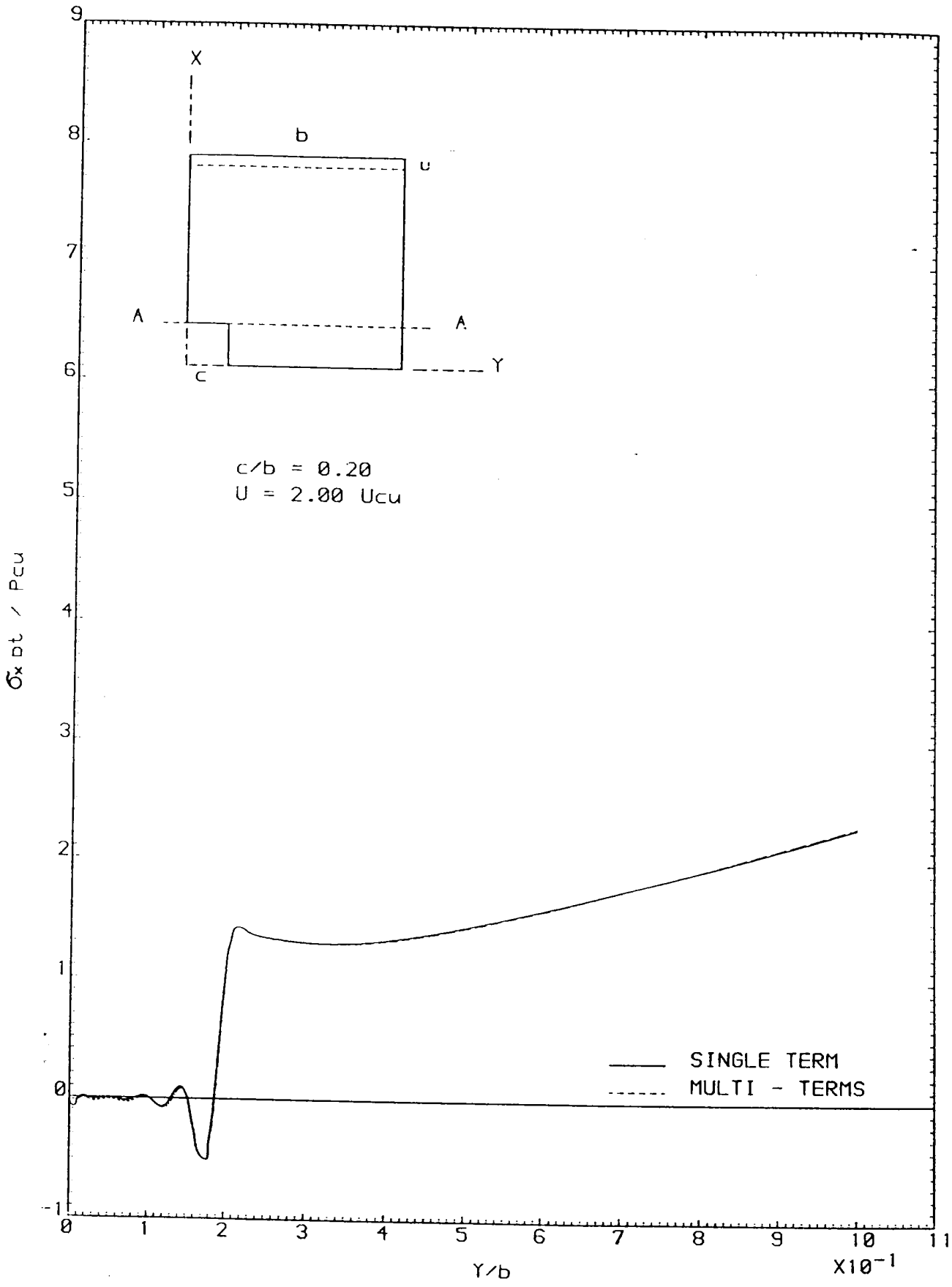

FIGURE 6·88 STRESSES AT SECTION A - A

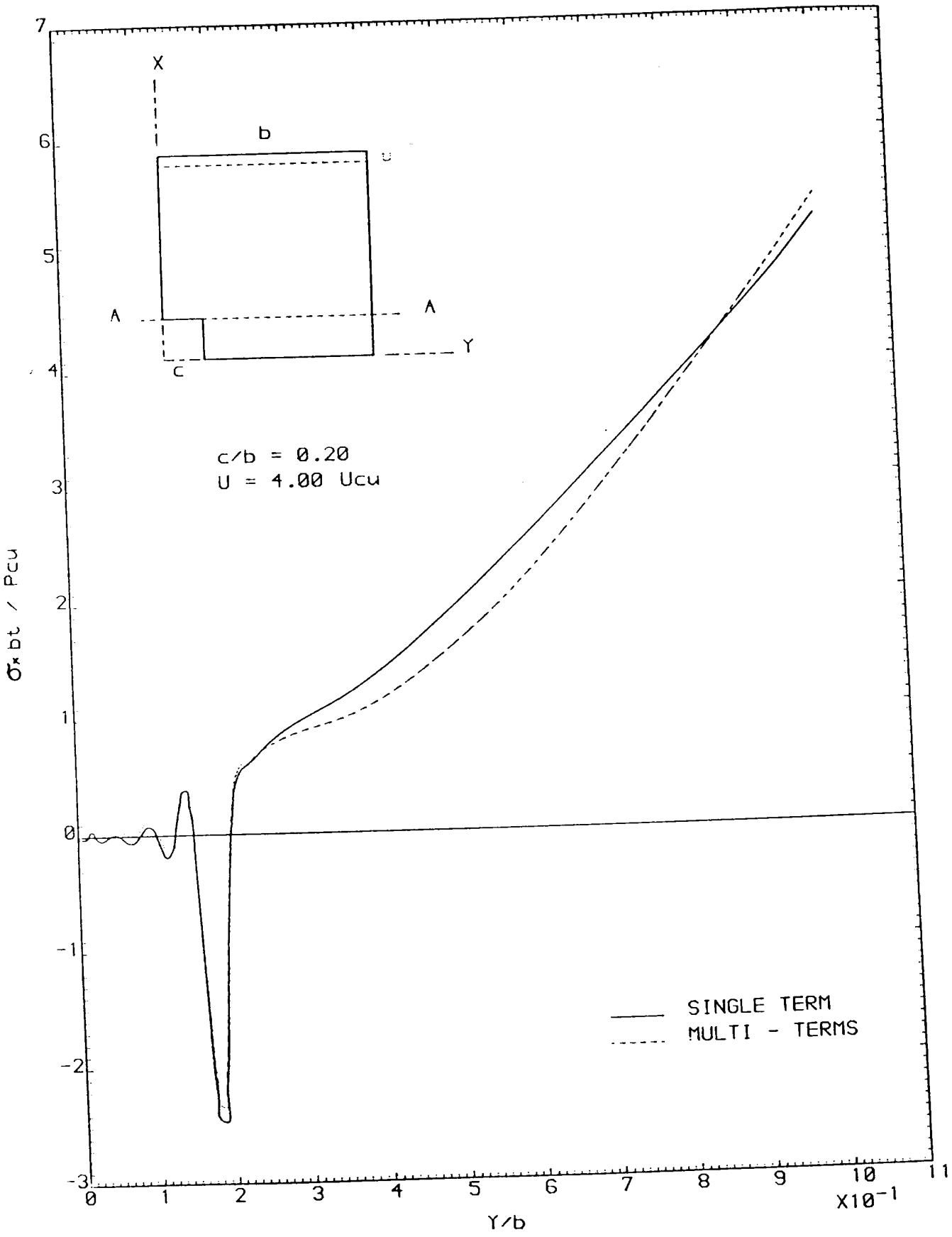

FIGURE 6·89 STRESSES AT SECTION A - A

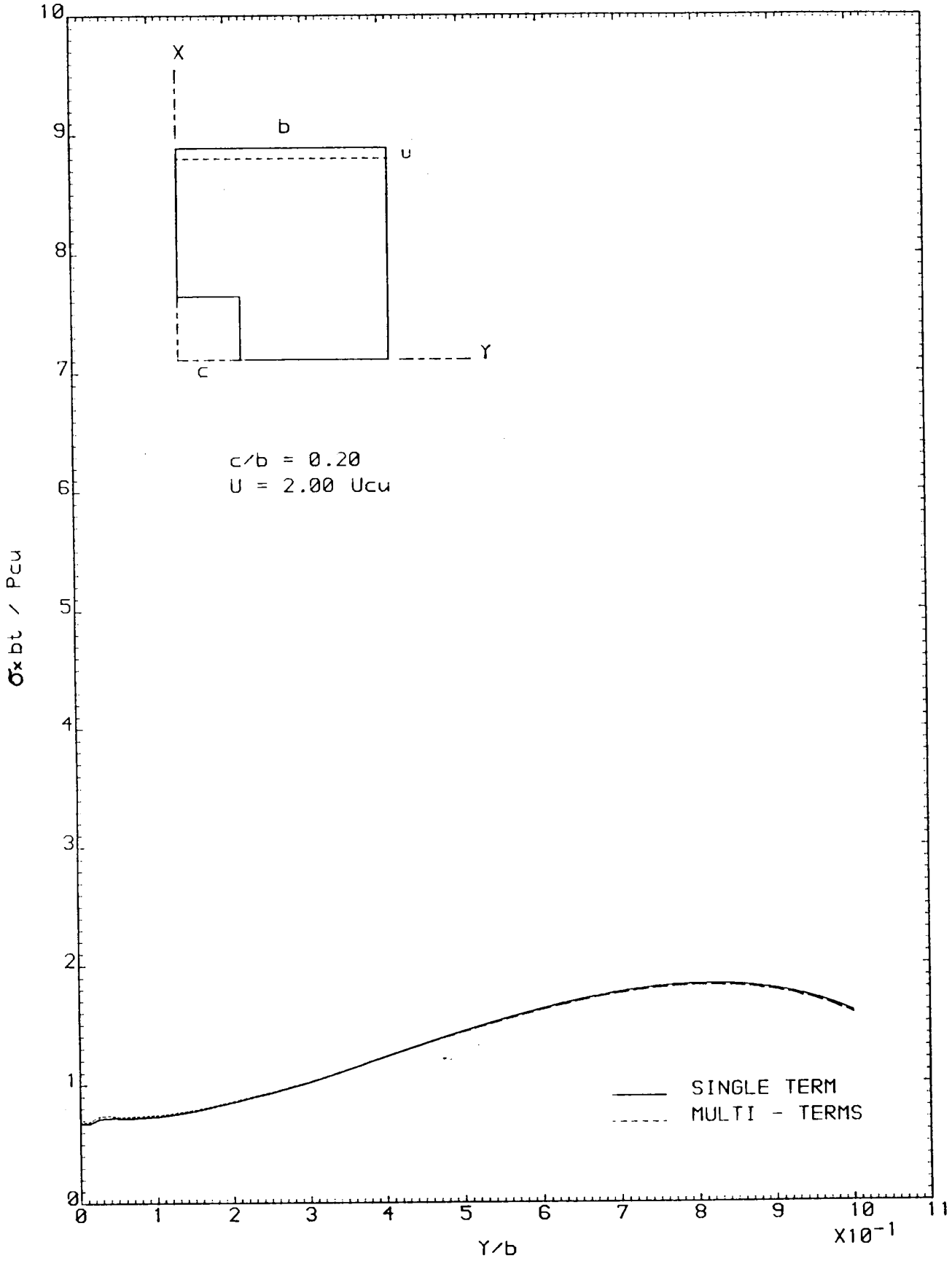

FIGURE 6·90 STRESSES AT THE LOADED EDGE

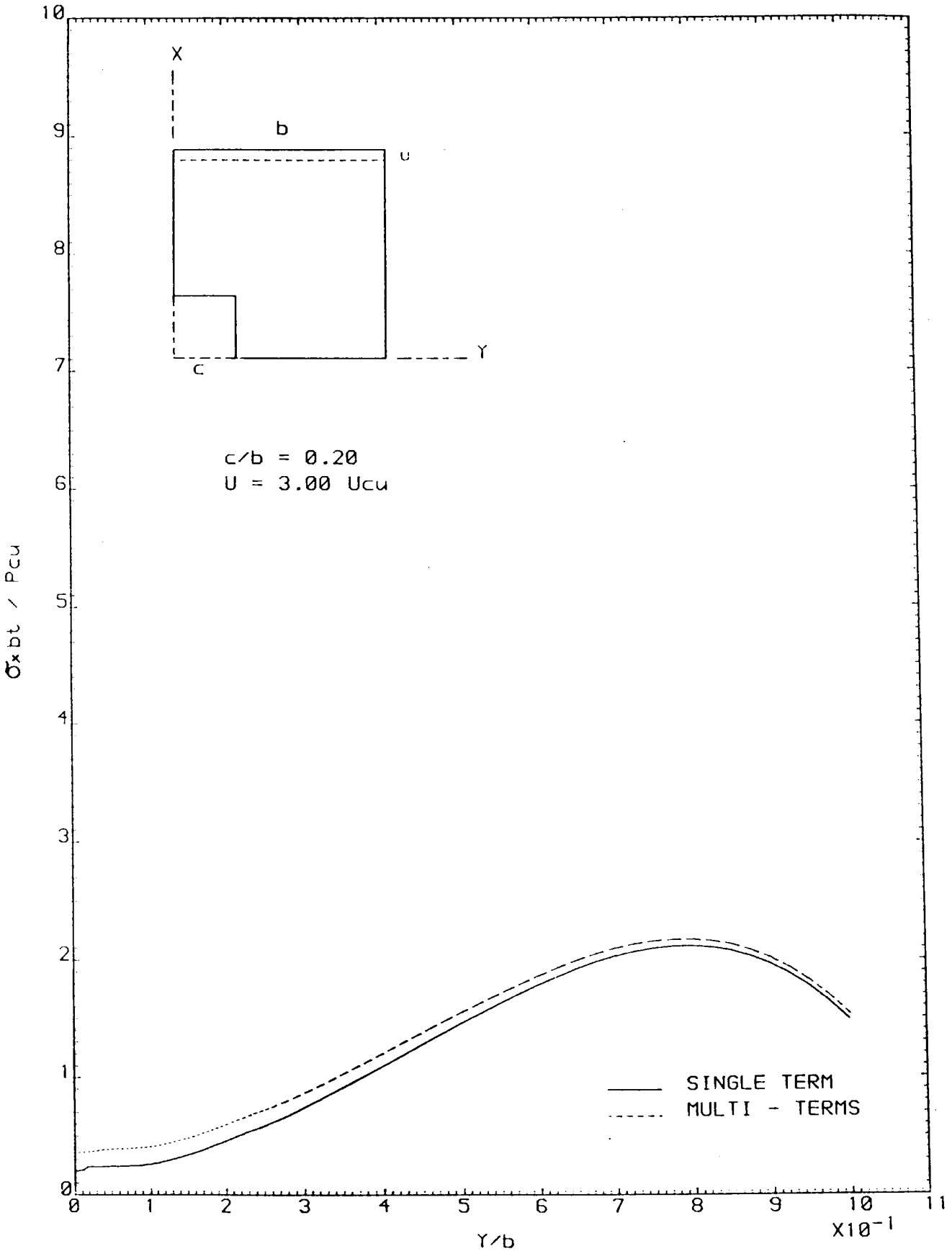

FIGURE 6·91 STRESSES AT THE LOADED EDGE

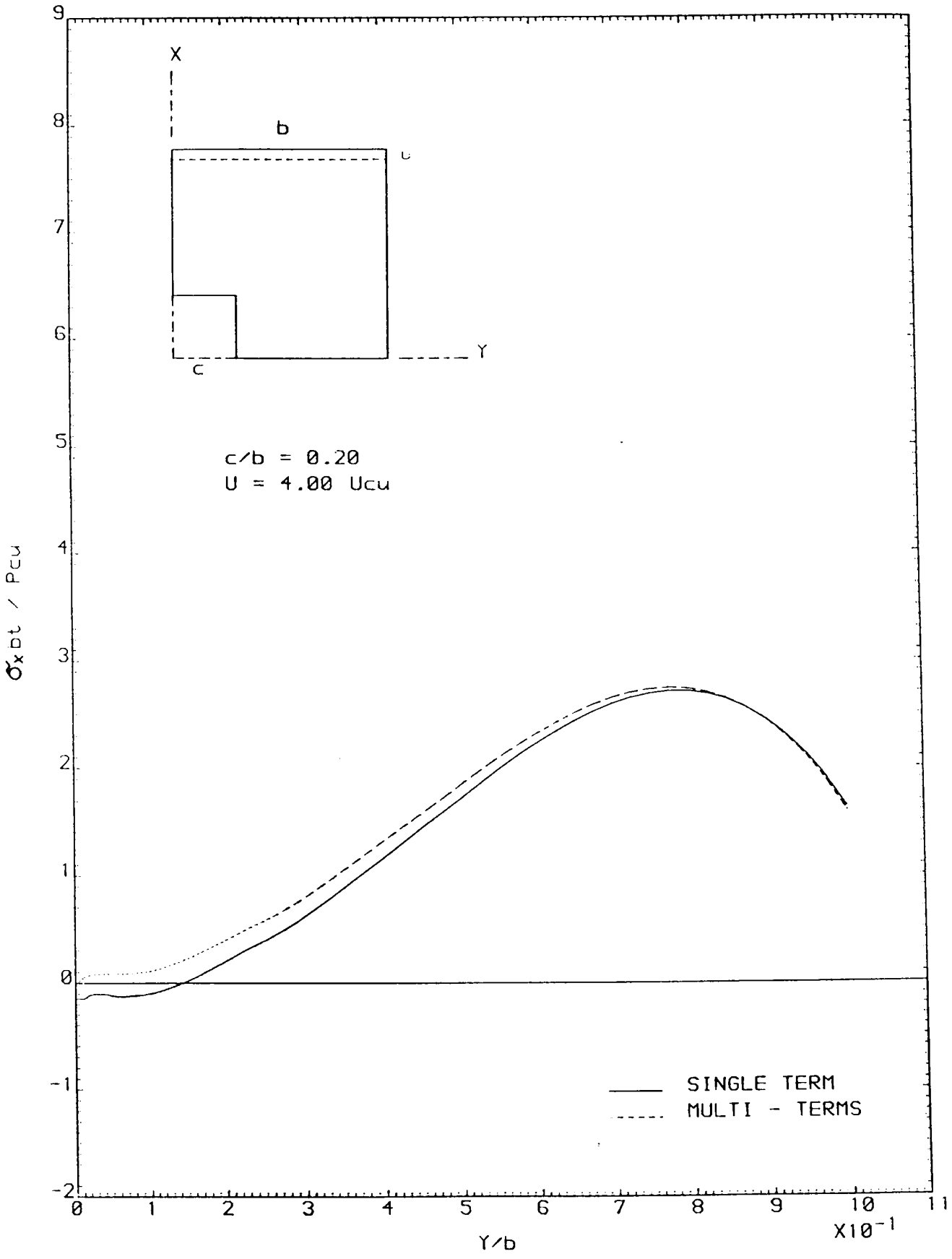

FIGURE 6-92 STRESSES AT THE LOADED EDGE

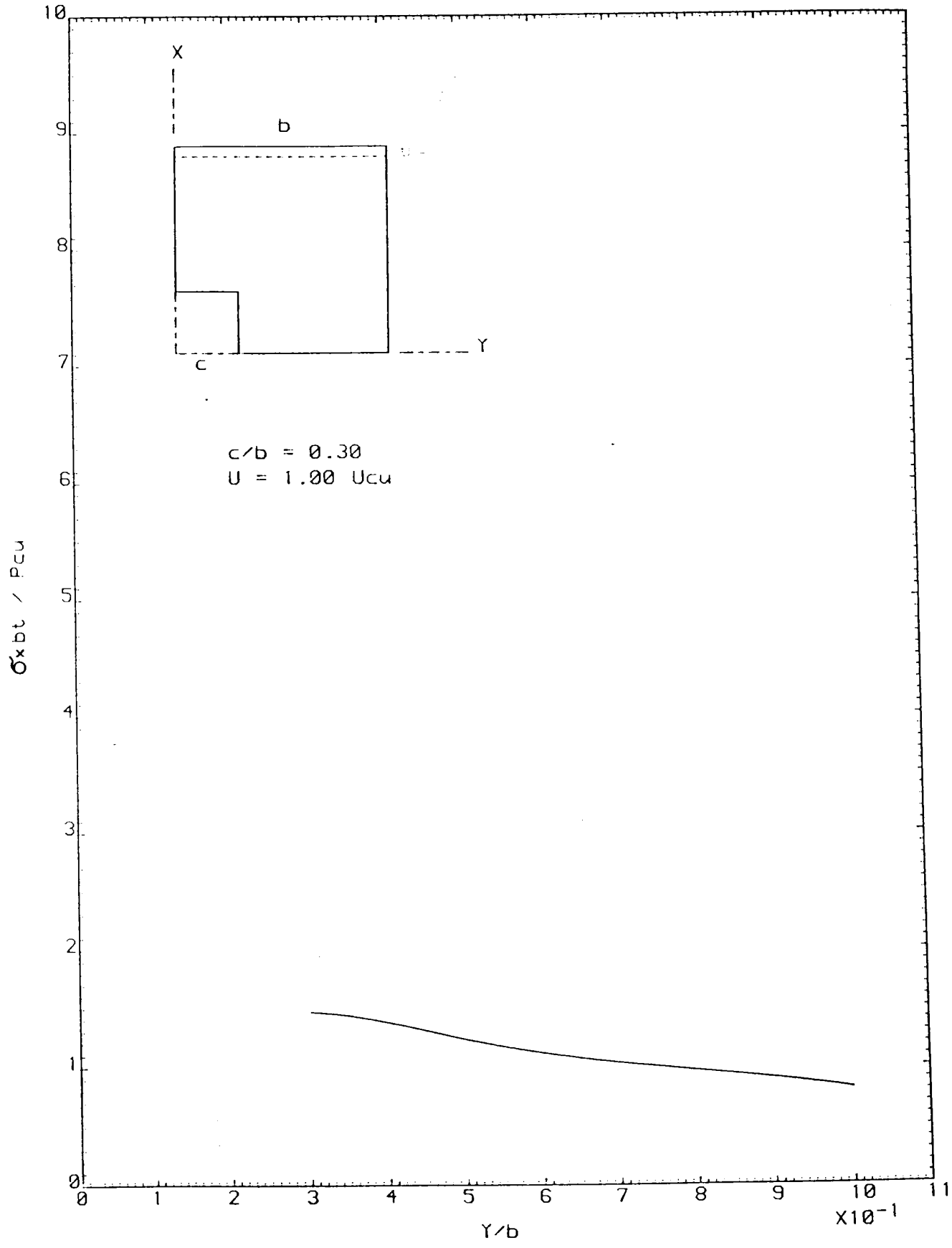

FIGURE 6·93 STRESSES AT THE MINIMUM SECTION

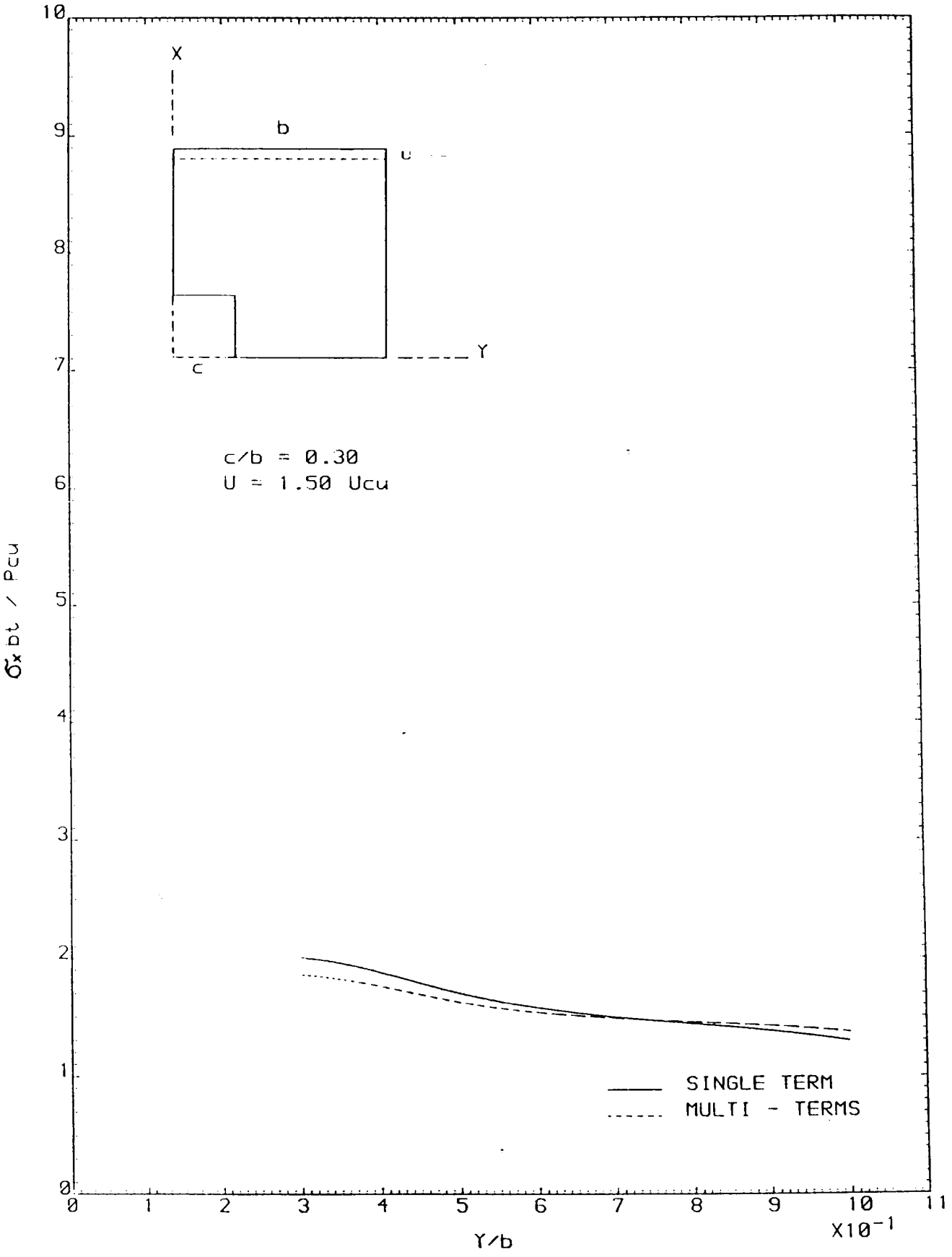

FIGURE 6·94 STRESSES AT THE MINIMUM SECTION

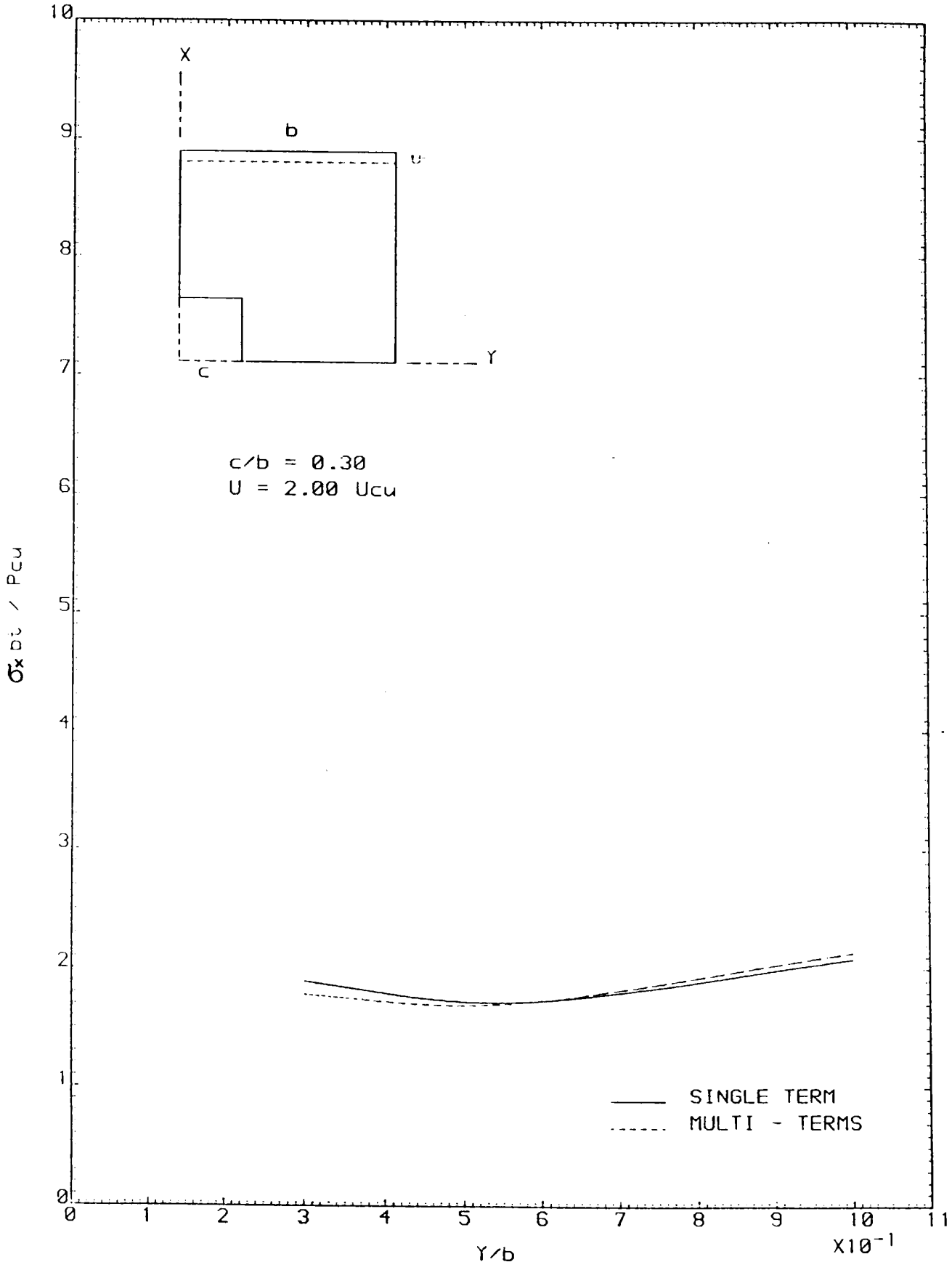

FIGURE 6·95 STRESSES AT THE MINIMUM SECTION

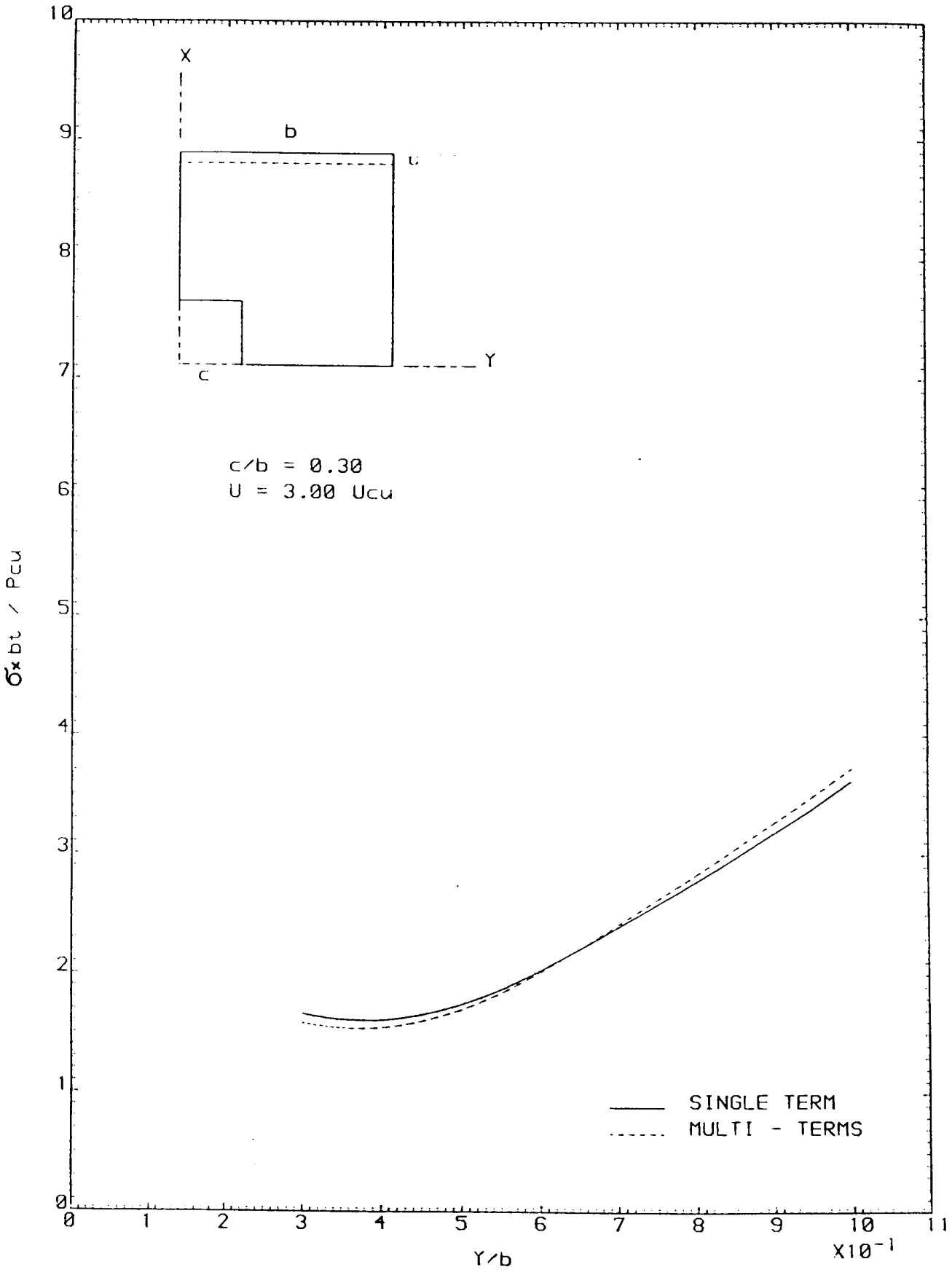

FIGURE 6·96 STRESSES AT THE MINIMUM SECTION

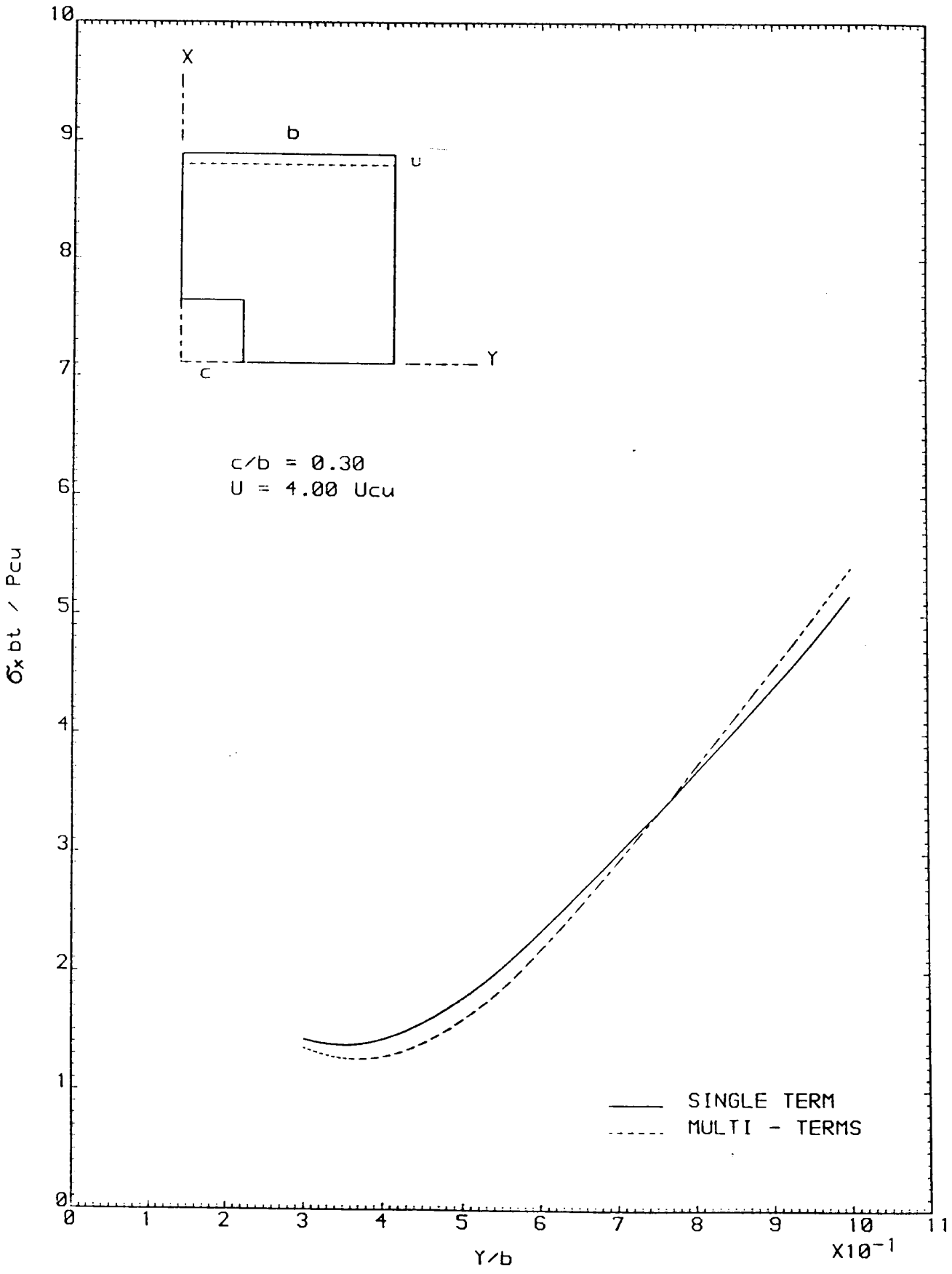

FIGURE 6·97 STRESSES AT THE MINIMUM SECTION

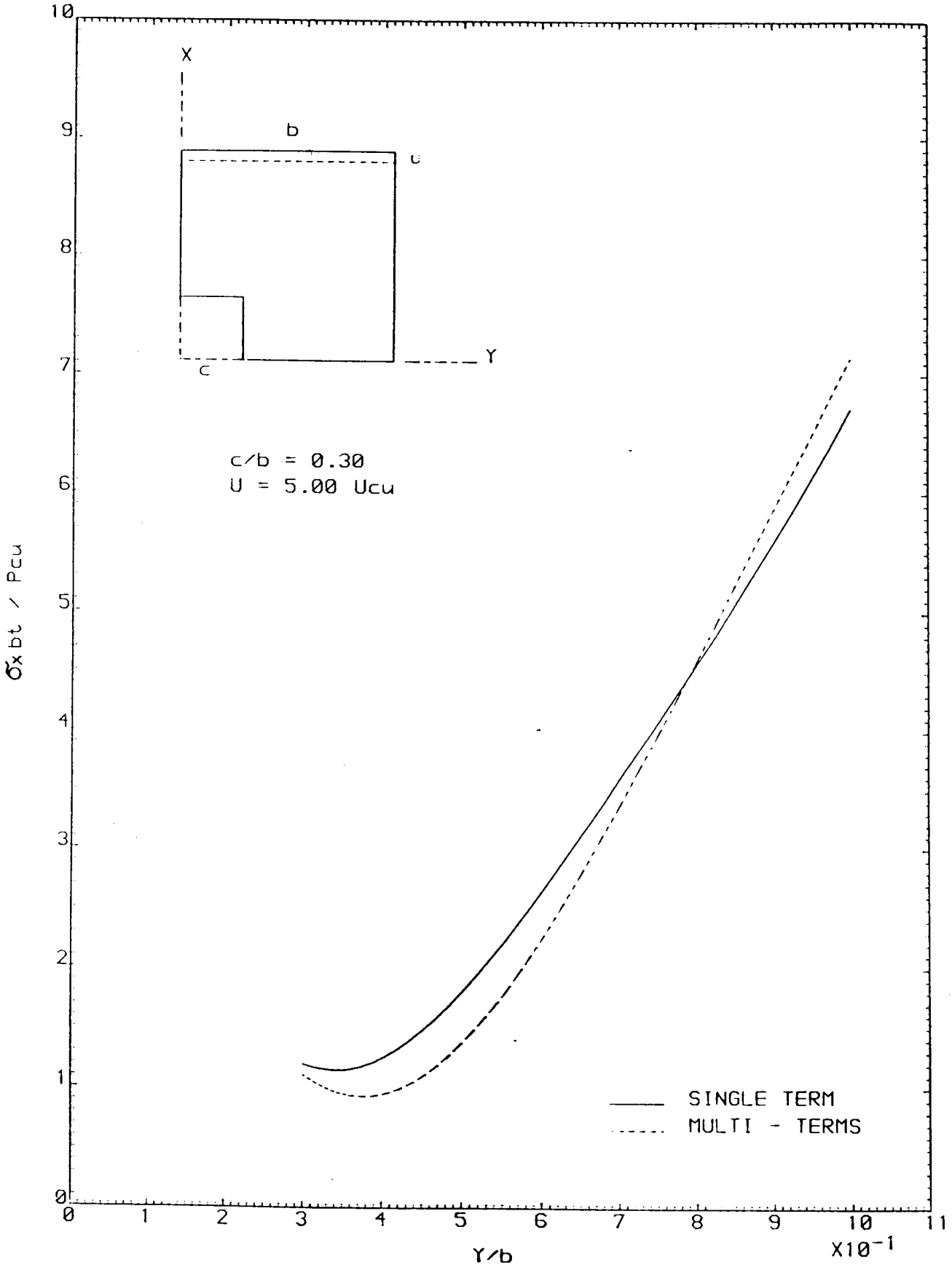

FIGURE 6-98 STRESSES AT THE MINIMUM SECTION

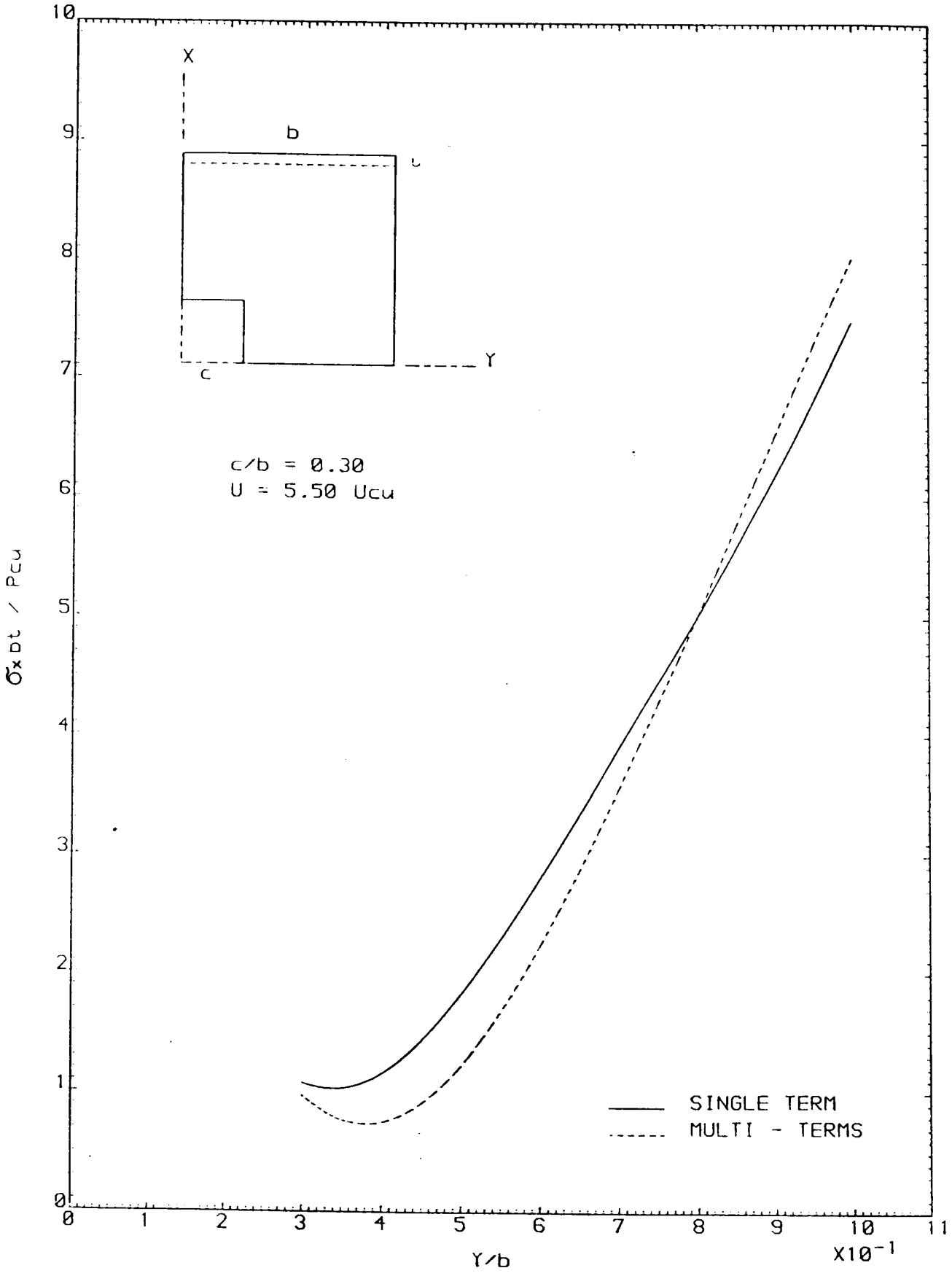

FIGURE 6·99 STRESSES AT THE MINIMUM SECTION

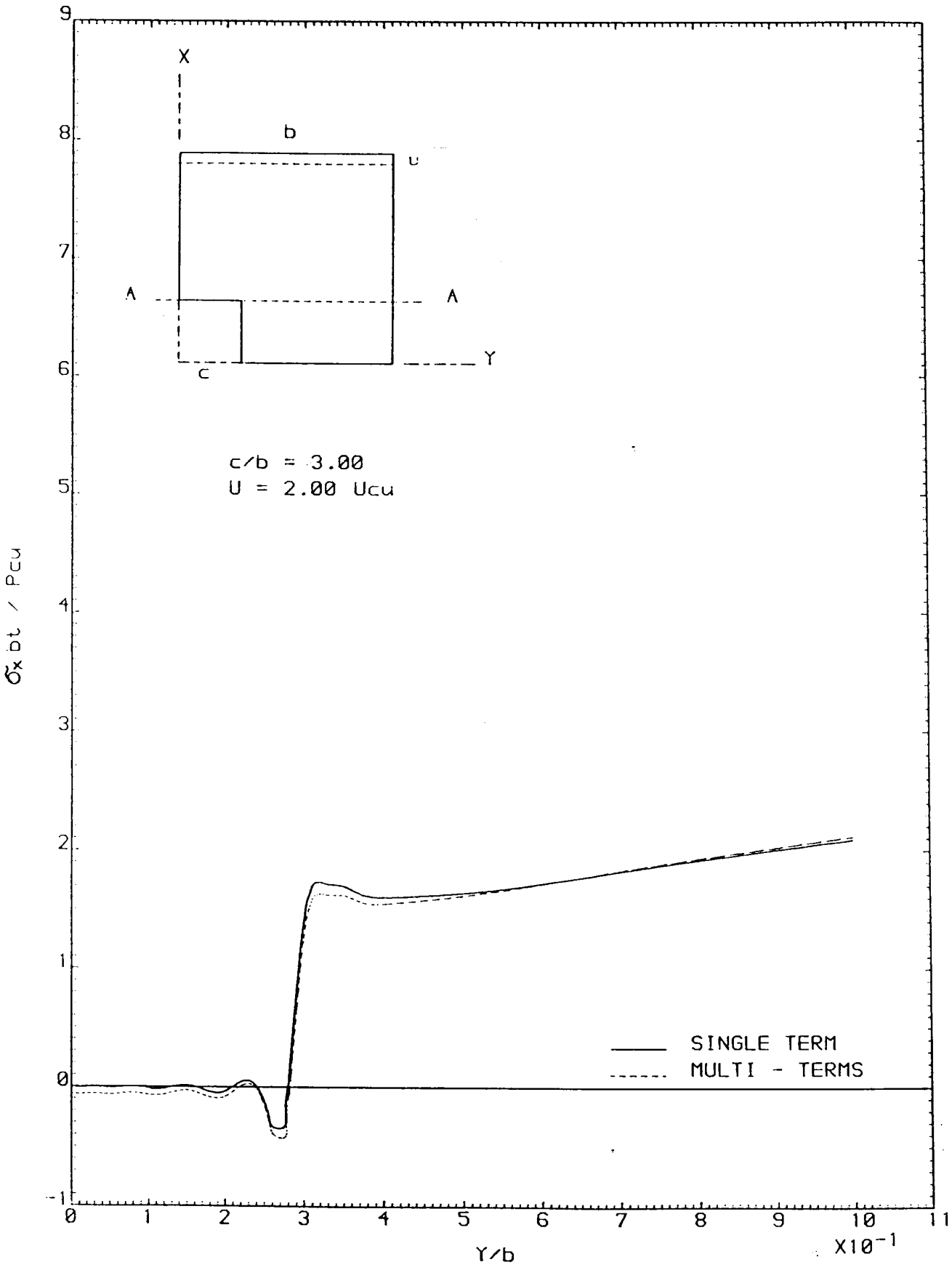

FIGURE 6·101 STRESSES AT SECTION A - A

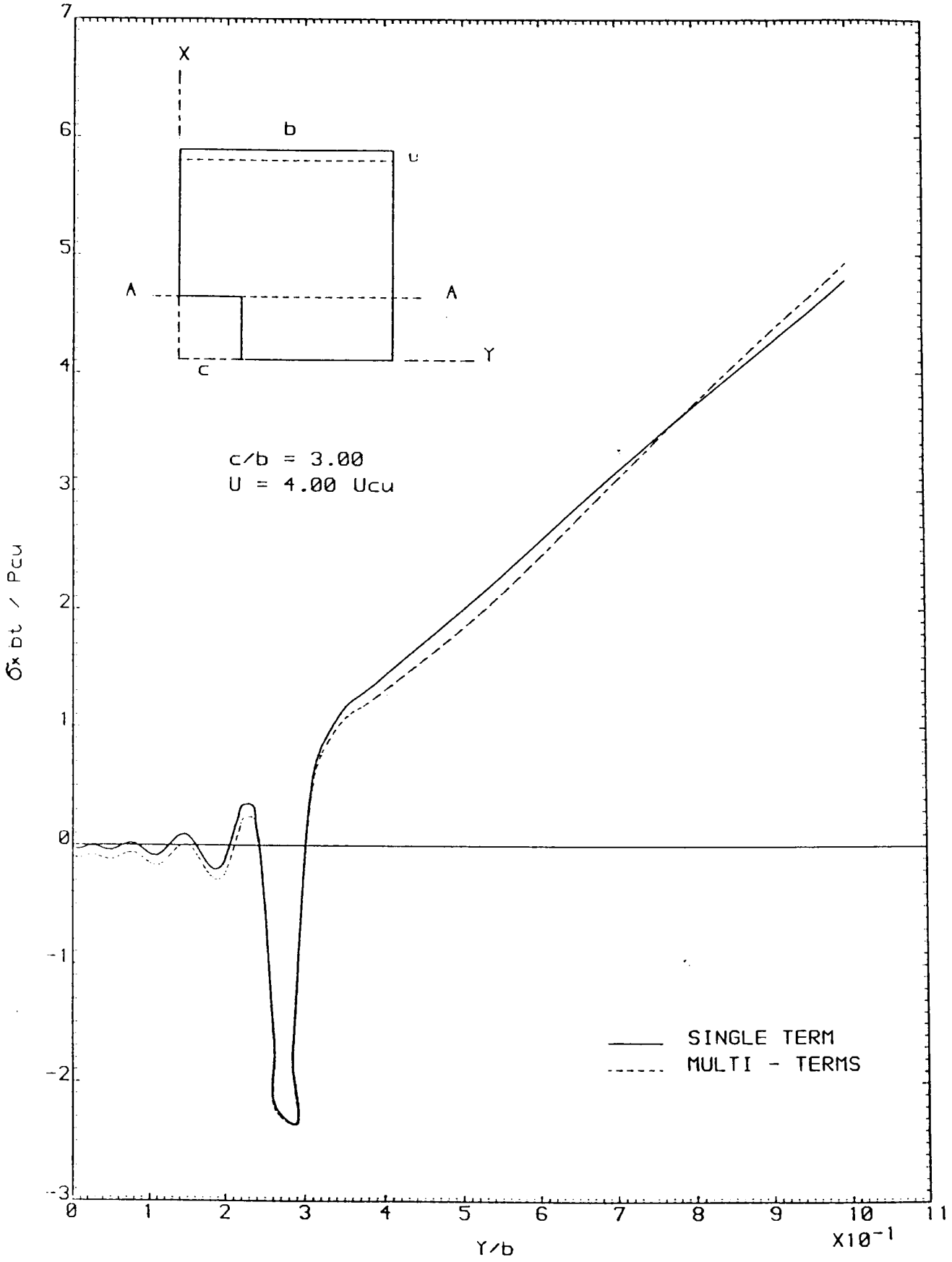

FIGURE 6·102 STRESSES AT SECTION A - A

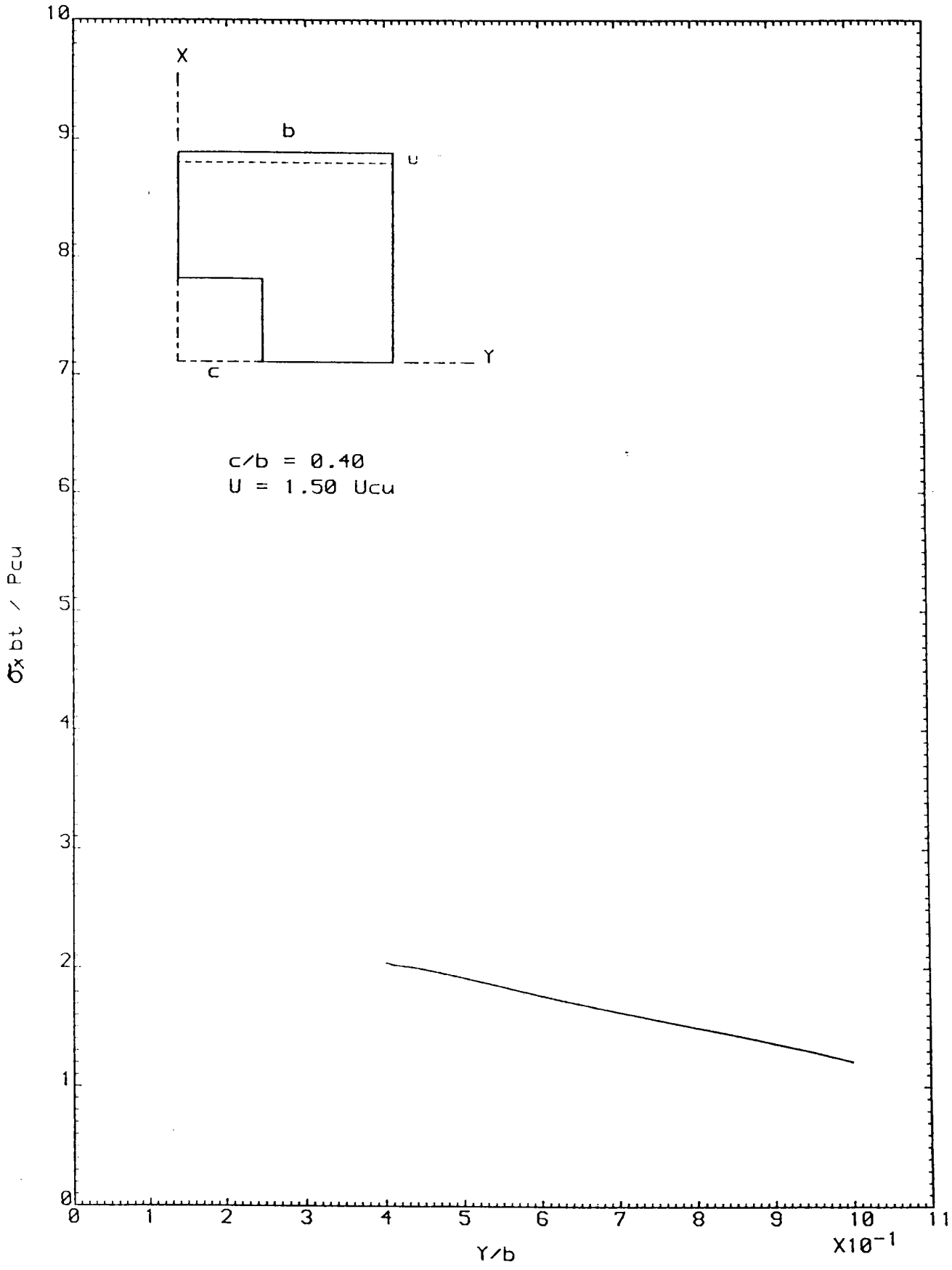

FIGURE 6·103 STRESSES AT THE MINIMUM SECTION

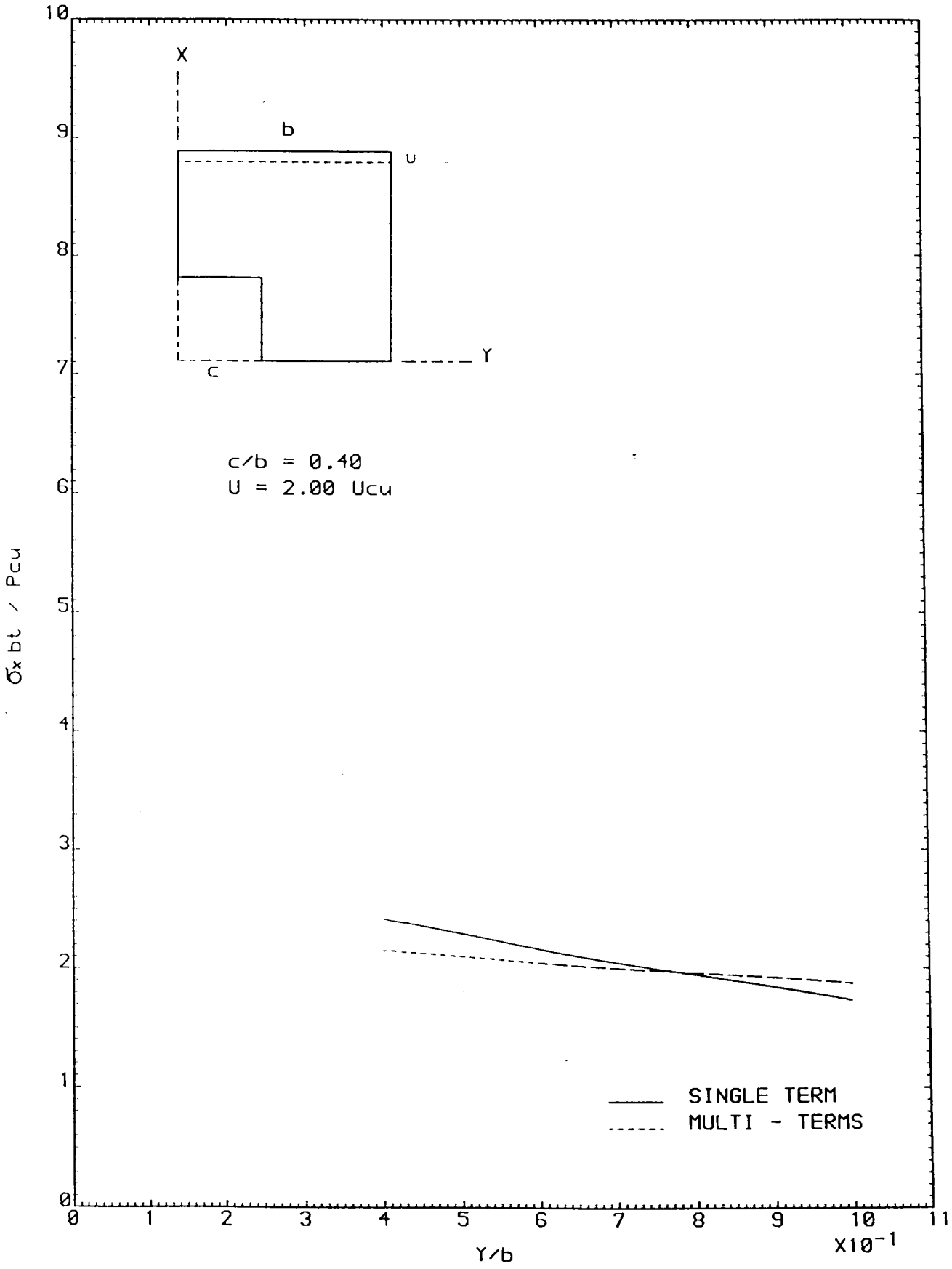

FIGURE 6·104 STRESSES AT THE MINIMUM SECTION

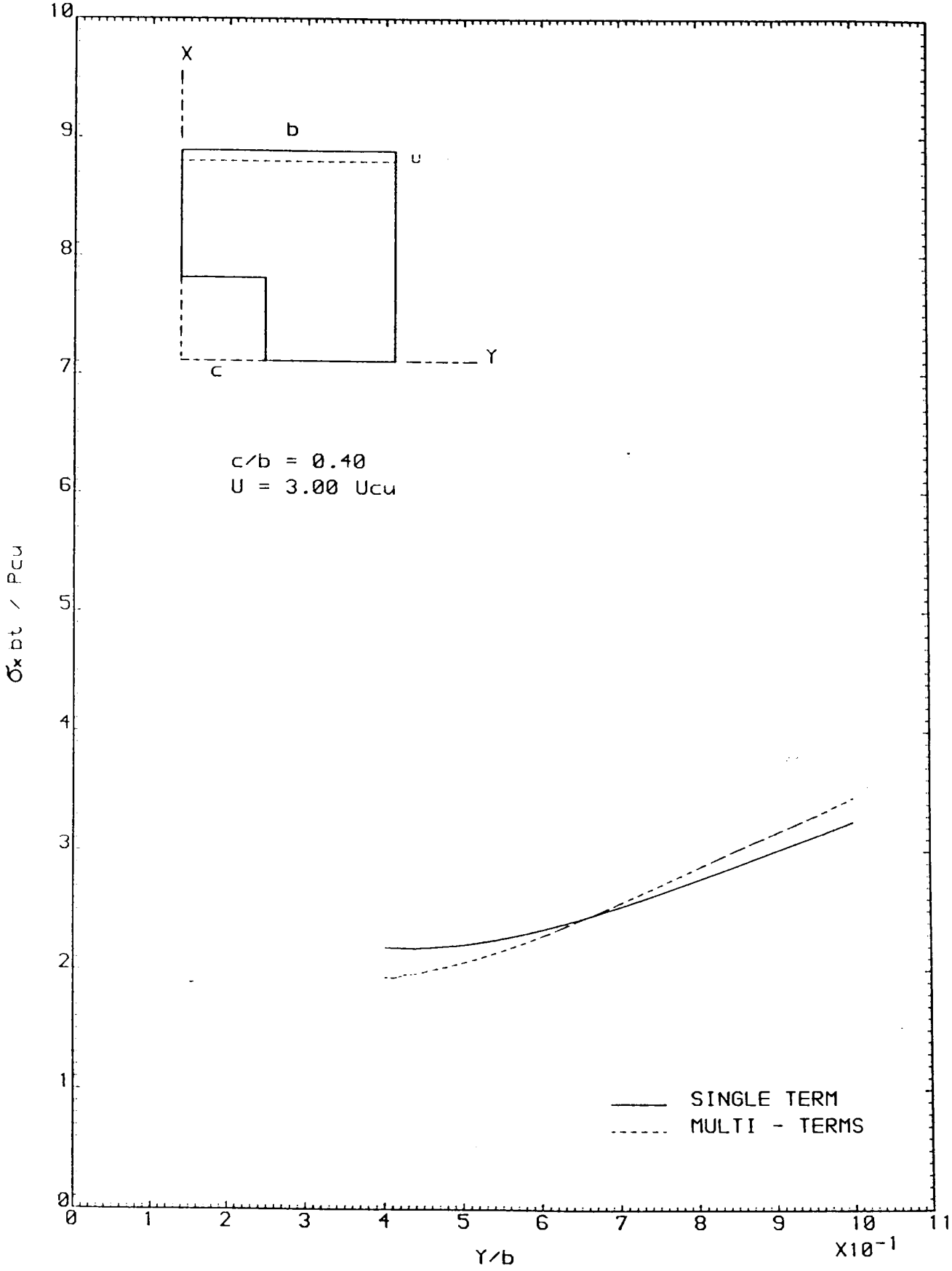

FIGURE 6·105 STRESSES AT THE MINIMUM SECTION

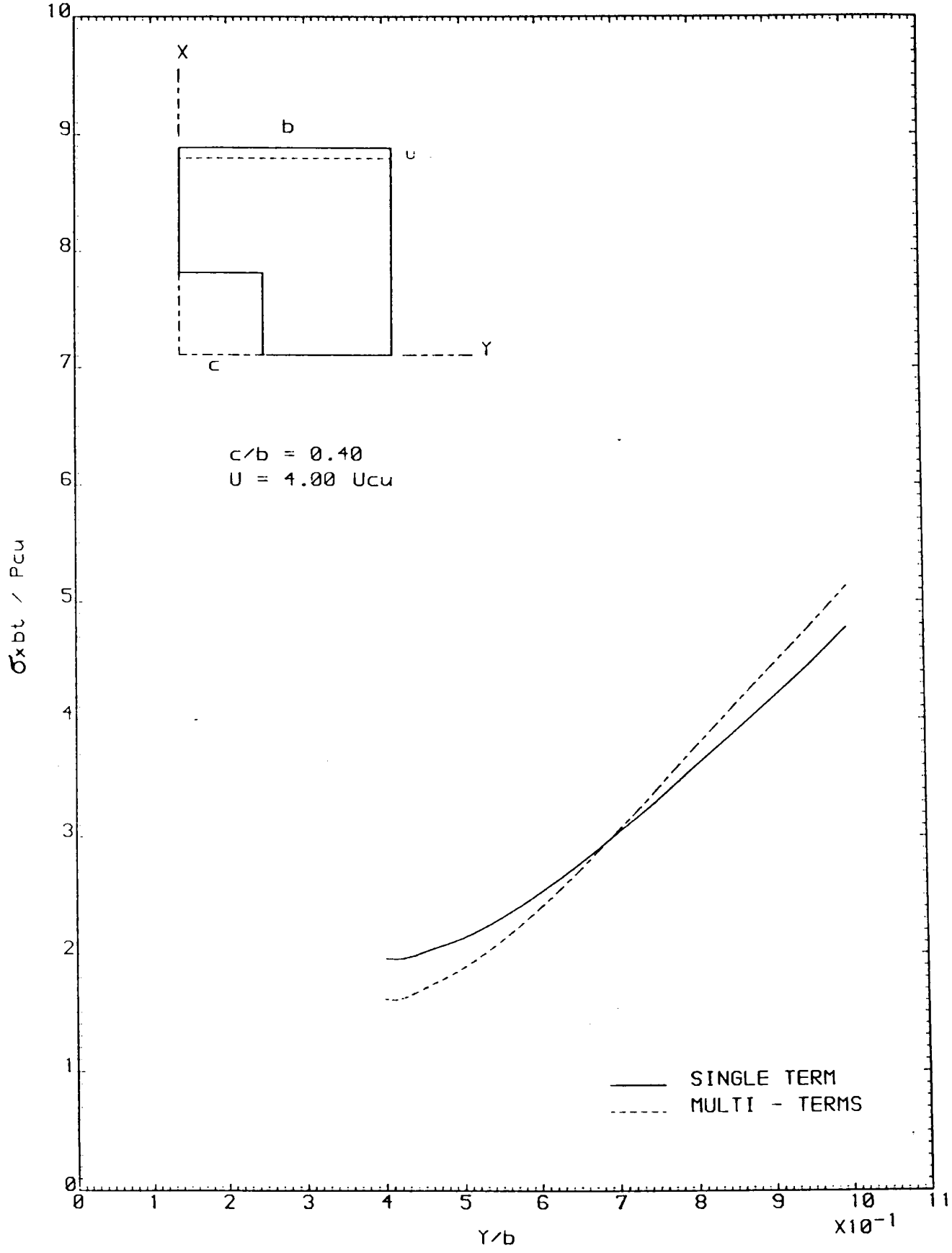

FIGURE 6·106 STRESSES AT THE MINIMUM SECTION

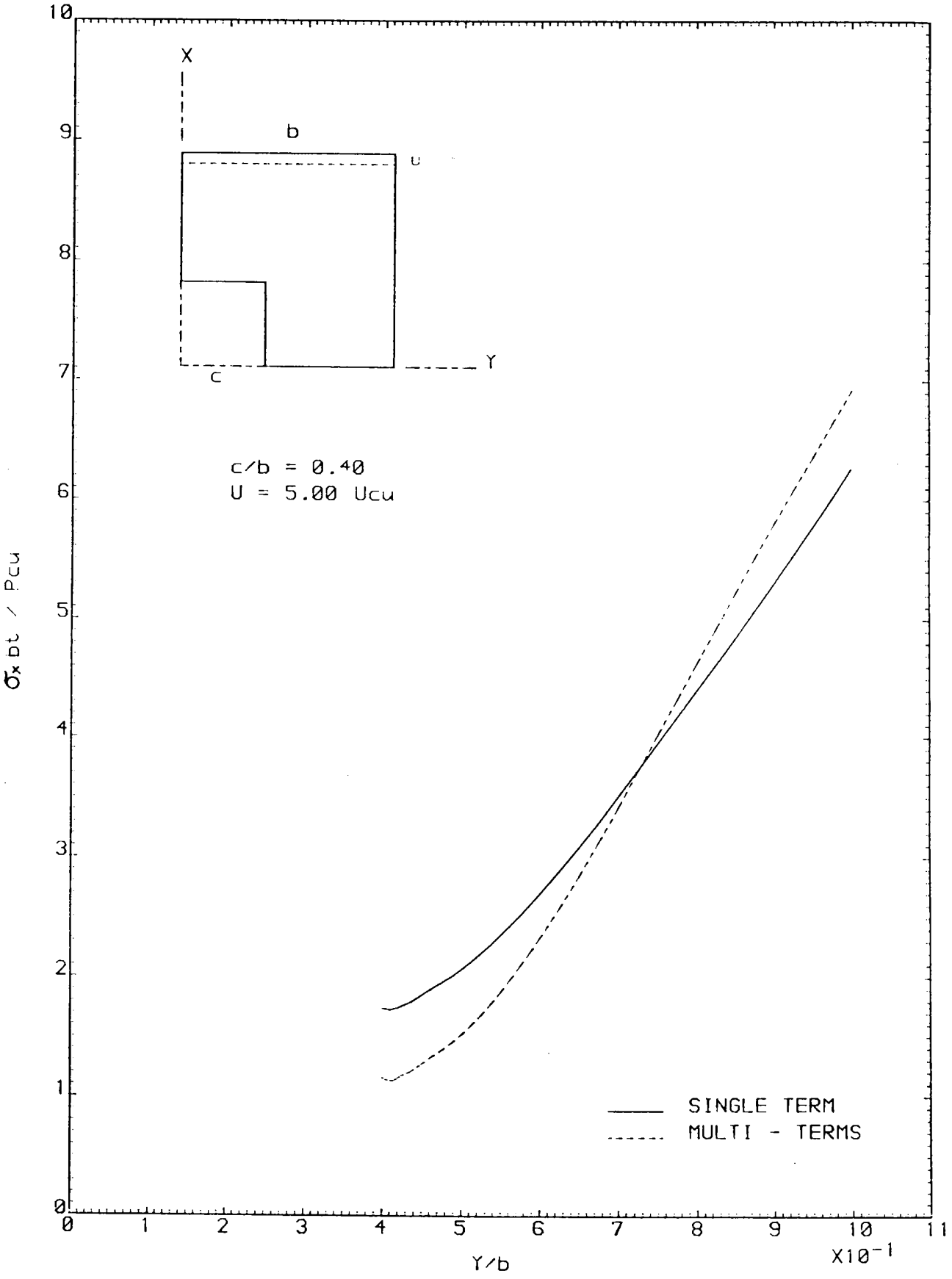

FIGURE 6·107 STRESSES AT THE MINIMUM SECTION

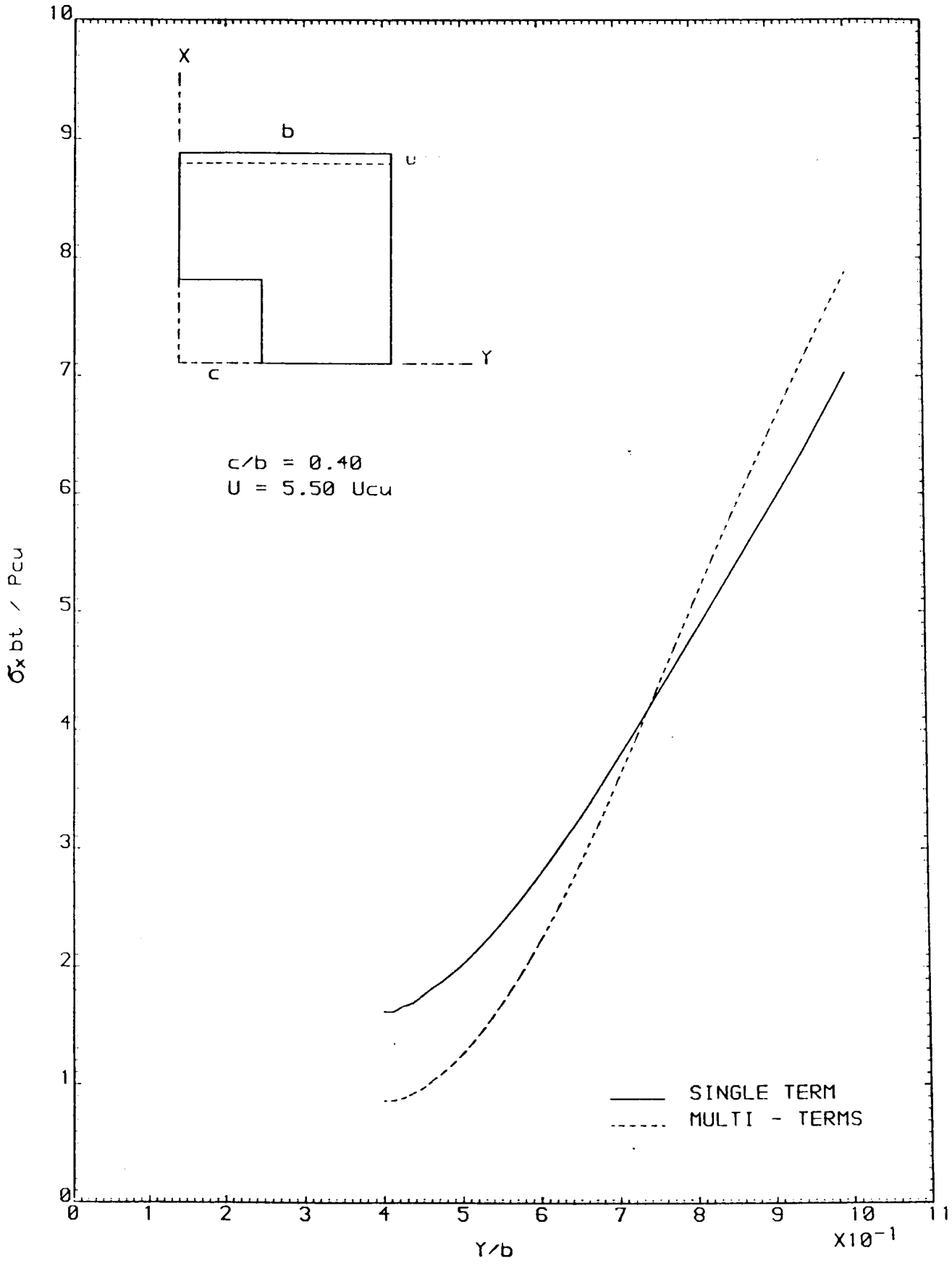

FIGURE 6·108 STRESSES AT THE MINIMUM SECTION

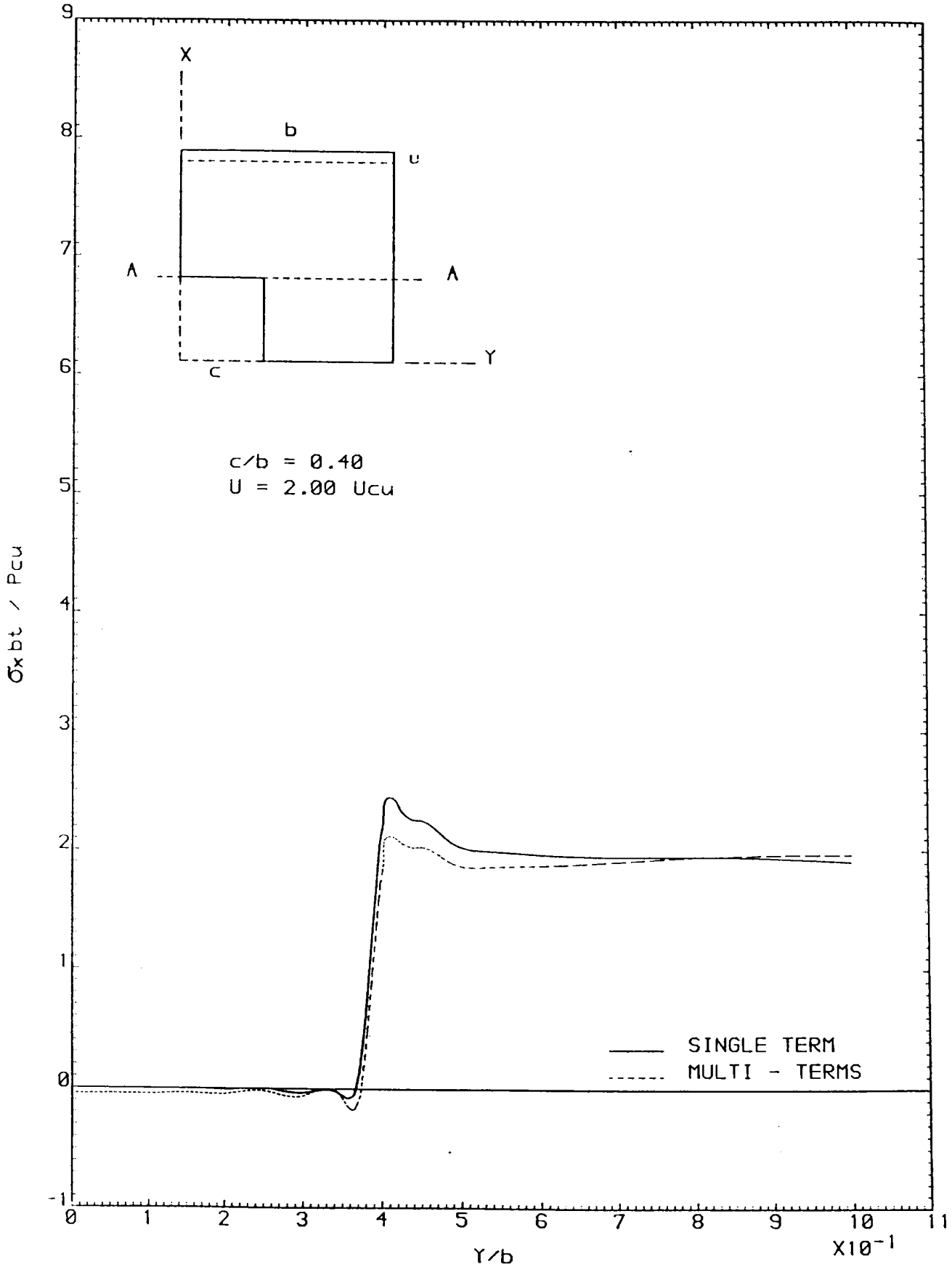

FIGURE 6·109 STRESSES AT SECTION A - A

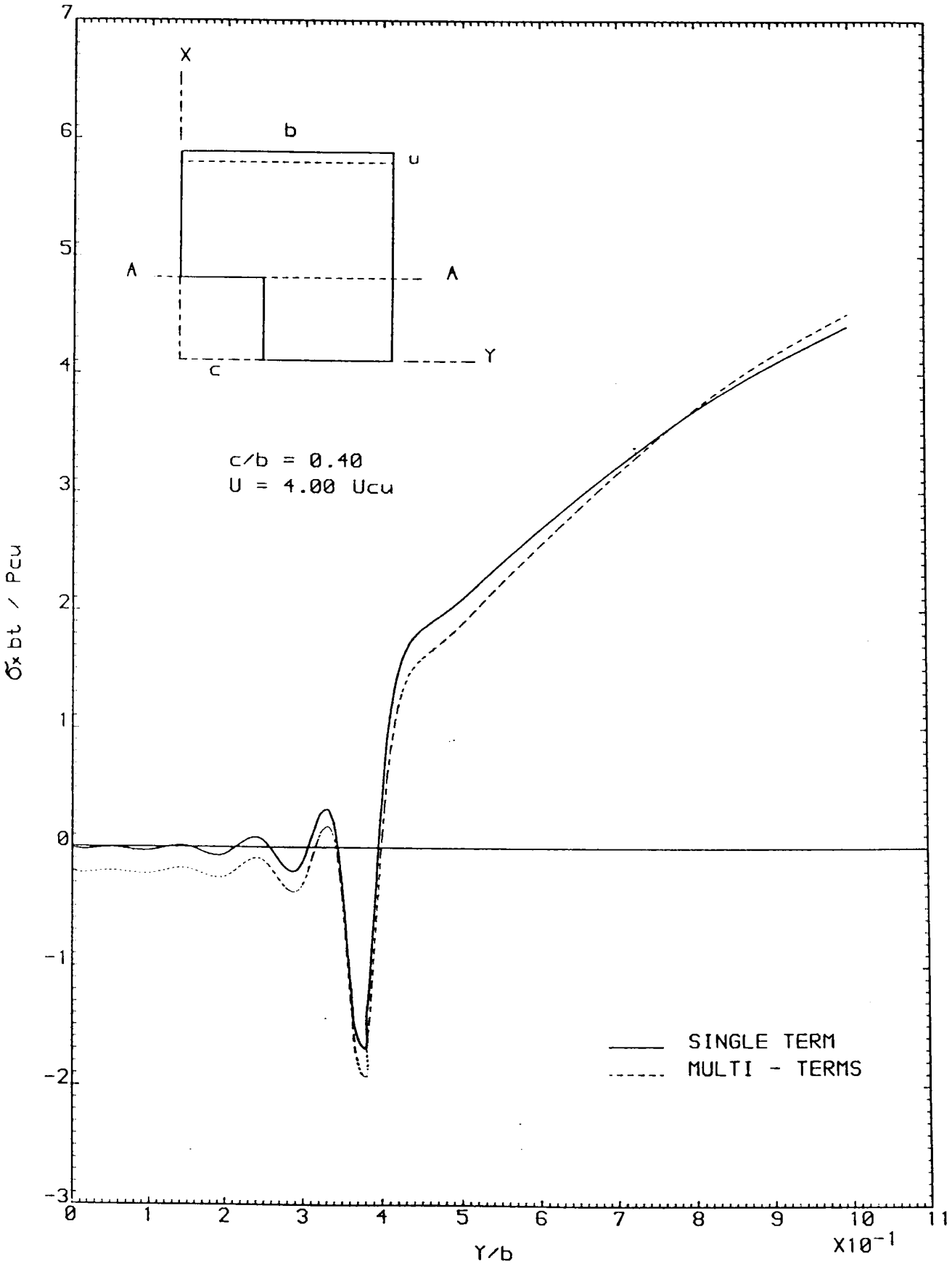

FIGURE 6·110 STRESSES AT SECTION A – A

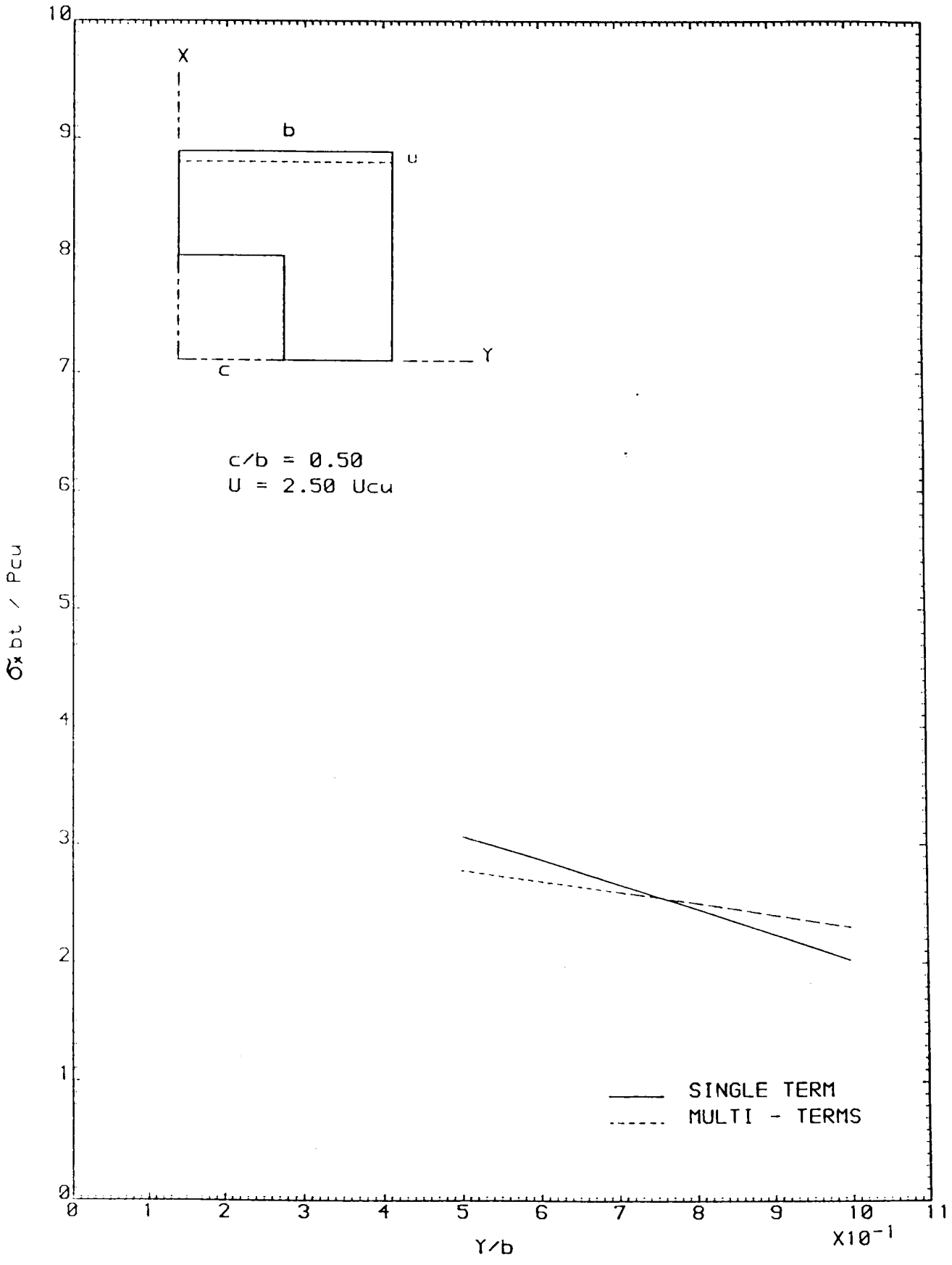

FIGURE 6·111 STRESSES AT THE MINIMUM SECTION

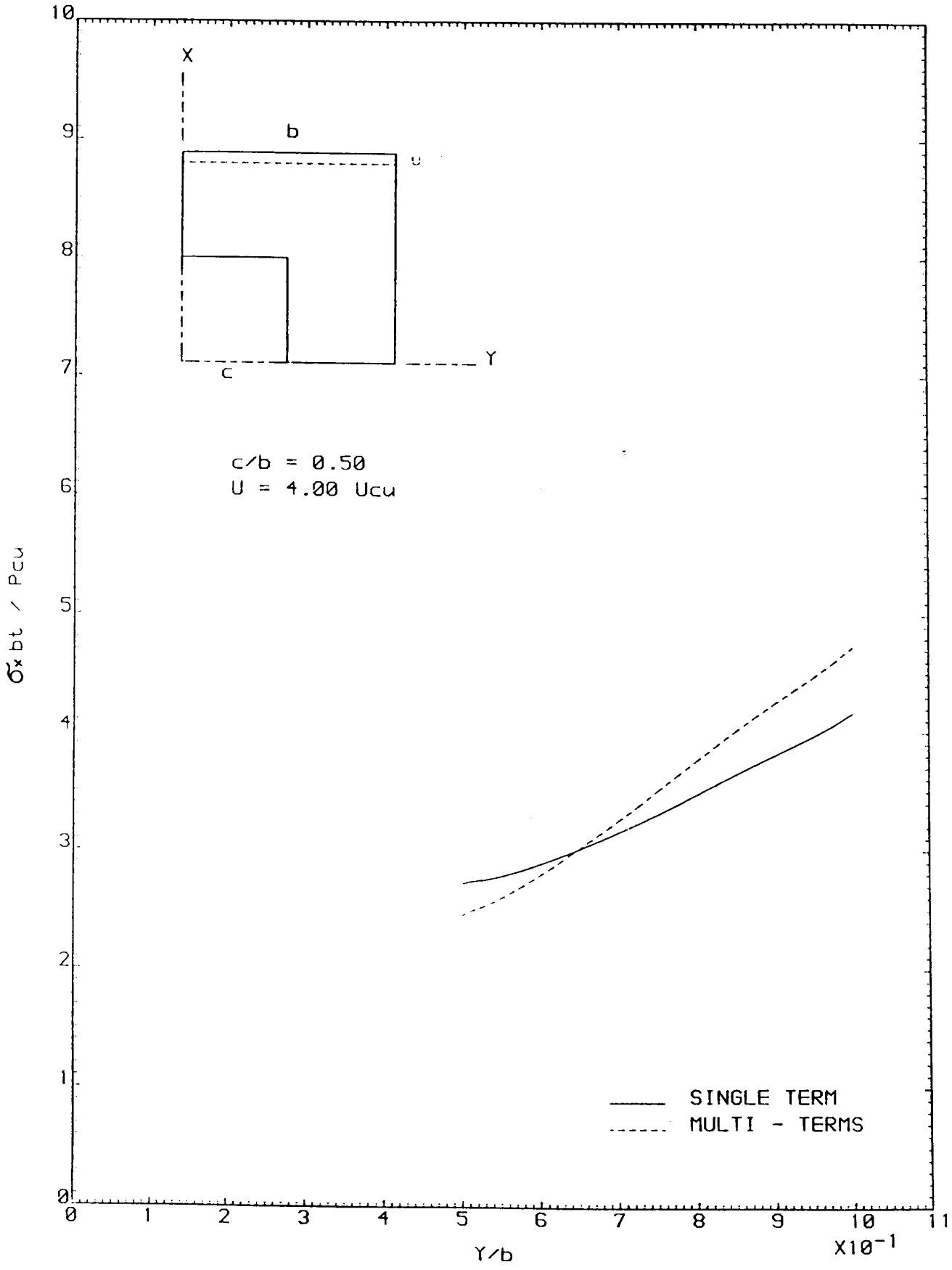

FIGURE 6·112 STRESSES AT THE MINIMUM SECTION

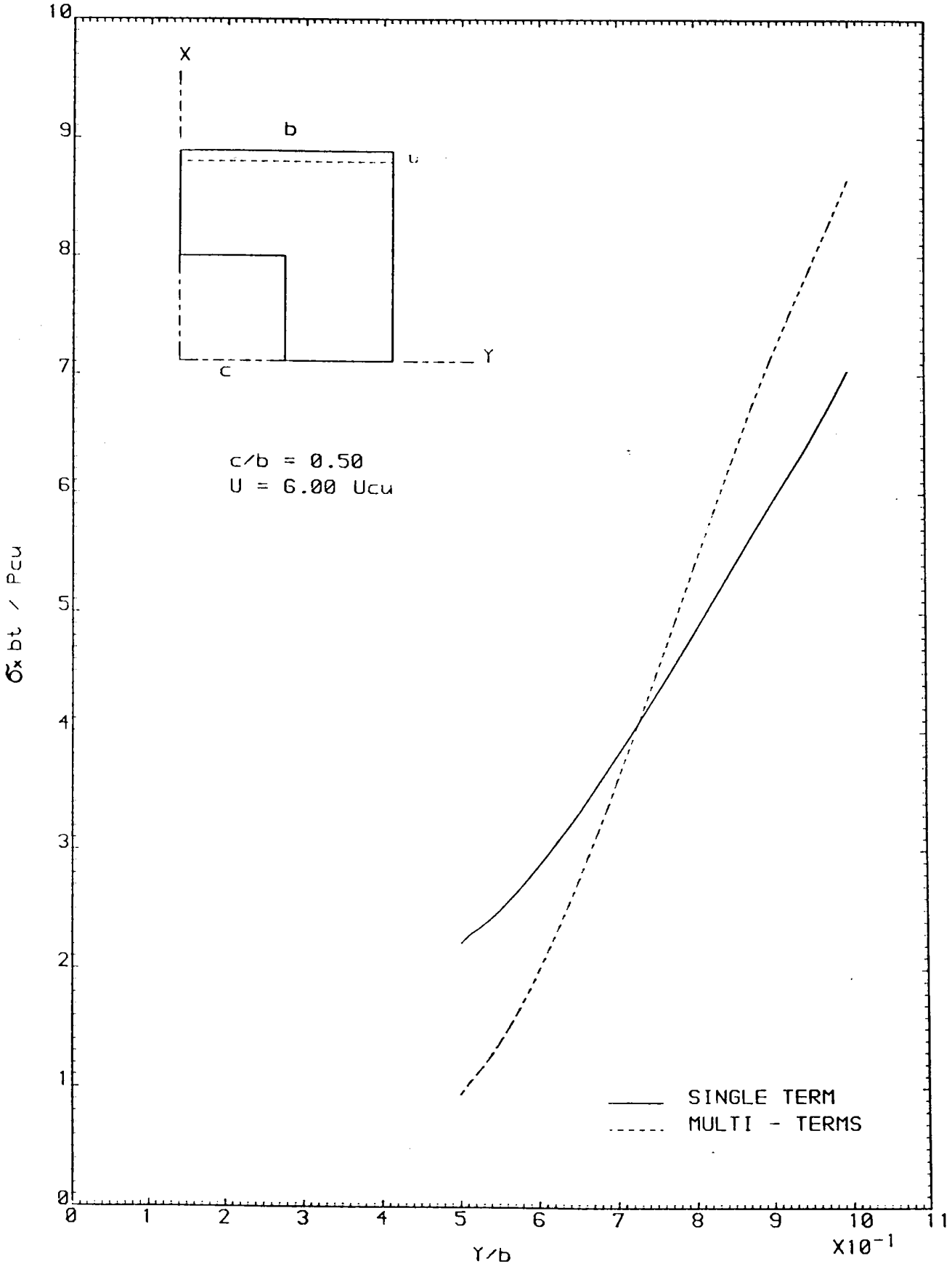

FIGURE 6·113 STRESSES AT THE MINIMUM SECTION

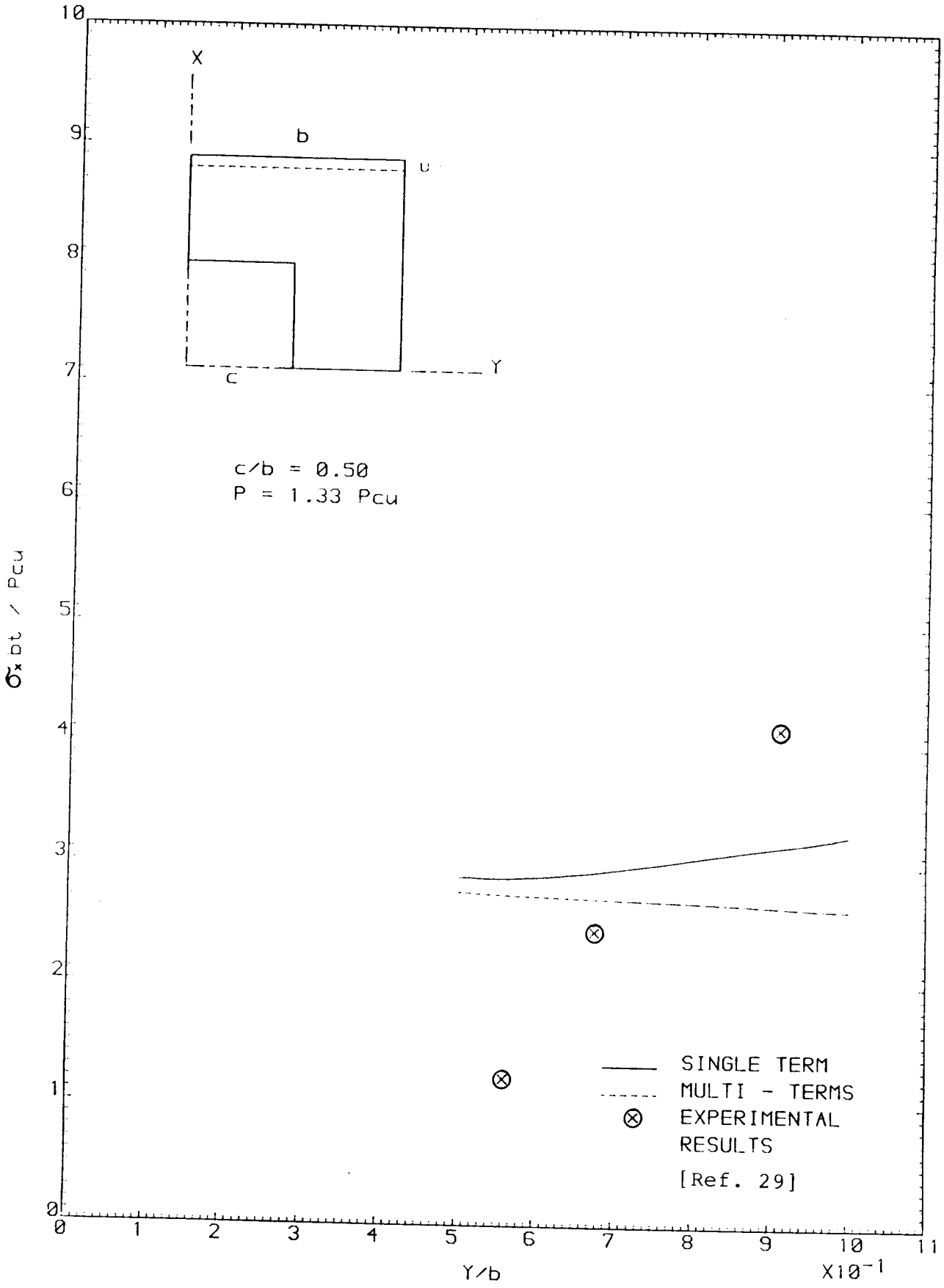

FIGURE 6·114 STRESSES AT THE MINIMUM SECTION

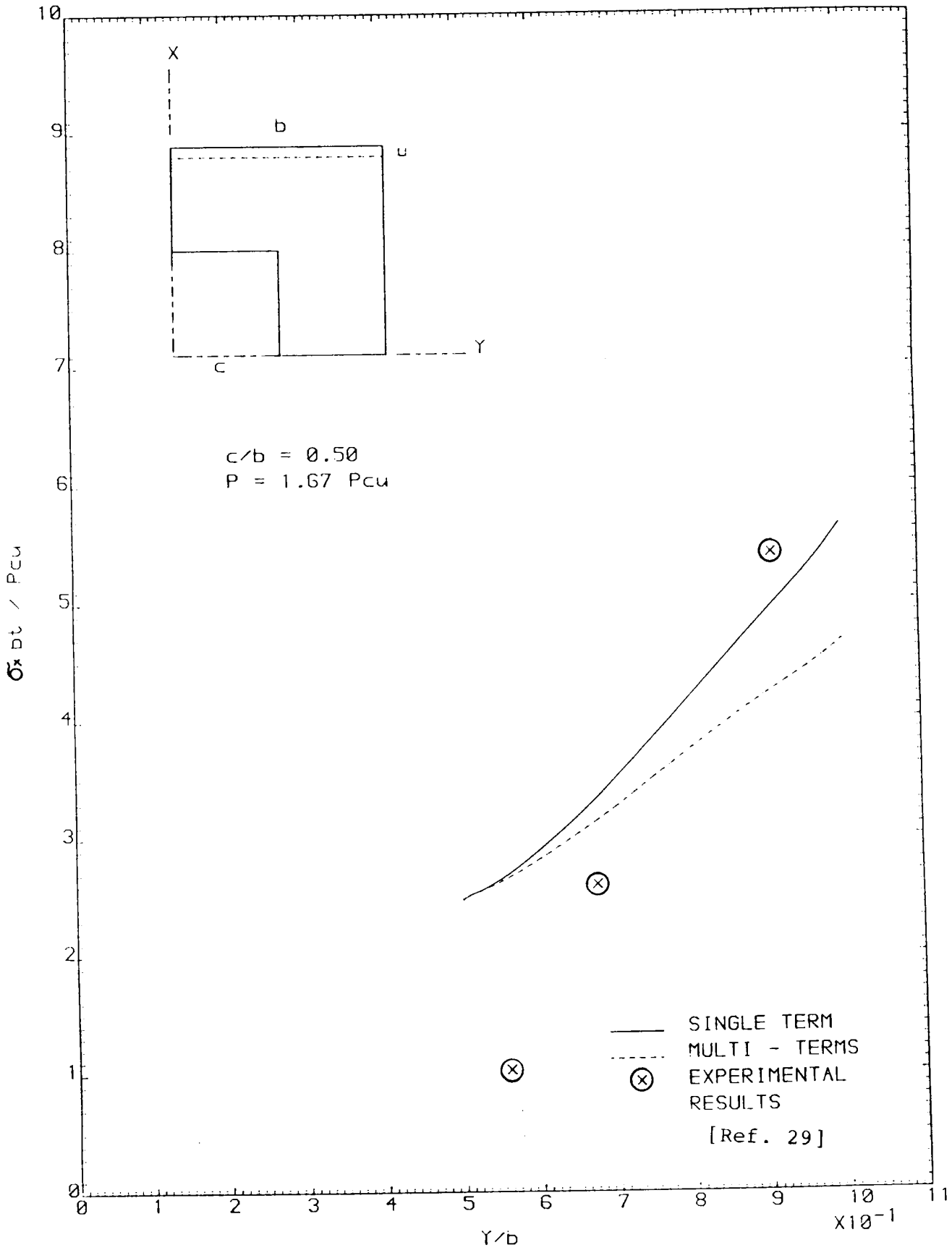

FIGURE 6·115 STRESSES AT THE MINIMUM SECTION

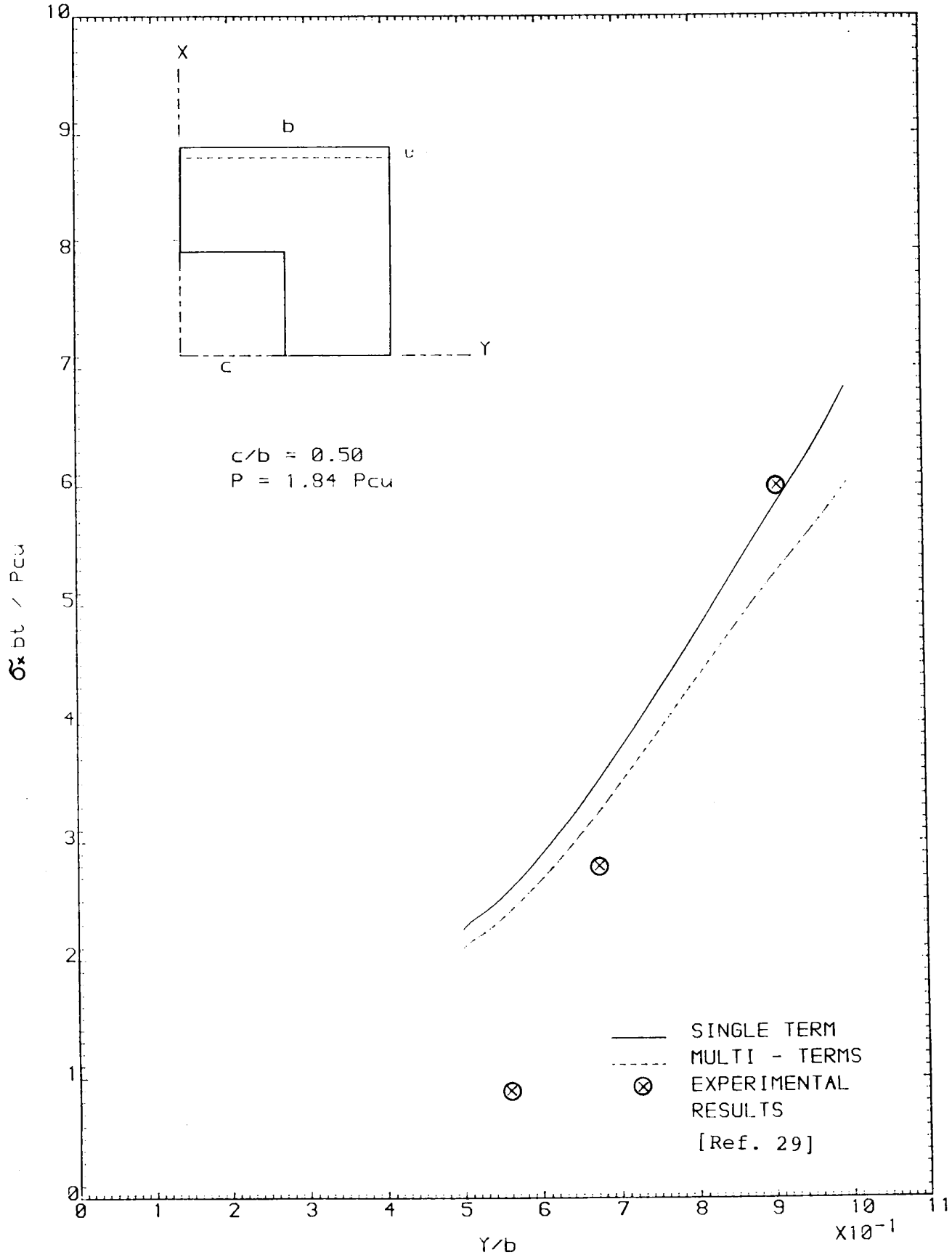

FIGURE 6·116 STRESSES AT THE MINIMUM SECTION

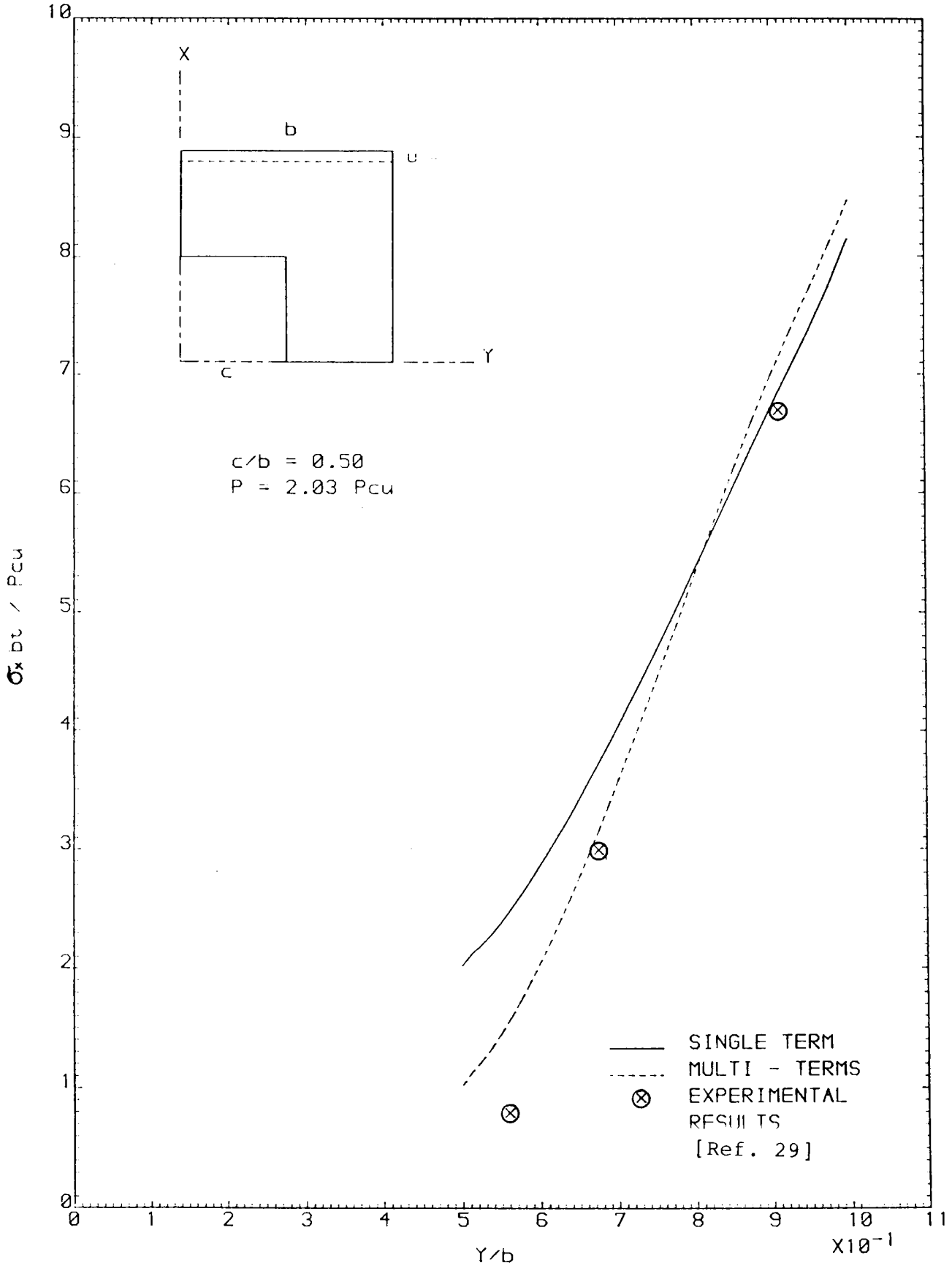

FIGURE 6·117 STRESSES AT THE MINIMUM SECTION

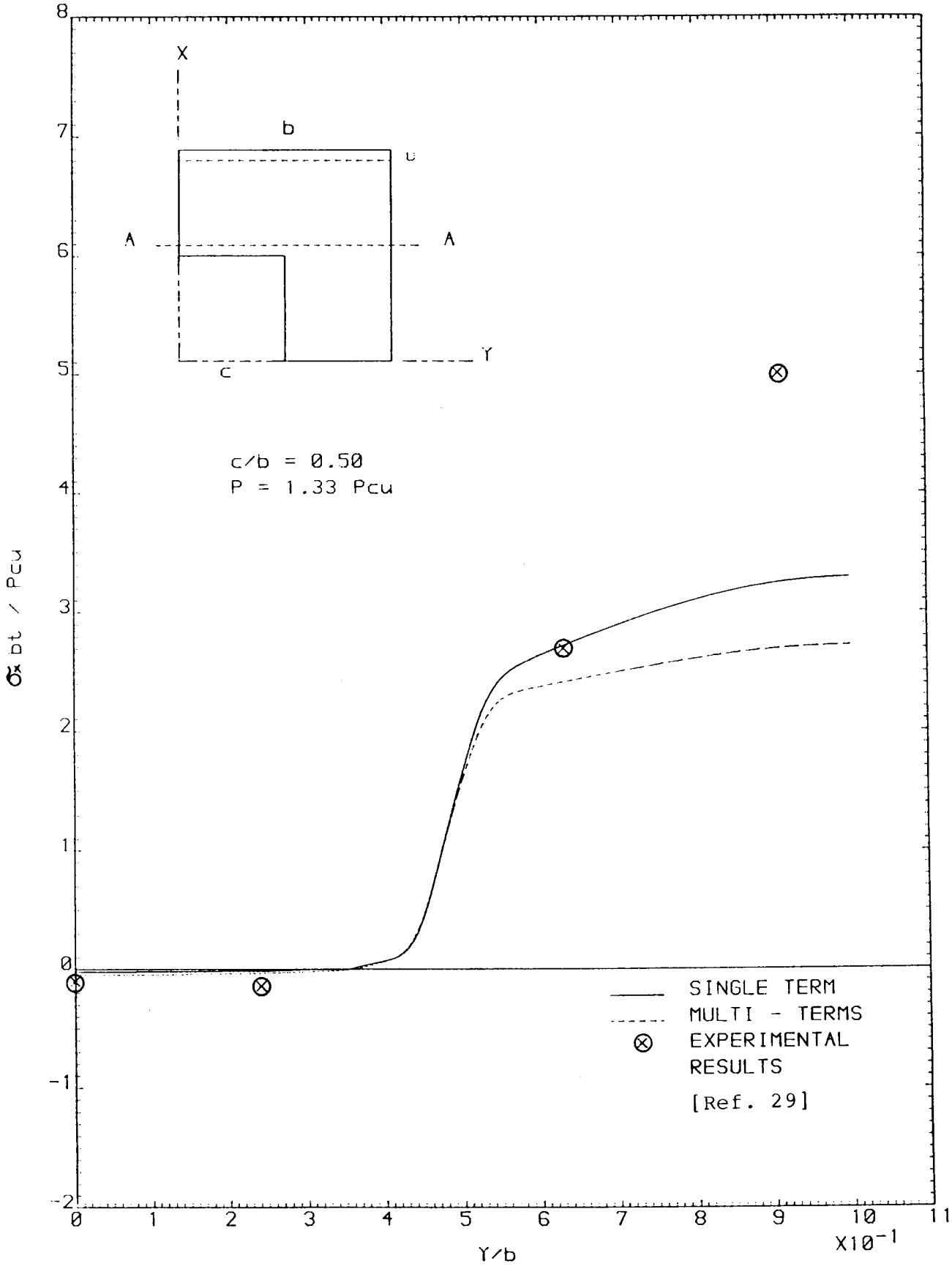

FIGURE 6·118 STRESSES AT SECTION A - A

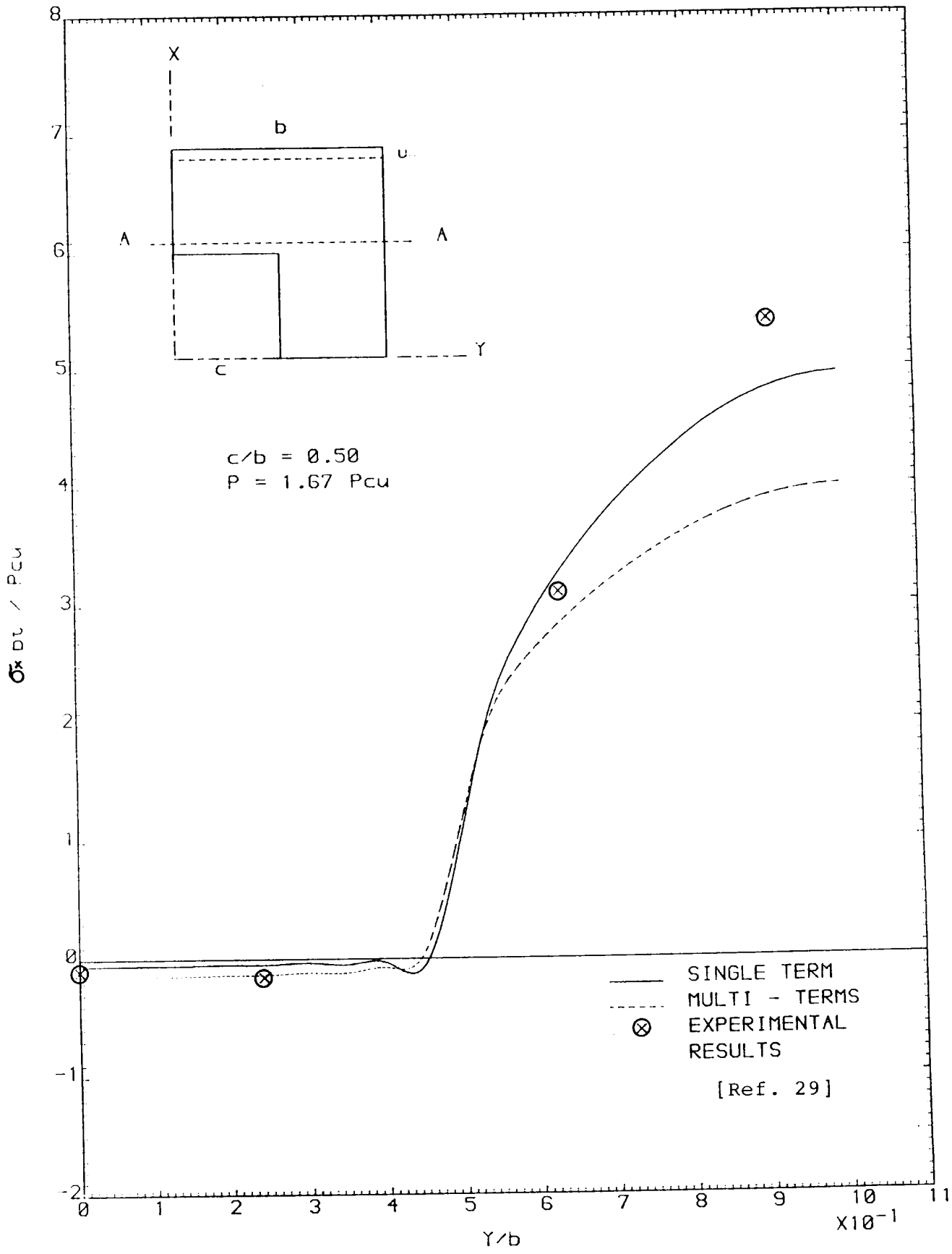

FIGURE 6·119 STRESSES AT SECTION A - A

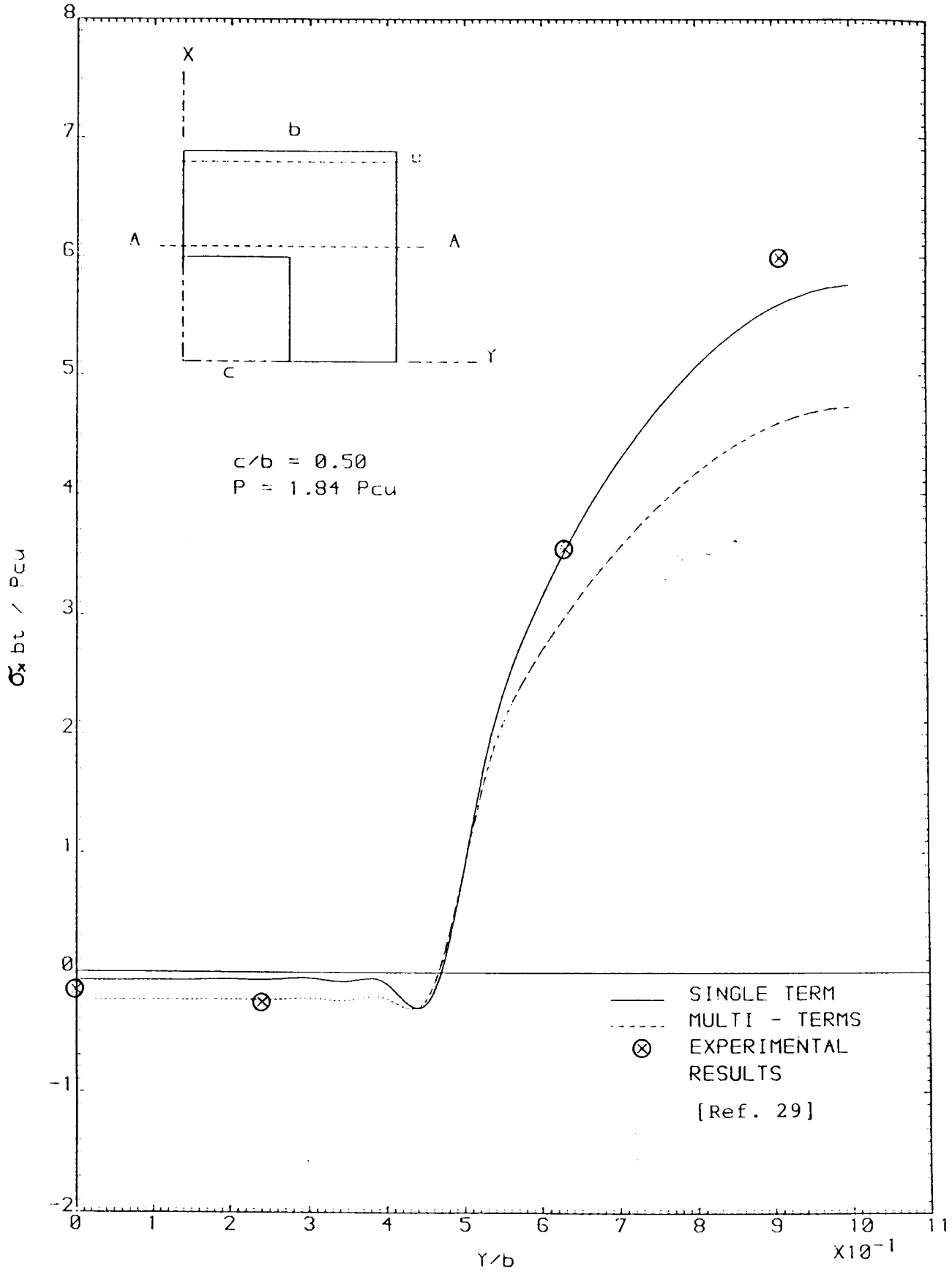

FIGURE 6·120 STRESSES AT SECTION A - A

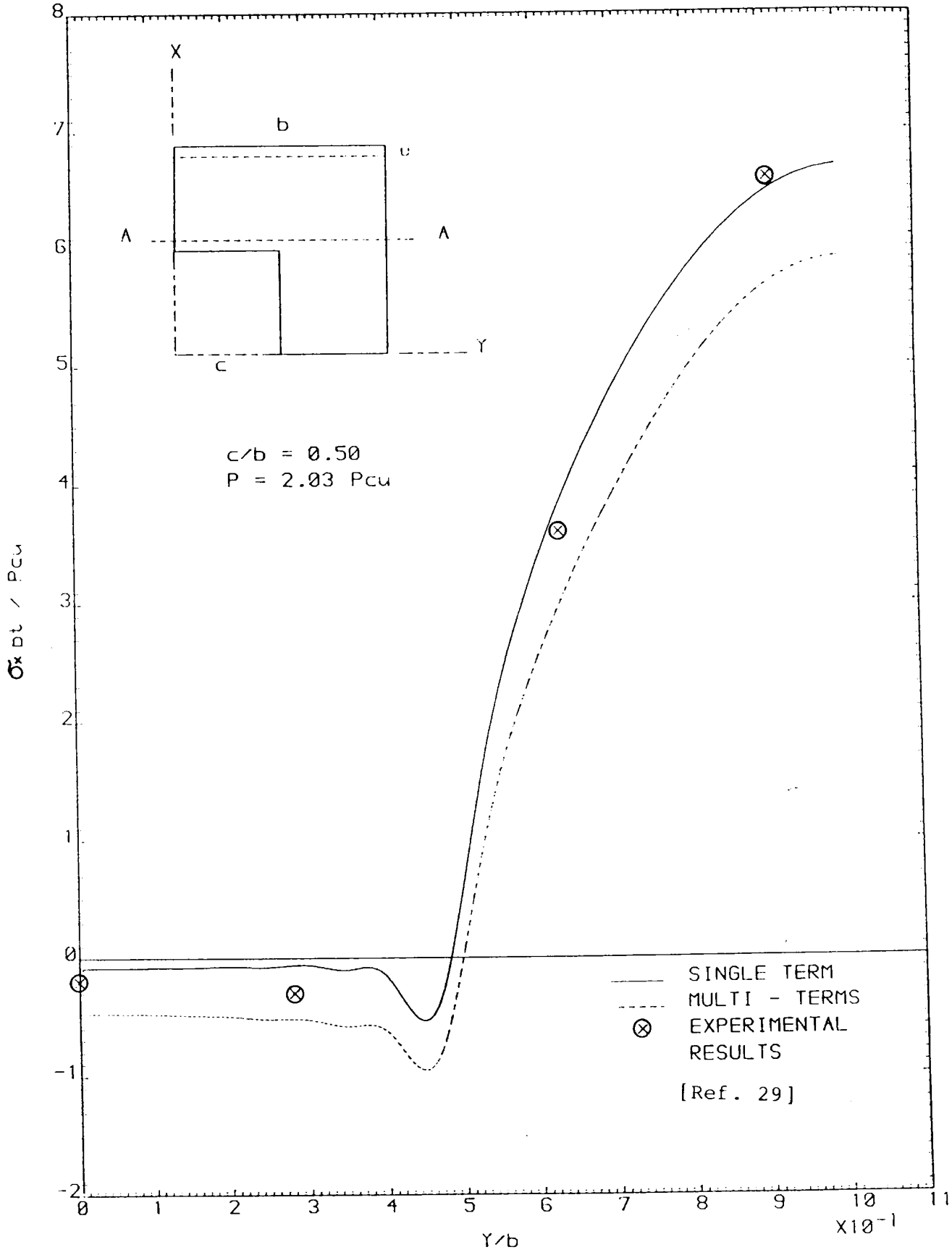

FIGURE 6·121 STRESSES AT SECTION A - A

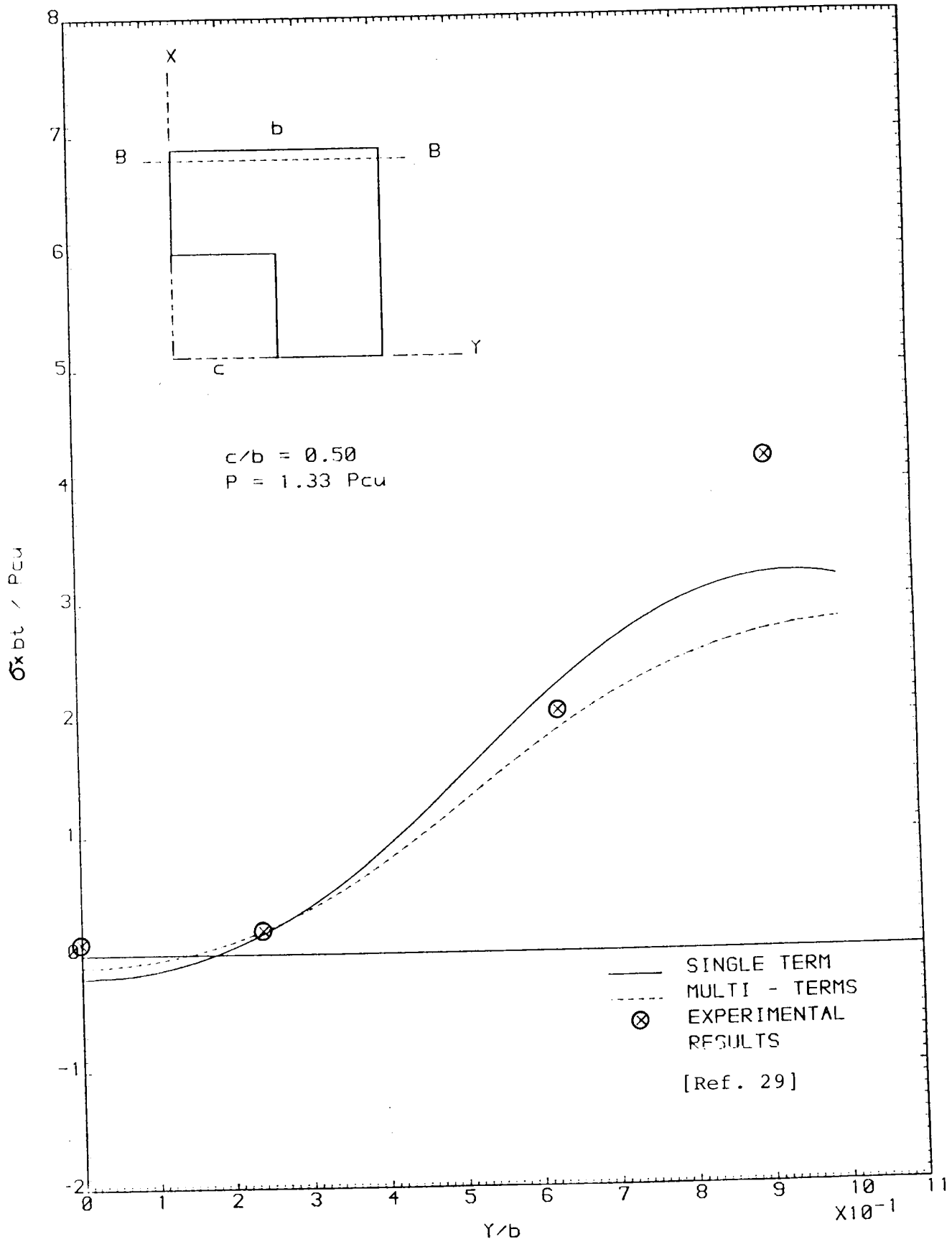

FIGURE 6·122 STRESSES AT SECTION B - B

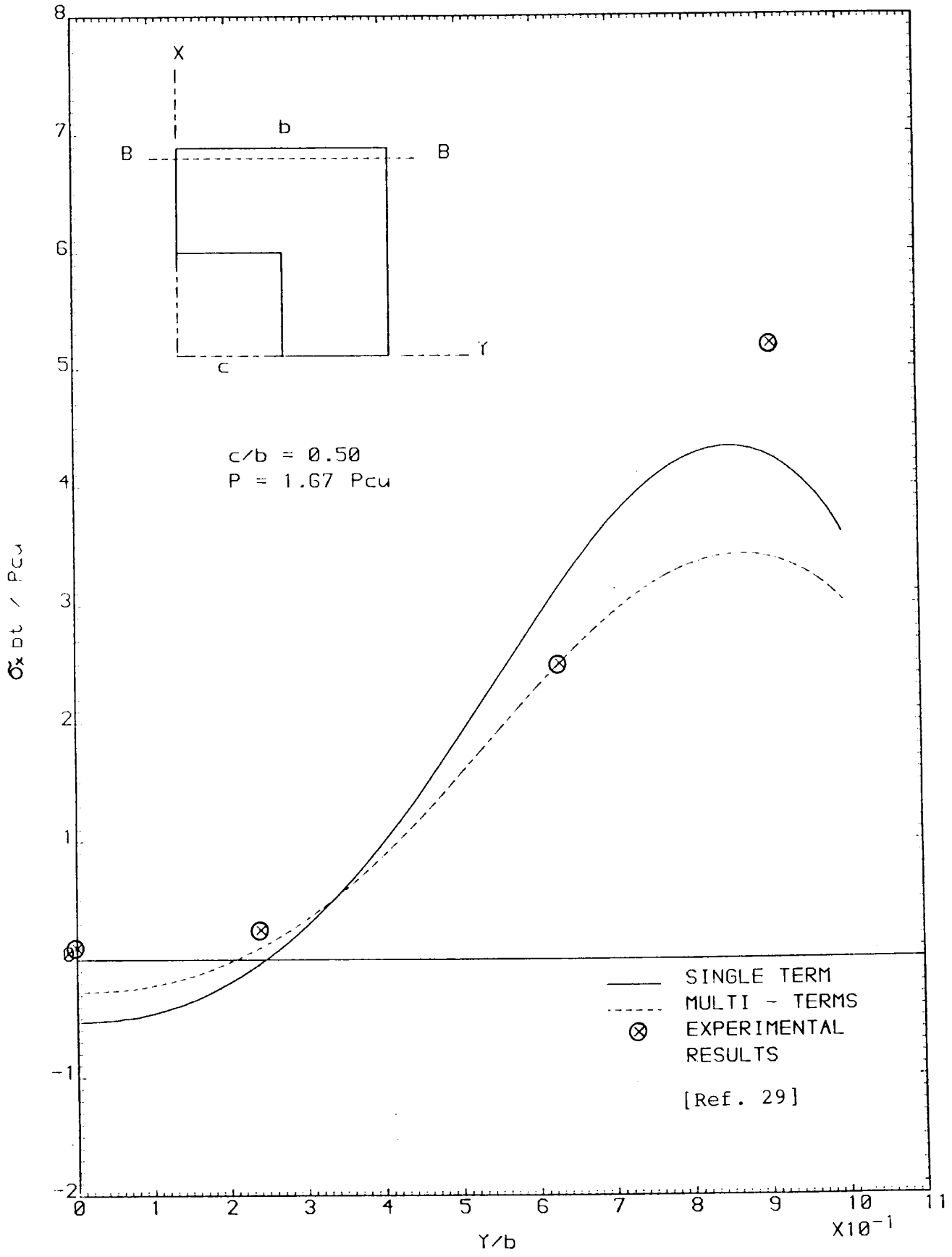

FIGURE 6·123 STRESSES AT SECTION B - B

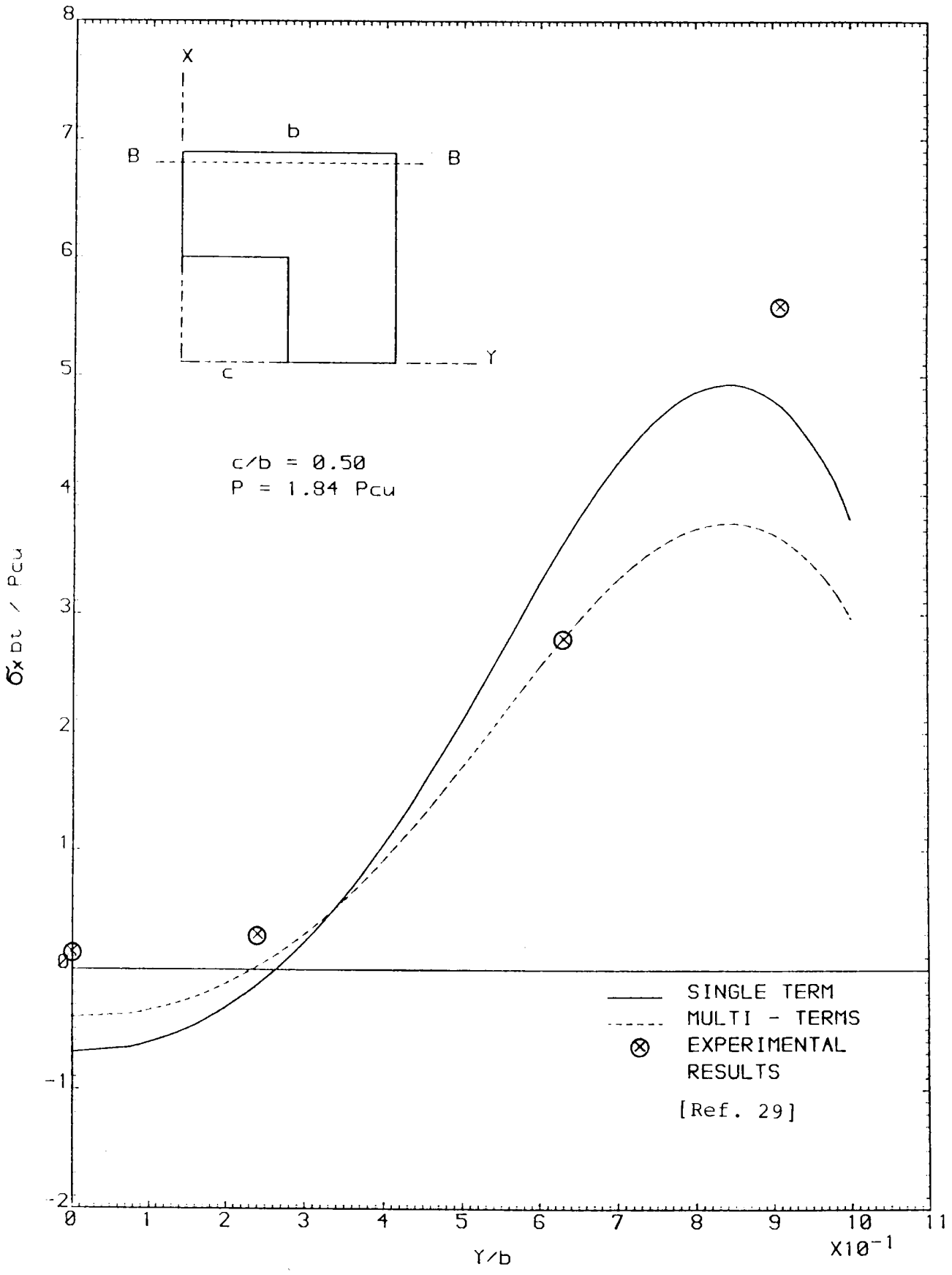

FIGURE 6·124 STRESSES AT SECTION B - B

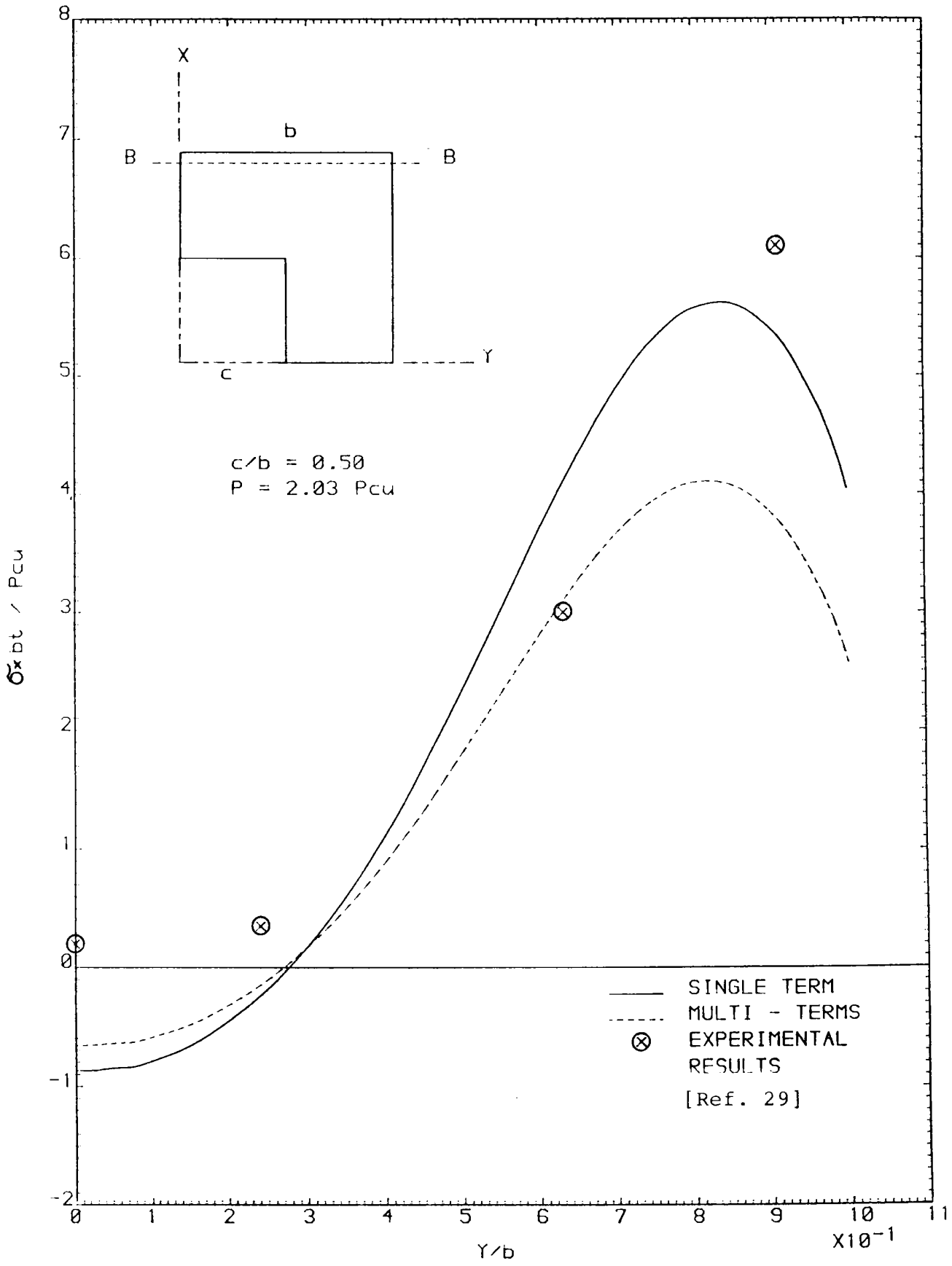

FIGURE 6·125 STRESSES AT SECTION B - B

CHAPTER SEVEN

CONCLUSIONS

CONCLUSIONS

The following conclusive remarks are made on the basis of investigations carried out on the buckling and post-buckling behaviour of simply supported square plates with centrally located circular and square cutouts.

1. Two types of loading cases investigated in buckling analysis, the uniform stress and uniform displacement loading, result in different variations of the buckling loads with the cutout size. For the uniform stress loading case the buckling loads was observed to decrease with the increase in the cutout size. For a more practical case of uniform displacement loading the variation in the buckling load is not significant up to a cutout size of about c/b=0.4, beyond which a marked increase in the buckling load is observed.

2. For cutout sizes up to about c/b=0.35 the variation of the buckling load is the same for plates with a circular and square cutout. For larger cutouts, however, the buckling loads of plates with a square cutout is noticed to be relatively higher than plates with a circular hole of the same nominal size.

3. The present theoretical Out-of-plane deflections and internal stresses variations are in good agreement with the experimental results from two different investigations [10,29]; for plates with a circular and square cutout of all the cutout sizes and at all levels the applied loads. This authenticates the validity of the current theoretical analysis.

4. It is observed that, in the post buckling region, the difference between the theoretical and experimental deflections and stresses reduced with the increase in the applied loading.

5. Both pre- and post buckling axial stiffness of the plate reduces with the increase in cutout size.

6. The redistribution of internal stresses after buckling occur in a manner similar to a plate with no cutout except around the hole boundary where the stress concentration because of the geometric discontinuity can be noticed at all levels of applied loads.

7. The theoretical analysis and experimental investigations show similar trend of redistribution of

membrane stresses in the post-buckling region for all types of plates investigated proving the effectiveness of the theoretical analysis in predicting these stresses.

8. Solutions where buckled shape was allowed to change improved the accuracy of the post-buckling analysis compared to those where buckled shape was kept fixed after the initial instability.

SUGGESTIONS FOR THE FUTURE WORK

1. The current work relates to the study of thin plates with simply supported loaded and unloaded edges and subjected to uniform compressive loading. The analysis procedure proposed may be extended to cover other types of loading and boundary conditions.

2. Plates with centrally located cutouts have been investigated. The analysis may be applied to study the post-buckling behaviour of plates with eccentric cutouts.

3. The analysis may be extended to carry out post-buckling analysis of plates with reinforced cutouts.

4. During the application of the current analysis finite element packages were used to evaluate the in-plane stresses. A massive data handling was required particularly for the multiterm solution to transfer the information from the finite element output to the spline data input. A finite element algorithm to carry out two dimensional stress analysis may be coupled with the current computer programme to avoid data handling.

BIBLIOGRAPHY

BIBLIOGRAPHY

BOOKS

1. TIMOSHENKO, S.P. AND GERE, J.M.

   "Theory of Elastic Stability".
   McGraw-Hill, 1961

2. ALLEN, H.G. AND BULSON, P.S.

   "Background to Buckling". 1980
   McGraw-Hill, 1980.

3. BULSON, P.S.

   "The Stability of Flat Plates".
   Chantto and Windus 1970

4. CHUEN-YUAN CHIA

   "Non Linear Analysis of Plates".
   McGraw-Hill, 1980.

5. COOK, R.D.

   "Concepts and Applications of Finite Element Analysis".
   John Willey and Sons. 1981

6. ZEINKIEWICZ, O.C.

   "The Finite Element Method in Engineering Science".
   McGraw-Hill

7. AHLBERG, J.H., NILSON, E.N., AND WALSH, J.L.

   "The Theory of Splines and their Application".
   Academic Press, 1967

REFERENCES ON PLATES WITH CUTOUTS

8. LEVY, S. WOOLLEY, M AND KROLL, W.D.

"Instability of a Simply Supported Square Plate with reinforced Circular Hole in Edge Compression".
Journal Research National Bureau of Standards, Vol. 39, pp. 571-577, 1947.

9. KUMAI, T.

"Elastic Stability of Square plate with a Central Circular Hole Under Edge Thrust".
Proceedings of the First Japan National Congress for Applied Mechanics, pp. 81-86, 1951.

10. RITCHIE, D.

"The Buckling and Post-Buckling Behaviour of Simply Supported Rectangular Plates with Centrally located Circular Holes".
Ph.D. Thesis, The University of Strathclyde 1975.

11. AZIZIAN, Z.G.

"Instability and Non-Linear Analysis of Thin Walled Structures".
Ph.D. Thesis. University College Cardiff, 1983.

12. KAWAI, T. AND OHTSUBO, H.

"A Method of Solution for the Complicated Buckling Problems of Elastic Plates with Combined Use of Rayleigh-Ritz Procedure in the Finite Element Method".
Proc. 2nd Air Force Conference on Matrix Method in Structural Mechanics October 1968.
Ref. AFTDL - TR-68-150. PP 967-994.

13. VOL´MIR, E.A., MAMEEVA, E.N. AND SIDORENKO, A.S.

"Study of the Stability of a Rectangular Plate with a Rectangular Cutout under the action of a compressive load".
Strength of Materials, Vol. 12, No. 6, Feb. 1981 pp. 769-772 (Translation)

14. TOSHIKI, M., FUJITA, Y. AND ARAI, H.

"Instability of Plates with Holes".(First Report) Proceedings:- Society of Noval Architects of Japan, pp. 137-145, Dec. 1967.

15. NICHOLAS, L. BASDEKAS

"Stability of Plates with Cutouts". Report National Science Foundation.

16. JENG - SHENG HUANG

"Buckling Finite Element Analysis of Flat Plates with a Rectangular Hole". Proceedings:- NCKU/ AAS International symposium on Engineering Science and Mechanics, pp. 694-709.

17. PREOBRAZHENSKII, I.N.

"Rerearch Pertaining to Stability of Thin Plates with Holes (Survey)". (Translation) Prikladnaya Mekhanika, Vol. 16, No. 7, pp. 3-25, July, 1980.

18. SABIR, A.B. AND CHOW, F.Y.

"Elastic Buckling of Flat Panels Containg Circular and Square Holes". Proceedings The Michael R Horne Conference on Instability and Platic Collapse of Steel Structures, pp. 311-321, 1983.

19. SABIR, A.B. AND CHOW, F.Y.

"Elastic Buckling of Plates Containing Eccentrically Located Circular Holes". Thin Walled Structures, Vol. 4, pp. 135-149, 1986.

20. BROWN, C.J. AND YETTRAM, A.L.

"The elastic Stability of Square Perforated Plates". Computers and Structures, Vol. 21, No. 6, pp. 1267-1272, 1985.

21. BROWN, C.J. AND YETTRAM, A.L.

"The elastic Stability of Square Perforated Plates Under biaxial Loading".
Computers and Structures, Vol. 22, No. 4, pp. 589-594, 1986.

22. BROWN, C.J. AND YETTRAM, A.L.

"The elastic Stability of Square Perforated Plates Under Combinations of Bending, Shear and Direct Load".
Thin-Walled Structures Vol. 4, pp. 239-246, 1986.

23. KURSHI, L.M. AND MATVEEV, K.A.

"Application of Energy Method to Problems Involving The Stability of Plates With Holes".

24. SCHLACK, J.L. Jr.

"Elastic Stability of Pierced Square Plates".
Proceedings Society of experimental Stress Analysis, Vol. 21, Pt. 1, pp. 167-172, 1964.

25. SCHLACK, A.L. Jr.

"Experimental Critical Loads for perforated square plates".
Proceedings Society of Experimental Stress Analysis, Vol. 25, Pt. 1, pp. 69-74, 1968.

26. RITCHIE, D. AND RHODES, J.

"Buckling and Post-Buckling Behaviour of Plates with Holes".
Aeronatical Quaterley, pp. 281-296, Nov. 1975

27. AZIZIAN, Z.G. AND ROBERTS, T.M.

"Buckling and Elasto-Plastic Collapse of Perforated Plates".
Proceedings:- The Michael R Horne Conference on Instability and Plastic Collapse of Steel Structures, pp. 322-328, 1983.

28. NARAYANAN, R AND CHOW, F.Y.

"Ultimate Capacity of Uniaxially Compressed Perforated Plates".
Thin Walled Structures, Vol. 2, No. 3, pp. 241-264, 1984.

29. BAIG, M.A.

"An Experimental Investigation of The Compressive Post-Buckling Behaviour of Thin Plates with Cutonts".
MSc. Thesis Cransfield Institute of Technology, 1985.

30. YU W.W., AND DAVIS, C.S.

"Buckling Behaviour and Post-Buckling Strength of Perforated Stiffened Compression Elelments".

31. SHANMUGAM, N.E. AND NARAYANAN, R.

"Elastic Buckling of Perforated Square Plates for various Loading and Edge Conditions".
International Conference on Finite Element Methods, Shanghai, 1982.

SHEAR WEBS

32. JARMILA COUGHLAN

"The Buckling and Colapse Behaviour of Plate Members containing Holes".
Msc. Thesis, University of Wales, 1970.

33. ROCKEY, K.C. ANDERSON, R.G. AND CHEUNG Y.K.

"The Behaviour of a Shear Web Having Circular Holes".
Proceedings of the Swansea Symposium on Thin Walled Structures, Crosby, Lockwood and sons, London, pp. 148-69, 1967.

34. HORNE, M.R.

"Basic Concepts in the Design of Webs".
Paper 10 Simen Engineering Laboratories University of Manchester.

35. NARAYANAN, R. AND DER AVANESSIAN, N.G.V.

"A Series of Reports on Ultimate Shear Capacity of plate girders containing cutouts".
University College, Cardiff, Reports, 1980, 1981a, 1981b, 1982a and 1982b.

36. NARAYANAN, R. AND ROCKEY, K.C.

"Ultimate Load Capacity of Plate Girders with Webs containing Circular Cutouts".
Proceedings of the Institute of Civil Engineers, Vol. 71, part 2, pp. 845-862, Sept. 1981.

37. NARAYANAN, R.

"Ultimate Shear Capacity of Plate Girders with openings in Webs".
Plated Structures, Edited by Narayanan, R.
Applied Science Publishers, 1982.

38. NARAYANAN, R. AND DER AVANESSIAN, N.G.V.

"Elastic Buckling of Perforated Plates Under Shear".
Thin Walled Structures, vol. 2, No. 1, 1984.

SPLINE ANALYSIS

39. HAYES, J.G. AND COX, M.G.

"Curve Fitting: A Guide and Suite of Algorithms for the Non-Specialist User".
NAC Report NAC 26, December 1973, Amended September 1974, National Physical Labororatory Division of Numerical Analysis and Computing

40. HAYES, J.G. AND HALLIDAY, J.

"The Least-Squares Fitting of Cubic Spline Surfaces to General Data Sets".
J. Inst. Math. Applics., Vol. 14, pp. 89-103, 1974

41. COX, M.G.

"The numerical Evaluation of B-spline".
J. Inst. Math. Applics., Vol. 10, pp. 134-149, 1972.

42. DE BOOR, C.

"On Calculation With B-Splines".
J. Approx. Theoy, 6, pp. 50-62, 1972.

43. SCHOENBERG, I.J.

Q. appl. Maths. vol. 4, pp. 45-99, 1946.

44. CUURY, H.B. AND SCHOENBERG, I.J.

J. Analyses Math., vol. 17, pp. 71-107. 1966.

45. COX, M.G.

J. Inst. Maths. Applics. 15, 95-108. 1975.

Report NAC 66, National Physical Laboratory, Teddington, Middlesex. 1973.

Report NAC 68, National Physical Laboratory, Teddington, Middlesex. 1976.

46. HAYES, J.G.

"Numerical Methpods for curve and surface fitting"
Bull. Inst. Maths. Applics. 10, 144-152.

47. ALHBERG, J.H., NILSON, E.N. AND WALSH, J.L

"The Theory of Splines and their Applications"
New York: Academic Press, 1967.

48. LOUGHLAN, J.

"Mode Interation in Lipped Channel Columns Under Concentric or Eceentric Loading".
Ph.D. Thesis the University of Strathclyde, 1979

49. YAMAKI, N.

"Post-Buckling Behaviour of Rectagular Plates with Small Initial Curvature Loaded in End Compression".
Jounal of Applied Mechanics, Vol. 26 pp. 407-414, 1959, and Vol. 27, pp. 335-342, 1960.

50. YAMAKI, N.

"Experiments on Post-Buckling Behaviour of Square plates loaded in Edge Compression".

51. SUPPLE, W.J. AND CHILVER, A.H.

"Elastic Post-Buckling of Compressed Rectangular Flat Plate".
Thin Walled Structure, A.H. Chilver, Chatto and Windus, 1967.

52. COAN, J.M.

"Large Deflection Theory for Plates with Small Initial Curvature Loaded in Edge Compression".
Journal of Applied Mechanics, pp.143-151, June 1951.

53. BULSON, P.S.

"The Plate Buckling Coefficient".
Technical Note, Journal of the Royal Aeronautical Society, Vol. 71, pp. 37-40, Jan. 1967.

54. RHODES, J.

"Effective Width in Plate Buckling".

55. RHODES, J. AND HARVEY, J.M.

"The Post-Buckling Behaviour of Thin Flat Plates in Compression with the Unloaded Edges Elastically Restrained against Rotation".
Jour. Mech. Eng. Sciences, Vol. 13(2), 1971.

56. RUSHTON, K.R.

"Post-Buckling of Rectangular Plates with various Boundary Conditions". The Aero. Quarty. May 1970.

57. DOMBOURIAN, E.M., SMITH, C.V. Jr. AND CARLSON, R.L.

"A Perturbation Solution to a Plate Post-Buckling Problem".
Int. Jour. Non-Linear Mechanics, Vol. 11, pp. 49-58, 1976.

58. VILNAY, O. AND ROCKEY, K.C.

"A Generalised Effective Width Method for Plates Loaded in Compression".
Journal of Constructional Steel Research, Vol. 1, No. 3, May 1981.

59. HORNE, M.R. AND NARAYANAN, R.

"Strength of axially loaded stiffened panels."
Memoires 36-I, International Association for Bridges and Structural Engineering, Zurich, 1976, pp. 125-57.

APPENDIX A

SOLUTION OF VON KARMAN COMPATIBILITY EQUATION

SOLUTION OF THE VON KARMAN COMPATIBILITY EQUATION

This appendix describes the solution of the Von Karman compatibility equation for a simply supported unperforated plate. The derivations have been carried out in conjunction with the theoretical analysis described in chapter four. The stress functions used during the analysis relate to the stress system 2 [section 4.5.1.2] which represents the post-buckling stresses in an unperforated plate assuming zero displacement of the loaded edges.

Consider a plate of length 2l, width 2b and thickness t, as shown in figure A.1. The deflection function used in chapter four for the theoretical analysis is rewritten here for convenience.

$$W = \sum \sum A_{ij} \operatorname{Cos} \frac{a_i \pi x}{l} \operatorname{Cos} \frac{b_j \pi y}{b} \qquad \text{A.1}$$

where A_{ij} are the deflection coefficients, a_i =1,3,5 etc. and b_j =1,3,5 etc. The deflection function automatically satisfies simple support boundary conditions at the loaded and unloaded edges. To simplify the derivations we will assume two terms along the loaded direction, i.e. put a_i=1,3 in equation A.1.

let

$$Y_j = \cos \frac{b_j \pi y}{b} \qquad \text{A.2}$$

Equation 4.1 can now be written in the following form :

$$w = \cos \frac{a_1 \pi x}{\ell} \sum A_{1j} Y_j + \cos \frac{a_2 \pi x}{\ell} \sum A_{2j} Y_j \qquad \text{A.3}$$

The Von Karman compatibility given by equation 2.19 is rewritten below :

$$\nabla^4 F = \frac{\partial^4 F}{\partial x^4} + 2\frac{\partial^4 F}{\partial x^2 \partial y^2} + \frac{\partial^4 F}{\partial y^4}$$

$$= E\left[\left(\frac{\partial^2 \omega}{\partial x \partial y}\right)^2 - \frac{\partial^2 \omega}{\partial x^2} \cdot \frac{\partial^2 \omega}{\partial y^2}\right] \qquad \text{A.4}$$

Taking the appropriate derivatives of w in equation A.3 and substituting in equation A.4 , we obtain the following equation.

$$\nabla^4 F = E\left(\frac{a_1\pi}{\ell}\right)^2 \sum\sum A_{1i}\, A_{1j} \left[Y_i' Y_j' \sin^2\frac{a_1\pi x}{\ell} + Y_i Y_j'' \cos^2\frac{a_1\pi x}{\ell} \right]$$

$$+ E\left(\frac{\pi}{\ell}\right)^2 \sum\sum A_{1i}\, A_{2j} \left[2 a_1 a_2 \sin\frac{a_1\pi x}{\ell} \sin\frac{a_2\pi x}{\ell} Y_i' Y_1' \right.$$

$$\left. + \cos\frac{a_1\pi x}{\ell} \cos\frac{a_2\pi x}{\ell} \left(a_1^2 Y_i Y_j'' + a_2^2 Y_j Y_i'' \right) \right] \quad \text{A.5}$$

$$+ E\left(\frac{a_2\pi}{\ell}\right) \sum\sum A_{2i}\, A_{2j} \left[Y_i' Y_j' \sin\frac{a_2\pi x}{\ell} \right.$$

$$\left. + Y_i Y_j'' \cos^2\frac{a_2\pi x}{\ell} \right]$$

Assuming $F = F_A + F_B + F_C$

The equation A.5 can be divided into the following three equations.

$$\nabla^4 F_A = E\left(\frac{a_1\pi}{\ell}\right)^2 \sum\sum A_{1i}\, A_{1j} \left[Y_i' Y_j' \sin^2\frac{a_1\pi x}{\ell} + Y_i Y_j'' \cos^2\frac{a_1\pi x}{\ell} \right] \quad \text{A.6}$$

$$\nabla^4 F_{CD} = E\left(\frac{\pi}{\ell}\right)^2 \sum\sum A_{1i} A_{2j}$$
$$\left[2 a_1 a_2 \sin\frac{a_1\pi x}{\ell} \sin\frac{a_2\pi x}{\ell} Y_i' Y_1'\right.$$
$$\left. + \cos\frac{a_1\pi x}{\ell} \cos\frac{a_2\pi x}{\ell} \left(a_1^2 Y_i Y_j'' + a_2^2 Y_j Y_i''\right)\right] \quad \text{A.7}$$

$$\nabla^4 F_B = E\left(\frac{a_2\pi}{\ell}\right) \sum\sum A_{2i} A_{2j} \left[Y_i' Y_j' \sin^2\frac{a_2\pi x}{\ell}\right. \quad \text{A.8}$$
$$\left. + Y_i Y_j'' \cos^2\frac{a_2\pi x}{\ell}\right]$$

Equations A.6, A.7, and A.8 are the differential equations in F_A, F_B and F_{CD} and can be solved independently; each one satisfying the boundary conditions at the loaded and unloaded edges. It may be noted that these equations have been derived by taking the first two x terms of the deflection function (A.1). If, however, more than two terms are desired along the the loaded direction, more differential equations of the similar type will emerge. For a special case of a fixed buckled shape F_B and F_{CD} are zero and a solution of the equation A.6 will be needed.

Solution of the Equation A.6

$$\nabla^4 F_A = E\left(\frac{a_1\pi}{\ell}\right)^2 \sum\sum A_{1i}\, A_{1j} \left[Y_i' Y_j' \sin^2\frac{a_1\pi x}{\ell} + Y_i Y_j'' \cos^2\frac{a_1\pi x}{\ell} \right]$$

Assume $$a_{11} = \frac{2\pi a_1}{\ell} \qquad \text{A.9}$$

Then

$$\sin^2\frac{\pi a_1 x}{\ell} = \sin^2\frac{a_{11}}{2} = \frac{1}{2}(1-\cos a_{11}x)$$

$$\cos^2\frac{\pi a_1 x}{\ell} = \cos^2\frac{a_{11}}{2} = \frac{1}{2}(1+\cos a_{11}x)$$

Substituting the above expressions in equation A.6 and separating the resulting equation as a function of y and as a function of x and y, we obtain the following equation.

$$\nabla^4 F_A = \left(\frac{E}{2}\right)\left(\frac{a_{11}}{2}\right)\sum\sum A_{1i}\, A_{1j} \left\{ (Y_i' Y_j' + Y_i Y_j'') - (Y_i' Y_j' - Y_i Y_j'')\cos a_{11}x \right\} \qquad \text{A.10}$$

The solution of the above equation may be written in the following form :

$$F_A = F_{1A} + F_{2A}\cos a_{11}x \qquad \text{A.11}$$

F_{1A} and F_{2A} are functions of y only. Substitution of equation A.11 into equation A.10 and separating the final equation into its component parts gives the following two equations from which the solutions of F_{1A} and F_{2A} are obtained.

$$F_{1A}'''' = \left(\frac{E}{2}\right)\left(\frac{a_{11}}{2}\right)^2 \sum\sum A_{1i}\, A_{1j}\, (Y_i' Y_j' + Y_i\, Y_j'') \quad \text{A.12}$$

$$F_{2A}'''' - 2a_{11}^2 F_{2A}'' + a_{11}^4 F_{2A} = \left(\frac{E}{2}\right)\left(\frac{a_{11}}{2}\right)^2 \sum\sum A_{1i}\, A_{1j}\, (Y_i\, Y_j'' - Y_i' Y_j') \quad \text{A.13}$$

Because F_{1A} is a function of y only, any derivative of F_{1A} with respect to x is zero, F_{1A} producing a stress in the x direction only, this being $\partial^2 F_{1A}/\partial y^2$ or F_{1A}''. Equation A.12 shall be solved up to second derivative, a sufficient derivation to describe stresses in the x direction.

The function F_{1A} is found by substituting equation A.2 into equation A.12 integrating twice, utilizing the standard procedure for integration by parts. The equation thus obtained will be of the following form.

$$F''_{1A} = \left(\frac{E}{2}\right)\left(\frac{a_{11}}{2}\right)^2 \sum\sum A_{1i} A_{1j} \cos\frac{b_i \pi y}{b} \cos\frac{b_j \pi y}{b} + C_1 y + C_2 \qquad \text{A.14}$$

The constants of integration C_1 and C_2 are obtained by satisfying the boundary conditions at the loaded edges.

Substitution of Y_i and Y_j from equation A.2 into equation A.13 will lead to the following equation.

$$F''''_{2A} - 2a_{11}^2 F''_{2A} + a_{11}^4 F_{2A} = -\left(\frac{E}{4}\right)\left(\frac{a_{11}}{2}\right)^2 \left(\frac{\pi}{b}\right)^2 \sum\sum A_{1i} A_{1j} \{(b_j^2 + b_i b_j)\cos b_{12} y + (b_j^2 - b_i b_j)\cos b_{21} y\} \qquad \text{A.15}$$

where

$$b_{12} = \frac{(b_j - b_i)\pi}{b} \qquad \text{A.16}$$

and

$$b_{21} = \frac{(b_j + b_i)\pi}{b} \qquad \text{A.17}$$

Assuming

$$F_{2A} = \left(\frac{E}{4}\right)\left(\frac{a_{11}}{2}\right)^2\left(\frac{\pi}{b}\right)^2 \psi_{2A} \qquad \text{A.18}$$

and substituting it in equation A.15 we obtain the following differential equation.

$$\psi_{2A}'''' - 2a_{11}^2 \psi_{2A}'' + a_{11}^4 \psi_{2A} = \sum\sum A_{1i} A_{1j}$$

$$\left\{\left(b_j^2 + b_i b_j\right)\cos b_{12} y + \left(b_j^2 - b_i b_j\right)\cos b_{12} y\right\} \qquad \text{A.19}$$

The equation A.19 has a particular integral and a complimentary function solution. Thus :

$$\psi_{2A} = \psi_{2A_{P.I}} + \psi_{2A_{C.F}} \qquad \text{A.20}$$

The particular integral solution of equation A.19 is of the following form.

$$\psi_{2A} = \sum\sum A_{1i} A_{1j} K_1 \cos b_{21} y + K_2 \cos b_{12} y \qquad \text{A.21}$$

Substituting equation A.21 into equation A.19 and equating the coefficients of the resulting equation, we

obtain the following expressions for the constants

$$K_1 = - \frac{b_j(b_j - b_i)}{(b_{21}^2 + a_{11}^2)^2} \qquad \text{A.22}$$

$$K_2 = - \frac{b_j(b_j + b_i)}{(b_{12}^2 + a_{11}^2)^2} \qquad \text{A.23}$$

The complimentary function of equation A.19 is given by :

$$(\psi_{2A})_{cf} = \sum \sum A_{1i} A_{1j} \gamma_{A1} \text{Cos h } a_{11} y + \gamma_{A2} \left(\frac{y}{b}\right) \text{Sinh } a_{11} y$$

A.24

where γ_{A1} and γ_{A2} are constants to be obtained by applying the appropriate boundary conditions. The solution for is given by the sum of the particular integral and complimentary function solutions given by equations A.23 and A.24 respectively which can be substituted in

equation A.20 to obtain the following equation.

$$\psi_{2A} = \sum\sum A_{1i} A_{1j} \left[\gamma_{A1} \cosh a_{11} y + \gamma_{A2} \left(\frac{y}{b}\right) \sin a_{11} y + K_1 \cos b_{21} y + K_2 \cos b_{12} y \right] \quad \text{A.25}$$

Constants of the Complimentary Function

These constants can be evaluated by applying zero normal and shear stress boundary conditions at the unloaded edge. These are :

$$\sigma_y = 0 \qquad \tau_{xy} = 0$$

$$\frac{\partial^2 F_{2A}}{\partial x^2} = 0 \qquad \frac{\partial^2 F_{2A}}{\partial x \partial y} = 0$$

Since F_{2A} is a function of y only, we can write :

$$F_{2A} = 0 \qquad F'_{2A} = 0$$

or

$$\psi_{2A} = 0 \qquad \psi'_{2A} = 0 \qquad \text{at } y = \frac{b}{2}$$

Substituting equation A.24 into the above equations , and then solving the two resulting simultaneous equations we obtain the following expressions for the constants of the complimentary functions.

$$\gamma_{A1} = -\left[\frac{\frac{a_{11}}{2}\cosh\frac{a_{11}b}{2} + \frac{1}{6}\sinh\frac{a_{11}b}{2}}{a_{11}\sinh\frac{a_{11}b}{2}}\right]\gamma_{A2} \qquad \text{A.26}$$

$$\gamma_{A2} = \frac{\tanh\frac{a_{11}b}{2}\left[K_1\cos\beta_2 + K_2\cos\beta_1\right]}{\frac{1}{a_{11}b}\sinh\frac{a_{11}b}{2} + \frac{1}{2}\cosh\frac{a_{11}b}{2} - \frac{1}{2}\sinh\frac{a_{11}b}{2}\tanh\frac{a_{11}b}{2}} \qquad \text{A.27}$$

Evaluation of the Constants C1 and C2

Constants C1 and C2 can be determined by applying boundary conditions at the loaded edge which are zero shear and zero edge displacement.

i.e.,

u=0 at x=1/2

Using equation 2.9(2), chapter two,

$$\varepsilon_x = \frac{\partial u}{\partial x} + \frac{1}{2}\frac{\partial^2 \omega}{\partial x^2}$$

we obtain the following equation for the in-plane displacement u.

$$u = \int_0^x \left[\varepsilon_x - \frac{1}{2}\left(\frac{\partial \omega}{\partial x}\right)^2\right] dx$$

The stress - strain relationship given by the equation 2.11(a), chapter two, is rewritten below.

$$\varepsilon_x = \frac{1}{E}\left[\sigma_x - \nu\sigma_y\right]$$

The stresses σ_x and σ_y can also be expressed in terms of the Airy stress function .

$$\sigma_x = \frac{\partial^2 F_A}{\partial y^2} \qquad \sigma_y = \frac{\partial^2 F_A}{\partial x^2}$$

Using these relations, the following equation for u can be derived.

$$= \int_0^x \left\{\frac{1}{E}\left(\frac{\partial^2 F_A}{\partial y^2} - \nu\frac{\partial^2 F_A}{\partial x^2}\right) - \frac{1}{2}\left(\frac{\partial w}{\partial x}\right)^2\right\} dx \qquad \text{A.28}$$

The out-of-plane deflection w is given by

$$w = \sum A_{ij} \cos\frac{a_i \pi x}{\ell} Y_j$$

Differentiating w with respect to x and squaring we get :

$$\left(\frac{\partial w}{\partial x}\right)^2 = \sum\sum A_{ii} A_{ij} \cos\left(\frac{a_i \pi}{\ell}\right)^2 \sin^2\frac{a_i \pi x}{\ell} Y_i Y_j$$

Substituting $\left(\frac{ow}{ox}\right)^2$ from above equation and derivatives of F_A from equation A.11 in equation 4.28, integrating

between the limits 0 - 1/2 and putting u=0 we get:

$$\frac{\ell}{2E}\left[C_1 y + C_2\right] = 0$$

Since the displacement is zero across the plate:

$C_1=0$ and, therefore, $C_2=0$

Final Expressions for F_A

After obtaining the constants of particular integral and complimentary functions, following expression for can be written.

$$F_A = F_{1A} + F_{2A} \cos a_{11} x \qquad \text{A.29}$$

$$F''_{1A} = \sum\sum A_{1i} A_{1j} C_b(y)$$

$$C_b(y) = \cos\frac{b_i \pi y}{b} \cos\frac{b_j \pi y}{b}$$

$$F_{2A} = \left(\frac{E}{2}\right)\left(\frac{a_{11}}{2}\right)\left(\frac{\pi}{b}\right)\sum\sum A_{1i} A_{1j} f_{2A_{ij}}(y) \qquad \text{A.30}$$

$$f_{2A_{ij}}(y) = \gamma_{A1}\cos a_{11} y + \gamma_{A2}\left(\frac{y}{b}\right)\sin a_{11} y + K_1 \cos b_{21} y + K_2 \cos b_{12} y$$

γ_{A1} and γ_{A2} are given by the equations A.26 and A.27.

Solution of the Equations A.7 and A.8

Since Equations A.6 - A.8 are identical, the solution procedure of A.6 given above can be followed to solve equations A.7 and A.8, each one independently satisfying boundary conditions at the loaded and the unloaded edges. The final solutions for F_B and F_{CD} are given on the following pages.

$$F_B = F_{1B} + F_{2B} \cos a_{22} x \qquad \text{A.31}$$

$$a_{22} = \frac{2\pi a_2}{\ell}$$

$$F''_{1B} = \sum\sum A_{2i} A_{2j} C_6(y) \qquad \text{A.32}$$

$$F_{2B} = \left(\frac{E}{2}\right)\left(\frac{a_{22}}{2}\right)^2\left(\frac{\pi}{b}\right)^2 \sum\sum A_{2i} A_{2j} f_{2B_{ij}}(y) \qquad \text{A.33}$$

$$f_{2Bij}(y) = \gamma_{B1} \cosh a_{22} y + \gamma_{B2}\left(\frac{y}{b}\right) \sinh a_{22} y + K_3 \cos b_{21} y + K_4 \cos b_{12} y$$

$$\gamma_{B1} = -\frac{\frac{a_{22}}{2}\cosh\frac{a_{22}b}{2} + \frac{1}{6}\sinh\frac{a_{22}b}{2}}{a_{22}\sinh\frac{a_{22}b}{2}}\,\gamma_{B2} \qquad \text{A.34}$$

$$\gamma_{B2} = \frac{\tanh\frac{a_{22}}{2}\left(K_3\cos\beta_2 + k_4\cos\beta_1\right)}{\frac{1}{a_{22}b}\sinh\frac{a_{22}b}{2} + \frac{1}{2}\cosh\frac{a_{22}b}{2} - \frac{1}{2}\sinh\frac{a_{22}b}{2}\tanh\frac{a_{22}b}{2}} \qquad \text{A.35}$$

$$K_3 = \frac{b_j(b_j - b_i)}{b_{21}^2 + a_{22}^2} \qquad \text{A.36}$$

$$K_4 = \frac{b_j(b_j + b_i)}{b_{12}^2 + a_{22}^2} \qquad \text{A.37}$$

$$F_{CD} = F_C \cos a_{12} x + F_D \cos a_{21} x \qquad \text{A.38}$$

$$F_C = \frac{E}{2}\left(\frac{\pi}{\ell}\right)^2\left(\frac{\pi}{b}\right)^2 \sum\sum A_{1i} A_{2j} f_C(y) \qquad \text{A.39}$$

$$F_D = \frac{E}{2}\left(\frac{\pi}{\ell}\right)^2\left(\frac{\pi}{b}\right)^2 \sum\sum A_{1i} A_{2j} f_D(y)$$

$$f_C(y) = \gamma_{C1} \cosh a_{12} y + \gamma_{C2} \left(\frac{y}{b}\right) \sinh a_{12} y + K_5 \cos b_{21} y + K_6 \cos b_{12} y$$

$$f_D(y) = \gamma_{D1} \cosh a_{21} y + \gamma_{D2} \left(\frac{y}{b}\right) \sinh a_{21} y + K_7 \cos b_{21} y + K_8 \cos b_{12} y$$

$$\gamma_{C1} = -\left[\frac{\frac{a_{11}}{2}\cosh\frac{a_{11}b}{2} + \frac{1}{6}\sinh\frac{a_{11}b}{2}}{a_{11}\sinh\frac{a_{11}b}{2}} \right]\gamma_{C_2} \qquad \text{A.40}$$

$$\gamma_{C2} = \frac{\tanh\frac{a_{11}b}{2}\left[K_5\cos\beta_2 + K_6\cos\beta_1\right]}{\frac{1}{a_{12}b}\sinh\frac{a_{12}b}{2} + \frac{1}{2}\cosh\frac{a_{12}b}{2} - \frac{1}{2}\sinh\frac{a_{12}b}{2}\tanh\frac{a_{12}b}{2}} \qquad \text{A.41}$$

$$\gamma_{D1} = -\left[\frac{\frac{a_{11}}{2}\cosh\frac{a_{11}b}{2} + \frac{1}{6}\sinh\frac{a_{11}b}{2}}{a_{11}\sinh\frac{a_{11}b}{2}} \right]\gamma_{D_2} \qquad \text{A.42}$$

$$\gamma_{D2} = \frac{\tanh\frac{a_{11}b}{2}\left[K_7\cos\beta_2 + K_8\cos\beta_1\right]}{\frac{1}{a_{12}b}\sinh\frac{a_{12}b}{2} + \frac{1}{2}\cosh\frac{a_{12}b}{2} - \frac{1}{2}\sinh\frac{a_{12}b}{2}\tanh\frac{a_{12}b}{2}} \qquad \text{A.43}$$

$$K_5 = \frac{b_j(b_j - b_i)}{b_{21}^2 + a_{12}^2} \qquad \text{A.44}$$

$$K_6 = \frac{b_j(b_j + b_i)}{b_{12}^2 + a_{12}^2} \qquad \text{A.45}$$

$$K_7 = \frac{b_j(b_j - b_i)}{b_{21}^2 + a_{21}^2} \qquad \text{A.46}$$

$$K_8 = \frac{b_j(b_j + b_i)}{b_{12}^2 + a_{21}^2} \qquad \text{A.47}$$

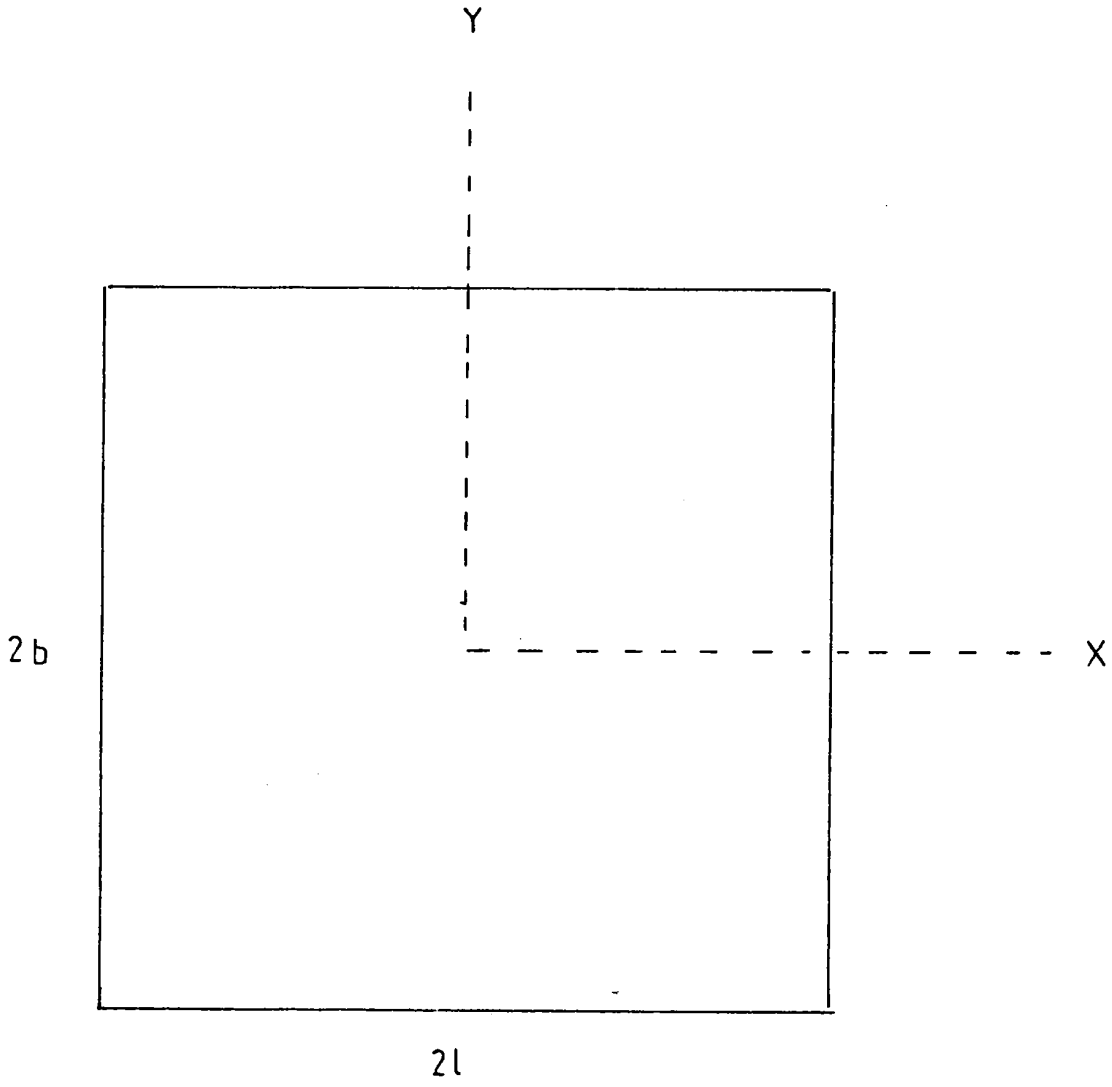

FIGURE A.1 A TYPICAL UNPERFORATED PLATE

APPENDIX B

DERIVATION OF THE ENERGY EXPRESSIONS

DERIVATION OF THE STRAIN ENERGY

DUE TO MEMBRANE STRESSES

Equation for the strain energy due to membrane stresses given by the equation 2.19, and is rewritten below:

$$V_m = \frac{t}{2E}\iint\left[\sigma_x^2 + \sigma_y^2 - 2\nu\sigma_x\sigma_y + 2(1+\nu)\tau_{xy}^2\right]dx\,dy \qquad \text{B.1}$$

The stresses σ_x, σ_y and τ_{xy} relate to the direct and shear stresses and are evaluated by combining the stresses from the three stress systems described in chapter four, section 4.2.2.

Thus :

$$\begin{aligned}\sigma_x &= \sigma_{x_1} + \sigma_{x_2} + \sigma_{x_3}\\ \sigma_y &= \sigma_{y_1} + \sigma_{y_2} + \sigma_{y_3}\\ \tau_{xy} &= \tau_{xy_1} + \tau_{xy_2} + \tau_{xy_3}\end{aligned} \qquad \text{B.2}$$

The mathematical expressions for the stresses of the three stress systems derived in chapter four and appendix A are represented in the following paragrphs.

The stress system 1 consist of the stresses σ_{x1}, σ_{y1} and τ_{xy1} which are generated in a perforated plate due to the applied displacement assuming no out-of-plane deflections. These stresses are independent of the deflection coefficients A_{ij} . These stresses are represented by the bi-cubic B-spline functions as described in chapter four, section 4.5.1.1. The stresses evaluated at the time of buckling can be multiplied by a load factor ϕ_p corresponding to any load level in the post-buckling region.

Thus:

$$\sigma_{x1} = \phi_p S_{1x}$$
$$\sigma_{y1} = \phi_p S_{1y}$$
$$\tau_{xy1} = \phi_p S_{1\tau} \qquad \text{B.3}$$

$$S_{1x} = \sum\sum C_{x_{ij}} M_i(x) N_j(y)$$

$$S_{1y} = \sum\sum C_{y_{ij}} M_i(x) N_j(y)$$

$$S_{1\tau} = \sum\sum C_{\tau_{ij}} M_i(x) N_j(y)$$

The stresses in system 2, σ_{x2}, σ_{y2} and τ_{xy2} are the post-buckling stresses of an unperforated plate assuming zero in-plane displacement of the loaded edges. The solution of Von Karman compatibility equation to obtain these stresses is given in appendix A. These stresses are expressed in the following form:

$$\sigma_{x_2} = \sum\sum A_{1i} A_{1j} S_{2xA_{ij}} + \sum\sum A_{2i} A_{2j} S_{2xB_{ij}} + \sum\sum A_{1i} A_{2j} S_{2xC_{ij}}$$

$$\sigma_{y_2} = \sum\sum A_{1i} A_{1j} S_{2yA_{ij}} + \sum\sum A_{2i} A_{2j} S_{2yC_{ij}} + \sum\sum A_{1i} A_{2j} S_{2yC_{ij}}$$

$$\tau_{xy_2} = \sum\sum A_{1i} A_{1j} S_{2TA_{ij}} + \sum\sum A_{2i} A_{2j} S_{2TB_{ij}} + \sum\sum A_{1i} A_{2j} S_{2TC_{ij}}$$

B.4

where

$$S_{2XA_{ij}} = \frac{\partial^2 F_A}{\partial Y^2} \quad , \quad S_{2YA_{ij}} = \frac{\partial^2 F_A}{\partial X^2} \quad , \quad S_{2TA_{ij}} = \frac{\partial^2 F_A}{\partial X \partial Y}$$

$$S_{2XB_{ij}} = \frac{\partial^2 F_B}{\partial Y^2} \quad , \quad S_{2YB_{ij}} = \frac{\partial^2 F_B}{\partial X^2} \quad , \quad S_{2TB_{ij}} = \frac{\partial^2 F_B}{\partial X \partial Y}$$

$$S_{2XC_{ij}} = \frac{\partial^2 F_{CD}}{\partial Y^2} \quad , \quad S_{2YC_{ij}} = \frac{\partial^2 F_{CD}}{\partial X^2} \quad , \quad S_{2TC_{ij}} = \frac{\partial^2 F_{CD}}{\partial X \partial Y}$$

Expressions for F_A F_B and F_{CD} can be found in appendix A, equations A.29, A.34 and A.38 respectively.

The stresses in system 3, σ_{x3}, σ_{y3} and τ_{xy3} are the stresses which are obtained after applying stresses from system2 at the hole edge for each combination of for a unit value. Therefore, σ_{x3}, σ_{y3} and τ_{xy3} are functions of A_{ij}, A_{mn}.

Thus :

$$\sigma_{x_3} = \sum\sum A_{1i} A_{1j} S_{3xA_{ij}} + \sum\sum A_{2i} A_{2j} S_{3xB_{ij}} + \sum\sum A_{1i} A_{2j} S_{3xC_{ij}}$$

$$\sigma_{y_3} = \sum\sum A_{1i} A_{1j} S_{3yA_{ij}} + \sum\sum A_{2i} A_{2j} S_{3yB_{ij}} + \sum\sum A_{1i} A_{2j} S_{3yC_{ij}}$$

$$\tau_{xy_3} = \sum\sum A_{1i} A_{1j} S_{3TA_{ij}} + \sum\sum A_{2i} A_{2j} S_{3TB_{ij}} + \sum\sum A_{12} S_{3TC_{ij}} \qquad \text{B.4A}$$

$$S_{3x} = \sum\sum C_{3x_{ij}} M_i(x) N_j(y)$$

$$S_{3y} = \sum\sum C_{3y_{ij}} M_i(x) N_j(y)$$

$$S_{3T} = \sum\sum C_{3T_{ij}} M_i(x) N_j(y)$$

Subtitution of the above expressions for the three stress systems from the equations above in equation B.1 and further simplifications to combine like terms together gives rise to the following equation for the strain energy due to membrane stresses.

$$U_M = \frac{t}{2E}\iint\Big[\sum\sum\sum\sum A_{1i}A_{1j}A_{1m}A_{1n}\psi_A + \sum\sum\sum\sum A_{1i}A_{1j}A_{1m}A_{2n}\psi_B + \sum\sum\sum\sum A_{1i}A_{1j}A_{2m}A_{2n}\psi_C + \sum\sum\sum\sum A_{1i}A_{2j}A_{1m}A_{2n}\psi_D + \sum\sum\sum\sum A_{1i}A_{2j}A_{2m}A_{2n}\psi_E + \sum\sum\sum\sum A_{2i}A_{2j}A_{2m}A_{2n}\psi_F + \sum\sum A_{1i}A_{1j}\psi_G + \sum\sum A_{1i}A_{2j}\psi_H + \sum\sum A_{2i}A_{2j}\psi_K\Big]\,dx\,dy \qquad \text{B.5}$$

ψ_A to ψ_K are given by the equations B.6 to B.14 in the following pages.

$$\psi_A = S2XA_{ij}\ S2XA_{mn} + S3XA_{ij}\ S3XA_{mn}$$
$$+ S2XA_{ij}\ S3XA_{mn} + S2YA_{ij}\ S2YA_{mn}$$
$$+ S3YA_{ij}\ S3YA_{mn} + S2YA_{ij}\ S3YA_{mn}$$
$$-2\nu\left[S2XA_{ij}\ S2YA_{mn} + S2XA_{ij}\ S3YA_{mn}\right.$$
$$\left. + S2YA_{ij}\ S3XA_{mn} + S3XA_{ij}\ S3YA_{mn}\right]$$
$$+ 2(1+\nu)\left[S2TA_{ij}\ S2TA_{mn} + S3TA_{ij}\ S3TA_{mn}\right.$$
$$\left. + 2\ S2TA_{ij}\ S3TA_{mn}\right] \qquad \text{B.6}$$

$$\psi_B = S2XA_{ij}\ S2XC_{mn} + S3XA_{ij}\ S3XC_{mn}$$
$$+ S2XA_{ij}\ S3XC_{mn} + S3XA_{ij}\ S2XC_{mn}$$
$$+ S2YA_{ij}\ S2YC_{mn} + S3YA_{ij}\ S3YC_{mn}$$
$$+ S2YA_{ij}\ S3YC_{mn} + S3YA_{ij}\ S2YC_{mn}$$
$$- 2\nu\left[S2XA_{ij}\ S2YC_{mn} + S2YA_{ij}\ S2XC_{mn}\right.$$
$$+ S2XA_{ij}\ S3YC_{mn} + S3YA_{ij}\ S2XC_{mn}$$
$$+ S2YA_{ij}\ S3XC_{mn} + S3XA_{ij}\ S2YC_{mn}$$
$$\left. + S3XA_{ij}\ S3YC_{mn} + S3YA_{ij}\ S3XC_{mn}\right]$$
$$+ 4(1+\nu)\left[S2TA_{ij}\ S2TC_{mn} + S3TA_{ij}\ S3TC_{mn}\right.$$
$$\left. + S2TA_{ij}\ S3TC_{mn} + S3TA_{ij}\ S2TC_{mn}\right] \qquad \text{B.7}$$

$$\psi_C = S2XA_{ij}\ S2XB_{mn} + S3XA_{ij}\ S3XB_{mn}$$
$$+ S2XA_{ij}\ S3XB_{mn} + S3XA_{ij}\ S2XB_{mn}$$
$$+ S2YA_{ij}\ S2YB_{mn} + S3YA_{ij}\ S3YB_{mn}$$
$$+ S2YA_{ij}\ S3YB_{mn} + S3YA_{ij}\ S2YB_{mn}$$
$$- 2\nu\left[S2XA_{ij}\ S2YB_{mn} + S2YA_{ij}\ S2XB_{mn}\right.$$
$$+ S2XA_{ij}\ S3YB_{mn} + S3YA_{ij}\ S2XB_{mn}$$
$$+ S2YA_{ij}\ S3XB_{mn} + S3XA_{ij}\ S2YB_{mn}$$
$$\left.+ S3XA_{ij}\ S3YB_{mn} + S3YA_{ij}\ S3XB_{mn}\right]$$
$$+ 4(1+\nu)\left[S2TA_{ij}\ S2TB_{mn} + S3TA_{ij}\ S3TB_{mn}\right.$$
$$\left.+ S2TA_{ij}\ S3TB_{mn} + S3TA_{ij}\ S2TB_{mn}\right] \qquad \text{B.8}$$

$$\psi_D = S2XC_{ij}\ S2XC_{mn} + S3XC_{ij}\ S3XC_{mn}$$
$$+ S2XC_{ij}\ S3XC_{mn} + S2YC_{ij}\ S2YC_{mn}$$
$$+ S3YC_{ij}\ S3YC_{mn} + S2YC_{ij}\ S3YC_{mn}$$
$$- 2\nu\left[S2XC_{ij}\ S2YC_{mn} + S2XC_{ij}\ S3YC_{mn}\right.$$
$$\left.+ S2YC_{ij}\ S3XC_{mn} + S3XC_{ij}\ S3YC_{mn}\right]$$
$$+ 2(1+\nu)\left[S2TC_{ij}\ S2TC_{mn} + S3TC_{ij}\ S3TC_{mn}\right.$$
$$\left.+ 2\ S2TC_{ij}\ S3TC_{mn}\right] \qquad \text{B.9}$$

$$\psi_E = S_{2XB_{ij}} S_{2XC_{mn}} + S_{3XB_{ij}} S_{3XC_{mn}}$$
$$+ S_{2XB_{ij}} S_{3XC_{mn}} + S_{3XB_{ij}} S_{2XC_{mn}}$$
$$+ S_{2YB_{ij}} S_{2YC_{mn}} + S_{3YB_{ij}} S_{3YC_{mn}}$$
$$+ S_{2YB_{ij}} S_{3YC_{mn}} + S_{3YB_{ij}} S_{2YC_{mn}}$$
$$- 2\nu \left[S_{2XB_{ij}} S_{2YC_{mn}} + S_{2YB_{ij}} S_{2XC_{mn}} \right.$$
$$+ S_{2XB_{ij}} S_{3YC_{mn}} + S_{3YB_{ij}} S_{2XC_{mn}}$$
$$+ S_{2YB_{ij}} S_{3XC_{mn}} + S_{3XB_{ij}} S_{2YC_{mn}}$$
$$\left. + S_{3XB_{ij}} S_{3YC_{mn}} + S_{3YB_{ij}} S_{3XC_{mn}} \right]$$
$$+ 4(1+\nu) \left[S_{2TB_{ij}} S_{2TC_{mn}} + S_{3TB_{ij}} S_{3TC_{mn}} \right.$$
$$\left. + S_{2TB_{ij}} S_{3TC_{mn}} + S_{3TB_{ij}} S_{2TC_{mn}} \right] \qquad \text{B.10}$$

$$\psi_F = S_{2XB_{ij}} S_{2XB_{mn}} + S_{3XB_{ij}} S_{3XB_{mn}}$$
$$+ S_{2XB_{ij}} S_{3XB_{mn}} + S_{2YB_{ij}} S_{2YB_{mn}}$$
$$+ S_{3YB_{ij}} S_{3YB_{mn}} + S_{2YB_{ij}} S_{3YB_{mn}}$$
$$- 2\nu \left[S_{2XB_{ij}} S_{2YB_{mn}} + S_{2XB_{ij}} S_{3YB_{mn}} \right.$$
$$\left. + S_{2YB_{ij}} S_{3XB_{mn}} + S_{3XB_{ij}} S_{3YB_{mn}} \right]$$
$$+ 2(1+\nu) \left[S_{2TB_{ij}} S_{2TB_{mn}} + S_{3TB_{ij}} S_{3TB_{mn}} \right.$$
$$\left. + S_{2TB_{ij}} S_{3TB_{mn}} \right] \qquad \text{B.11}$$

$$\psi_G = 2\phi\left[S_{1X}\left(S_{2XA_{ij}} + S_{3XA_{ij}} - \gamma\left(S_{2YA_{ij}} + S_{3YA_{ij}}\right.\right.\right.$$

$$+ S_{1Y}\left(S_{2YA_{ij}} + S_{3YA_{ij}} - \gamma\left(S_{2XA_{ij}} + S_{3XA_{ij}}\right)\right)$$

$$\left. + 2\ S_{1T(1+\gamma)}\left(S_{2TA_{ij}} + S_{3TA_{ij}}\right)\right] \qquad \text{B.12}$$

$$\psi_H = 2\phi\left[S_{1X}\left(S_{2XC_{ij}} + S_{3XC_{ij}} - \gamma\left(S_{2YC_{ij}} + S_{3YC_{ij}}\right)\right)\right.$$

$$+ S_{1Y}\left(S_{2YC_{ij}} + S_{3YC_{ij}} - \gamma\left(S_{2XC_{ij}} + S_{3XC_{ij}}\right)\right)$$

$$\left. + 2\ S_{1T(1+\gamma)}\left(S_{2TC_{ij}} + S_{3TC_{ij}}\right)\right] \qquad \text{B.13}$$

$$\psi_K = 2\phi\left[S_{1X}\left(S_{2XB_{ij}} + S_{3XB_{ij}} - \gamma\left(S_{2YB_{ij}} + S_{3YB_{ij}}\right)\right)\right.$$

$$+ S_{1Y}\left(S_{2YB_{ij}} + S_{3YB_{ij}} - \gamma\left(S_{2XB_{ij}} + S_{3XB_{ij}}\right)\right)$$

$$\left. + 2\ S_{1T(1+\gamma)}\left(S_{2TB_{ij}} + S_{3TB_{ij}}\right)\right] \qquad \text{B.14}$$